

# **NMR Spectroscopic Investigations on Zintl Anions, Palladium Complexes, and Non-Classical Fullerene Topology**

## **Dissertation**

Zur Erlangung des Doktorgrades der Naturwissenschaften

(Dr. rer. nat.)

an der Fakultät für Chemie und Pharmazie

der Universität Regensburg



vorgelegt von

**Florian Hastreiter**

aus Straubing

**Juni 2019**



Die vorliegende Dissertation beruht auf Arbeiten, die zwischen Februar 2014 und September 2018 am Arbeitskreis von Frau Professor Dr. Ruth M. Gschwind am Institut für Organische Chemie der Universität Regensburg durchgeführt wurden.

Promotionsgesuch eingereicht am:	27.06.2019
Die Arbeit wurde angeleitet von:	Prof. Dr. Ruth M. Gschwind
Promotionsausschuss:	
Vorsitzender:	Prof. Dr. Alkwin Slenczka
1. Gutachter:	Prof. Dr. Ruth M. Gschwind
2. Gutachter:	Prof. Dr. Nikolaus Korber
3. Prüfer:	Prof. Dr. Julia Rehbein



An dieser Stelle möchte ich mich bei allen bedanken, die zum Gelingen dieser Arbeit beigetragen haben. Besonderer Dank gilt meiner Doktormutter Frau Prof. Dr. Ruth M. Gschwind für die interessante und anspruchsvolle Themenstellung, sowie für alles was ich in meiner Zeit am Arbeitskreis Gschwind gelernt habe.

Herrn Prof. Dr. Nikolaus Korber danke ich für die Übernahme des Zweitgutachtens und die Möglichkeit zur Bearbeitung äußerst spannender Kooperationsprojekte.

Bei Frau Prof. Dr. Julia Rehbein und Herrn Prof. Dr. Alkwin Slenczka möchte ich mich für die Ausübung des Amtes als Prüfer bzw. als Vorsitzender recht herzlich bedanken.

Meinen Kooperationspartnern auf dem Gebiet der Zintl-Phasen, Corinna Lorenz und Stefanie Gärtner möchte ich für die konstruktiven Diskussionen und die erfolgreiche Zusammenarbeit danken. Susanne Tiefenthaler und Verena Steitferdt danke ich für die Weiterführung der Forschung auf diesem Gebiet und wünsche ihnen viel Erfolg und weiterhin tolle Ergebnisse.

Claudia Heindl und Barbara Krämer vom Arbeitskreis von Prof. Dr. Manfred Scheer danke ich für die erfolgreiche Zusammenarbeit auf dem Gebiet nichtklassischer Fulleren-Topologika.

Ich danke auch Dr. Robert Wilson vom Arbeitskreis von Frau Prof. Dr. Stefanie Dehnen und PD Dr. Florian Weigend für die Zusammenarbeit auf dem Gebiet endohedralem Kobalt in Zinn-Antimon-Cluster.

Den Forschungspraktikanten Markus Baum, Julian Müller, Matthias Weiß und Patrick Neckermann danke ich für ihre engagierte Mitarbeit.

Besonderen Dank möchte ich an meine ehemaligen und aktuellen Kollegen aussprechen, die mich sowohl mit wertvollen Ratschlägen und Anregungen unterstützt haben als auch so manchen Arbeitstag mit Kaffeepausen, Grillabenden, Feierabendbiere und anderen anregenden Aktionen (insbesondere Bouldern) bereichert haben. Vielen Dank euch allen: Dr. Carina Koch, Dr. Felicitas v. Rekowski, Dr. Nils Sorgenfrei, Dr. Hanna Bartling, Dr. Michael Haindl, Dr. Michael Hammer, Dr. Julian Greindl, Dr. Andreas Seegerer, Dr. Johnny Hioe, Dr. Nanjundappa Lokesh, Dr. Matej Zabka, Dr. Fabio Morana, Philipp Nitschke, Kerstin Rothermel, Verena Streitferdt, Nele Berg, Johannes „Gizzmo“ Gramüller und Willibald „Paper Willi“ Stockerl.

Ich danke Nikola Kastner-Pustet und allen Mitarbeitern der NMR-Abteilung, Dr. Ilya Shenderovich, Fritz Kastner, Annette Schramm, Georgine Stühler und Veronika Scheidler, sowie unserer Sekretärin Ulrike Weck für ihre stets freundliche Hilfe und Unterstützung in technischen und bürokratischen Dingen.

Großer Dank gilt allen meinen Freunden, die mir außerhalb der Universität die nötige Ablenkung verschafft haben, insbesondere der „Bangerz-Gang“ und meinen Schulfreunden.

Meiner Freundin Vroni danke ich für ihre Unterstützung und Motivierung vor allem in den letzten Monaten. Ebenso danke ich der gesamten Familie Oberneder für ihre herzliche Aufnahme.

Zuletzt, aber nicht weniger dankbar bin ich für die Unterstützung meiner Familie, besonders meinen Eltern und meinen Geschwistern danke ich für ihren Rückhalt während meines bisherigen Werdegangs.

**Vielen Dank!**



**NMR Spectroscopic Investigation on  
Zintl Anions, Palladium Complexes,  
and Non-Classical Fullerene Topology**





# Table of Contents

1	Introduction and Outline.....	1
1.1	Zintl anions and spherical supramolecules .....	1
1.2	References .....	4
2	Structure of $[\text{HSi}_9]^{3-}$ in Solid State and Its Unexpectedly High Dynamics in Solution .....	7
2.1	Abstract .....	8
2.2	Introduction.....	8
2.3	Results and Discussion .....	10
2.4	Conclusions.....	15
2.5	Supporting Information.....	16
2.5.1	General experimental details .....	16
2.5.1.1	Synthesis of the Zintl phases and solvate structure.....	16
2.5.1.2	Solid phase characterization .....	17
2.5.1.3	Details of Single Crystal X-Ray diffraction .....	19
2.5.2	Sample preparation for NMR .....	26
2.5.2.1	Solvation of the Zintl phases in liquid ammonia .....	26
2.5.2.2	NMR procedures.....	26
2.5.2.3	Temperature dependent NMR measurements (203 – 243 K).....	26
2.5.2.4	Comparison of experimental and calculated $^1\text{H}^{29}\text{Si}$ -HMQC intensity buildup for $\text{Si}_8$ moiety	28
2.5.2.5	2D $^1\text{H}^{29}\text{Si}$ -HMQC experiment .....	29
2.5.2.6	Estimation of exchange rate constant range by line width analysis and CEST experiments.....	30
2.5.2.7	CEST measurements .....	30
2.5.3	Theoretical calculations.....	31
2.5.3.1	Theoretical calculated values for chemical shifts and coupling constants .....	31
2.5.3.2	MD simulation of the $[\text{HSi}_9]^{4-}$ cluster .....	32
2.5.3.3	Detailed description of the averaging of the $\text{Si}_8$ moiety .....	33
2.5.3.4	Computational Details.....	33
2.5.3.5	Calculated Geometry.....	34
2.5.3.6	Marcus analysis of the scrambling process via TS1.....	37
2.5.3.7	Thermochemical analysis of the Zintl cluster.....	38
2.6	References .....	39
3	Elusive Zintl Ions $[\mu\text{-HSi}_4]^{3-}$ and $[\text{Si}_5]^{2-}$ in Liquid Ammonia: Protonation States, Sites, and Bonding Situation Evaluated by NMR and Theory .....	43

3.1	Abstract .....	44
3.2	Introduction.....	44
3.3	Results and Discussion .....	45
3.4	Conclusions.....	52
3.5	Supporting Information.....	53
3.5.1	General experimental details .....	53
3.5.1.1	Synthesis of the Zintl phase.....	53
3.5.1.2	Solid phase characterization .....	53
3.5.2	NMR spectroscopy.....	55
3.5.2.1	Solvation of the Zintl phases in liquid ammonia .....	55
3.5.2.2	General NMR procedures.....	55
3.5.2.3	Overview of $^1\text{H}$ and $^{29}\text{Si}$ spectra .....	56
3.5.2.4	$^1\text{H}^{29}\text{Si}$ HMQC spectra .....	57
3.5.2.5	Steady state NOE-type experiment.....	57
3.5.2.6	Byproducts and degradation products in liquid ammonia.....	58
3.5.2.7	Selected $^{29}\text{Si}$ spectra under different experimental conditions .....	60
3.5.2.8	VT-NMR spectra.....	61
3.5.3	Theoretical calculations.....	62
3.5.3.1	ELI-D analysis .....	62
3.5.3.2	NBO analysis .....	65
3.5.3.3	Computational Details.....	70
3.5.3.4	Cartesian Coordinates .....	71
3.6	Additional Findings .....	72
3.7	References.....	78
4	$[\text{Co}@_{\text{Sn}_6}\text{Sb}_6]^{3-}$ : An Off-Center Endohedral 12-Vertex Cluster.....	83
4.1	Abstract .....	84
4.2	Introduction.....	84
4.3	Results and Discussion .....	86
4.4	Conclusions.....	92
4.5	Supporting Information.....	93
4.5.1	Experimental .....	93
4.5.1.1	General considerations.....	93
4.5.1.2	Synthesis of compounds.....	93
4.5.2	Single Crystal X-Ray Diffraction .....	96
4.5.2.1	General considerations.....	96
4.5.2.2	Structure refinement details for $[\text{K}(\text{crypt-222})]_3[\text{Co}@_{\text{Sn}_6}\text{Sb}_6]_{0.825}[\text{Co}_2@_{\text{Sn}_5}\text{Sb}_7]_{0.175} \cdot 2\text{dmf} \cdot 2\text{tol}$ .....	96

4.5.2.3	Structure refinement details for [K(crypt-222)] <sub>3</sub> [Co <sub>2</sub> @Sn <sub>5</sub> Sb <sub>7</sub> ] .....	100
4.5.2.4	Structure refinement details for [K(crypt-222)] <sub>3</sub> [Ni <sub>2</sub> @Sn <sub>7</sub> Sb <sub>5</sub> ]·2en·2tol .....	105
4.5.3	Mass Spectrometry.....	107
4.5.3.1	Methods .....	107
4.5.3.2	High resolution mass signals obtained from crystals of [K(crypt-222)] <sub>3</sub> [Co@Sn <sub>6</sub> Sb <sub>6</sub> ] <sub>0.825</sub> [Co <sub>2</sub> @Sn <sub>5</sub> Sb <sub>7</sub> ] <sub>0.175</sub> ·2dmf·2tol .....	108
4.5.3.3	High resolution mass signals obtained from powder from crude synthesis of [K(crypt-222)] <sub>3</sub> [Co <sub>2</sub> @Sn <sub>5</sub> Sb <sub>7</sub> ] .....	114
4.5.3.4	High resolution mass signals obtained from single crystals of [K(crypt-222)] <sub>3</sub> [Ni <sub>2</sub> @Sn <sub>7</sub> Sb <sub>5</sub> ]·2en·2tol .....	117
4.5.3.5	High resolution mass signals obtained from powder from crude synthesis of [K(crypt-222)] <sub>3</sub> [Ni <sub>2</sub> Sn <sub>7</sub> Sb <sub>5</sub> ] .....	120
4.5.4	Micro-X-ray Fluorescence Spectroscopy (μ-XFS).....	122
4.5.5	<sup>119</sup> Sn NMR .....	125
4.5.5.1	Methods .....	125
4.5.6	Quantum Chemical Investigations .....	129
4.5.6.1	Quantum Chemical Methods and Comparison of Isomers .....	129
4.5.6.2	Comparison of bond lengths .....	130
4.5.6.3	Study of the influence of electron numbers on the structures.....	131
4.5.6.4	Calculation of chemical shifts .....	132
4.6	References .....	136
5	<i>cyclo</i> -P <sub>4</sub> Building Blocks: Achieving Non-Classical Fullerene Topology and Beyond .....	139
5.1	Abstract .....	140
5.2	Introduction.....	140
5.3	Results and Discussion .....	142
5.4	Conclusions.....	149
5.5	Supporting Information.....	150
5.5.1	Experimental Part.....	150
5.5.1.1	Synthesis of [Cp''Ta(CO) <sub>2</sub> (η <sup>4</sup> -P <sub>4</sub> )] (1b).....	150
5.5.1.2	Synthesis of [{Cp''Ta(CO) <sub>2</sub> (μ <sub>5</sub> -η <sup>4</sup> :η <sup>1</sup> :η <sup>1</sup> :η <sup>1</sup> :η <sup>1</sup> -P <sub>4</sub> )} <sub>6</sub> {CuBr} <sub>7.6</sub> ] (2b) .....	150
5.5.1.3	Synthesis of [{Cp''Ta(CO) <sub>2</sub> (μ <sub>5</sub> -η <sup>4</sup> :η <sup>1</sup> :η <sup>1</sup> :η <sup>1</sup> :η <sup>1</sup> -P <sub>4</sub> )} <sub>6</sub> {CuCl} <sub>7.4</sub> ] (2c) .....	151
5.5.1.4	Synthesis of [{Cp''Ta(CO) <sub>2</sub> (μ <sub>5</sub> -η <sup>4</sup> :η <sup>1</sup> :η <sup>1</sup> :η <sup>1</sup> :η <sup>1</sup> -P <sub>4</sub> )} <sub>6</sub> {CuBr} <sub>7.7</sub> ] (2d) .....	152
5.5.1.5	Synthesis of [{Cp''Ta(CO) <sub>2</sub> (μ <sub>5</sub> -η <sup>4</sup> :η <sup>1</sup> :η <sup>1</sup> :η <sup>1</sup> :η <sup>1</sup> -P <sub>4</sub> )} <sub>6</sub> {Cp''Ta(CO) <sub>2</sub> (μ <sub>4</sub> -η <sup>4</sup> :η <sup>1</sup> :η <sup>1</sup> :η <sup>1</sup> :η <sup>1</sup> -P <sub>4</sub> )} <sub>4</sub> {Cu <sub>14</sub> I <sub>10</sub> (μ-I) <sub>2</sub> (μ <sub>3</sub> -I) <sub>2</sub> }] (3) and [{Cp''Ta(CO) <sub>2</sub> (μ <sub>5</sub> -η <sup>4</sup> :η <sup>1</sup> :η <sup>1</sup> :η <sup>1</sup> :η <sup>1</sup> -P <sub>4</sub> )} <sub>5</sub> {Cu <sub>12</sub> I <sub>3</sub> (μ-I) <sub>8</sub> (μ <sub>4</sub> -I)(MeCN) <sub>5</sub> }] (4).....	153
5.5.1.6	Selective synthesis of [{Cp''Ta(CO) <sub>2</sub> (μ <sub>5</sub> -η <sup>4</sup> :η <sup>1</sup> :η <sup>1</sup> :η <sup>1</sup> :η <sup>1</sup> -P <sub>4</sub> )} <sub>5</sub> {Cu <sub>12</sub> I <sub>3</sub> (μ-I) <sub>8</sub> (μ <sub>4</sub> -I)(MeCN) <sub>5</sub> }] (4) .....	153
5.5.1.7	Synthesis of [{Cp''Ta(CO) <sub>2</sub> (μ <sub>5</sub> -η <sup>4</sup> :η <sup>1</sup> :η <sup>1</sup> :η <sup>1</sup> :η <sup>1</sup> -P <sub>4</sub> )} <sub>6</sub> {Cu <sub>4</sub> (μ <sub>3</sub> -I) <sub>4</sub> }] <sub>n</sub> (5) .....	154

5.5.2	X-ray Structure Analysis.....	155
5.5.2.1	General remarks .....	155
5.5.2.2	Crystal structure of 1b.....	161
5.5.2.3	Crystal structure of 2b.....	162
5.5.2.4	Preliminary data on the crystal structure of 2c.....	165
5.5.2.5	Crystal structure of 2d.....	167
5.5.2.6	A comparison of the supramolecules in 2b and 2d.....	170
5.5.2.7	Crystal structure of 3.....	171
5.5.2.8	Topological interrelation between inorganic scaffolds of the supramolecules 2 and 3 174	
5.5.2.9	Crystal structures and isomerism in compound 4.....	175
5.5.2.10	Crystal structure of 5.....	178
5.5.3	Size Estimation from DOSY Experiments.....	180
5.5.3.1	Spectroscopic Details.....	180
5.5.3.2	Size Estimation .....	180
5.5.4	Additional Figures.....	181
5.6	References .....	182
6	A Nano-sized Supramolecule Beyond the Fullerene Topology .....	185
6.1	Abstract .....	186
6.2	Introduction.....	186
6.3	Results and Discussion .....	187
6.4	Conclusions.....	191
6.5	Supporting Information.....	193
6.5.1	Experimental Part.....	193
6.5.1.1	Synthesis of $(\text{CH}_2\text{Cl}_2)_{3.4}@\{[\text{Cp}^{\text{Bn}}\text{Fe}(\mu_6\text{-}\eta^5\text{:}\eta^1\text{:}\eta^1\text{:}\eta^1\text{:}\eta^1\text{-P}_5)\}_{12}(\text{CuI})_{54}(\text{CH}_3\text{CN})_{1.46}\}$ (2).....	193
6.5.1.2	Synthesis of $[\{\text{Cp}^{\text{Bn}}\text{Fe}(\mu_5\text{-}\eta^5\text{:}\eta^1\text{:}\eta^1\text{:}\eta^1\text{-P}_5)\}_2\{\text{Cu}_6(\mu\text{-I})_2(\mu_3\text{-I})_4\}]_n$ (3) .....	194
6.5.2	X-Ray Structure Analysis.....	195
6.5.2.1	Data Collection and Refinement .....	195
6.5.2.2	Description of crystal structure 2 .....	198
6.5.2.3	Selected Bond distances.....	201
6.5.3	Size Estimation from DOSY.....	206
6.5.3.1	Spectroscopic Details.....	206
6.5.3.2	Size Estimation .....	206
6.6	References .....	207
7	NMR investigations on Phosphoramidite Palladium Complexes and the Supramolecular Balance 211	
7.1	Abstract .....	212

7.2	Introduction.....	212
7.3	Results and Discussion .....	215
7.3.1	Symmetric Phosphoramidite Ligands.....	215
7.3.2	Theoretical Calculations and Asymmetric Phosphoramidite Ligands .....	217
7.3.3	Assignment Strategy for Phosphoramidite Ligands .....	220
7.3.4	Formation Trends for different ligand combinations.....	226
7.4	Outlook.....	227
7.5	Conclusions.....	228
7.6	Supporting Information.....	229
7.6.1	Preparation of phosphoramidite ligands.....	229
7.6.1.1	Sample preparation for NMR .....	229
7.6.1.2	General remarks on NMR.....	229
7.6.2	Theoretical Calculations .....	239
7.7	References.....	241
8	Summary.....	243
9	Appendix.....	247
9.1	Curriculum Vitae.....	247
9.2	Publications and Conferences .....	248



# 1 Introduction and Outline

## 1.1 Zintl anions and spherical supramolecules

Already in the beginning of the 19<sup>th</sup> century Charles Babbage designed the first mechanical calculating machines, i.e. the difference engine and the analytical engine, which represent the precursor to our modern-day computers. The first fully functional digital computer – previous computers such as the Z1, the Turing machine, the Colossus and the ABC were not yet programmable – was the Electronic Numerical Integrator and Computer (ENIAC) built by J. Presper Eckert and John Mauchly in 1946. Their computer occupied nearly 170 m<sup>2</sup> and weighed almost 50 tons. Today – merely over 70 years later – smartphones are used daily which seem ridiculously miniscule compared to their ancestor but excel them tremendously in efficiency and processing power. In those 70 years computers went from taking up space of a whole building to fitting in a pocket, yet an ever-growing demand for still smaller, faster, and more efficient electronic devices is inevitable in the modern age of computer technology. Silicon is the main component in integrated circuits, semiconductors, microelectronic devices, and solar cells.<sup>[1-5]</sup> However, the diminishing of these microelectronic devices – is limited by their preparation techniques. The state of art techniques for microfabrication are photolithography, thin film deposition, and etching; the most prominent being chemical vapor deposition (CVD) technique on solid substrates.<sup>[5,6]</sup>

These top-down approaches are susceptible to defects in their crystal structures, i.e. vacancies, self-interstitials, substitutional impurities, edge dislocation, and dislocation loops.<sup>[5]</sup> This is especially true for substitutional impurities, e.g. such as phosphorus or nitrogen atoms, which are used in doping of silicon crystals to enhance their properties as semiconductors. However, the introduction of these impurities in a controlled and systematic manner is quite challenging.<sup>[5]</sup> Therefore, a bottom-up approach, i.e. the syntheses and handling of nanostructured molecular assemblies, avoiding the aforementioned challenges is highly desirable.

The most important class of self-assembling silicon-based clusters comprises the highly charged Zintl anions. The reaction of alkaline or earth alkaline metals with elements of group 11 to 16 in the periodic table yields intermetallic compounds, i.e. Zintl phases. These Zintl phases consist of preshaped cluster (e.g.  $[E_4]^{4-}$ ,  $[E_5]^{2-}$ ,  $[E_9]^{x-}$  ( $x=2-4$ ) with  $E = Si^{[7-10]}$ ,  $Sn^{[11]}$ ,  $Pb^{[12]}$ ; see Figure 1), which could be characterized in solid-state by crystal structures.

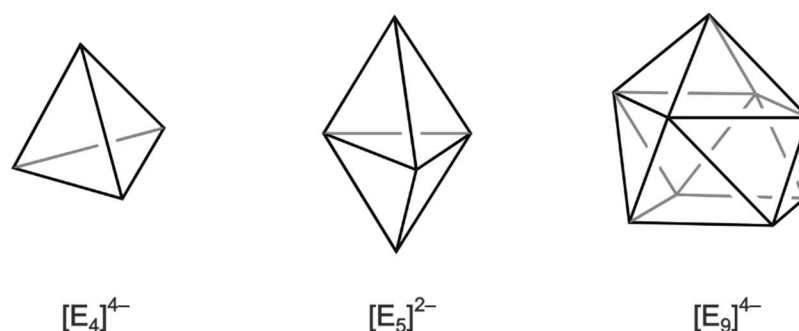


**Figure 1.** Examples of preshaped clusters in Zintl phases. From left to right: Tetrahedral, trigonal bipyramidal, and monocapped quadratic antiprismatic cluster shapes.

In contrast, most reactions to modify these polyanions are carried out in solution. NMR spectroscopy definitely represents the method of choice for investigations in solution. However, owing to their poor solubility as well as the poor NMR properties of silicon, NMR spectroscopic investigations are impeded. Therefore, samples must be  $^{29}\text{Si}$  enriched and dissolved in liquid ammonia (the only appropriate solvent). The first and second chapter of this thesis is concerned with the first NMR spectroscopic investigation on silicon Zintl anions in solution.

Furthermore, the reaction of these cage molecules with transition metals yields endohedral clusters, e.g.  $[\text{Cu}@E_9]^{3-}$  ( $E = \text{Sn}, \text{Pb}$ ),<sup>[13]</sup>  $[\text{Sn}_9\text{M}_2\text{L}]^{x-}$  ( $M = \text{Pt}, \text{Ni}$ ;  $L = \text{PPh}_3, \text{CO}$ ;  $x = 2-3$ ),<sup>[14]</sup> and a ternary functionalized Zintl cluster.<sup>[15]</sup> These clusters represent a fascinating class of supramolecular compounds, which might lead to novel materials for microelectronic devices. Hence, further investigation into characteristics is highly desirable. Chapter three addresses the characterization of a novel ternary 12-vertex cluster with an endohedral Co atom  $[\text{Co}@\text{Sn}_6\text{Sb}_6]^{3-}$  by means of x-ray crystallography and ESI-MS in solid-state, as well as preliminary  $^{119}\text{Sn}$  NMR spectroscopy in solution. Furthermore, this raises the question of the size limitation of such aggregates. Indeed, the largest known spherical supramolecules are represented by spherical carbon clusters, i.e. fullerenes  $\text{C}_{60}$  and  $\text{C}_{70}$ . They consist of five- and six-membered carbon rings and show very intriguing optic and electronic properties, and hence gained increasing attention in nanotechnology and material science.<sup>[16]</sup>



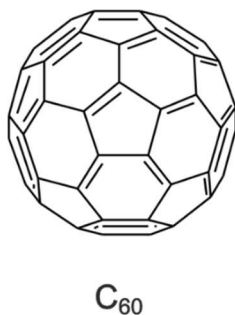


**Figure 2.** Spherical supramolecular carbon cluster, namely fullerene  $C_{60}$ .

In chapter four and five, even larger supramolecules with fullerene-like topology are realized using the self-assembly of pentaphosphaferrocene ( $P_5$  building blocks) or tantalum complexes containing *cyclo*- $P_4$  building blocks with copper(I) halides. They are characterized by x-ray structure analysis in solid-state and their presence in solution was demonstrated by diffusion-ordered spectroscopy (DOSY).

The self-assembly of these aggregates is mostly driven by their electronic properties. Additionally, especially for the spherical supramolecules with substituted cyclopentadienyl ligands, non-covalent interactions might play a significant role in their stabilization. Various theoretical studies on dispersive interactions have been performed.<sup>[17, 18]</sup> However, thus far only a few concepts for an experimental measurement of dispersive interactions have been presented,<sup>[19-21]</sup> hence the main challenge hereby lies in the separation of dispersive interaction from solvent effects.<sup>[22, 23]</sup> Chapter six addresses the concept of the Supramolecular Balance suggested by Gschwind and coworkers<sup>[21]</sup> using phosphoramidite palladium complexes and tests its application upon substitution of the phosphoramidite ligands.

## 1.2 References

- [1] X. Sun, Z. J. Pei, X. J. Xin, M. Fouts, *International Journal of Machine Tools and Manufacture* **2004**, 44, 1, 11-19.
- [2] X. H. Zhang, Z. J. Pei, G. R. Fisher, *International Journal of Machine Tools and Manufacture* **2006**, 46, 3-4, 397-403.
- [3] E. Kayabasi, H. Kurt, E. Celik, *Journal of Materials Science: Materials in Electronics* **2017**, 28, 18, 14085-14090.
- [4] I. S. Yahia, F. Yakuphanoglu, O. A. Azim, *Solar Energy Materials and Solar Cells* **2011**, 95, 9, 2598-2605.
- [5] S. A. Campbell, *The Science and Engineering of Microelectronic Fabrication 2<sup>nd</sup> edition* **2001**, Oxford University Press, New York.
- [6] Y. S. Shcherbyna, T. V. Torchynska, *Thin Solid Films* **2010**, 518, S204-S207; T. Miyazaki, T. Uda, I. Stich, K. Terakura, *Chem. Phys. Lett.* **1996**, 261, 346-352; G. A. Rechtsteiner, O. Hampe, M. F. Jarrold, *J. Phys. Chem. B* **2001**, 105, 4188-4194; H. Murakami, T. Kanayama, *Appl. Phys. Lett.* **1995**, 67, 2341-2343; W. M. M. Kessels, M. C. M. van de Sanden, D. C. Schram, *Appl. Phys. Lett.* **1998**, 72, 2397-2399; T. V. Torchynska, *Superlattices and Microstruct.* **2009**, 45, 267-270; D. K. Yu, R. Q. Zhang, S. T. Lee, *J. Appl. Phys.* **2002**, 92, 7453-7458; G. Belomoin, J. Therrien, A. Smith, S. Rao, R. Twesten, S. Chaieb, M. H. Nayfeh, L. Wagner, L. Mitas, *Appl. Phys. Lett.* **2002**, 80, 841-843.
- [7] S. Scharfe, F. Kraus, S. Stegmaier, A. Schier, T. F. Fassler, *Angew. Chem. Int. Ed.* **2011**, 50, 3630-3670.
- [8] S. Joseph, C. Suchenrunk, F. Kraus, N. Korber, *Eur. J. Inorg. Chem.* **2009**, 2009, 4641-4647; J. M. Goicoechea, S. C. Sevov, *Inorg. Chem.* **2005**, 44, 2654-2658; T. Henneberger, W. Klein, T. F. Fässler, *Z. Anorg. Allg. Chem.* **2018**; T. F. Fässler, L. Schiegerl, A. Karttunen, J. Tillmann, S. Geier, G. Raudaschel-Sieber, M. Waibel, *Angew. Chem. Int. Ed.* **2018**, 130; C. Lorenz, F. Hastreiter, J. Hioe, L. Nanjundappa, S. Gärtner, N. Korber, R. M. Gschwind, *Angew. Chem.* **2018**.
- [9] J. D. Corbett, P. A. Edwards, *Chem. Comm.* **1975**, 984-985; M. Somer, W. Carrillo-Cabrera, E. M. Peters, K. Peters, M. Kaupp, H. G. von Schnering, *Z. Anorg. Allg. Chem.* **1999**, 625, 37-42; C. Lorenz, S. Gärtner, N. Korber, *Z. Anorg. Allg. Chem.* **2017**, 643, 141-145; C. B. Benda, T. Henneberger, W. Klein, T. F. Fassler, *Z. Anorg. Allg. Chem.* **2017**, 643, 146-148.
- [10] S. Joseph, C. Suchentrunk, N. Korber, *Z. Naturforsch.* **2010**, B65, 1059-1065; J. M. Goicoechea, S. C. Sevov, *J. Am. Chem. Soc.* **2004**, 126, 6860-6861.

- [11] J. D. Corbett, P. A. Edwards, *Chem. Comm.* **1975**, 984-985; M. Somer, W. Carrillo-Cabrera, E. M. Peters, K. Peters, M. Kaupp, H. G. von Schnering, *Z. Anorg. Allg. Chem.* **1999**, 625, 37-42; S. Scharfe, F. Kraus, S. Stegmaier, A. Schier, T. F. Faessler, *Angew. Chem., Int. Ed.* **2011**, 50, 3630-3670.
- [12] K. Wiesler, K. Brandl, A. Fleischmann, N. Korber, *Z. Anorg. Allg. Chem.* **2009**, 635, 508-512; C. Lorenz, S. Gärtner, N. Korber, *Crystals* **2018**, 8.
- [13] S. Scharfe, T. F. Fässler, S. Stegmaier, S. D. Hoffmann, K. Ruhland, *Chem. Eur. J.* **2008**, 14, 4479-4483.
- [14] B. Kesanli, J. Fettinger, D. R. Gardner, B. Eichhorn, *J. Am. Chem. Soc.* **2002**, 124, 17, 4779-4786.
- [15] C. Liu, L.-J. Li, X. Jin, J. E. McGrady, Z.-M. Sun, *Inorg. Chem.* **2018**, 57, 6, 3025-3034.
- [16] a) A. Popov, S. Yang, L. Dunsch, *Chem. Rev.* **2013**, 113, 5989-6113; b) D. Jariwala, V. K. Sangwan, L. J. Lauhon, T. J. Marks, M. C. Hersam, *Chem. Soc. Rev.* **2013**, 42, 2824-2860; c) C.-Z. Li, H.-L. Yip, A. K. Y. Jen, *J. Mater. Chem.* **2012**, 22, 4161-4177; d) F. D'Souza, O. Ito, *Chem. Soc. Rev.* **2012**, 41, 86-96; e) R. W. Sallfrank, A. Scheurer, *Top. Curr. Chem.* **2012**, 134, 125-170; f) M. S. Dresselhaus, G. Dresselhaus, P. C. Eklund, *Science of Fullerenes and Carbon Nanotubes*, Academic Press, **1996**; g) P. W. Fowler, D. E. Manolopoulos, *An Atlas of Fullerenes*, Clarendon Press, **1995**; h) H. W. Kroto, J. R. Heath, S. C. O'Brien, R. F. Curl, R. E. Smalley, *Nature* **1985**, 318, 162-163.
- [17] S. Grimme, R. Huehnerbein, S. Ehrlich, *ChemPhysChem.* **2011**, 12, 1258-1261; S. E. Wheeler, *J. Am. Chem. Soc.* **2011**, 133, 10262-10274; C. A. Hunter, *Angew. Chem. Int. Ed.* **2004**, 43, 5310-5324; L. Goerigk, S. Grimme, *Phys. Chem. Chem. Phys.* **2011**, 13, 6670-6688; M. Lewis, C. Bagwill, L. K. E. Hardebeck, S. Wireduah, *Comput. Struct. Biotechnol. J.* **2012** Mar 6, 1:e201204004. doi: 10.5936/csbj.201204004.
- [18] a) P. Schreiner, L. Chernish, P. Gunchenko, E. Tikhonchuk, H. Hausmann, M. Serafin, S. Schlecht, J. Dahl, R. Carlson, A. Fokin, *Nature* **2011**, 477, 308-312. b) A. A. Fokin, D. Gerbig, P. R. Schreiner, *J. Am. Chem. Soc.* **2011**, 133, 20036-20039.
- [19] B. Bhayana, C. S. Wilcox, *Angew. Chem. Int. Ed.* **2007**, 46, 6833-6836; S. Paliwal, S. Geib, C. S. Wilcox, *J. Am. Chem. Soc.* **1994**, 116, 4497; E.-I. Kim, S. Paliwal, C. S. Wilcox, *J. Am. Chem. Soc.* **1998**, 120, 11192.
- [20] F. R. Fischer, W. B. Schweizer, F. Diederich, *Angew. Chem. Int. Ed.* **2007**, 46, 8270; F. R. Fischer, P. A. Wood, F. H. Allen, F. Diederich, *Proc. Natl. Acad. Sci.*

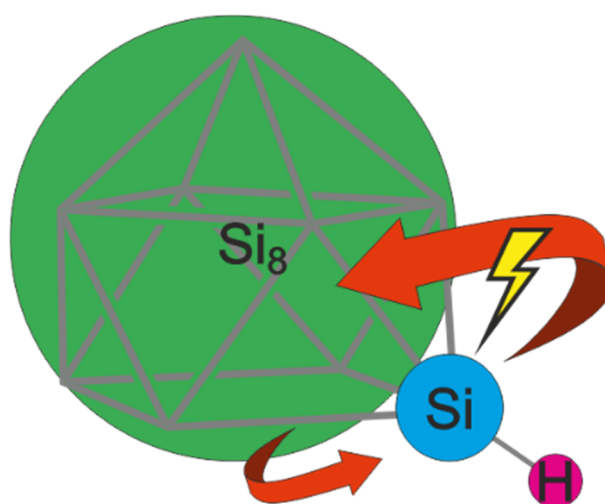
*U.S.A.* **2008**, 105, 17290; F. R. Fischer, W. B. Schweizer, F. Diederich, *Chem. Commun.* **2008**, 34, 4031.

[21] E. Hartmann, R. M. Gschwind, *Angew. Chem. Int. Ed.* **2013**, 52, 2350-2354.

[22] D. Chandler, *Nature* **2005**, 437, 640–647.

[23] R. Cabot, C. A. Hunter, *Chem. Soc. Rev.* **2012**, 41, 3485–3492; C. A. Hunter, *Chem. Sci.* **2013**, 4, 834-848.

## 2 Structure of $[\text{HSi}_9]^{3-}$ in Solid State and Its Unexpectedly High Dynamics in Solution



The NMR spectroscopic investigations were performed in close collaboration with Lokesh Nanjundappa. The theoretical calculations were performed by Johnny Hioe. The synthesis and characterization of the solids as well as the sample preparation were performed by Corinna Lorenz and Stefanie Gärtner.

---

Corinna Lorenz,<sup>+</sup> Florian Hastreiter,<sup>+</sup> Johnny Hioe, N. Lokesh, Stefanie Gärtner, Nikolaus Korber\* and Ruth M. Gschwind\*

[<sup>+</sup>] Both authors contributed equally to the publication.

*Angew. Chem. Int. Ed.* **2018**, 57, 39, 12956-12960.

DOI: 10.1002/anie.201807080

© 2018 Wiley-VCH Verlag GmbH & Co. KGaA. Reproduced with permission.

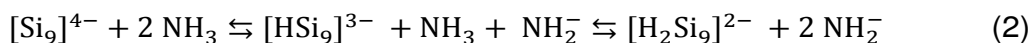
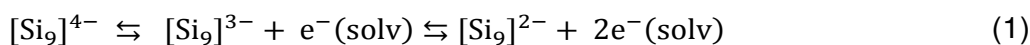
## 2.1 Abstract

We report on the first unambiguous detection of the elusive [HSi<sub>9</sub>]<sup>3-</sup> anion in solutions of liquid ammonia by various <sup>29</sup>Si and <sup>1</sup>H NMR experiments including chemical exchange saturation transfer (CEST). The characteristic multiplicity patterns of both the <sup>29</sup>Si and <sup>1</sup>H resonances together with CEST and a partially reduced <sup>1</sup>H,<sup>29</sup>Si coupling constant indicate the presence of a highly dynamic Si<sub>8</sub> entity and Si-H moiety with a slow proton hopping. Theoretical calculations corroborate both reorganization of Si<sub>8</sub> on the picosecond timescale via low vibrational modes and proton hopping. In addition, in a single-crystal X-ray study of (K(DB[18]crown-6))(K([2.2.2]crypt))<sub>2</sub>[HSi<sub>9</sub>]·8.5NH<sub>3</sub>, the H atom was unequivocally localized at one vertex of the basal square of the monocapped square-antiprismatic cluster. Thus, experimental studies and theoretical considerations provide unprecedented insight into both the structure and the dynamic behavior of these cluster anions, which hitherto had been considered to be rigid.

## 2.2 Introduction

The Group 14 element silicon can be regarded as the “carrier of inorganic life”<sup>[1]</sup> owing to its importance for several semiconductor-based devices, such as photovoltaics, microprocessors, and sensors, that are of particular significance in our everyday life.<sup>[2]</sup> In the underlying industrial processes for the production of such devices, for example, in chemical vapour deposition on solid substrates, well-defined hydrogenated cluster species of silicon (Si<sub>n</sub>H<sub>m</sub>; n>m, n = 4-100) are thought to play a dominant role.<sup>[3]</sup> Therefore, a better understanding of silicon cage molecules is an indispensable necessity and implies an obvious challenge in the field of basic research. To generate defined silicon species that are stable in solution, two approaches are widely used. On the one hand, in a bottom-up approach, molecular monomers are reacted to form different molecular species.<sup>[4]</sup> In contrast, in a top-down approach, naked silicon clusters are synthesized by solid-state reactions where elemental silicon is reduced by an alkali metal under formation of polyanionic salts, for which the term Zintl phase holds true.<sup>[5, 6]</sup> Some of these phases are to a certain extent soluble in anhydrous liquid ammonia, which is the only appropriate solvent for this kind of silicide materials.<sup>[7, 8]</sup> Especially A<sub>12</sub>Si<sub>17</sub> phases (A = K, K/Rb, Rb), which contain [Si<sub>4</sub>]<sup>4-</sup> and [Si<sub>9</sub>]<sup>4-</sup> cage anions in the ratio of 2:1,<sup>[5]</sup> are widely used in recrystallization and solution experiments, owing to their sufficient solubility in liquid ammonia.<sup>[8, 9]</sup> Previous X-Ray diffraction studies revealed the presence of nine-atom silicon species [Si<sub>9</sub>]<sup>x-</sup> (x = 2-4) in solvate structures.<sup>[8, 10]</sup> The overall cluster charge of -2

or  $-3$  can be explained either by oxidation<sup>[11]</sup> [Eq.(1)] or by hydrogenation<sup>[12]</sup> [Eq. (2)], where  $[\text{Si}_9]^{4-}$  can be considered as a base and  $[\text{HSi}_9]^{3-}$  as the formal conjugate acid.



For  $[\text{Sn}_9]^{4-}$  as the heavier Group 14 homologue, both reaction sequences have been reported in the literature, and specifically the hydrogen involvement was unambiguously confirmed by NMR experiments.<sup>[12]</sup> The obvious question arises as to whether the silicide  $[\text{Si}_9]^{4-}$  clusters are subject to similar protolytic reactions.

Additionally, the  $[\text{Sn}_9]^{4-}$  cluster, which has the shape of a monocapped square antiprism in the solid state according to X-ray crystallography,<sup>[13]</sup> was shown to be not rigid but fluctuating in solution.<sup>[14]</sup> Fast exchange of all nine atoms on the NMR timescale results in a singlet resonance in the  $^{119}\text{Sn}$  spectrum. For  $[\text{Pb}_9]^{4-}$ , similar behaviour has been reported.<sup>[14]</sup> The core properties of the NMR-active germanium isotope  $^{73}\text{Ge}$  did not yet allow for further investigations. However, the fluctuation of  $[\text{Sn}_9]^{4-}$  and  $[\text{Pb}_9]^{4-}$  clusters is very reasonable owing to the comparatively weak bonds between heavy main group elements (e.g., Sn-Sn:  $146 \text{ kJ mol}^{-1}$  [1]). On the other hand, the Si-Si bond energies of approximately  $222 \text{ kJ mol}^{-1}$  [1] would seem to make a similar fluctuating character of  $[\text{Si}_9]^{4-}$  much less likely, especially at low temperatures in liquid ammonia. In addition, our previous investigations suggested a rigid bonding situation for  $[\text{Si}_9]^{4-}$ .<sup>[8]</sup> Consequently, detailed NMR experiments on solutions of  $^{29}\text{Si}$ -enriched  $[\text{Si}_9]^{4-}$  clusters, which would shed light on the behavior of the lightest homologue of the group, were highly desirable.

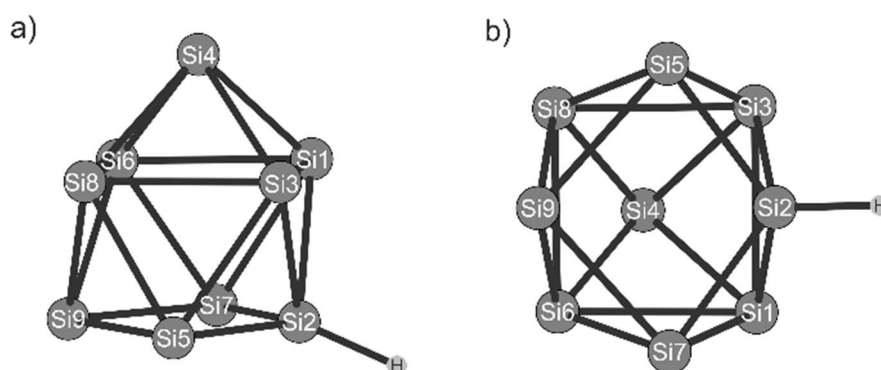


**Figure 1.** The anionic moiety  $[\text{HSi}_9]^{3-}$  in  $\text{K}(\text{DB}[18]\text{crown-6})(\text{K}([2.2.2]\text{crypt}))_2[\text{HSi}_9] \cdot 8.5\text{NH}_3$ ; selected distances within the anion [ $\text{\AA}$ ]: Si2-H = 1.44(4), Si2-Si5 = 2.3386(12), Si7-Si2 = 2.3353(12), Si5-Si9 = 2.5249(13), Si9-Si7 = 2.5404(12), Si3-Si1 = 2.6765(12), Si1-Si6 = 2.6096(12), Si6-Si8 = 2.6422(12), Si8-Si3 = 2.6272(13).

We here report on the first unambiguous detection of the elusive [HSi<sub>9</sub>]<sup>3-</sup> cluster and its fluctuating nature, both by solid-state X-ray structure analysis and by solution NMR experiments in liquid ammonia. Highly temperature- and moisture-labile crystals of (K(DB[18]crown-6))(K([2.2.2]crypt))<sub>2</sub>[HSi<sub>9</sub>]<sup>3-</sup>·8.5NH<sub>3</sub> include [HSi<sub>9</sub>]<sup>3-</sup> as the anionic moiety and represent the first protonated [Si<sub>9</sub>]<sup>4-</sup> silicon cluster.<sup>[15]</sup> As already mentioned in the introduction, the ideal geometry of the naked [Si<sub>9</sub>]<sup>4-</sup> is best described as a monocapped square antiprism with C<sub>4v</sub> symmetry. Although the cluster [HSi<sub>9</sub>]<sup>3-</sup> also derives from the same oxidation state, a distortion towards C<sub>s</sub> due to the protonation becomes apparent (see the Supporting Information and Figure 1b). The H atom could be unambiguously located in the Fourier difference map (see the Supporting Information). The bond lengths of (H-Si2)-Si7 and (H-Si2)-Si5 are reduced while the other two Si-Si bonds of the basal square plane are extended (Figure 1b). The bond lengths within the central square plane are elongated (Figure 1b).<sup>[8]</sup> Owing to the overall space group symmetry, the crystallographic point group of the cluster in the crystal structure is C<sub>1</sub>. The Si-H distance of 1.44(4) Å is in good agreement with literature values (Si-H: 1.48(2) Å<sup>[16]</sup>). The threefold negative charge of [HSi<sub>9</sub>]<sup>3-</sup> is compensated by three potassium cations, two of which are sequestered by [2.2.2]cryptand and the remaining one by DB[18]crown-6 (see the Supporting Information).

### 2.3 Results and Discussion

For the NMR studies, K<sub>6</sub>Rb<sub>6</sub>Si<sub>17</sub> was directly placed in an NMR tube together with two equivalents of [2.2.2]cryptand and dissolved in liquid ammonia. Low-temperature measurements at 203 K were performed to slow down potential exchange processes within the silicide clusters because in the temperature range down to 233 K, exclusively singlets were observed in the <sup>29</sup>Si-spectra (see the Supporting Information). Indeed, at 203 K, pronounced scalar coupling patterns were observed in 1D <sup>1</sup>H and <sup>29</sup>Si spectra as well as 2D <sup>1</sup>H<sup>29</sup>Si HMQC spectra (Figure 2). The <sup>1</sup>H spectrum showed a doublet at -2.85 ppm with a large coupling constant of 156 Hz and high-level fine splitting (averaged coupling constant <J<sub>Hsi</sub>> = 3 Hz) to an even number of chemically equivalent Si atoms, which indicates a protonated silicon cluster Si<sub>n</sub>-Si-H (n = 6 or 8) (Figure 2a). Based on our NMR-spectroscopic expertise with Sn and Si clusters,<sup>[9, 17, 18]</sup> two <sup>29</sup>Si NMR resonances were observed at 203 K; one from the Si-H silicon and the other one arising from the remaining eight Si atoms. The former was detected through <sup>1</sup>H<sup>29</sup>Si DEPT experiment (Figure 2b) whereas the latter was observed through direct detection (Figure 2c). Additionally, these two <sup>29</sup>Si resonances were also detected in 2D <sup>1</sup>H<sup>29</sup>Si HMQC spectra at



$\delta = -158.5$  ppm and  $-358.5$  ppm, respectively (see the Supporting Information). For the first time, well resolved scalar coupling patterns in the  $^{29}\text{Si}$  resonances of anionic silicon Zintl clusters could be detected ( $^1J_{\text{SiH}} = 156$  Hz,  $\langle J_{\text{SiH}} \rangle = 3$  Hz,  $\langle J_{\text{SiSi}} \rangle = 22$  Hz). In the  $^1\text{H}^{29}\text{Si}$  HMQC (Figure 2d), the spectrum with the highest sensitivity, the signal at  $\delta = -158.5$  ppm clearly shows the intensity pattern of a nonet, revealing a highly dynamic  $\text{Si}_8$  cluster acting as single entity in terms of scalar couplings ( $\text{Si}_8$ -Si-H see Figure 2e). The corresponding  $^{29}\text{Si}$  signals in the 1D  $^{29}\text{Si}$  spectra corroborate this cluster structure ( $\text{Si}_8$ -Si-H:  $\delta = -158.5$  ppm, doublet of nonets,  $^1J_{\text{HSi}} = 156$  Hz,  $\langle J_{\text{SiSi}} \rangle = 22$  Hz, Figure 2b; Si $_8$ -Si-H:  $\delta = -358.5$  ppm, doublet of doublets,  $\langle J_{\text{HSi}} \rangle = 3$  Hz,  $\langle J_{\text{SiSi}} \rangle = 22$  Hz, Figure 2c).

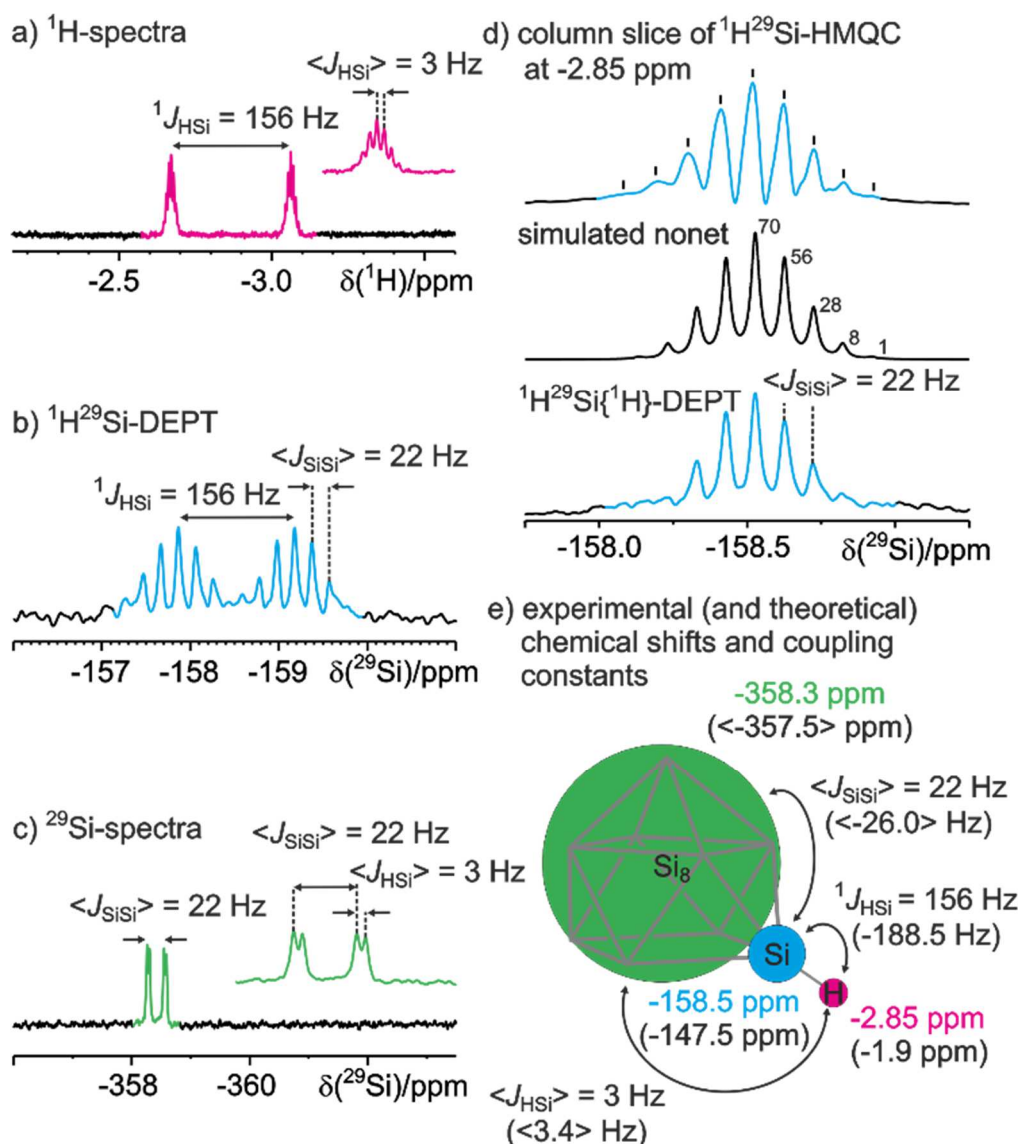


**Figure 2.** Experimental NMR-spectroscopic evidence for a flexible  $\text{Si}_8$  entity within  $[\text{HSi}_9]^{3-}$  in liquid ammonia at 203 K using a 400 MHz (a,c) or 600 MHz (b,d) spectrometer: a)  $^1\text{H}$ , b)  $^1\text{H}^{29}\text{Si}$  DEPT, and c)  $^{29}\text{Si}$  spectra with pronounced scalar coupling patterns. d) Conformation of the nonet structure by comparison of the column slice at  $\delta = -2.85$  ppm of the  $^1\text{H}^{29}\text{Si}$  HMQC experiment, simulation of the nonet, and the proton-decoupled

<sup>1</sup>H<sup>29</sup>Si DEPT experiment (from top to bottom). e) Schematic representation of a highly dynamic [HSi<sub>9</sub>]<sup>3-</sup> cluster structure with a Si-H (blue and magenta) and a flexible Si<sub>8</sub> moiety (green), including experimental (and theoretical) chemical shifts and coupling constants (averaged values given in < >).

Furthermore, theoretical calculations validate the cluster structure with one Si-H moiety coupled to a highly flexible Si<sub>8</sub> entity (Figure 2e). Especially the averaged calculated chemical shifts and scalar couplings of the Si<sub>8</sub> entity match the experimental values.

However, the chemical shifts and scalar couplings of the Si-H moiety noticeably deviate from the experimental values, especially the <sup>1</sup>J<sub>H<sub>Si</sub> values (exp. 156 Hz, calc. 188.5 Hz; Figure 2e). To investigate this further, <sup>1</sup>H<sup>29</sup>Si HMQC experiments for the Si<sub>8</sub> moiety (−358.5 ppm) were performed with different coupling values (3, 13, 22, and 156 Hz). Interestingly, the corresponding intensity pattern does not correlate to a static Si-H bond situation as the strongest intensity is not observed for 3 Hz, but for 156 Hz (see the Supporting Information for spectra and detailed analysis). This indicates a slow exchange of the Si-H bond on the NMR timescale. This H hopping over the entire Si<sub>9</sub> cluster is in line with the observed partial decoupling of the <sup>1</sup>J<sub>H<sub>Si</sub> scalar couplings, the intensity pattern in the <sup>1</sup>H<sup>29</sup>Si HMQC experiments, and in the temperature-dependent spectra (see the Supporting Information).</sub></sub>

To corroborate this exchange, a more straightforward direct Si to Si NMR exchange measurement, namely the more sensitive chemical exchange saturation transfer (CEST) technique was applied,<sup>[19]</sup> as conventional EXSY NMR spectroscopy is not suitable owing to the low concentration of the species and the low negative gyromagnetic ratio of <sup>29</sup>Si.

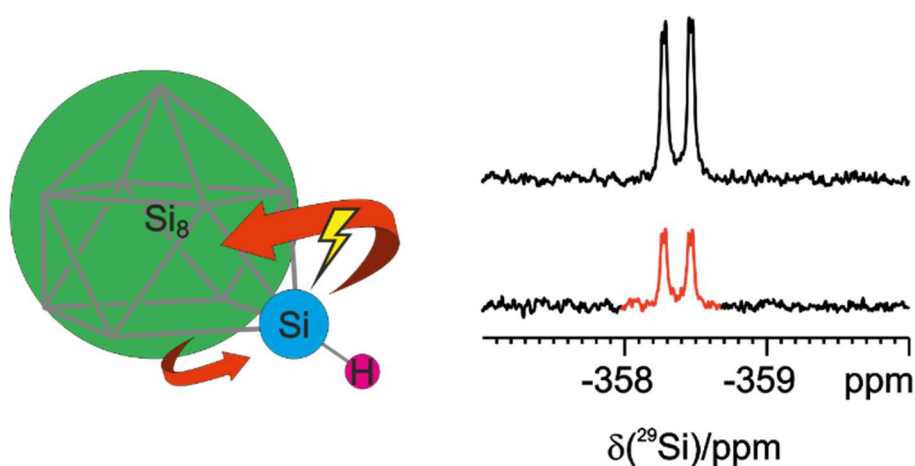


**Figure 3.** 1D CEST experiment as direct experimental evidence for the H hopping in liquid ammonia at 203 K (600 MHz spectrometer). Schematic representation (left) with saturation at  $\delta = -158.5$  ppm (yellow arrow) and saturation transfer due to mutual exchange by H hopping (red arrow). Comparison of control experiment without saturation (top right) and the experiment with saturation at  $\delta = -158.5$  ppm (bottom right), which shows a strong decrease in intensity for the signal at  $\delta = -358.5$  ppm (in red).

Therefore, two 1D  $^{29}\text{Si}$  CEST experiments were acquired for observing the  $\text{Si}_8$  moiety at  $\delta = -358.5$  ppm, with and without saturation at  $-158.5$  ppm. The obtained CEST spectra are given in Figure 3. The lower spectrum shows a pronounced intensity decrease due to chemical exchange saturation transfer from the Si atom of Si-H to a Si of the  $\text{Si}_8$  moiety. To determine approximate rate constants for this H hopping, both the line widths of Si peaks and the CEST intensity pattern were analyzed (see the Supporting Information). The relative narrow line widths (3-5 Hz) and the CEST intensity analysis suggest a rate constant of approximately  $10^{-1} \text{ s}^{-1}$ . This confirms our H hopping mechanism of the  $[\text{Si}_9\text{H}]^{3-}$  cluster, which is slow on the NMR timescale compared to the extremely rapid scrambling of the  $\text{Si}_8$  moiety. This first application of CEST to study the dynamics of inorganic clusters demonstrates impressively the potential of this method in this field.

To gain deeper insight into the structure, dynamics, protonation preference and thermodynamics of the  $[\text{HSi}_9]^{3-}$  cluster, theoretical calculations were performed. According to the crystal structure, the H atom is located at a vertex atom of the basal square plane of the  $\text{Si}_9$  cluster (Figure 1). Quantum-chemical calculations evince a cluster rearrangement upon protonation of the cluster in any other position, corroborating the crystal structure as the global minimum (Figure 4, structure GS). In addition, a high-lying ( $+68.5 \text{ kJ mol}^{-1}$ ), transient local minimum was found (INT1) with a shared proton on the edge of the basal plane. Our results are in good agreement with the investigations of Eichhorn and co-workers for  $[\text{HSn}_9]^{3-}$ .<sup>[12]</sup>

Contrary to the earlier assumption of rigid  $\text{Si}_9$  cluster structures,<sup>[8]</sup> the presented NMR measurement of  $[\text{HSi}_9]^{3-}$  clusters showed a fast  $\text{Si}_8$  scrambling and a slower H hopping process in terms of the NMR timescale. The rearrangement of the  $[\text{HSi}_9]^{3-}$  cluster has been demonstrated quantitatively by high-level theoretical calculation (DLPNO-CCSD(T)/def2-QZVPP). Three different rearrangement processes were simulated to describe the measured coupling pattern and chemical shifts (Figure 4). For the scrambling of the  $\text{Si}_8$  entity, two pathways proceeding through simultaneous Si-Si bond breaking and bond forming are possible, where the H atom stays at a vertex silicon atom. In pathway A two bonds and in pathway B four bonds are involved in bond-forming and bond-breaking processes. Both exchange processes are extremely rapid even at 203 K (ns to ps time frame). The first transition state TS1 is lower in energy ( $+9.4 \text{ kJ mol}^{-1}$ ) than the second transition state TS2 ( $+14.7 \text{ kJ mol}^{-1}$ ). This is in agreement with the NMR measurements not being able to resolve the scrambling process, and hence detecting an average of eight silicon atoms. The start and end of both rearrangement processes are degenerated (GS). Hence, the activation barrier is the intrinsic barrier and equals to the quarter of the reorganization energy.<sup>[20]</sup> Additionally, vibrational analysis of the transition states yielded

a very low negative frequency (small curvature, see the Supporting Information). Owing to the low barrier and a very flat potential surface, a low reorganization energy is observed.

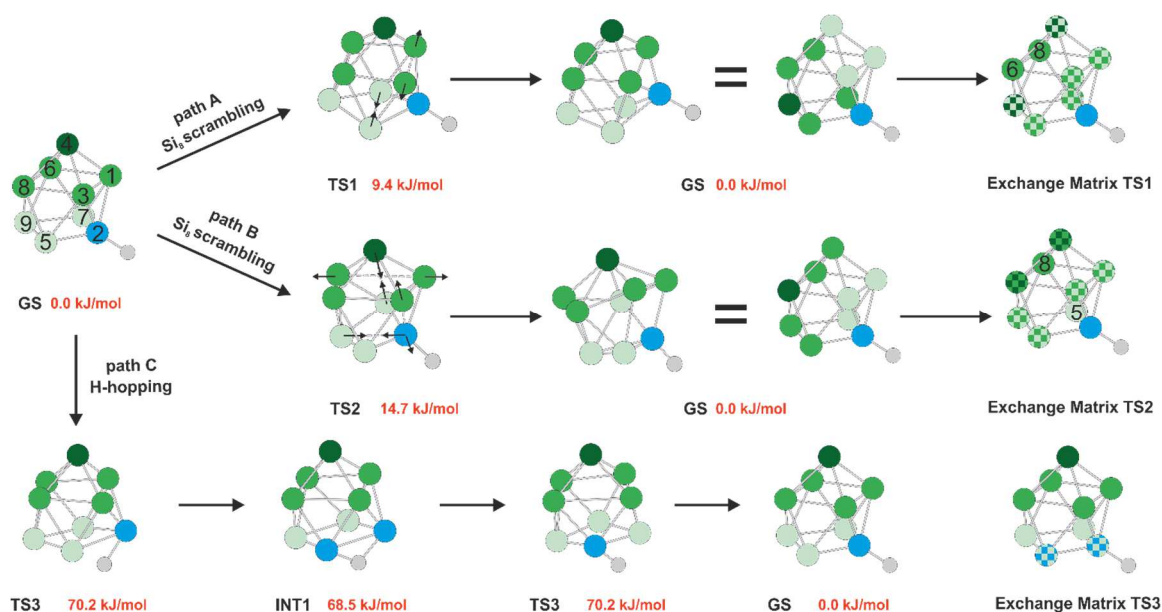


**Figure 4.** Simulation of dynamic processes in solution with the resulting exchange matrices via the three lowest-energy pathways calculated (checkered pattern for Si atoms that mutually exchange, colored in respect to their starting and end position). The fast  $\text{Si}_8$  scrambling occurs by reorganization of the  $[\text{HSi}_9]^{3-}$  cluster by simultaneous bond breaking and bond forming, involving either two bonds (path A) or four bonds (path B). For the averaging of the chemical shifts as observed in NMR spectroscopy, either exclusively path B has to be active or both path A and B, which lead to a complete exchange of all eight Si atoms. Owing to vibrational movement of the H atom and the eccentricity of the Si5-Si2 bond, the H atom can bond to a neighboring Si atom in the basal square plane of the  $[\text{HSi}_9]^{3-}$  cluster, thus effecting a partial decoupling of the Si-H couplings (H hopping, path C). This is in agreement with the deviating experimental values compared to the calculated ones. Note that all resulting clusters obtained through path A, B, and C as well as the GS are degenerate, only differing in the relative positions of the Si atoms.

The permutation of these two reorganization processes was analyzed to check whether they lead to a complete averaging of all atoms within the  $\text{Si}_8$  moiety as shown by the NMR spectra. In path A, six Si atoms exchange their position in terms of planes, while Si-6 and Si-8 exchange only the position but not the plane, leaving them chemically equivalent, but distinguishable from the others (see Figure 4 pathway A: GS and exchange matrix). Therefore, with only pathway A being active, the NMR spectra cannot be reproduced (see the Supporting Information for details). Similarly, six Si atoms exchange position in path B, but Si-5 and Si-8 exchange both their position and the plane (see Figure 4 pathway B: GS and exchange matrix). Another cycle following path B will scramble all eight silicon atoms (for details, see the Supporting Information). In conclusion, to achieve the complete scrambling of the  $\text{Si}_8$  entity detected by NMR analysis, either only path B is

operative or both pathways A and B proceed, the latter being more probable in light of the TS energies.

Subsequently, the H hopping was analyzed (see Figure 4, pathway C), which generates a highly energetic intermediate ( $\Delta G_{203}(\text{INT1}) = +68.5 \text{ kJ mol}^{-1}$ ) via a nearby transition state TS3 ( $\Delta G_{203}^{\ddagger}(\text{TS3}) = +70.2 \text{ kJ mol}^{-1}$ ). Although the adjacent process passing the second TS3 leads to the same cluster, the reaction pathway cannot be classified as an ergoneutral reaction, and hence the barrier is not intrinsic. Furthermore, the Si-H bond has to be highly deformed, causing a high reorganization energy. At 203 K, the calculations predict this process to be extremely slow ( $\mu\text{s}$  timescale) even in a continuum of  $\text{NH}_3$ . Compared to the rate obtained from CEST ( $r \approx 10^{-1} \text{ s}^{-1}$  equivalent to  $\Delta G_{203}^{\ddagger} \approx +52\text{-}53 \text{ kJ mol}^{-1}$ ), the calculated rate is significantly lower. However, this process is still slow on the NMR timescale at 203 K (for temperature-dependent measurements, see the Supporting Information).

Perhaps our previously suggested model for the acidification of  $\text{NH}_3$  in the presence of alkali metal cations might also explain the accelerated H hopping in experiment.<sup>[17]</sup>

## 2.4 Conclusions

To conclude, we have revealed the highly dynamic behavior of the protonated  $[\text{Si}_9]^{4-}$  cage anion  $[\text{HSi}_9]^{3-}$  in solutions of liquid ammonia, which is due to low reorganization energies within a  $\text{Si}_8$  entity. As preliminary ab initio MD simulations of the naked  $[\text{Si}_9]^{4-}$  cluster showed a similar reorganization behavior (see the Supporting Information) as for the heavier homologues  $[\text{Sn}_9]^{4-}$  and  $[\text{Pb}_9]^{4-}$ ,<sup>[12]</sup> the high flexibility might be an intrinsic property of the  $[\text{Tt}_9]^{4-}$  cluster family.

## 2.5 Supporting Information

### 2.5.1 General experimental details

All operations were carried out under argon atmosphere using standard Schlenk and Glovebox techniques. The reaction vessels were dried in vacuo. Liquid ammonia was dried and stored with sodium metal in a dry ice cooled Dewar vessel for at least 48 h. DB[18]crown-6 (systematic name: 2,3,11,12-Dibenzo-1,4,7,10,13,16-Hexaoxacyclooctadeca-2,11-dien) was purchased from Merck Eurolab GmbH, [2.2.2]cryptand (systematic name: 4,7,13,16,21,24-Hexaoxa-1,10-diazabicyclo[8.8.8]hexa-cosane) and Mesitylcopper(I) from ABCR. The chelating agents were used as received. <sup>29</sup>Si was provided by Chemgas. Rubidium was synthesized according to Hackspill.<sup>[1]</sup> Rubidium and potassium were distilled for purification.

#### 2.5.1.1 Synthesis of the Zintl phases and solvate structure

**K<sub>6</sub>Rb<sub>6</sub><sup>29</sup>Si<sub>17</sub>**: For the 100% enriched solid-state phase K<sub>6</sub>Rb<sub>6</sub><sup>29</sup>Si<sub>17</sub>, K (0.123 g, 3.15 mmol), Rb (0.269 g, 3.15 mmol) and <sup>29</sup>Si (0.25 g, 8.60 mmol) were enclosed in tantalum containers and jacketed in an evacuated ampoule of fused silica. A heating rate of 25 K·h<sup>-1</sup> to 973.1 K was chosen. The temperature was maintained for 24 h. The ampoule was cooled to room temperature with a rate of 20 K·h<sup>-1</sup>. The metallic black material was stored in a glove box under argon.

**K<sub>12</sub>Si<sub>17</sub>**: K (0.45 g, 19.57 mmol) and Si (2.6 g, 35.79 mmol) were placed in tantalum containers. The containers were heated to 1223.15 K with a rate of 25 K·h<sup>-1</sup>. The temperature was kept for 2 hours. The cooling process was performed with a rate of 20 K·h<sup>-1</sup> to room temperature. The black metallic precursor was stored in a glove box under argon.

**(K(DB[18]crown-6))(K[2.2.2]crypt)<sub>2</sub>[HSi<sub>9</sub>]·8.5NH<sub>3</sub>**: 0.020 g (0.021 mmol) K<sub>12</sub>Si<sub>17</sub>, 0.0076 g (0.021 mmol) DB[18]crown-6, 0.008 g (0.021 mmol) [2.2.2]cryptand and 0.008 g (0.042 mmol) Mesitylcopper(I) were dissolved in about 20 ml of liquid ammonia in a three times baked out reaction vessel. The Schlenk tube with the brownish reaction mixture was stored at 237 K. After a few months orange crystals with the composition of (K(DB[18]crown-6))(K[2.2.2]crypt)<sub>2</sub>[HSi<sub>9</sub>]·8.5NH<sub>3</sub> (yield: 10%) could be isolated and characterized by means of X-Ray diffraction studies.

### 2.5.1.2 Solid phase characterization

$\text{K}_6\text{Rb}_6^{29}\text{Si}_{17}$ : **Figure S1** and **S2** show the diffraction pattern of the compound  $\text{K}_6\text{Rb}_6^{29}\text{Si}_{17}$ . For comparison, the theoretical diffraction pattern (calculated from single-crystal structure data) of  $\text{K}_{12}\text{Si}_{17}$  and  $\text{Rb}_{12}\text{Si}_{17}$  are also depicted in the figures. In **Figure S2** an enlarged part of the diffraction pattern is provided. It is obvious that the reflections of the starting material are located between the reflections of  $\text{K}_{12}\text{Si}_{17}$  and  $\text{Rb}_{12}\text{Si}_{17}$ . Thus, the elements of  $\text{K}_6\text{Rb}_6\text{Si}_{17}$  are stoichiometrically weighed in tantalum containers, it can be assumed, that the starting material can be considered as phase pure (no characteristic reflections of elemental silicon can be found) according to the formula  $(\text{K,Rb})_{12}\text{Si}_{17}$ .

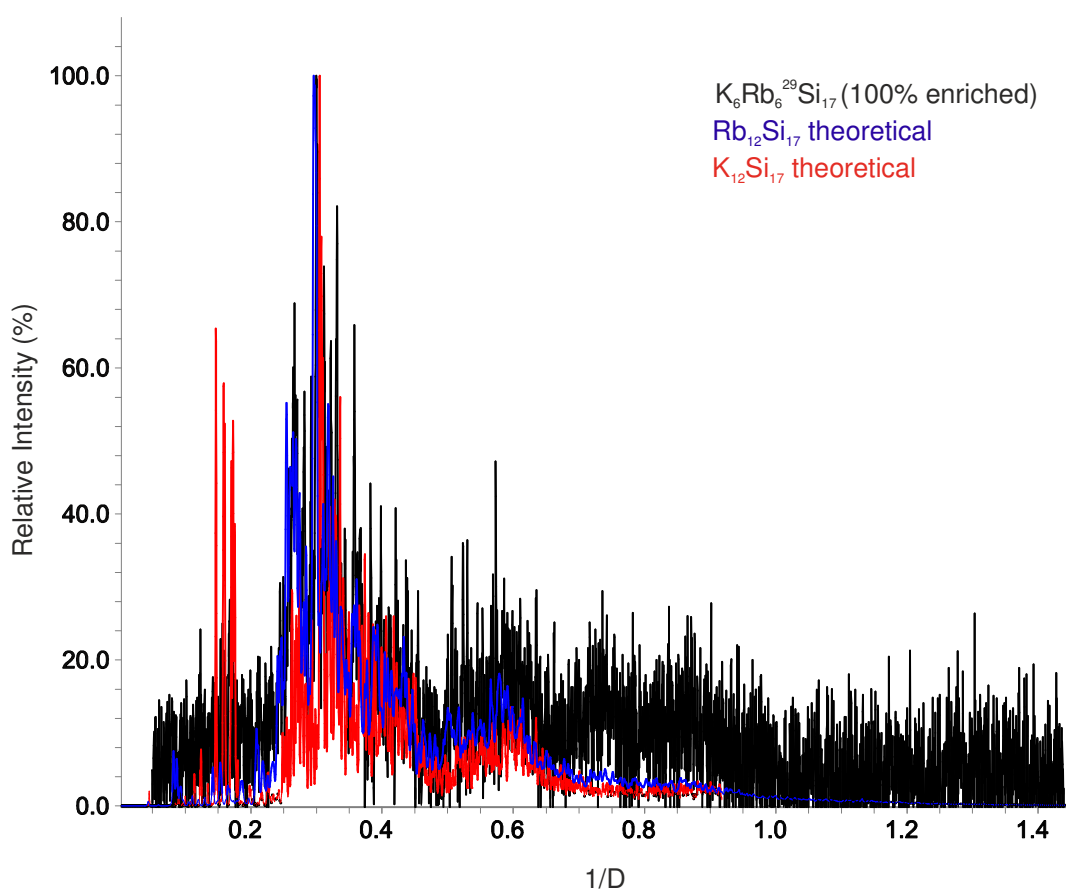


**Figure S5.** Comparison of experimental ( $\text{K}_6\text{Rb}_6\text{Si}_{17}$ , black) and theoretical ( $\text{K}_{12}\text{Si}_{17}$ , red;  $\text{Rb}_{12}\text{Si}_{17}$ , blue) diffraction pattern. The latter ones are calculated from single crystal data.

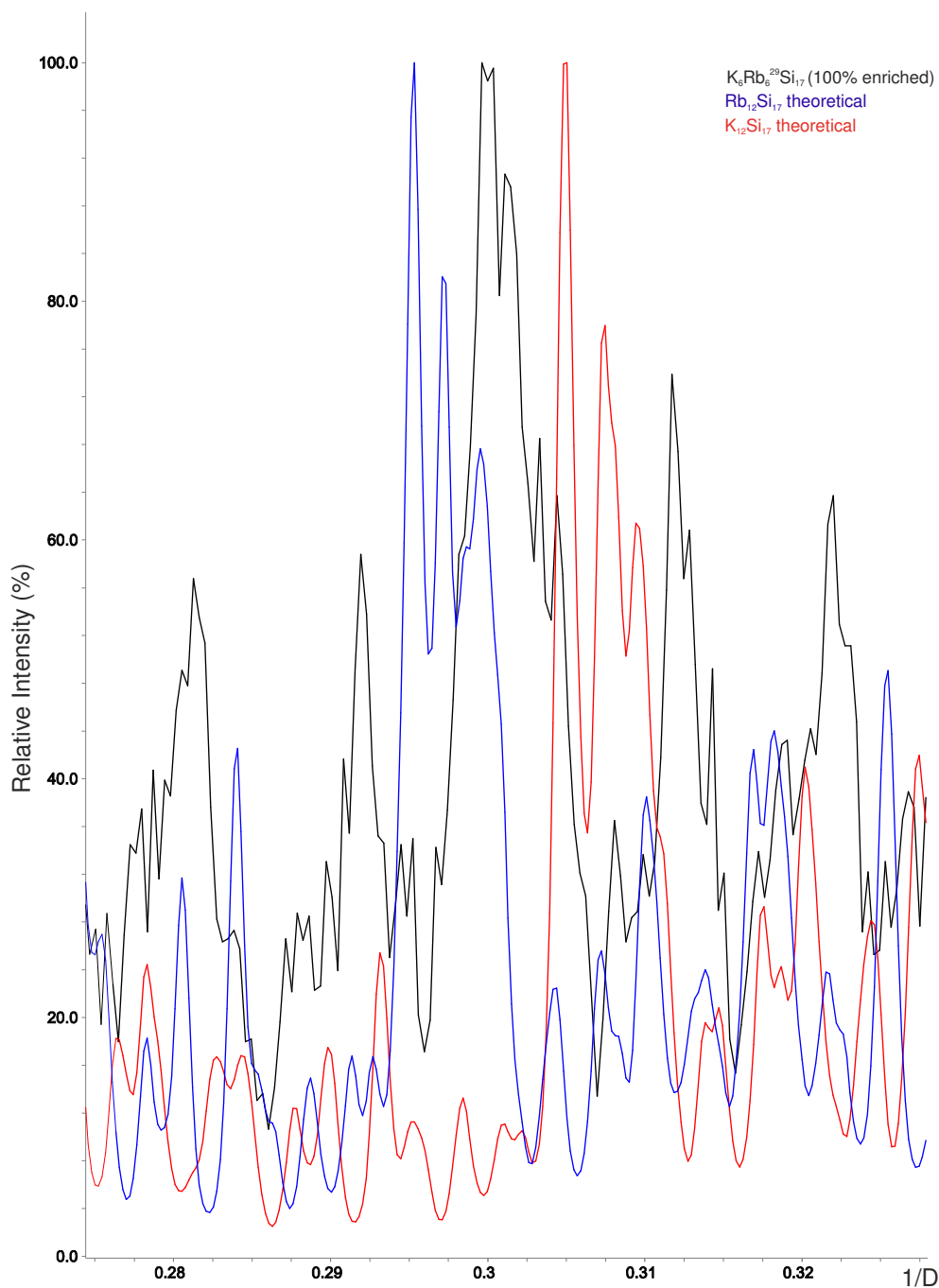


**Figure S6.** Part of the powder diffraction pattern of Figure S1. It is shown, that the reflexes of the mixed cationic phase  $K_6Rb_6^{29}Si_{17}$  are centered between the reflexes of  $K_{12}Si_{17}$  and  $Rb_{12}Si_{17}$ .

**$K_{12}Si_{17}$ :** Figure S3 depicts the powder patterns of  $K_{12}Si_{17}$  (experimental and theoretical).  $K_{12}Si_{17}$  can be considered as phase pure material, as there are no additional reflections of e.g. elemental silicon.



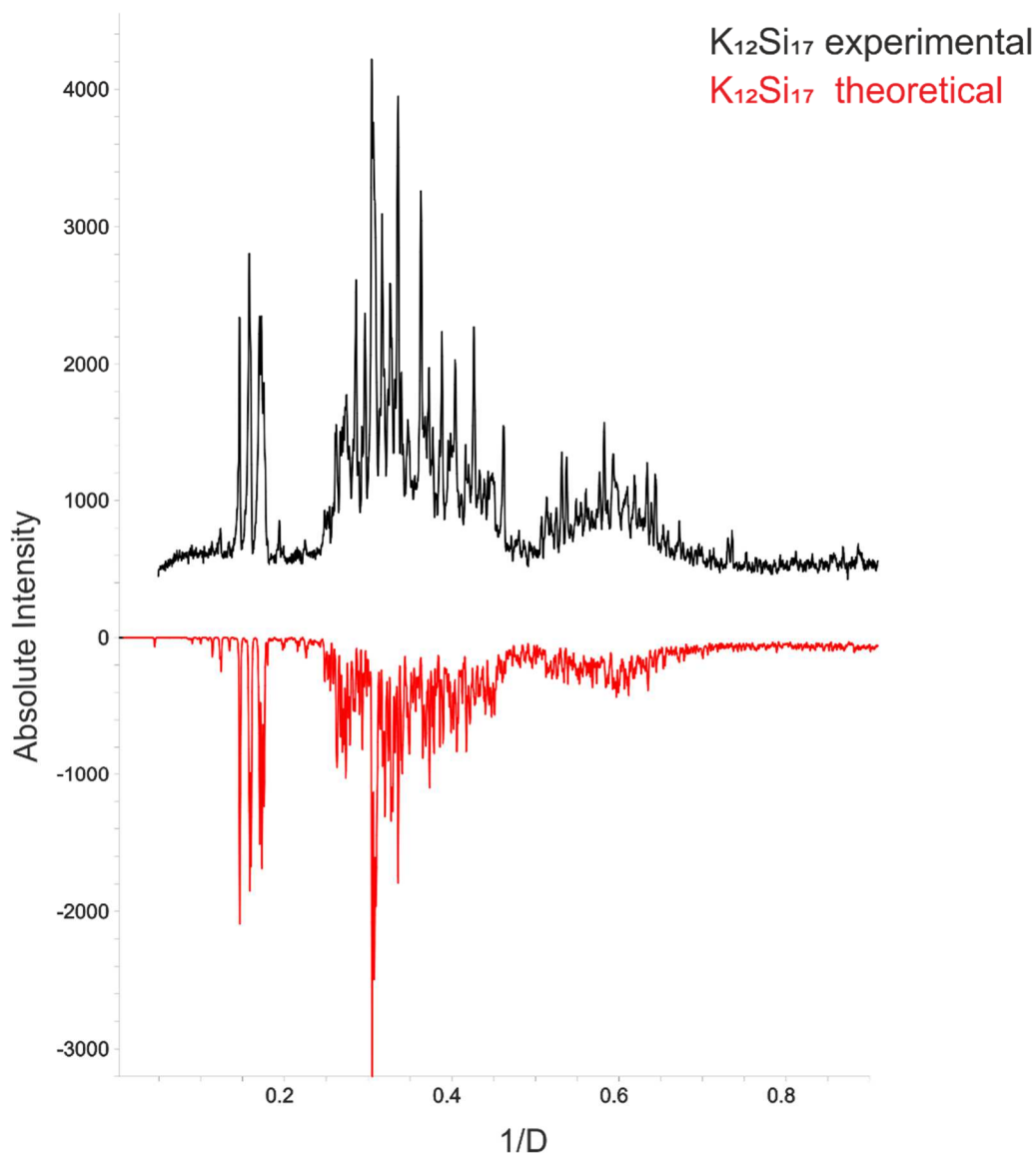


**Figure S7.** Comparison of experimental (black) and theoretical (red) diffraction pattern of  $K_{12}Si_{17}$ . The latter one is calculated from single crystal data.

### 2.5.1.3 Details of Single Crystal X-Ray diffraction

Crystal preparation was carried out in nitrogen cooled perfluorinated ether oil (Galden<sup>®</sup> HT 230, Fa. Ausimont, USA)<sup>[1]</sup> due to the temperature, air- and moisture sensitivity of the crystals.

#### **(K(DB[18]crown-6))(K([2.2.2]crypt))<sub>2</sub>[HSi<sub>9</sub>]·8.5NH<sub>3</sub>**

For X-Ray diffraction studies, an appropriate crystal was mounted on a loop (MiTeGen, 100  $\mu$ m). SHELXT was used for structure solution, SHELXL for the refinement (from the SHELX package) within OLEX<sup>2</sup>.<sup>[2]</sup> Single crystal X-ray diffraction was performed

on a SuperNova (Agilent Technologies) with a microfocus Mo X-Ray source ( $\lambda = 0.71072 \text{ \AA}$ ) and a CCD detector (EOS) at 123 K. DIAMOND was used for illustrations.<sup>[3]</sup>

The space group found for compound (K(DB[18]crown-6))(K([2.2.2]crypt))<sub>2</sub>[HSi<sub>9</sub>]<sup>3-</sup>·8.5NH<sub>3</sub> (*C2/c*) was confirmed by PLATON.<sup>[4]</sup> One of the cryptand molecules showed a slight disorder (17.4(6) %), which could be resolved by applying SADI and SIMU restraints to the splitted moieties. The hydrogen atoms of the disordered cryptand molecule were placed at calculated positions using a riding model (HFIX 23), most of the remaining ones of the chelating agents as well as ammonia molecules have been located in the fourier difference maps. The hydrogen atom of the anionic moiety [HSi<sub>9</sub>]<sup>3-</sup> was found as maximum in the fourier difference maps (see **Figure S4**). CCDC-1848999 contains the supplementary crystallographic data for this paper. These data can be obtained free of charge from The Cambridge Crystallographic Data Centre.

**Table S1.** Crystallographic data for (K(DB[18]crown-6))(K([2.2.2]crypt))<sub>2</sub>[HSi<sub>9</sub>]·8.5NH<sub>3</sub>

Compound	<i>(K(DB[18]crown-6))(K([2.2.2]crypt))<sub>2</sub>[HSi<sub>9</sub>]·8.5NH<sub>3</sub></i>
Empirical formula	C <sub>56</sub> H <sub>122.5</sub> K <sub>3</sub> N <sub>12.5</sub> O <sub>18</sub> Si <sub>9</sub>
Formula weight [g·mol <sup>-1</sup> ]	1629.27
Crystal size [mm]	0.12 x 0.52 x 0.031
Crystal shape	prism
Crystal colour	orange
Crystal system	monoclinic
Space group	<i>C2/c</i>
<i>a</i> [Å]	17.2979(3)
<i>b</i> [Å]	21.7541(5)
<i>c</i> [Å]	44.8900(9)
$\alpha$	90.0°
$\beta$	91.925(2)
$\gamma$	90.0°
Volume [Å <sup>3</sup> ]	16882.6(6)
Z	8
Calculated density [g·cm <sup>-3</sup> ]	1.282
Absorption coefficient [mm <sup>-1</sup> ]	0.355
Absorption correction	numerical
2 $\theta$ - range for data collection [°]	5.886 – 56.524
Reflection collected	62087 / 18079
independent	
Data / restraints / parameters	18079 / 43 / 1214
Goodness-of-fit on F <sup>2</sup>	1.043
Final <i>R</i> indices [ <i>I</i> > 2 $\sigma$ ( <i>I</i> )]	<i>R</i> 1 = 0.0558, <i>wR</i> 2 = 0.1152
<i>R</i> indices (all data)	<i>R</i> 1 = 0.0925, <i>wR</i> 2 = 0.1294
<i>R</i> <sub>int</sub>	0.0583
Largest diff. peak and hole [e·Å <sup>-3</sup> ]	0.35/ -0.48

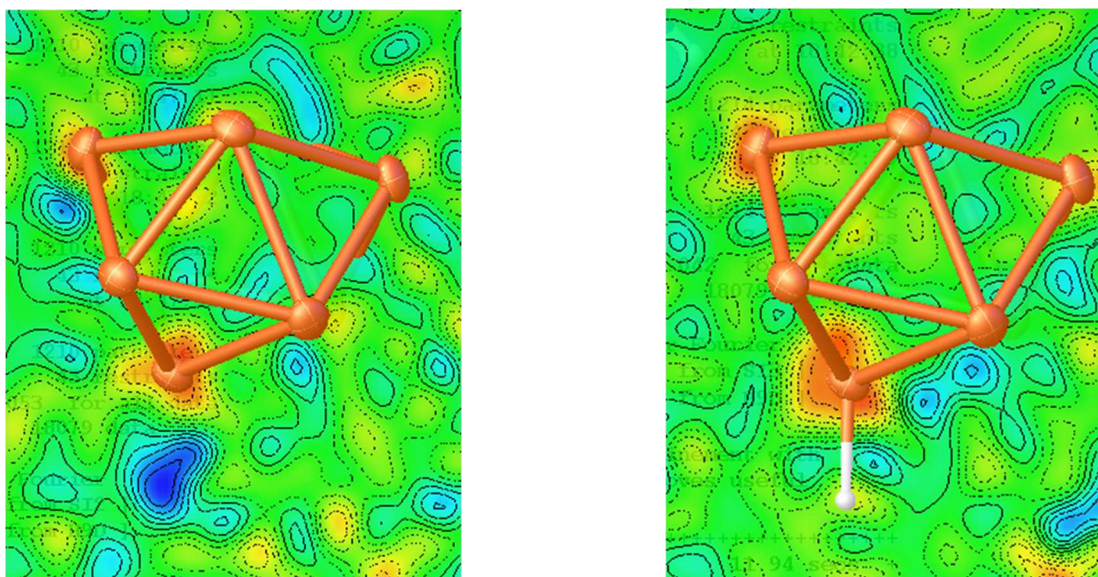


**Figure S8.** The hydrogen atom of the anionic moiety [HSi<sub>9</sub>]<sup>3-</sup> can clearly be found as a maximum in the fourier difference map (picture on the left-hand side). The picture on the right-hand side shows the improvement of the difference map after refining a hydrogen atom at the position of the max peak, which clearly supports the model of a [HSi<sub>9</sub>]<sup>3-</sup> entity.

**Selected crystallographic data of (K(DB[18]crown-6))(K([2.2.2]crypt))<sub>2</sub>[HSi<sub>9</sub>].8.5NH<sub>3</sub>**Table S2 Bond lengths within the [HSi<sub>9</sub>]<sup>3-</sup> cluster.

<b>(K(DB[18]crown-6))(K([2.2.2]crypt))<sub>2</sub>[HSi<sub>9</sub>].8.5NH<sub>3</sub></b>	
Si6-Si1	2.6096(12)
Si6-Si7	2.4034(12)
Si6-Si8	2.6422(12)
Si6-Si9	2.4263(12)
Si6-Si4	2.4421(12)
Si1-Si2	2.4260(12)
Si1-Si7	2.3353(12)
Si1-Si3	2.6765(12)
Si1-Si4	2.4267(12)
Si2-Si7	2.3353(12)
Si2-Si5	2.3386(12)
Si2-Si3	2.4193(12)
Si7-Si9	2.5404(12)
Si5-Si8	2.4361(13)
Si5-Si3	2.5141(13)
Si5-Si9	2.5249(13)
Si8-Si3	2.6272(13)
Si8-Si9	2.4243(13)
Si8-Si4	2.4335(13)
Si3-Si4	2.4108(13)

## Cluster shape

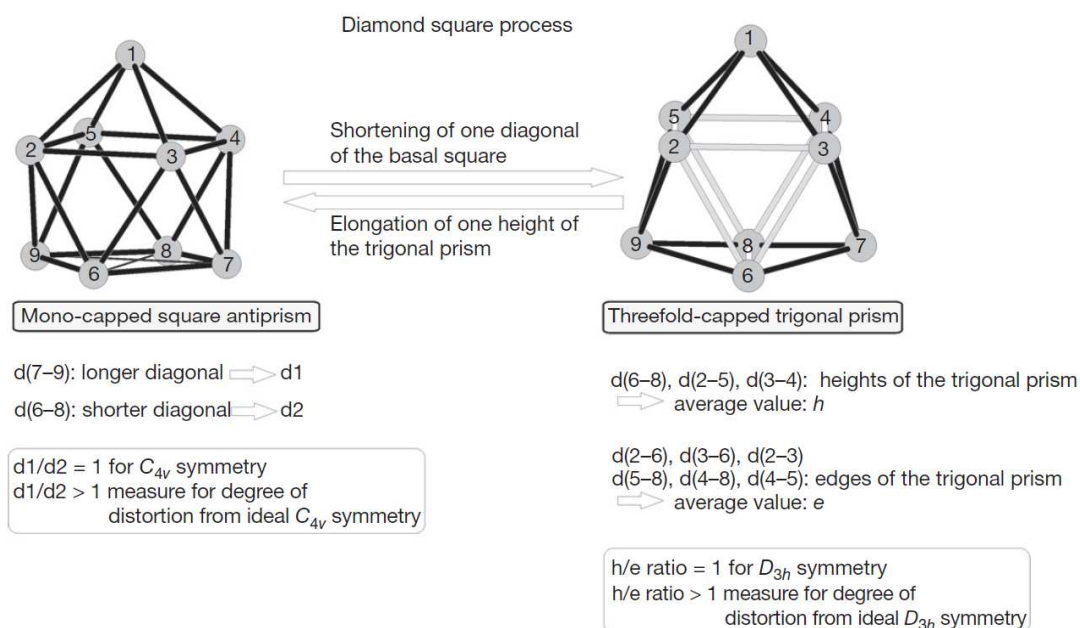


**Figure S9.** The diamond square process describes the transformation from a monocapped square antiprism to a threefold-capped trigonal prism and vice versa. Both geometries are very similar in energy to [E<sub>9</sub>]<sup>x-</sup> (x = 2-4) clusters, therefore distorted variants of both border symmetries are found in real crystal structures. Reprinted from Comprehensive Inorganic Chemistry II., Second Edition, S. Gärtner, N. Korber, Chapter 1.09 - Zintl Anions, Pages 251-267, 2013, with permission from Elsevier. <sup>[5]</sup>

**Table S3.** Parameters of the [HSi<sub>9</sub>]<sup>3-</sup> cluster.

cluster shape	tricapped trigonal prism $D_{3h}$	monocapped square antiprism $C_{4v}$	[HSi <sub>9</sub> ] <sup>3-</sup> $C_1$
point group symmetry	$D_{3h}$	$C_{4v}$	$C_1$
prism heights $h_1, h_2, h_3$	$h_1 = h_2 = h_3$	$h_1 > h_2, h_3$	$h_1$ (Si7-Si9) = 3.7458(13) > $h_2$ (Si3-Si1) = 2.67613(4); $h_3$ (Si8-Si6) = 2.64221(4)
h/e-ratio ratio of the diagonals d1/d2	$h/e = 1$ $d1/d2 > 1$	$h/e > 1$ $d1/d2 = 1$	$h/e = 1.19$ $d1/d2 = 1.21$

The prism heights of the cluster in (K(DB[18]crown-6))(K([2.2.2]crypt))<sub>2</sub>[HSi<sub>9</sub>]<sup>3-</sup>·8.5NH<sub>3</sub>, as well as the h/e-ratio of 1.19 differ widely from ideal  $D_{3h}$  symmetry. (Table S2). Also, the value for the ratio of diagonals of 1.21 is quite far away from the ideal value of 1 for the  $C_{4v}$  symmetry. The protonation obviously results in a severe distortion of the Si<sub>9</sub> moiety, which is in between the ideal  $C_{4v}$  and  $D_{3h}$  geometries. The crystallographic point group of the cluster of course is  $C_1$ .

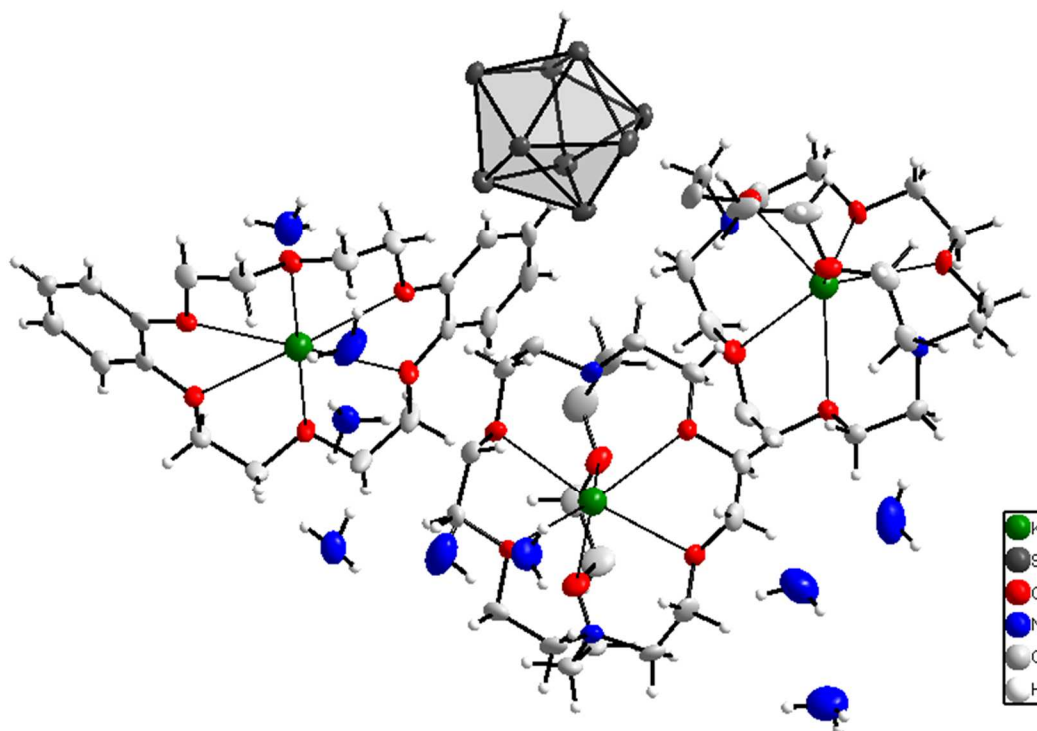


**Figure S10.** Asymmetric unit of  $(\text{K}(\text{DB}[18]\text{crown-6}))(\text{K}([2.2.2]\text{crypt}))_2[\text{HSi}_9]\cdot 8.5\text{NH}_3$ . Anisotropic displacement ellipsoids at 50 % probability level.

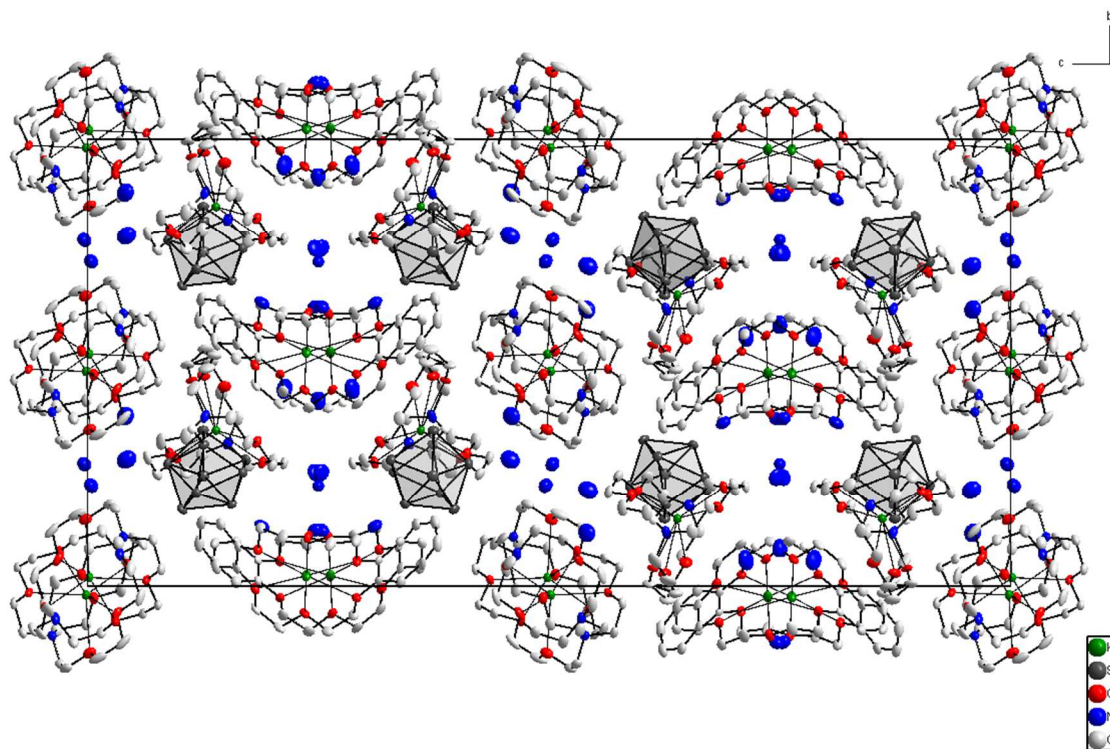


**Figure S11.** Projection of  $(\text{K}(\text{DB}[18]\text{crown-6}))(\text{K}([2.2.2]\text{crypt}))_2[\text{HSi}_9]\cdot 8.5\text{NH}_3$  along the crystallographic  $a$ -axis. Anisotropic displacement ellipsoids at 50 % probability level. For reasons of clarity, the hydrogen atoms of the chelating agents and the ammonia molecules of crystallization are omitted.

## 2.5.2 Sample preparation for NMR

### 2.5.2.1 Solvation of the Zintl phases in liquid ammonia

For NMR studies, 0.0125 g (0.0101 mmol)  $K_6Rb_6^{29}Si_{17}$  and 0.0076 g (0.0203 mmol) [2.2.2]cryptand were placed in heavy wall precision NMR sample tubes (Pyrex) under argon atmosphere. Anhydrous ammonia was condensed at 195 K. The glass tube was sealed under atmosphere to ensure that the moisture and air sensitive probe did not decompose.

### 2.5.2.2 NMR procedures

All NMR-spectroscopic measurements were recorded on either a Bruker Avance 400 MHz spectrometer equipped with a 5 mm PABBO BB-H/D probe with z-gradient or a Bruker Avance III 600 MHz spectrometer equipped with a 5 mm TBI-probe ( $^1H$ , X,  $^{19}F$ ) with z-gradient. For the low temperature measurements at 203 K, a  $N_2$  evaporator unit was used. The  $^{29}Si$  measurements were performed using a standard Bruker pulse program (zg) with 4k number of scans, TD = 65k with relaxation delay of 5 s. Data were processed with the Bruker software TOPSPIN 3.2 using the processing parameters SI = 130k, WDW = EM and LB = 0.3 Hz. The chemical shifts are reported in ppm relative to a constant stable silicon signal at -325 ppm. The  $^1H^{29}Si$ -DEPT measurements were performed using the standard Bruker pulse program (dept135) with 5k number of scans, TD = 2k with relaxation delay of 5 s with and without  $^1H$  decoupling. Data were processed with the Bruker software TOPSPIN 3.2 using the processing parameters SI = 130k, WDW = EM, LB = 6 Hz. The chemical shifts are reported in ppm relative to a constant stable silicon signal at -325 ppm after initial external referencing on TMS. The  $^1H^{29}Si$ -HMQC experiments were performed using the standard Bruker pulse program (hmqcgpqf) with 256 number of scans, DS = 16, TD(F2) = 2k, TD(F1) = 512 with a relaxation delay of 1.5 s and various  $\tau$  for 3, 13, 22, and 156 Hz coupling constants. The data were processed with the Bruker software TOPSPIN 3.2 using the processing parameters SI = 2k (F2 and F1), WDW = EM (F2 and F1), LB(F2) = 1 Hz, LB(F1) = 6 Hz.

### 2.5.2.3 Temperature dependent NMR measurements (203 – 243 K)

The NMR spectra at 233 K were recorded on a Bruker Avance III 600 MHz spectrometer equipped with a 5 mm TBI-probe ( $^1H$ , X,  $^{19}F$ ) with z-gradient. For the temperature dependent measurements (203 - 243 K), a  $N_2$  evaporator unit was used. The



$^{29}\text{Si}$  measurements were performed using a standard Bruker pulse program (zg) with 512 number of scans, TD = 65k with relaxation delay of 5 s. Data were processed with the Bruker software TOPSPIN 3.2 using the processing parameters SI = 130k, WDW = EM and LB = 1 Hz. The chemical shifts are reported in ppm relative to a constant stable silicon signal at -325 ppm after initial external referencing on TMS.

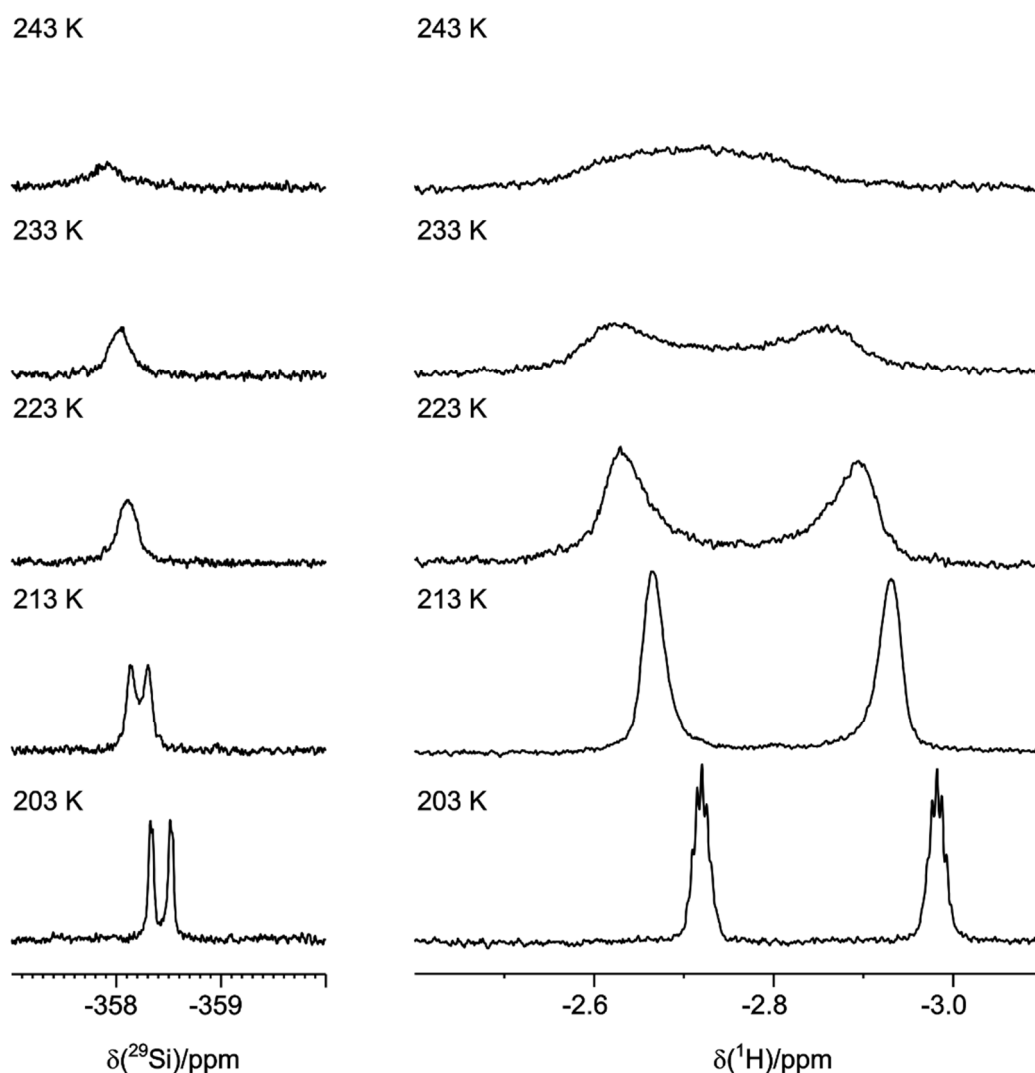


**Figure S8.** Temperature dependent  $^{29}\text{Si}$ - (left,  $\text{Si}_8$  unit at -358 ppm) and  $^1\text{H}$ - spectra (right,  $\text{Si-H}$  at -2.85 ppm) of a sample of  $\text{K}_6\text{Rb}_6\text{Si}_{17}$  with [2.2.2]cryptand (1:2) in liquid  $\text{NH}_3$  from 203 to 243 K (in 10 K intervals, from bottom to top) showing decreasing Si-Si and Si-H coupling constants with increasing temperature. The coalescence point was reached at 243 K. The  $^{29}\text{Si}$  signal of the Si-H silicon atom at -158 ppm is not included here due to its low sensitivity being close to the detection limit.

### 2.5.2.4 Comparison of experimental and calculated $^1\text{H}^{29}\text{Si}$ -HMQC intensity buildup for $\text{Si}_8$ moiety

The observed coupling constant between  $\text{Si}_8$  and the H atom is  $\approx 3$  Hz, Therefore, even accounting  $T_2$  relaxation one could expect high intensity in HMQC for 3 Hz, however the experimental results show a different intensity pattern, which is tabulated in SX below. The highest observed intensity for 156 Hz, and least intensity for 3 Hz is only possible if there is proton hopping between  $\text{Si}_8$  and Si-H in  $[\text{Si}_8\text{-Si-H}]^{3-}$ . For Intensity calculation, the  $T_2$  relaxation is indirectly obtained from linewidths of the 1D  $^{29}\text{Si}$  spectrum.

$$I \propto \sin^2(\pi J_{\text{SiH}}\tau) e^{-\frac{t}{T_2}}$$

$$T_2 = \frac{1}{\pi \Delta\delta}$$

$$\tau = (2J)^{-1}$$

Here,  $I$  is intensity,  $T_2$  is transverse relaxation,  $t$  is experimental time per one scan,  $\tau$  is modulated according to varied coupling values,  $\Delta\delta$  is the line width in Hz.

**Table S4.** Comparison of the theoretical relative intensities for  $\text{Si}_8$  moiety of  $[\text{HSi}_9]^{3-}$ , expected in a static Si-H bond situation, and those observed in the  $\tau$ -modulated  $^1\text{H}^{29}\text{Si}$ -HMQC experiments.

$J$ [Hz]	Relative Calculated Intensity	Relative Experimental Intensity
3	1	1
13	0.1257	5.2974
22	0.0452	4.0878
156	0.0009	7.4459

1D row slice of  $^1\text{H}^{29}\text{Si}$ -HMQC experiments with different time delays  $\tau$  optimized for corresponding coupling constants

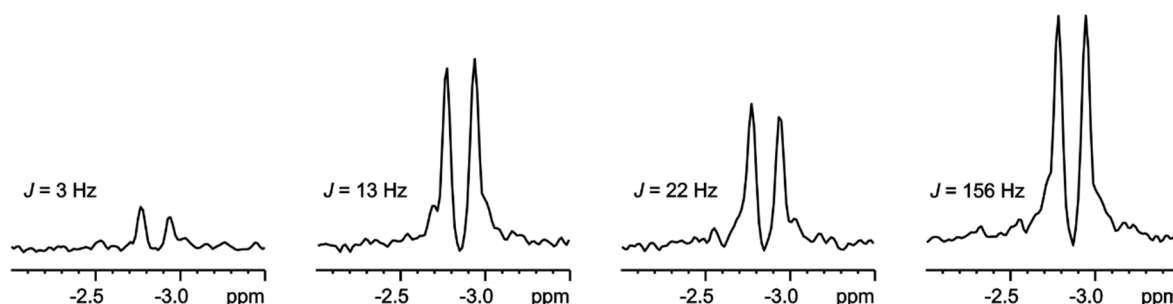


**Figure S9.** Unexpected behavior of the  $\text{Si}_8$  moiety in  $\tau$ -modulated HMQC experiments. Here, the 1D slices extracted from the 2D  $^1\text{H}^{29}\text{Si}$ -HMQC experiments are shown.

2.5.2.5 2D  $^1\text{H}^{29}\text{Si}$ -HMQC experiment

The 2D  $^1\text{H}^{29}\text{Si}$ -HMQC experiment with  $\tau$  for coupling constant 156 Hz shows a cross signal with nonet pattern for the H-Si at -158.5 ppm. This pattern was also observed for the  $\text{Si}_8$  moiety at -358.5 ppm due to chemical exchange of both entities via H-hopping.

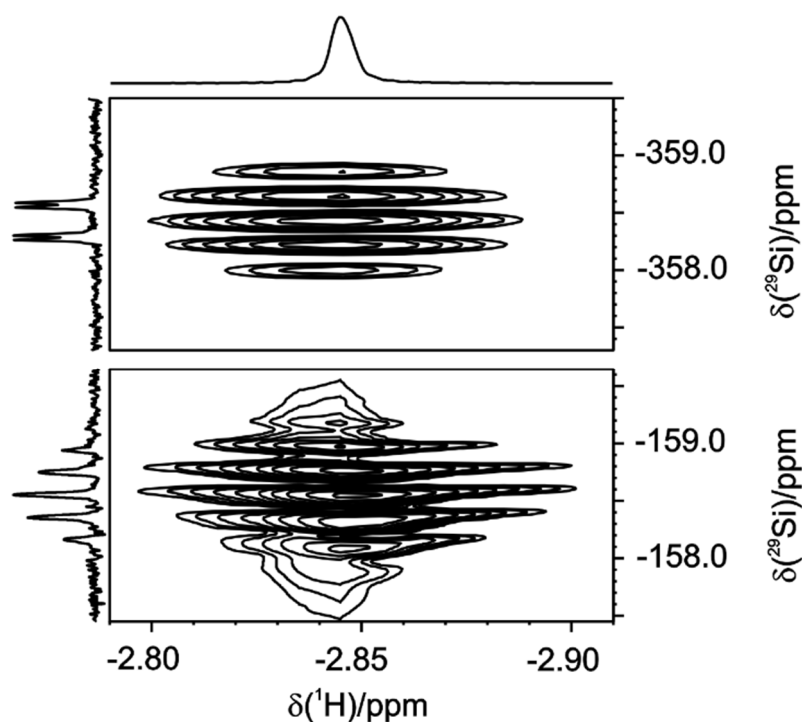


**Figure S10.** Obtained coupling pattern for the  $\text{Si}_8$  at -358.5 ppm moiety and as well as Si-H at -158.5 ppm due to mutual exchange caused by H-hopping. The spectra were recorded at 203 K. The projection in the  $^1\text{H}$  dimension is a  $^1\text{H}\{^{29}\text{Si}\}$  spectra with solvent presaturation. In the  $^{29}\text{Si}$  dimension a standard  $^{29}\text{Si}$  spectrum (-358.5 ppm) and a  $^1\text{H}^{29}\text{Si}\{^1\text{H}\}$ -DEPT spectrum (-158.5 ppm) was used as projections.

### 2.5.2.6 Estimation of exchange rate constant range by line width analysis and CEST experiments

Comparison of obtained experimental linewidth of  $^{29}\text{Si}$  peak with simulated  $^{29}\text{Si}$  spectrum suggests  $k_{\text{ex}} < 10 \text{ s}^{-1}$  for the H-hopping. The simulation was carried out in SpinWorks with the DNMR3 suit. The different line widths were simulated by varying rate constants for a two-site exchange model.

**Table S5.** Estimation of exchange rate constant by dynamic NMR simulation (SpinWorks; DNMR3).

k	sim $\Delta\delta$	exp $\Delta\delta$
0	0.8 Hz	
1	1 Hz	
5	2 Hz	
10	4 Hz	3.5 Hz
20	7 Hz	
50	15 Hz	
100	32 Hz	

### 2.5.2.7 CEST measurements

The Graphical representation of the used CEST pulse sequence is given below. It consists of continuous saturation pulse (CW) and a reading  $90^\circ$  pulse. The saturation at -158.5 ppm is achieved by continuous wave with  $B_1$  field strength of 530 Hz for 1 sec. The other experimental parameters have been kept similar to normal  $^{29}\text{Si}$  1D experiment. <sup>[6]</sup>

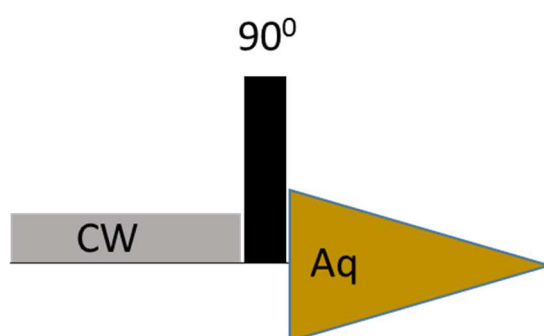


**Figure S11.** Graphical representation of the Chemical Exchange Saturation Transfer (CEST) experiment.

Two CEST experiments were measured for the detection of the  $\text{Si}_8$  moiety with and without saturation of the protonated Si (-158.5 ppm), while keeping all other experimental parameters constant.

The CEST intensity analysis gives approximate one direct rate constant  $k_1$  (eq. 1). Here,  $T_{1sat}$  is longitudinal relaxation time with saturation, which is assumed around 3 s for  $\text{Si}_9\text{H}^{3-}$  based on our earlier experience.  $M_S$  and  $M_0$  are intensities of  $\text{Si}_8$  moiety measured without and with saturation of the protonated Si.

$$k_1 = \frac{1}{T_{1sat}} \left( 1 - \frac{M_S}{M_0} \right) \quad (1)$$

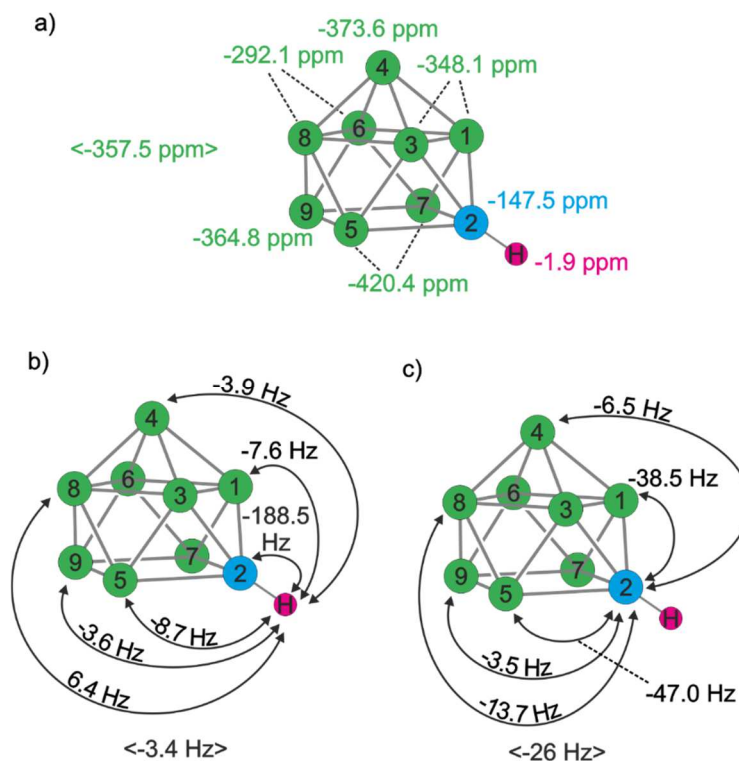
$$\approx \frac{1}{3} (1 - 0.47) = 0.177$$

$$k_1 \approx 10^{-1}$$

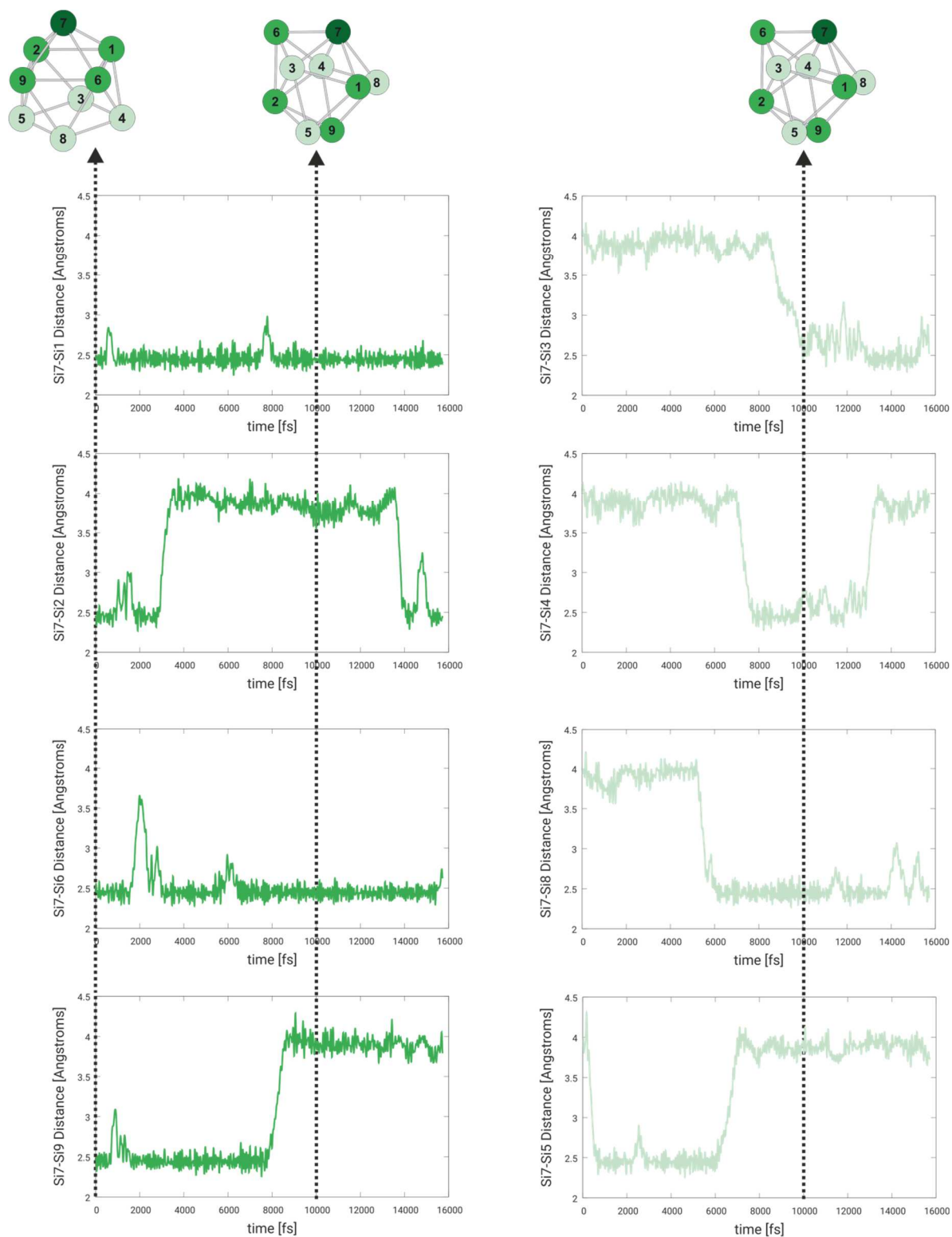
To obtain accurate values, it requires complete CEST profile development, which is quite difficult and time consuming for the present system. Nevertheless, one can access approximate range of the rate constant.

### 2.5.3 Theoretical calculations

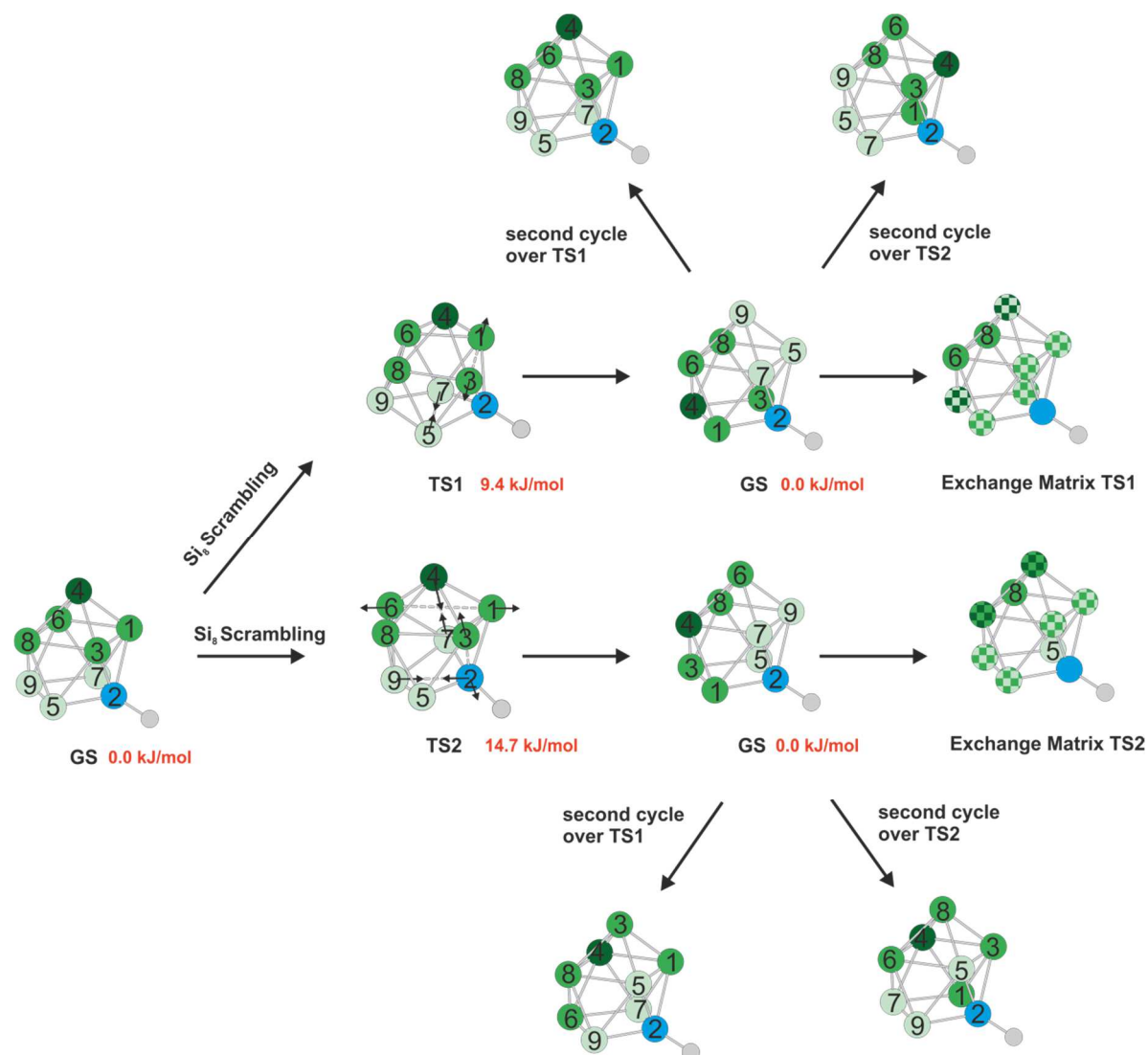
#### 2.5.3.1 Theoretical calculated values for chemical shifts and coupling constants



**Figure S12.** Theoretical calculated values for a) chemical shifts, b) Si-H coupling and c) Si-Si coupling in respect to each Si- and H-atom. Averaged values are given in  $\langle \rangle$ .

2.5.3.2 MD simulation of the [HSi<sub>9</sub>]<sup>4-</sup> cluster

**Figure S13.** Si7-Si*N* interatomic distances of an ab initio MD at 300 K in continuum of NH<sub>3</sub>. At the beginning Si7 is the cap atom, at 10k fs Si6 is the cap. The cage is scrambled within picosecond time frame.

2.5.3.3 Detailed description of the averaging of the Si<sub>8</sub> moiety

**Figure S14.** Si<sub>8</sub> scrambling via TS1 and TS2 and their generated exchange matrices. Only through TS2, all Si<sub>8</sub> will be scrambled and hence produce chemical equivalent nuclei in the NMR. When exclusively TS1 is active, Si6 and Si8 will not be scrambled.

## 2.5.3.4 Computational Details

Geometry, NMR shifts and scalar coupling constant calculations were performed with Gaussian09 Revision D.01.<sup>[7]</sup> All clusters and their transition states were optimized at TPSSH/6-311+G(d,p) level of theory in continuum of NH<sub>3</sub> using SMD model.<sup>[8]</sup> The dielectric of NH<sub>3</sub> was modified to 22.63 to mimic low temperature measurement. However, the impact on the geometry is not substantial. Frequency analysis for determination of saddle points and thermochemical correction were performed at the same level of theory. Single points were conducted on the optimized geometry at DLPNO-CCSD(T)/def2-

QZVPP level of theory using ORCA version 4.0.1.2.<sup>[9]</sup> NMR calculations were done at TPSSH/pcsseg-4 level of theory. For the preliminary ab initio MD of Si<sub>9</sub><sup>4-</sup> cluster with TURBOMOLE 7.1,<sup>[10]</sup> canonical ensemble (NVT) at 300 K in continuum of NH<sub>3</sub> were chosen. The time step was 65 a.u. and the MD was performed for 10000 steps (~15722 fs). Nosé-Hoover thermostat relaxation time was 130 a.u.. TPSSH functional and def2-TZVP basis set were used in the MD.<sup>[11]</sup>

### 2.5.3.5 Calculated Geometry

#### Si<sub>9</sub><sup>4-</sup>

```
1\1\GINC-WORKER0\FOpt\RTPSSH\6-311+G(d,p)\Si9(4-)\JHIOE\20-Jul-2016\0\
\#p tpssh/6-311+g(d,p) opt scrf=(smd,solvent=generic) int=ultrafine fr
eq\title\ -4,1\Si,-0.7026469778,-1.3509516475,1.3258670271\Si,-0.7026
469778,-1.3509516475,-1.3258670271\Si,-2.1781754502,0.1017221546,0.\Si
,-0.7244873184,1.0654434722,1.7719956074\Si,-0.7244873184,1.0654434722
,-1.7719956074\Si,1.5158696901,0.1543489858,1.3290169713\Si,1.29049786
27,-1.896790089,0.\Si,0.710205799,2.0573873161,0.\Si,1.5158696901,0.15
43489858,-1.3290169713\Version=ES64L-G09RevD.01\State=1-A\HF=-2606.0
918647\RMSD=2.435e-09\RMSF=1.610e-05\Dipole=0.2529445,-0.3770646,0.\Qu
adropole=-0.1067783,1.6822787,-1.5755004,-2.5089872,0.,0.\PG=CS [SG(Si
3),X(Si6)]\@
```

#### [HSi<sub>9</sub>]<sup>3-</sup> (GS)

```
1\1\GINC-WORKER0\FOpt\RTPSSH\6-311+G(d,p)\H1Si9(3-)\JHIOE\20-Mar-2018\
0\#p tpssh/6-311+g(d,p) opt scrf=(smd,solvent=generic) int=ultrafine
freq\title\ -3,1\Si,0.8157881381,-1.8698286905,-0.2663573772\Si,0.229
1970665,-0.1349419578,-1.8626457672\Si,-1.7050481663,-0.9382350415,-0.
6325257131\Si,-0.7696705813,-1.4947695056,1.5594967567\Si,-1.276896174
2,1.5264729698,-1.1186785528\Si,1.2060855478,-0.0226258285,1.590509839
7\Si,2.1985175407,0.2433759718,-0.613144464\Si,-1.2776359088,0.8935740
886,1.2290387411\Si,0.7084995416,2.0490678658,0.3838351538\H,0.2449689
959,-0.650069872,-3.2701626171\Version=ES64L-G09RevD.01\State=1-A\HF=
-2606.616615\RMSD=8.000e-09\RMSF=3.044e-05\Dipole=0.0147517,-0.3895549
```



,-1.0938858\Quadrupole=-3.3243911,-3.3862391,6.7106302,0.0668431,-1.51  
7122,-0.0868214\PG=C01 [X(H1Si9)]\@

### [HSi<sub>9</sub>]<sup>3-</sup> Shared (INT1)

1\1\GINC-WORKER1\FOpt\RTPSSh\6-311+G(d,p)\H1Si9(3-)\JHIOE\30-May-2018\  
0\#p tpssh/6-311+g(d,p) opt scrf=(smd,solvent=generic) int=ultrafine  
freq\title\ -3,1\Si,1.0336150912,-1.351822356,0.9917224696\Si,-0.6862  
078022,-0.0632518253,2.1622615395\Si,0.9897971887,1.4113383986,1.16858  
42368\Si,2.2078695184,0.1176944891,-0.5138130612\Si,-1.2241837507,1.90  
90125438,0.2662848749\Si,0.2912767943,-1.3042328059,-1.4573046128\Si,-  
1.2955106039,-1.729412047,0.3795446261\Si,0.3320893263,1.2567493498,-1  
.5068658031\Si,-1.7714131842,0.0367775938,-1.317567844\H,-1.867832488,  
0.9172097391,1.4687532243\Version=ES64L-G09RevD.01\State=1-A\HF=-2606  
.5882388\RMSD=8.270e-09\RMSF=9.500e-05\Dipole=0.2431356,0.3003519,0.24  
63691\Quadrupole=2.63575,-2.0545724,-0.5811776,-1.8629413,-3.2918641,0  
.7473239\PG=C01 [X(H1Si9)]\@

### [HSi<sub>9</sub>]<sup>3-</sup> (TS1)

1\1\GINC-LOGIN\SP\RTPSSh\6-311+G(d,p)\H1Si9(3-)\JHIOE\07-Jun-2018\0\#  
p tpssh/6-311+g(d,p) scrf=(smd,solvent=generic,externaliteration,dovac  
uum) int=ultrafine\title\ -3,1\Si,0,-1.256289,1.62004,0.696505\Si,0,0  
.002308,-0.000102,1.921499\Si,0,-1.257266,-1.619419,0.696328\Si,0,-2.0  
0966,0.000702,-1.028423\Si,0,1.257355,-1.620931,0.693981\Si,0,-0.00087  
2,1.371882,-1.442965\Si,0,1.258326,1.620155,0.694128\Si,0,-0.001743,-1  
.371724,-1.443083\Si,0,2.007594,-0.000589,-1.031768\H,0,0.003459,-0.00  
0177,3.413172\Version=ES64L-G09RevD.01\State=1-A\HF=-2606.6060024\RMS  
D=4.758e-09\Dipole=0.0007019,-0.0000725,1.4038816\Quadrupole=-2.729592  
5,-4.1417931,6.8713856,0.0000958,0.0157235,-0.0008971\PG=C01 [X(H1Si9)  
]\@

### [HSi<sub>9</sub>]<sup>3-</sup> (TS2)

1\1\GINC-WORKER1\SP\RTPSSh\6-311+G(d,p)\H1Si9(3-)\JHIOE\07-Jun-2018\0\  
\#p tpssh/6-311+g(d,p) scrf=(smd,solvent=generic,externaliteration,dov  
acuum) int=ultrafine\title\ -3,1\Si,0,-1.577877,1.212784,-0.967862\Si

,0,0.238116,-0.156941,-1.719801\Si,0,0.771194,1.892861,-0.360439\Si,0,  
-0.887926,1.452923,1.371948\Si,0,2.27576,-0.119193,-0.508516\Si,0,-1.0  
35469,-1.060972,1.548952\Si,0,-1.628858,-1.324282,-0.81007\Si,0,1.1569  
44,0.085486,1.6269\Si,0,0.658945,-1.964838,0.047475\H,0,0.408389,-0.24  
958,-3.200205\\Version=ES64L-G09RevD.01\State=1-A\HF=-2606.6044788\RMS  
D=2.983e-09\Dipole=0.5860685,-0.1472601,-1.2819361\Quadrupole=-0.20043  
77,-3.7229806,3.9234183,-0.130567,-1.8947287,0.8776048\PG=C01 [X(H1Si9  
)]\@

### [HSi<sub>9</sub>]<sup>3-</sup> (TS3)

1\1\GINC-LOGIN\SP\RTPSSh\6-311+G(d,p)\H1Si9(3-)\JHIOE\07-Jun-2018\0\#  
p tpssh/6-311+g(d,p) scrf=(smd,solvent=generic,externaliteration,dovac  
uum) int=ultrafine\\title\\-3,1\Si,0,1.809144,-1.093496,-0.06052\Si,0,  
-0.349243,-2.11024,-0.26311\Si,0,0.015742,-0.780443,1.852904\Si,0,1.59  
0329,0.95714,1.28174\Si,0,-2.09277,-0.597076,0.54028\Si,0,0.739077,1.7  
52497,-0.845819\Si,0,0.644546,-0.39423,-2.078747\Si,0,-0.887755,1.4876  
57,1.037471\Si,0,-1.438415,0.896313,-1.326068\H,0,-0.42917,-1.653717,-  
1.933823\\Version=ES64L-G09RevD.01\State=1-A\HF=-2606.5783392\RMSD=2.3  
62e-09\Dipole=0.174509,-0.1488566,-0.3116813\Quadrupole=-1.2439775,0.4  
873935,0.756584,2.1501201,0.8530561,2.8151509\PG=C01 [X(H1Si9)]\@

## 2.5.3.6 Marcus analysis of the scrambling process via TS1

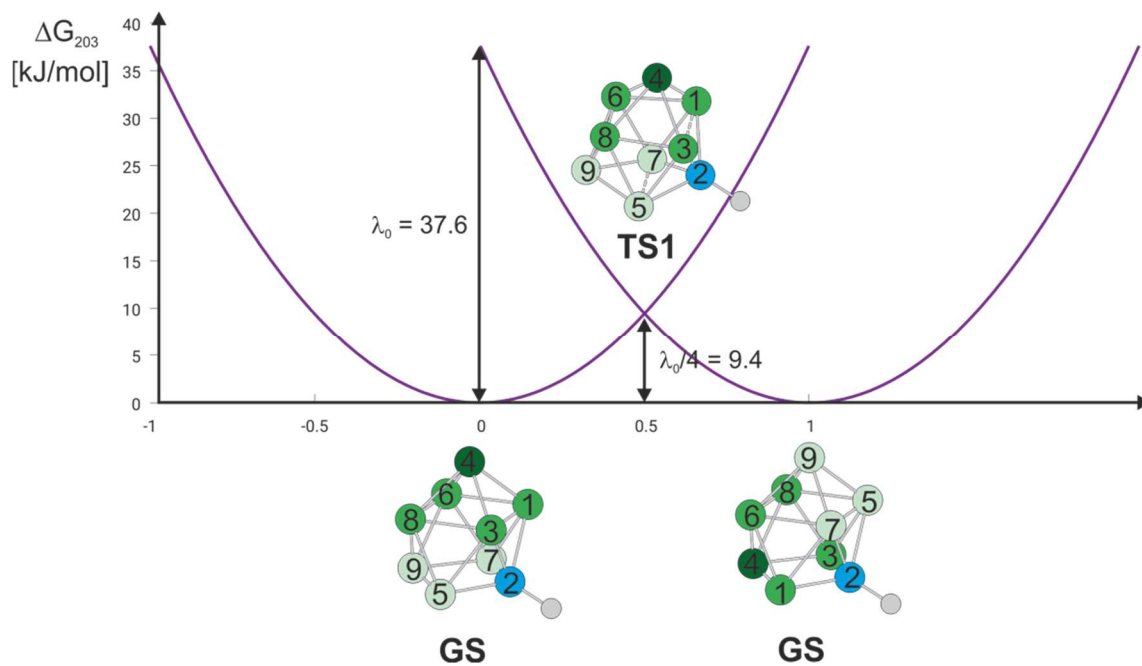


**Figure S15.** Rearrangement process of the  $\text{Si}_8$  entity via TS1. The low intrinsic barrier indicates low reorganization energy for the cluster.

## 2.5.3.7 Thermochemical analysis of the Zintl cluster

Table S6. Decomposition of thermochemical correction.

GS (Nimag=0)		Contribution to internal thermal energy [kcal/mol]	Entropy [cal/(mol K)]
	Translational	0.605	40.573
	Rotational	0.605	30.230
	Vibrational	16.192	21.615
	Σ	17.402	92.418
		<b>H<sub>corr</sub>(T=203)</b>	<b>T*S (T=203)</b>
		17.805 kcal/mol	18.760 kcal/mol
<b>TS1</b> (Nimag=1; -76.7944 cm <sup>-1</sup> )			
	Translational	0.605	40.573
	Rotational	0.605	30.240
	Vibrational	15.885	18.394
	Σ	17.096	89.207
		<b>H<sub>corr</sub>(T=203)</b>	<b>T*S (T=203)</b>
		17.499 kcal/mol	18.109 kcal/mol
<b>TS2</b> (Nimag=1; -32.2534 cm <sup>-1</sup> )			
	Translational	0.605	40.573
	Rotational	0.605	30.226
	Vibrational	15.905	18.569
	Σ	17.115	89.368
		<b>H<sub>corr</sub>(T=203)</b>	<b>T*S (T=203)</b>
		17.518	18.142
<b>INT1</b> (Nimag=0)			
	Translational	0.605	40.573
	Rotational	0.605	30.279
	Vibrational	15.344	23.042
	Σ	16.554	93.894
		<b>H<sub>corr</sub>(T=203)</b>	<b>T*S (T=203)</b>
		16.957	19.061
<b>TS3</b> (Nimag=1; -75.1744 cm <sup>-1</sup> )			
	Translational	0.605	40.573
	Rotational	0.605	30.275
	Vibrational	14.858	19.663
	Σ	16.068	90.510
		<b>H<sub>corr</sub>(T=203)</b>	<b>T*S (T=203)</b>
		16.471	18.374

**Table S6** shows the decomposed thermochemical correction. In all cases, the entropy term is larger than the contribution to the internal thermal energy. Consequently, the thermal correction to Gibbs free energy is negative. This hints that the rearrangement process is driven by entropy.

## 2.6 References

- [1] A. F. Holleman, E. Wiberg, N. Wiberg, *Anorganische Chemie*, 103<sup>rd</sup> ed., Walter de Gruyter GmbH, Germany, 2017.
- [2] W. Lu, C. M. Lieber, *Nat. Mater.* **2007**, *6*, 841-850; M. L. Snedaker, Y. C. Zhang, C. S. Birkel, H. Wang, T. Day, Y. F. Shi, X. L. Ji, S. Kraemer, C. E. Mills, A. Moosazadeh, M. Moskovits, G. J. Snyder, G. D. Stucky, *Chem. Mater.* **2013**, *25*, 4867-4873; B. K. Teo, X. H. Sun, *Chem. Rev.* **2007**, *107*, 1454-1532; L. Venema, *Nature* **2011**, *479*, 309-309.
- [3] Y. S. Shcherbyna, T. V. Torchynska, *Thin Solid Films* **2010**, *518*, S204-S207; T. Miyazaki, T. Uda, I. Stich, K. Terakura, *Chem. Phys. Lett.* **1996**, *261*, 346-352; G. A. Rechtsteiner, O. Hampe, M. F. Jarrold, *J. Phys. Chem. B* **2001**, *105*, 4188-4194; H. Murakami, T. Kanayama, *Appl. Phys. Lett.* **1995**, *67*, 2341-2343; W. M. M. Kessels, M. C. M. van de Sanden, D. C. Schram, *Appl. Phys. Lett.* **1998**, *72*, 2397-2399; T. V. Torchynska, *Superlattices and Microstruct.* **2009**, *45*, 267-270; D. K. Yu, R. Q. Zhang, S. T. Lee, *J. Appl. Phys.* **2002**, *92*, 7453-7458; G. Belomoin, J. Therrien, A. Smith, S. Rao, R. Twesten, S. Chaieb, M. H. Nayfeh, L. Wagner, L. Mitas, *Appl. Phys. Lett.* **2002**, *80*, 841-843.
- [4] Y. Heider, D. Scheschkewitz, *Dalton Trans.* **2018**, *47*, 7104-7112; P. Willmes, K. Leszczynska, Y. Heider, K. Abersfelder, M. Zimmer, V. Huch, D. Scheschkewitz, *Angew. Chem., Int. Ed.* **2016**, *55*, 2907-2910; D. Scheschkewitz, *Angew. Chem., Int. Ed.* **2005**, *44*, 2954-2956.
- [5] V. Queneau, E. Todorov, S. C. Sevov, *J. Am. Chem. Soc.* **1998**, *120*, 3263-3264.
- [6] C. Hoch, M. Wendorff, C. Rohr, *J. Alloys Compd.* **2003**, *361*, 206-221; S. Scharfe, F. Kraus, S. Stegmaier, A. Schier, T. F. Faessler, *Angew. Chem., Int. Ed.* **2011**, *50*, 3630-3670; E. Zintl, *Angew. Chem.* **1939**, *52*, 1-6.
- [7] N. Korber, F. Richter, *Angew. Chem., Int. Ed.* **1997**, *36*, 1512-1514; C. Lorenz, S. Gartner, N. Korber, *Z. Anorg. Allg. Chem.* **2017**, *643*, 141-145; M. Reil, N. Korber, *Z. Anorg. Allg. Chem.* **2007**, *633*, 1599-1602.
- [8] S. Joseph, C. Suchenrunk, F. Kraus, N. Korber, *Eur. J. Inorg. Chem.* **2009**, *2009*, 4641-4647.
- [9] M. Neumeier, F. Fendt, S. Gaertner, C. Koch, T. Gaertner, N. Korber, R. M. Gschwind, *Angew. Chem., Int. Ed.* **2013**, *52*, 4483-4486.
- [10] J. M. Goicoechea, S. C. Sevov, *J. Am. Chem. Soc.* **2004**, *126*, 6860-6861; J. M. Goicoechea, S. C. Sevov, *Inorg. Chem.* **2005**, *44*, 2654-2658; S. Joseph, C. Suchentrunk, N. Korber, *Z. Naturforsch.* **2010**, *B65*, 1059-1065.

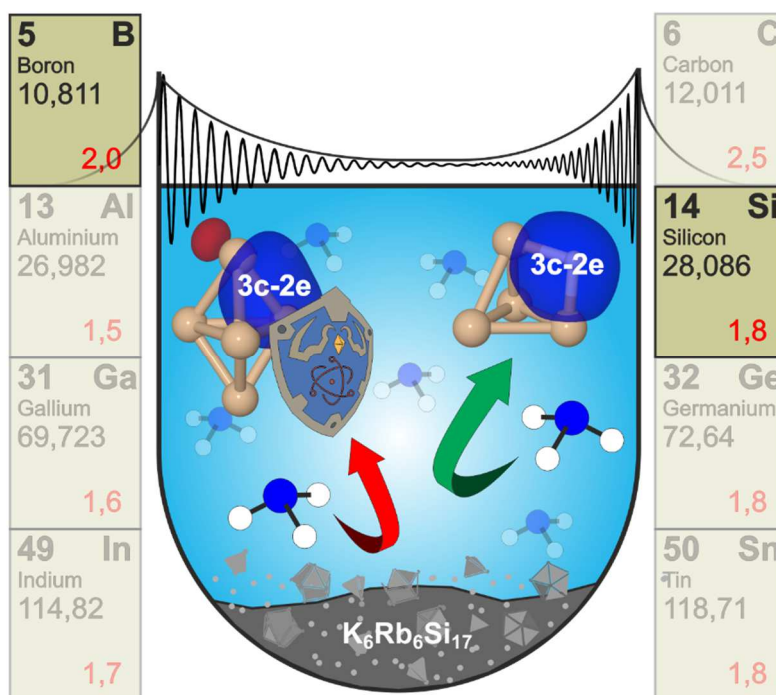
- [11] A. Ugrinov, S. C. Sevov, *Chem. Eur. J.* **2004**, *10*, 3727-3733.
- [12] F. S. Kocak, D. O. Downing, P. Zavalij, Y. F. Lam, A. N. Vedernikov, B. Eichhorn, *J. Am. Chem. Soc.* **2012**, *134*, 9733-9740.
- [13] J. D. Corbett, P. A. Edwards, *J. Am. Chem. Soc.* **1977**, *99*, 3313-3317.
- [14] F. S. Kocak, B. Eichhorn, *Structure and Bonding, Vol. 140*, Springer-Verlag, Berlin/Heidelberg, **2011**.
- [15] Shortly after the submission of this Communication, a single-crystal study on the compound [K(18-crown-6)]<sub>3</sub>[HSi<sub>9</sub>]·2NH<sub>3</sub>·2thf, which also contains the [HSi<sub>9</sub>]<sup>3-</sup> anion, was published: T. Henneberger, W. Klein and T. F. Fässler, *Z. Anorg. Allg. Chem.* **2018** <https://doi.org/10.1002/zaac.201800227>; parallel to the present Communication, evidence for an [H<sub>2</sub>Si<sub>9</sub>]<sup>2-</sup> anion obtained by solution NMR spectroscopy was published in: L. J. Schiegerl, A. J. Karttunen, J. Tillmann, S. Geier, G. Raudaschl-Sieber, M. Waibel, T. F. Fässler. *Angew. Chem. Int. Ed.* **2018**, *57*, <https://doi.org/10.1002/anie.201804756>; *Angew. Chem.* **2018**, *130*, <https://doi.org/10.1002/ange.201804756>, which was submitted significantly earlier.
- [16] S. Chtchian, R. Kempe, C. Krempner, *J. Organomet. Chem.* **2000**, *613*, 208-219.
- [17] F. Fendt, C. Koch, M. Neumeier, S. Gartner, R. M. Gschwind, N. Korber, *Eur. J.* **2015**, *21*, 14539-14544.
- [18] F. Fendt, C. Koch, S. Gartner, N. Korber, *Dalton Trans.* **2013**, *42*, 15548-15550.
- [19] L. Hackspill, *Helv. Chim. Acta* **1928**, *11*.
- [20] T. Kottke, D. Stalke, *J. Appl. Crystallogr.* **1993**, *26*, 615-619; O. V. Dolomanov, L. J. Bourhis, R. J. Gildea, J. A. K. Howard, H. Puschmann, *J. Appl. Crystallogr.* **2009**, *42*, 339-341; G. M. Sheldrick, *Acta Crystallogr. Sect C* **2015**, *71*, 3-8.
- [21] K. Brandenburg, *Vol. Version 3.2k*, Crystal Impact GbR, Bonn, Germany, **2014**.
- [22] U. University, Utrecht, The Netherlands, **1998**.
- [23] S. Gärtner, N. Korber, in *Structure and Bonding, Vol. 140* (Ed.: T. F. Fässler), Springer, Berlin, Heidelberg, **2011**.
- [24] K. M. Ward, A. H. Aletras, R. S. Balaban *J. Magn. Res.* **1999**, *143*, 79-87
- [25] Gaussian 09, Revision D.01, M. J. Frisch, G. W. Trucks, H. B. Schlegel, G. E. Scuseria, M. A. Robb, J. R. Cheeseman, G. Scalmani, V. Barone, G. A. Petersson, H. Nakatsuji, X. Li, M. Caricato, A. Marenich, J. Bloino, B. G. Janesko, R. Gomperts, B. Mennucci, H. P. Hratchian, J. V. Ortiz, A. F. Izmaylov, J. L. Sonnenberg, D. Williams-Young, F. Ding, F. Lipparini, F. Egidi, J. Goings, B. Peng, A. Petrone, T. Henderson, D. Ranasinghe, V. G. Zakrzewski, J. Gao, N. Rega, G. Zheng, W. Liang, M. Hada, M. Ehara, K. Toyota, R. Fukuda, J. Hasegawa, M. Ishida, T. Nakajima, Y. Honda, O. Kitao, H. Nakai, T. Vreven, K. Throssell, J. A. Montgomery, Jr., J. E. Peralta, F. Ogliaro, M. Bearpark, J. J. Heyd, E. Brothers, K.

- N. Kudin, V. N. Staroverov, T. Keith, R. Kobayashi, J. Normand, K. Raghavachari, A. Rendell, J. C. Burant, S. S. Iyengar, J. Tomasi, M. Cossi, J. M. Millam, M. Klene, C. Adamo, R. Cammi, J. W. Ochterski, R. L. Martin, K. Morokuma, O. Farkas, J. B. Foresman, and D. J. Fox, Gaussian, Inc., Wallingford CT, **2016**.
- [26] A. V. Marenich, C. J. Cramer, and D. G. Truhlar, "Universal solvation model based on solute electron density and a continuum model of the solvent defined by the bulk dielectric constant and atomic surface tensions," *J. Phys. Chem. B* **2009**, 113, 6378-96.
- [27] a) Neese, F.; "Software update: the ORCA program system, version 4.0" *WIREs Comput Mol Sci* **2017**, e1327;  
b) Riplinger, C.; Sandhoefer, B.; Hansen, A.; Neese, F. *J. Chem. Phys.* **2013**, 139, 134101;  
c) Riplinger, C.; Neese, F. *J. Chem. Phys.* **2013**, 138, 034106.
- [28] TURBOMOLE V7.1 2016, a development of University of Karlsruhe and Forschungszentrum Karlsruhe GmbH, 1989-2007, TURBOMOLE GmbH, since 2007; available from <http://www.turbomole.com>.
- [29] a) V. N. Staroverov, G. E. Scuseria, J. Tao and J. P. Perdew, "Comparative assessment of a new nonempirical density functional: Molecules and hydrogen-bonded complexes," *J. Chem. Phys.*, **2003**, 119, 12129.  
b) J. M. Tao, J. P. Perdew, V. N. Staroverov, and G. E. Scuseria, "Climbing the density functional ladder: Nonempirical meta-generalized gradient approximation designed for molecules and solids," *Phys. Rev. Lett.* **2003**, 91, 146401.





### 3 Elusive Zintl Ions $[\mu\text{-HSi}_4]^{3-}$ and $[\text{Si}_5]^{2-}$ in Liquid Ammonia: Protonation States, Sites, and Bonding Situation Evaluated by NMR and Theory



The NMR spectroscopic investigations were performed in close collaboration with Lokesh Nanjundappa. The theoretical calculations were performed by Johnny Hioe. The synthesis and characterization of the solids as well as the sample preparation were performed by Corinna Lorenz and Stefanie Gärtner. Furthermore, Florian Hastreiter did the probability calculation, the figures and the writing of the Additional Findings.

---

Florian Hastreiter,<sup>+</sup> Corinna Lorenz,<sup>+</sup> Johnny Hioe,<sup>+</sup> Stefanie Gärtner, Nanjundappa Lokesh, Nikolaus Korber\*, and Ruth M. Gschwind\*

[+] These authors contributed equally to the publication.

*Angew. Chem. Int. Ed.* **2019**, 58, 3133-3137.

DOI: 10.1002/anie.201812955

© 2019 Wiley-VCH Verlag GmbH & Co. KGaA. Reproduced with permission.

### 3.1 Abstract

The existence of  $[\mu\text{-HSi}_4]^{3-}$  in liquid ammonia solutions is confirmed by  $^1\text{H}$  and  $^{29}\text{Si}$  NMR experiments. Both NMR and quantum chemical calculations reveal that the H atom bridges two Si atoms of the  $[\text{Si}_4]^{4-}$  cluster, contrary to the expectation that it is located at one vertex Si of the tetrahedron. The calculations also indicate that in the formation of  $[\mu\text{-HSi}_4]^{3-}$ , protonation is driven by a high charge density and an increase of electron delocalization compared to  $[\text{Si}_4]^{4-}$ . Additionally,  $[\text{Si}_5]^{2-}$  was detected for the first time and characterized by NMR. Calculations show that it is resistant to protonation, owing to a strong charge delocalization, which is significantly reduced upon protonation. Thus, our methods reveal three silicides in liquid ammonia: unprotonated  $[\text{Si}_5]^{2-}$ , terminally protonated  $[\text{HSi}_9]^{3-}$ , and bridge-protonated  $[\mu\text{-HSi}_4]^{3-}$ . The protonation trend can be roughly predicted by the difference in charge delocalization between the parent compound and the product, which can be finely tuned by the presence of counter ions in solution.

### 3.2 Introduction

Molecular cluster-shaped building blocks are widely known for the main-group elements boron (for example,  $[\text{B}_6\text{H}_6]^{2-}$ ,<sup>[1]</sup>  $[\text{B}_9\text{H}_9]^{2-}$ ,<sup>[2]</sup>  $[\text{B}_{12}\text{H}_{12}]^{2-}$ <sup>[3]</sup>) and phosphorous ( $[\text{P}_4]$ ,  $[\text{P}_7]^{3-}$ ,<sup>[4]</sup>  $[\text{P}_8]^{5-}$ ). For the element silicon, its position in the periodic table would suggest cluster formation because of the diagonal relationship to boron, whereas the pseudo-element concept would imply an analogy to phosphorous compounds.<sup>[6]</sup> However, for silicon, different cluster categories are known. There are ligand-stabilized cluster compounds  $(\text{ER})_n$ , metalloid clusters  $\text{Si}_n\text{R}_m$  ( $n > m$ ) that include unsubstituted silicon atoms, and furthermore siliconoids, which include substituted, unsubstituted, and negatively charged silicon atoms.<sup>[7]</sup> The only ligand-free silicon clusters known to date are negatively charged polyanions, commonly known as silicide anions, for which the term Zintl ions holds true.<sup>[8, 9]</sup> These Zintl anions exist as preshaped clusters. Numerous crystal structures containing four-, five-, seven-, and nine-atomic Zintl anions like  $[\text{Pb}_4]^{4-}$ ,<sup>[10, 11]</sup>  $[\text{Sn}_5]^{2-}$ ,<sup>[12]</sup>  $[\text{P}_7]^{3-}$ ,<sup>[4, 9]</sup> and  $[\text{Sn}_9]^{4-}$ <sup>[9]</sup> are known in solid-state materials as well as solvate crystal structures. However, it is far more difficult to investigate which of these species actually exist in solution. Owing to the good NMR properties of lead, tin, and phosphorous, NMR studies have been attempted from early on.<sup>[13–15]</sup> But only for phosphorous polyanions, a versatile solution chemistry is known, shown by the landmark  $^{31}\text{P}$  studies of Baudler *et al.*<sup>[16]</sup> In contrast, no similar polyanion solution chemistry was known for silicon, which is certainly one of the technologically most relevant main group elements. In 1998, Sevov

and co-workers reported the first crystal structure of a binary Zintl phase  $\text{Rb}_{12}(\text{Si}_4)_2(\text{Si}_9)$ .<sup>[17]</sup> Subsequent dissolution experiments of  $\text{A}_{12}\text{Si}_{17}$  ( $\text{A}=\text{K}, \text{K}/\text{Rb}, \text{Rb}$ ) yielded several solvate crystal structures of the nine-atom cluster  $[\text{Si}_9]^{x-}$  ( $x=2-4$ )<sup>[9, 18-21]</sup> and  $[\text{H}_n\text{Si}_9]^{x-}$  ( $n=1, 2; x=3, 2$ ),<sup>[21-23]</sup>  $[\text{Si}_4]^{4-}$ ,<sup>[11, 24, 25]</sup> and the trigonal bipyramidal  $[\text{Si}_5]^{2-}$  species.<sup>[19]</sup> Generally, anhydrous liquid ammonia proved to be the only appropriate solvent for the very moisture- and air-sensitive silicide precursor Zintl phases.<sup>[18, 24]</sup> However, the solubilities are, generally, rather poor. Additionally, due to the very low natural abundance of  $^{29}\text{Si}$ , which is the only NMR-active Si nucleus, labelling of the precursor phase is indispensable.<sup>[13, 23]</sup> All of this combined with the very difficult and delicate sample handling accounts for the lack of an established solution chemistry of silicides.

Owing to the predominant role of silicon-based materials in technology,<sup>[26]</sup> it is highly important to understand the nature of ligand-free silicon clusters in solution and therefore, the development of a solvation chemistry for silicon should be rewarding. The fundamental research in this field of silicon main group chemistry, however, is also highly interesting, especially with respect to the application of novel preparative and NMR detection techniques. Recently, we succeeded in detecting the highly charged  $[\text{E}_4]^{4-}$  species ( $\text{E}=\text{Si}, \text{Sn}$ ) in liquid ammonia.<sup>[13]</sup> Here, the atom positions are chemically equivalent and thus only a singlet can be observed in NMR spectra, which unfortunately does not allow a statement about the dynamic behavior of the  $[\text{E}_4]^{4-}$  anions. Recently, we were able to show via a complete NMR coupling pattern that an unexpected fluctuating behaviour can be observed in protonated  $[\text{Si}_9]^{4-}$  clusters, which is in analogy to  $[\text{Sn}_9]^{4-}$ ,<sup>[23, 27]</sup> independently and simultaneously also proposed by Fässler *et al.*<sup>[22]</sup> The third cluster species known from recrystallization experiments, trigonal bipyramidal shaped  $[\text{E}_5]^{2-}$ , has not been unambiguously detected in solution yet,<sup>[28]</sup> only incomplete data is reported for  $[\text{Pb}_5]^{2-}$ .<sup>[15]</sup> Due to our unique expertise in NMR studies in liquid ammonia, we focused on the detection of the elusive  $[\text{Si}_5]^{2-}$  clusters in solution. By serendipity, we were also able to detect a protonated  $[\text{HSi}_4]^{3-}$  species during the investigations.

### 3.3 Results and Discussion

For the NMR spectroscopic investigations, a sample of  $\text{K}_6\text{Rb}_6\text{Si}_{17}$  with two equivalents of [2.2.2]cryptand was dissolved in liquid ammonia and measured at 233 K. For  $[\text{HSi}_4]^{3-}$ , two resonances were observed in the  $^{29}\text{Si}$  spectra at  $\delta = -327.8$  ppm (Figure 1a, blue spectrum) and at  $\delta = -404.5$  ppm (green spectrum). In both signals, triplet multiplicities originating from a common Si-Si scalar coupling were detected ( $^1J_{\text{SiSi}} = 45$  Hz), indicative for a  $[\text{Si}_4]^{4-}$  cluster derivative with a  $\text{C}_{2v}$  symmetry. Furthermore, the resonance at  $\delta = -327.8$  ppm shows a doublet splitting caused by a scalar coupling to

one hydrogen atom ( $^1J_{\text{SiH}} = 12$  Hz), which clearly indicates a protonated  $[\text{Si}_4]^{4-}$  cluster. Also, the complete spin network was corroborated by  $^1\text{H}^{29}\text{Si}$  HMQC spectroscopy (see Supporting Information). The corresponding  $^1\text{H}$  signal shows an extreme high field shift of  $-10.61$  ppm. Intriguingly, a clear triplet is observed in the  $^1\text{H}$  spectra ( $^1J_{\text{SiH}} = 12$  Hz) indicating a single scalar coupling to two Si atoms (Figure 1b).

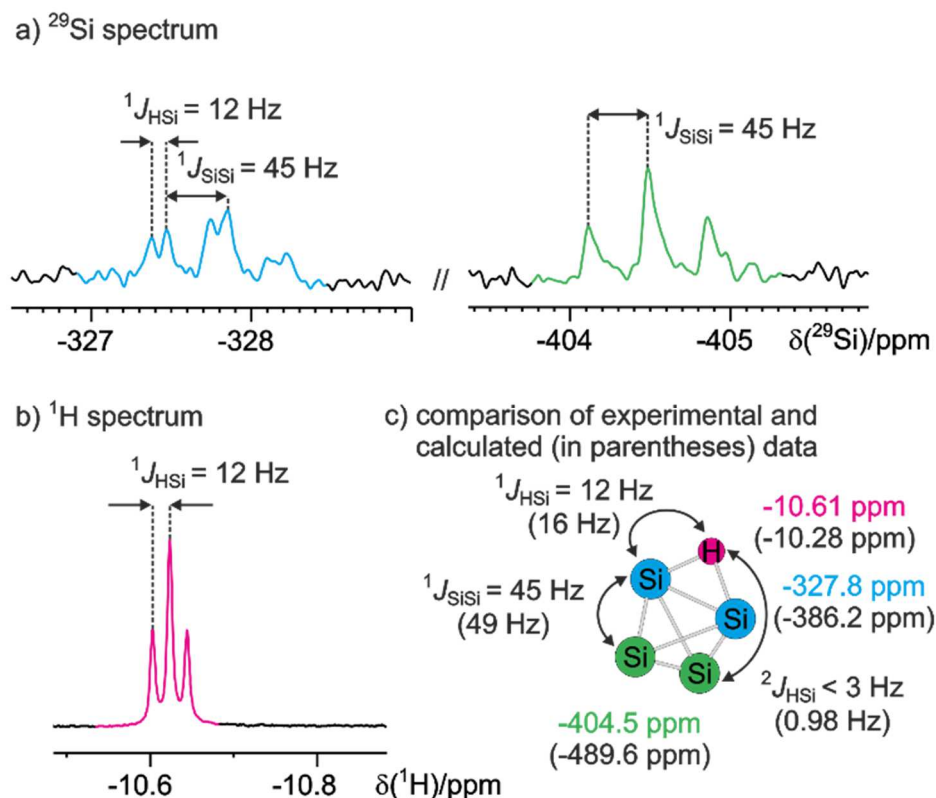


**Figure 1.** Experimental evidence for the protonated Si cluster  $[\text{HSi}_4]^{3-}$  in liquid ammonia ( $T = 233$  K, 600 MHz NMR spectrometer): a)  $^{29}\text{Si}$  spectrum showing the protonated (left, blue) and unprotonated Si atoms (right, green). Both signals have a triplet pattern with  $^1J_{\text{SiSi}} = 45$  Hz. The resonance at  $\delta = -327.8$  ppm shows an additional  $^1J_{\text{SiH}} = 12$  Hz scalar coupling also visible in b) the  $^1\text{H}$  spectrum. c) Overview of the experimental chemical shifts and coupling constants (calculated values given in parentheses).

In contrast to the terminal Si-H bond observed in the  $[\text{HSi}_9]^{3-}$  cluster with a  $^1J_{\text{SiH}}$  of 156 Hz,<sup>[23]</sup> the protonated  $[\text{Si}_4]^{4-}$  cluster shows a significantly smaller  $^1J_{\text{SiH}}$  of 12 Hz. Also, a comparison to silanes, which have  $^1J_{\text{SiH}}$  values between 160 and 300 Hz, reveals a non-trivial Si-H bonding situation: Both the classical triplet pattern and the small  $^1J_{\text{SiH}}$  value of the proton signal indicate a bridging proton in between two Si atoms ( $[\mu\text{-HSi}_4]^{3-}$ ; Figure 1c). Thus, this unprecedented silicon species with a bridging H atom represents the missing link to borane chemistry. In both cases, the H atom shows a hydridic character, which is corroborated for  $[\mu\text{-HSi}_4]^{3-}$  by its extremely high-field-shifted proton ( $-10.61$  ppm). However, despite structural and electronic similarities, borane chemistry is well known for

its electron-deficient nature, while in contrast,  $[\mu\text{-HSi}_4]^{3-}$  obviously has a balanced electron count. According to the pseudo-element concept, analogous behavior can be observed in phosphorus compounds. Recently, spectroscopic investigations of a protonated  $\text{P}_4$  species  $[\text{P}_4\text{H}]^+$  were reported, revealing protonation over an edge of the tetrahedron under formation of a 3c-2e bond,<sup>[29]</sup> analogous to our results.

Furthermore, this  $[\mu\text{-HSi}_4]^{3-}$  cluster shows a totally different dynamic behavior than the recently observed  $[\text{HSi}_9]^{3-}$  cluster.<sup>[22, 23]</sup> While for the  $[\text{HSi}_9]^{3-}$  cluster, several dynamic regimes were observed, NMR could not reveal any dynamics for  $[\mu\text{-HSi}_4]^{3-}$ . In the  $^1\text{H}^{29}\text{Si}$  HMQC, only specific cross-signals were observed, according to the scalar couplings (< 3 and 13 Hz; see Supporting Information). The  $^2J_{\text{HSi}}$  coupling constant was calculated to be 0.98 Hz, which is below the linewidth even with optimized processing parameters.<sup>[30]</sup> Contrary to the situation for the  $[\text{HSi}_9]^{3-}$  cluster, no temperature dependence was observed for the  $^1\text{H}$  and  $^{29}\text{Si}$  signals of the  $[\text{HSi}_4]^{3-}$  cluster (see Supporting Information). Also, theoretical calculation of the relative chemical shifts and the scalar couplings corroborate both the structure and the rigidity of the  $[\mu\text{-HSi}_4]^{3-}$  cluster (see Figure 1c).

In the same sample, a third non-protonated cluster species  $[\text{Si}_5]^{2-}$  besides the protonated clusters  $[\mu\text{-HSi}_4]^{3-}$  and  $[\text{HSi}_9]^{3-}$  was observed in NMR for the first time. It shows two extremely separated  $^{29}\text{Si}$  signals with an offset of almost 700 ppm ( $\delta = +348.7$  ppm and  $-347.8$  ppm; Figure 2). To the best of our knowledge, the most down-field-shifted  $^{29}\text{Si}$  signals have been reported for silenes ( $\delta = 126.5$  ppm and  $144.2$  ppm)<sup>[31]</sup>, phosphasilenes ( $\delta = 151.2$  ppm)<sup>[32]</sup>, arsilenes ( $\delta = 183.6$  ppm)<sup>[33]</sup> and bis(hypersilyl)lead ( $\delta = 196.9$  ppm).<sup>[34]</sup> Intriguingly, the  $^{29}\text{Si}$  resonance at  $\delta = +348.7$  ppm observed by us exceeds this range by far. The scalar coupling constants of both resonances ( $^1J_{\text{SiSi}} = 41.8$  Hz) are in the typical range of classical  $^1J_{\text{SiSi}}$  couplings. Considering the extreme offset and the typical range of  $^1J_{\text{SiSi}}$ , the spin system connectivity was tested and confirmed by steady-state NOE-type experiments (see Supporting Information). Furthermore, the observed triplet and quartet combination of the two signals can be directly translated into a Si network with two axial and three equatorial Si atoms. This structure is in accordance with recrystallization experiments that revealed a trigonal bipyramidal  $[\text{Si}_5]^{2-}$  cluster. The distinguishable separated Si signals observed for non-equivalent Si atoms in  $[\text{Si}_5]^{2-}$  in NMR indicate the silicon skeleton is rigid on the NMR timescale. Again, the calculated chemical shifts and scalar couplings (Figure 2, in parentheses) are in excellent agreement with the experimental values.

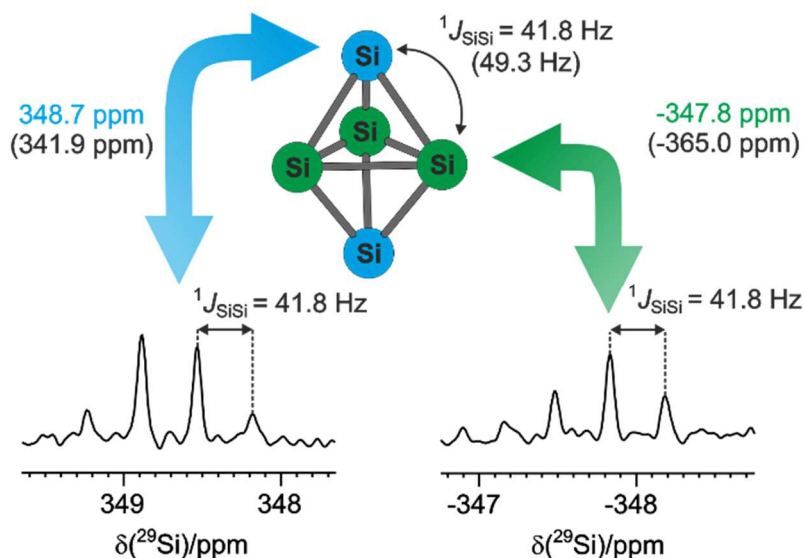


**Figure 2.** Experimental evidence for the unprotonated  $[\text{Si}_5]^{2-}$  cluster in liquid ammonia ( $T = 233\text{ K}$ , 600 MHz NMR spectrometer):  $^{29}\text{Si}$  NMR spectrum showing a quartet for the axial Si atoms (left, blue atoms) and a triplet for the equatorial Si atoms (right, green atoms) with a common  $^1J_{\text{SiSi}} = 41.8\text{ Hz}$  (calculated values given in parentheses).

Combining the data presented here with those for  $[\text{HSi}_9]^{3-}$ ,<sup>[23]</sup> the NMR experiments revealed three different protonation states, that is, terminally protonated  $[\text{HSi}_9]^{3-}$ , bridge-protonated  $[\mu\text{-HSi}_4]^{3-}$ , and unprotonated  $[\text{Si}_5]^{2-}$ . To understand the different preferences for protonated and unprotonated states as well as the position of the proton in the clusters, quantum chemical calculations ( $\Delta G_{203}$ , the free Gibbs energy at 203 K, CCSD(T)/def2-TZVPP) were performed. First, the thermodynamic protonation equilibria were investigated. For  $[\text{Si}_4]^{4-}$ , protonation of the cluster by  $\text{NH}_3$  [Eq. (1); blue numbers in Figure 3] is thermodynamically highly favorable by  $-219.9\text{ kJ}\cdot\text{mol}^{-1}$ , which can be rationalized by the highly charged character of  $[\text{Si}_4]^{4-}$ , a strong base in  $\text{NH}_3$ . The formation of the corresponding  $\text{NH}_2^-$  anion was observed via NMR in these samples (see Supporting Information) and also in previous studies<sup>[23]</sup>. As expected, the protonation of  $[\text{Si}_9]^{4-}$  is less favored in  $\text{NH}_3$  due to the reduced charge density,<sup>[35]</sup> that is, endergonic by  $+27.7\text{ kJ}\cdot\text{mol}^{-1}$  [Eq. (2)]. Experimentally,  $[\text{HSi}_9]^{3-}$  was detected.<sup>[23]</sup> Thus, the cations, not considered in the calculations, seem to acidify the liquid ammonia and reduce the thermal energy demand. For the  $[\text{Si}_5]^{2-}$  cluster, which has a similar charge density as  $[\text{Si}_9]^{4-}$ , the unprotonated species has been detected exclusively so far (see above). Furthermore, the protonation of  $[\text{Si}_5]^{2-}$  by  $\text{NH}_3$  [Eq. (3)] requires a tremendous amount of energy ( $+185.3\text{ kJ}\cdot\text{mol}^{-1}$ ). Hence, the simplified assumption of uniform delocalization fails to explain the strong difference in the protonation trend between  $[\text{Si}_9]^{4-}$  and  $[\text{Si}_5]^{2-}$ . This demonstrates that for protonation trends, the differences in delocalization in both the protonated and unprotonated clusters should be included (see discussion below).



Afterward, the protonation site preferences in  $[\text{HSi}_9]^{3-}$ ,  $[\text{HSi}_4]^{3-}$  and  $[\text{HSi}_5]^-$  were addressed. For the ligand-free cluster  $[\text{Si}_4]^{4-}$ , each Si atom carries exactly one single negative charge according to the charge analysis. Thus, protonation on one vertex is expected, as already shown for  $[\text{HSi}_9]^{3-}$ <sup>[23]</sup> and predicted for  $[\text{HSi}_5]^-$  (vertex position preferred by +21.5 kJ·mol<sup>-1</sup>; see Supporting Information). In contrast, for the protonation of  $[\text{Si}_4]^{4-}$ , calculations and experiments revealed a cluster structure with a bridging hydrogen atom  $[\mu\text{-HSi}_4]^{3-}$  (blue numbers in Figure 3),<sup>[36]</sup> while the terminally protonated cluster  $[\text{HSi}_4]^{3-}$  is predicted to be +59.7 kJ·mol<sup>-1</sup> higher in energy. Thus, not only the protonation state but also the protonation site depends on the individual cluster. While  $[\mu\text{-HSi}_4]^{3-}$  is more stable than  $[\text{HSi}_4]^{3-}$ , terminal protonation is preferred in case of  $[\text{HSi}_5]^-$  and  $[\text{HSi}_9]^{3-}$ .<sup>[37]</sup>

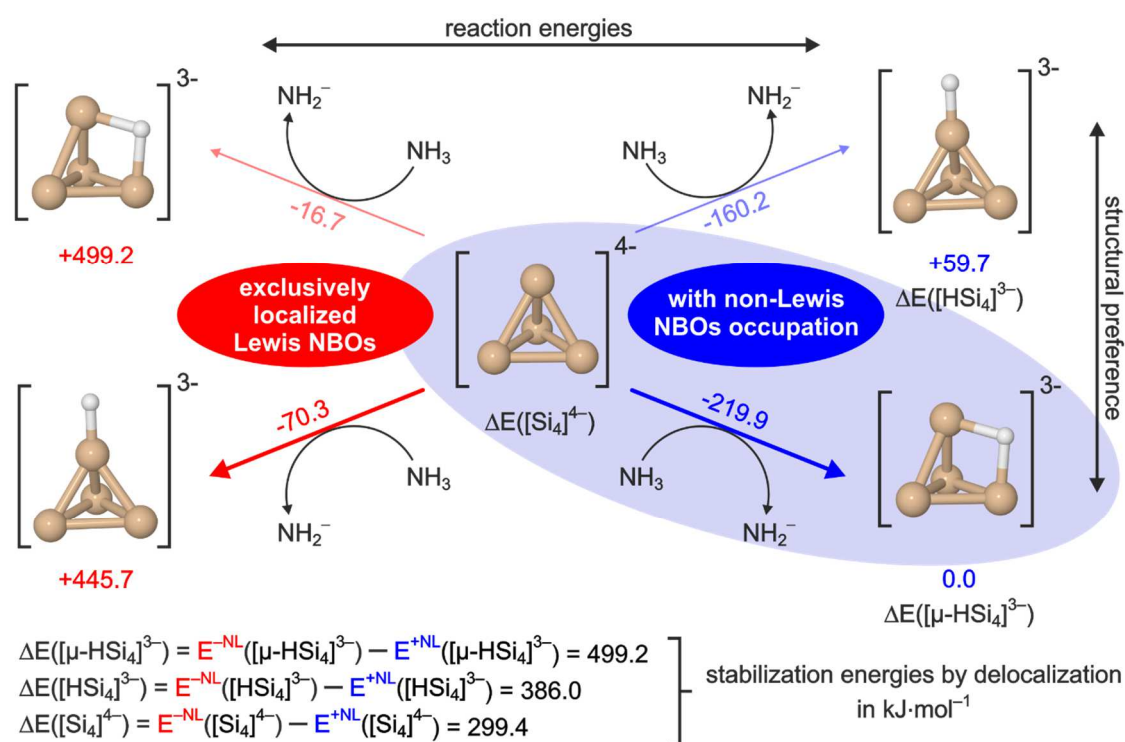


**Figure 3.** Protonation energies of  $[\text{Si}_4]^{4-}$  and structural preferences of the protonated cluster: The experimentally detected  $[\mu\text{-HSi}_4]^{3-}$  is the most preferred structure under consideration of delocalization (inclusion of non-Lewis NBOs). Terminal protonation leading to  $[\text{HSi}_4]^{3-}$  is less favored by +59.7 kJ·mol<sup>-1</sup> (right side). Using localized Lewis NBOs exclusively, terminal  $[\text{HSi}_4]^{3-}$  becomes +53.5 kJ·mol<sup>-1</sup> more stable than  $[\mu\text{-HSi}_4]^{3-}$  (left side). Furthermore, the delocalization promotes exergonic protonation.

To find a rationale for the protonation site and state preferences, natural bond orbital (NBO)<sup>[38]</sup> analyses were performed (for an ELI-D analysis, see the Supporting Information). First, the unusual bonding situation in  $[\mu\text{-HSi}_4]^{3-}$  was investigated and compared to the bare  $[\text{Si}_4]^{4-}$  cluster. The non-Lewis NBOs in  $[\text{Si}_4]^{4-}$  are marginally occupied due to delocalization. However, this energetic contribution is important, because the neglect of delocalized orbitals in  $[\text{Si}_4]^{4-}$  leads to a huge destabilization of  $\Delta E([\text{Si}_4]^{4-}) = 299.4 \text{ kJ mol}^{-1}$  (Figure 3; for details, see Supporting Information). In  $[\mu\text{-HSi}_4]^{3-}$ , the delocalization degree to the non-Lewis NBOs is even higher. While the Lewis 3C (three-center) NBO is properly localized ( $1.997 e^-$ ), two non-Lewis NBOs are significantly occupied (a lesser three-center 3Cn NBO and an antibonding three-center 3C\* NBO, see Figure 4). Indeed, second order perturbation analysis reveals strong donor–acceptor interactions to these non-Lewis 3Cn/3C\* NBOs, from the lone pair NBO of the vertex atom as well as the Si–Si bonding NBO. The deletion of delocalization in  $[\mu\text{-HSi}_4]^{3-}$  leads to an even more drastic destabilization of  $\Delta E([\mu\text{-HSi}_4]^{3-}) = 499.2 \text{ kJ mol}^{-1}$  (see Figure 3). For the terminally protonated cluster  $[\text{HSi}_4]^{3-}$ , the deletion of delocalization resulted in a smaller but still remarkable destabilization of  $386.0 \text{ kJ mol}^{-1}$ . Furthermore, without delocalization, protonation of the bare cluster  $[\text{Si}_4]^{4-}$  is less exergonic and  $[\text{HSi}_4]^{3-}$  is more stable than  $[\mu\text{-HSi}_4]^{3-}$  (Figure 3, left side). Thus, the NBO analysis suggests that the delocalization of non-Lewis NBOs is decisive for the preference of the bridging position over the vertex position in  $[\mu\text{-HSi}_4]^{3-}$  and furthermore provides an additional driving force for protonation.

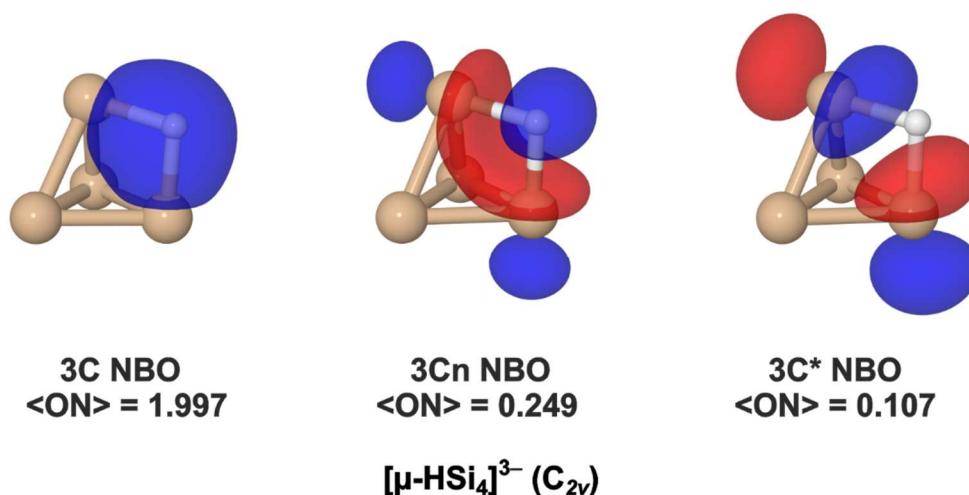


**Figure 4.** NBO analysis for  $[\mu\text{-HSi}_4]^{3-}$ , clearly demonstrating the presence of a 3c-2e bond. 3C NBO (H-Si1-Si4) of  $[\mu\text{-HSi}_4]^{3-}$  with occupation number (ON) of  $1.997 e^-$ .



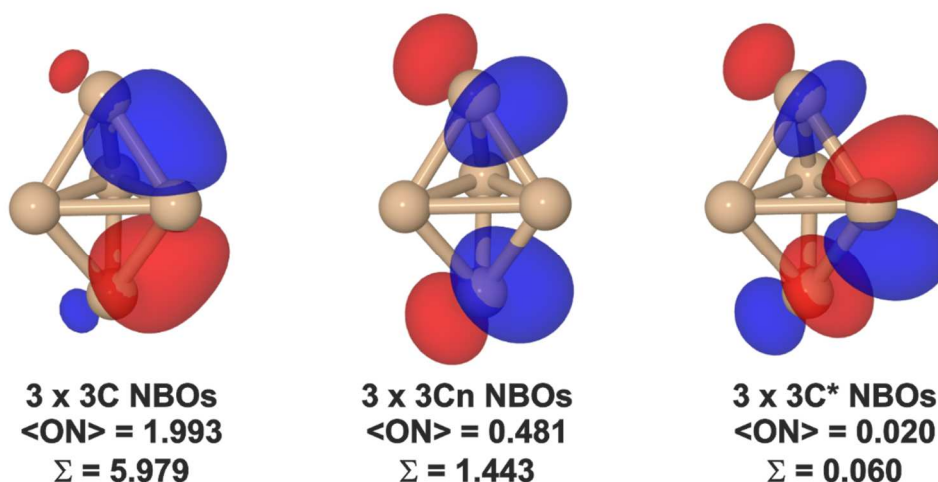


**Figure 5.** NBO analysis of  $[\text{Si}_5]^{2-}$  indicating three localized 3c-2e bonds ( $1.993 e^-$ ) over each edge of the trigonal bipyramidal cluster with a node at the equatorial  $\text{Si}^{\text{eq}}$ . Three 3Cn NBOs of  $[\text{Si}_5]^{2-}$  with a high occupation number of  $0.481 e^-$  were obtained due to delocalization from lone pairs at  $\text{Si}^{\text{eq}}$  and the  $\text{Si}^{\text{eq}}-\text{Si}^{\text{eq}}$  bond. ON: Occupation number.

Afterwards, NBO analysis was applied to address whether delocalization plays a similar key role in  $[\text{Si}_5]^{2-}$  (Figure 5). According to the assumed Lewis structure (four single bonds for each equatorial  $\text{Si}^{\text{eq}}$  and three single bonds for each axial  $\text{Si}^{\text{ax}}$ ), a single negative charge is expected on each  $\text{Si}^{\text{ax}}$ . However, NBO charge analysis revealed completely delocalized electrons with higher partial charges for  $\text{Si}^{\text{eq}}$  than for  $\text{Si}^{\text{ax}}$ . Hence, the charges are by far more delocalized than anticipated by the Lewis structure, providing less driving force for protonation. For the NBO analysis of  $[\text{Si}_5]^{2-}$ , the “best” Lewis structure is illustrated by three bonding orbitals between the  $\text{Si}^{\text{eq}}$  atoms and three 3C orbitals, each reflecting the bonds between two  $\text{Si}^{\text{ax}}$  and one  $\text{Si}^{\text{eq}}$ ,<sup>[39]</sup> with the latter being properly occupied ( $1.993 e^-$ ; see Figure 5 and the Supporting Information). In contrast to the borane-like Si–H–Si bond in  $[\mu\text{-HSi}_4]^{3-}$ , the  $\text{Si}^{\text{ax}}-\text{Si}^{\text{eq}}-\text{Si}^{\text{ax}}$  3C bond exhibits a node at the  $\text{Si}^{\text{eq}}$  position, indicating a p-type atomic orbital (see Figure 5 and, for further description, the Supporting Information). Similar to the situation in  $[\mu\text{-HSi}_4]^{3-}$ , the second order perturbation analysis again shows an extremely strong delocalization from the lone pair at  $\text{Si}^{\text{eq}}$  and the  $\text{Si}^{\text{eq}}-\text{Si}^{\text{eq}}$  bond to 3Cn NBOs ( $\Sigma E^{(2)} = 4738.9 \text{ kJ}\cdot\text{mol}^{-1}$ ). In contrast to  $[\text{H}^{\text{ax}}\text{Si}_5]^-$ , a significant decrease of delocalization compared to  $[\text{Si}_5]^{2-}$  is predicted (see Supporting Information for details and data on  $[\mu\text{-HSi}_5]^-$  and  $[\text{H}^{\text{eq}}\text{Si}_5]^-$ ). Thus, it seems that protonation is prevented not only by delocalized charges in  $[\text{Si}_5]^{2-}$ , but also reduction of delocalization in  $[\text{H}^{\text{ax}}\text{Si}_5]^-$  compared to  $[\text{Si}_5]^{2-}$  and the fact that the trigonal bipyramidal dianion can be considered as a *closo*-cluster with an ideal number of bonding electrons.<sup>[19, 40,41]</sup>

### 3.4 Conclusions

In summary, two silicon clusters, [ $\mu$ -HSi<sub>4</sub>]<sup>3-</sup> and [Si<sub>5</sub>]<sup>2-</sup>, could be detected and fully characterized in liquid ammonia via NMR spectroscopy. The bridged protonated [ $\mu$ -HSi<sub>4</sub>]<sup>3-</sup> cluster closes the gap between silicon and borane chemistry. Theoretical calculations in combination with the experiments reveal huge differences in the protonation trends of [Si<sub>4</sub>]<sup>4-</sup>, [Si<sub>5</sub>]<sup>2-</sup>, and [Si<sub>9</sub>]<sup>4-</sup>, possibly fine-tuned by the counter ions. The data on these three clusters suggest that not only charge distribution in the parent compounds, but also delocalization of correlated electrons in the products play a major role for protonation trends and hydride positions (terminal vs. bridged). The proof of the existence of unprotonated [Si<sub>5</sub>]<sup>2-</sup>, terminally protonated [HSi<sub>9</sub>]<sup>3-</sup>, and bridged protonated [ $\mu$ -HSi<sub>4</sub>]<sup>3-</sup> in solution might imply the breaking ground for a versatile solution chemistry of silicon clusters, similar to the well-established phosphorus and borane compounds.

## 3.5 Supporting Information

### 3.5.1 General experimental details

All operations were carried out under argon atmosphere using standard Schlenk and Glovebox techniques. Liquid ammonia was dried with potassium in a dry ice cooled Dewar vessel for at least 48 h [2.2.2]cryptand (systematic name: 4,7,13,16,21,24-Hexaoxa-1,10-diazabicyclo[8.8.8]hexa-cosane) was purchased from ABCR and used as received.  $^{29}\text{Si}$  Silicon was provided by Chemgas. Rubidium was synthesized according to Hackspill.<sup>[42]</sup> Rubidium and potassium were distilled for purification.

#### 3.5.1.1 Synthesis of the Zintl phase

$\text{K}_6\text{Rb}_6^{29}\text{Si}_{17}$ : 0.123 g (3.15 mmol) K, 0.269 g (3.15 mmol) Rb and 0.25 g (8.60 mmol)  $^{29}\text{Si}$  were enclosed in tantalum containers and jacketed in an evacuated ampoule of fused silica. The containers were heated to 973.1 K ( $25\text{ K}\cdot\text{h}^{-1}$ ), annealed at 973.1 K for at least 24 h, and cooled to room temperature ( $20\text{ K}\cdot\text{h}^{-1}$ ). The 100% enriched solid-state phase  $\text{K}_6\text{Rb}_6^{29}\text{Si}_{17}$  was stored in a glove box under argon.

#### 3.5.1.2 Solid phase characterization

$\text{K}_6\text{Rb}_6^{29}\text{Si}_{17}$ : Figure S1 and S2 show the diffraction pattern of the 100% enriched compound  $\text{K}_6\text{Rb}_6^{29}\text{Si}_{17}$ . The two figures additionally show the theoretical diffraction pattern (calculated from single-crystal structure data) of  $\text{K}_{12}\text{Si}_{17}$  and  $\text{Rb}_{12}\text{Si}_{17}$ . In Figure S2 an enlarged part of the diffraction pattern is depicted. The section clearly shows that the reflexes of the starting material are located between the reflexes of  $\text{K}_{12}\text{Si}_{17}$  and  $\text{Rb}_{12}\text{Si}_{17}$ . As described in **1.1 Synthesis of the Zintl phase** for the synthesis of  $\text{K}_6\text{Rb}_6\text{Si}_{17}$ , stoichiometric amounts of the elements were used, thus it can be assumed, that the starting material can be considered as phase pure according to the formula  $(\text{K,Rb})_{12}\text{Si}_{17}$ .

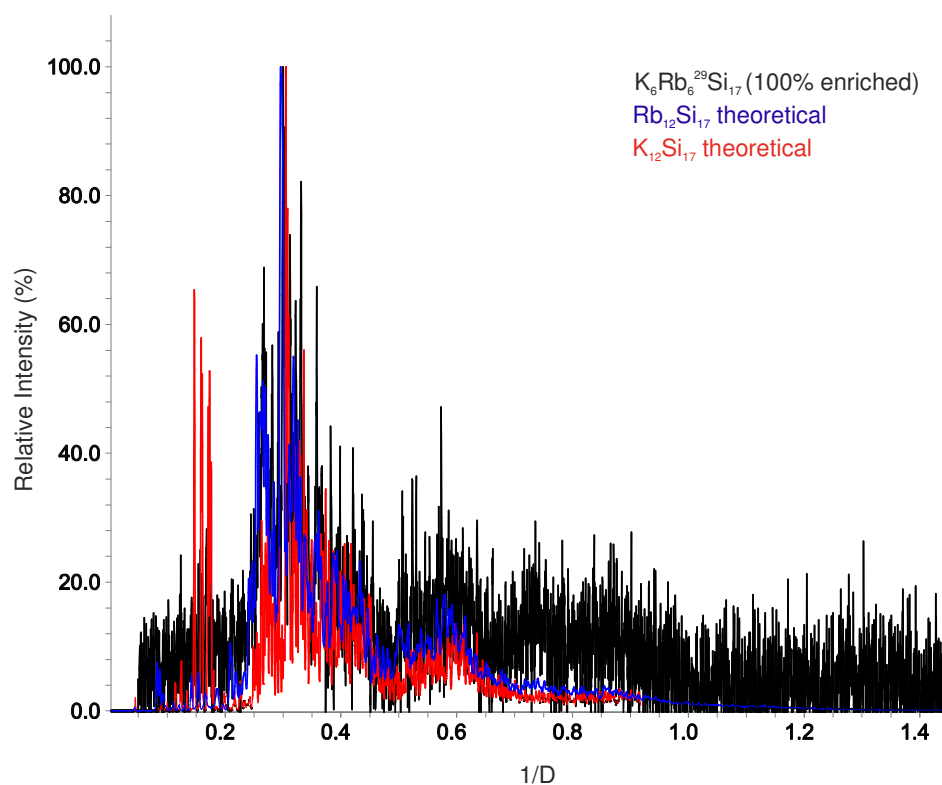


**Figure S1.** Comparison of experimental ( $\text{K}_6\text{Rb}_6\text{Si}_{17}$ , black) and theoretical ( $\text{K}_{12}\text{Si}_{17}$ , red;  $\text{Rb}_{12}\text{Si}_{17}$ , blue) diffraction pattern. The latter ones are calculated from single crystal data.

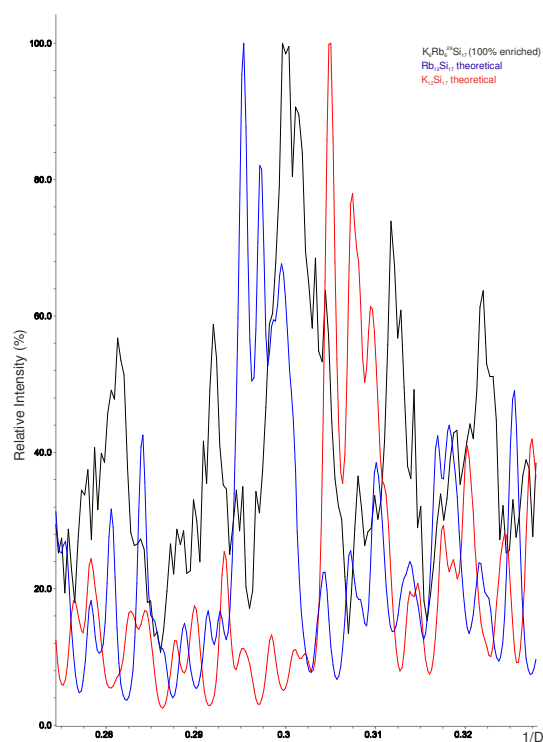


**Figure S2** Part of the powder diffraction pattern of Figure S1. The reflexes of the mixed cationic phase  $\text{K}_6\text{Rb}_6^{29}\text{Si}_{17}$  are located between the reflexes of  $\text{K}_{12}\text{Si}_{17}$  and  $\text{Rb}_{12}\text{Si}_{17}$ .

### 3.5.2 NMR spectroscopy

#### 3.5.2.1 Solvation of the Zintl phases in liquid ammonia

For the NMR spectra presented in the main manuscript, 0.0125 g (0.0101 mmol)  $K_6Rb_6^{29}Si_{17}$  and 0.0076 g (0.0203 mmol) [2.2.2]cryptand were placed in heavy wall precision NMR sample tubes (Pyrex) under argon atmosphere. Then, anhydrous ammonia was condensed at 195 K. The glass tube was sealed under argon atmosphere to ensure that the moisture and air sensitive sample did not decompose. To achieve optimal signal to noise ratios, the sample was stored, and test measurements were conducted over several months. The optimal signals were detected after approximately one month. Furthermore, we tried several experimental conditions and a selection of the best ones is given in Figure S9. The time course of the dissolution process varied within the different samples most probably due to variation of the water content of the [2.2.2]cryptand. The most intense signal detectable in all samples is that at -325 ppm previously assigned to  $[Si_4]^{4-}$ .<sup>[13]</sup> There is a second signal at -358.3 ppm with a smaller intensity detectable in all of the samples with the experimental conditions described above. This was previously assigned to  $[HSi_9]^{3-}$ .<sup>[23]</sup> Only under optimized conditions (for a selection see Figure S9) the signals of  $[Si_5]^{2-}$  and  $[\mu-HSi_4]^{3-}$  can be detected. There are still a couple of very small signals we haven't be able to assign so far.

#### 3.5.2.2 General NMR procedures

All NMR-spectroscopic measurements were recorded on a Bruker Avance III 600 MHz spectrometer equipped with a 5 mm TBI-probe ( $^1H$ , X,  $^{19}F$ ) with z-gradient. For low temperature measurements at 203 K, a  $N_2$  evaporator unit was used. Temperature at 233 K was controlled via BCU II. The  $^{29}Si$  measurements were performed using a standard Bruker pulse program (zg) with 4k number of scans, TD = 65k with relaxation delay of 5 s. Data were processed with the Bruker software TOPSPIN 3.2 using the processing parameters SI = 130k, WDW = EM and LB = 0.3 Hz. The chemical shifts are reported in ppm relative to a constant stable silicon signal at -325 ppm. The  $^1H^{29}Si$ -HMQC experiments were performed using the standard Bruker pulse program (hmqcgpqf) with 256 number of scans, DS = 16, TD(F2) = 2k, TD(F1) = 512 with a relaxation delay of 1.5 s and various  $\tau$  for 3 and 13 Hz coupling constants. The data were processed with the Bruker software TOPSPIN 3.2 using the processing parameters SI = 2k (F2 and F1), WDW = EM (F2 and F1), LB(F2) = 1 Hz, LB(F1) = 6 Hz.

### 3.5.2.3 Overview of $^1\text{H}$ and $^{29}\text{Si}$ spectra

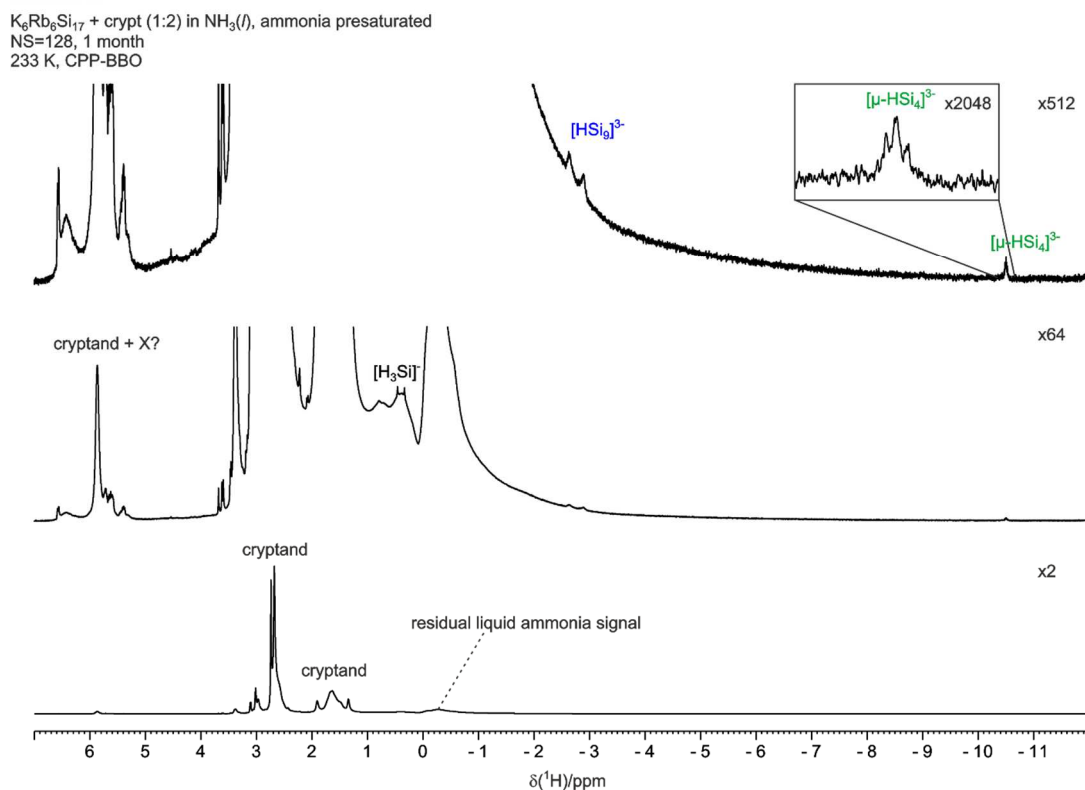


**Figure S3.** Ammonia presaturated  $^1\text{H}$  spectra of a sample of  $\text{K}_6\text{Rb}_6\text{Si}_{17}$  + crypt (1:2) in liquid ammonia at 233 K measured on a 600 MHz spectrometer with CPP-BO probe head, one month after sample preparation. Magnification (from bottom to top) of factors x2, x64, x512 and magnification of the signal at -10.61 ppm of a factor x2048.

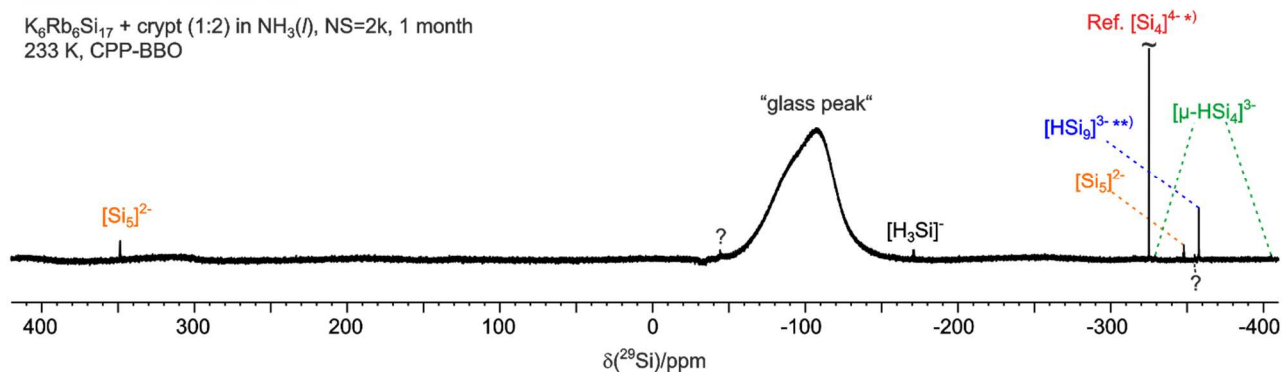


**Figure S4.**  $^{29}\text{Si}$  spectra of a sample of  $\text{K}_6\text{Rb}_6\text{Si}_{17}$  + crypt (1:2) in liquid ammonia at 233 K measured on a 600 MHz spectrometer with CPP-BO probe head, one month after sample preparation.

\*) The reference signal was previously assigned to  $[\text{Si}_4]^{4-}$ .<sup>[13]</sup>

\*\*\*) The signal of  $[\text{HSi}_9]^{3-}$  was reported previously.<sup>[23]</sup>

### 3.5.2.4 $^1\text{H}^{29}\text{Si}$ HMQC spectra

Two  $^1\text{H}^{29}\text{Si}$  HMQC spectra were recorded at 203 K with  $J_{\text{SiH}}$  scalar couplings of 13 and 3 Hz, respectively (Figure S3). Thus, validating directly the protonation of a tetrahedral  $[\text{Si}_4]^{4-}$  cluster.

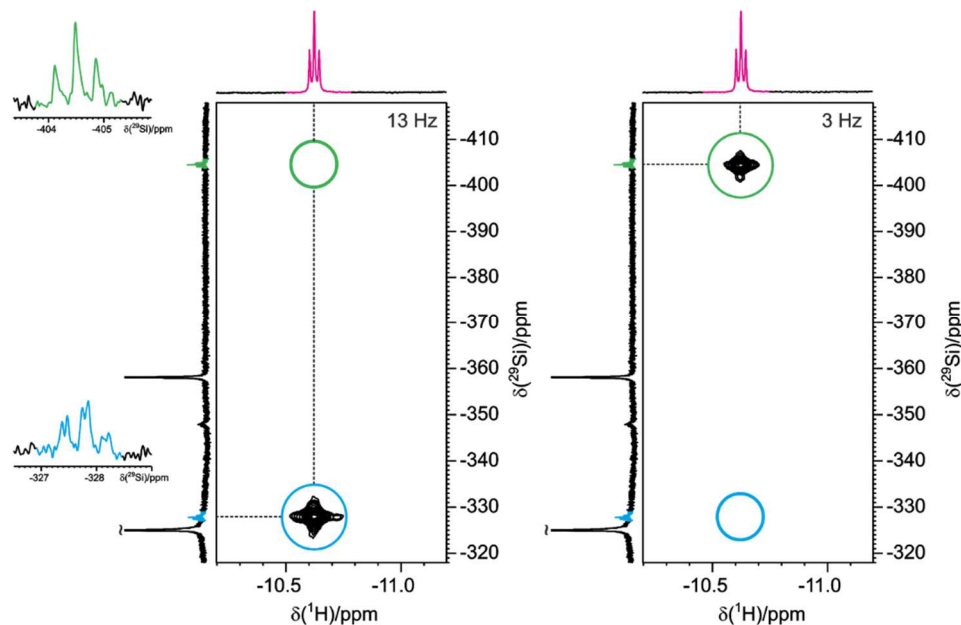


**Figure S5.**  $^1\text{H}^{29}\text{Si}$  HMQC spectra with 13 (left) and 3 Hz (right). Only specific cross signals were observed according to the scalar couplings.

\*) The reference signal was previously assigned to  $[\text{Si}_4]^{4-}$ .<sup>[13]</sup>

\*\*\*) The signal of  $[\text{HSi}_9]^{3-}$  was reported previously.<sup>[23]</sup>

### 3.5.2.5 Steady state NOE-type experiment

The pulse sequence of the steady state NOE-type experiment is given below. Two experiments are recorded with equal experimental time and same number of scans (each one for 8 hours, 5k scans), one with the initial saturation block and another one without the initial saturation block. The saturation is applied at +348.7 ppm and signal was observed for -347.9 ppm. Since two peaks (+348.7 ppm and -347.9 ppm.) are quite well separated, therefore one can use quite high power of saturation. Here we used 2000 Hz power.

The experiments were performed at 233 K (Figure S6). Without saturation, the control experiment was measured (bottom spectrum), as well as an experiment with saturation at the resonance at  $\delta = +348.7$  ppm (yellow arrow; middle spectrum). The difference in intensity between two spectra are non-zero for the peak at  $\delta = -347.8$  ppm (top spectrum) whereas the signal at -356 ppm and others completely cancel out. Suggesting a Si nuclei corresponding to peaks at +348.7 ppm and -347.8 ppm are nearby or coupled.

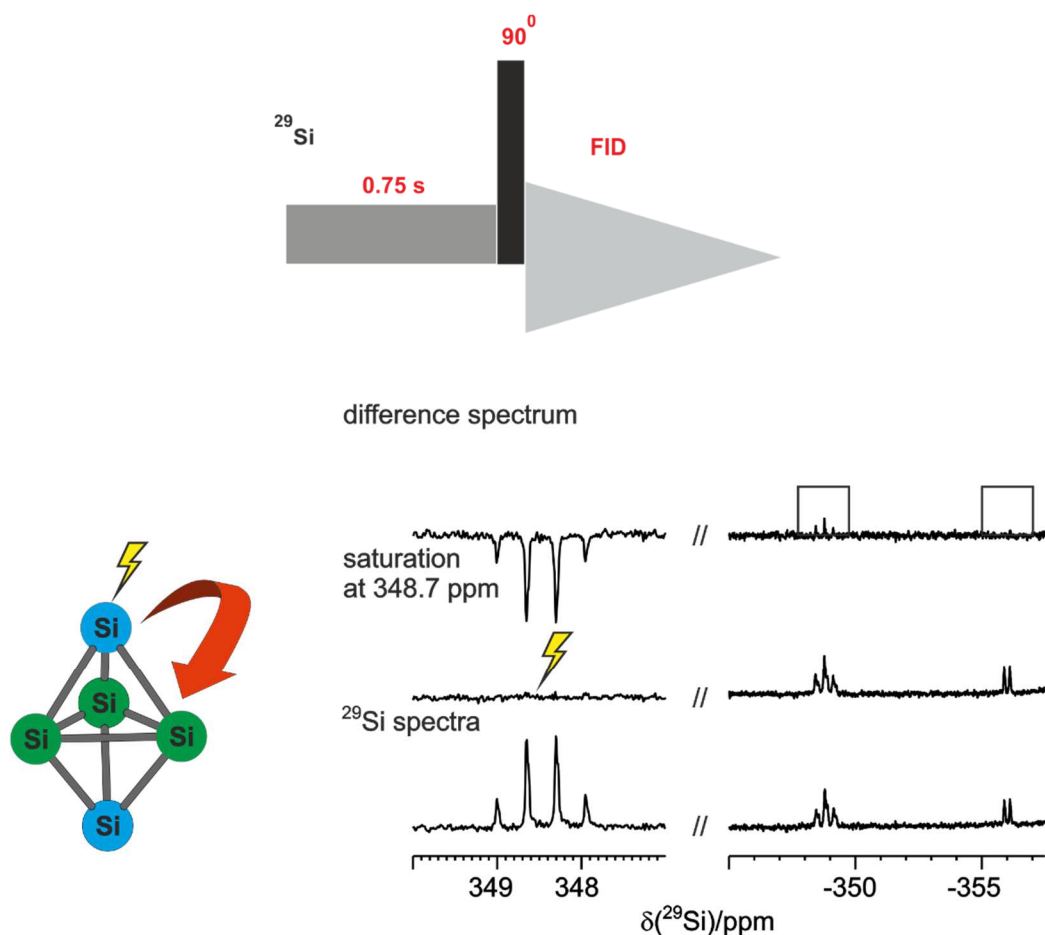


**Figure S6.** Steady state NOE-type experiment. The pulse sequence used is given on the top. The experiments were performed at 233 K (bottom): The control experiment without saturation (bottom spectrum), as well as an experiment with saturation at the resonance at  $\delta = +348.7$  ppm (yellow arrow, middle spectrum) were recorded. The difference in intensity between both spectra (top spectrum) is non-zero for the signal at  $\delta = -347.8$  ppm, whereas the signal at  $-356$  ppm and others completely cancel out. This suggests that the signals at  $\delta = 348.7$  and  $-347.8$  ppm are nearby or coupled.

### 3.5.2.6 Byproducts and degradation products in liquid ammonia

The protonation byproduct  $\text{NH}_2^-$  of the formation of  $[\mu\text{-HSi}_4]^{3-}$  was detected in the  $^1\text{H}$  spectra at 203 K (Figure S5). Its chemical shift ( $\delta = -3.62$  ppm) in liquid ammonia was previously reported.<sup>[14]</sup> Also the degradation product  $\text{SiH}_3^-$  was detected in the  $^{29}\text{Si}$  and  $^1\text{H}$  spectra (Figure S6). Both resonances  $\delta(^{29}\text{Si}) = -174.5$  ppm and  $\delta(^1\text{H}) = 0.40$  ppm share a common scalar coupling constant  $^1J_{\text{SiH}} = 75$  Hz.



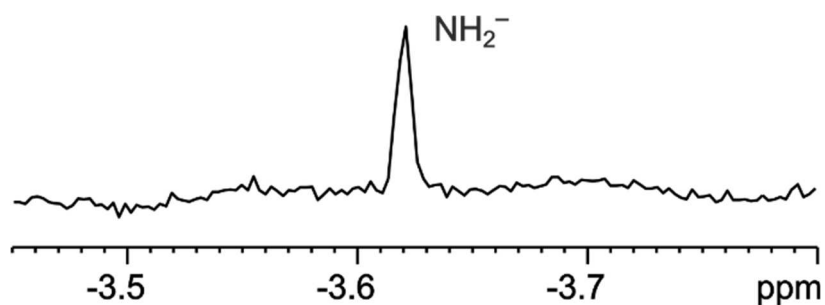


**Figure S7.** <sup>1</sup>H spectra of NH<sub>2</sub><sup>-</sup> the byproduct of the protonation of [Si<sub>4</sub>]<sup>4-</sup> at 203 K. Its chemical shift at  $\delta = -3.62$  ppm was already detected in liquid ammonia previously.<sup>[14]</sup>

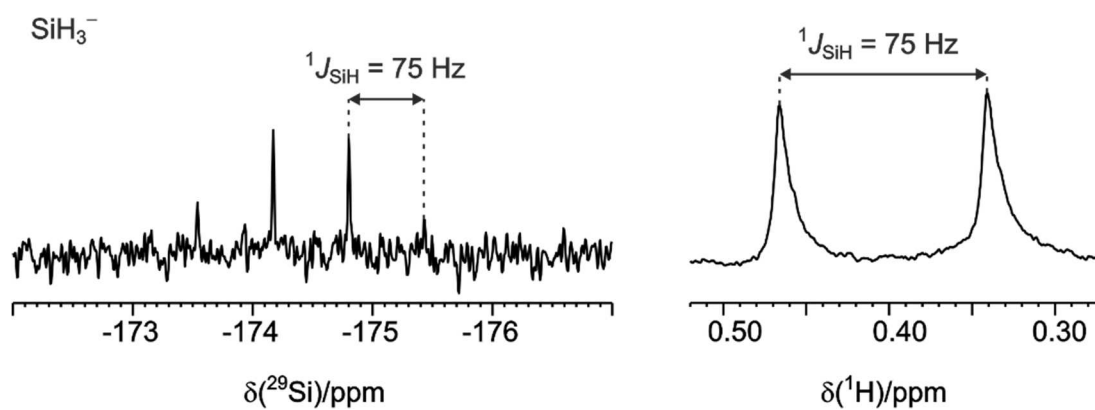


**Figure S8.** Detection of the degradation product SiH<sub>3</sub><sup>-</sup> in the <sup>29</sup>Si (left) and <sup>1</sup>H spectra (right). Both resonances  $\delta(^{29}\text{Si}) = -174.5$  ppm and  $\delta(^1\text{H}) = 0.40$  ppm share a common scalar coupling constant  $^1J_{\text{SiH}} = 75$  Hz.

### 3.5.2.7 Selected $^{29}\text{Si}$ spectra under different experimental conditions

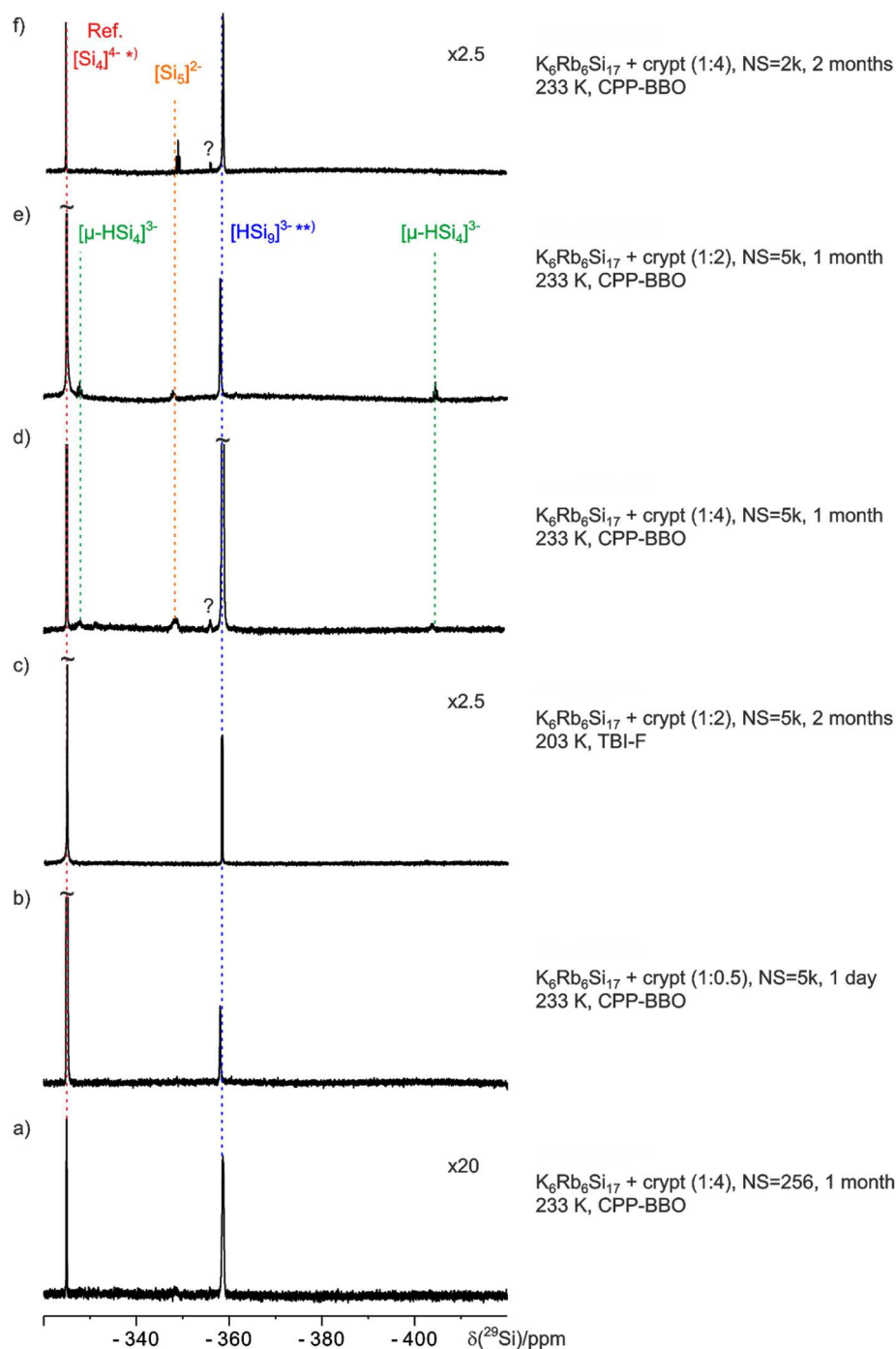


**Figure S9.** Selected  $^{29}\text{Si}$  spectra (600 MHz spectrometer) of ammonia solutions of  $\text{K}_6\text{Rb}_6\text{Si}_{17}$  with 100%  $^{29}\text{Si}$  enrichment under different experimental conditions (age of the sample, temperature, number of scans, amount of cryptand and probe heads) showing various factors for the formation of  $[\text{HSi}_9]^{3-}$  (blue),  $[\mu\text{-HSi}_4]^{3-}$  (green) and  $[\text{Si}_5]^{2-}$  (orange) respectively: a) to c) show exclusively  $[\text{HSi}_9]^{3-}$  (blue) and the reference signal\*) (red); d) and e) show all aforementioned silicides being present; And f) shows exclusively  $[\text{HSi}_9]^{3-}$  (blue),  $[\text{Si}_5]^{2-}$  (orange) and the reference signal\*) (red). In addition, d) and f) reveal a further signal  $\sim -355$  ppm, thus far unassigned.

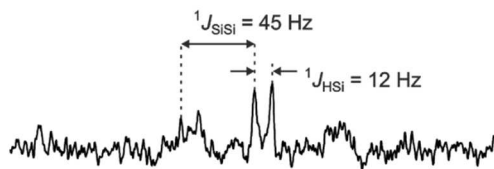
\*) The reference signal was previously assigned to  $[\text{Si}_4]^{4-}$ .<sup>[13]</sup>

\*\*\*) The signal of  $[\text{HSi}_9]^{3-}$  was reported previously.<sup>[23]</sup>

## 3.5.2.8 VT-NMR spectra

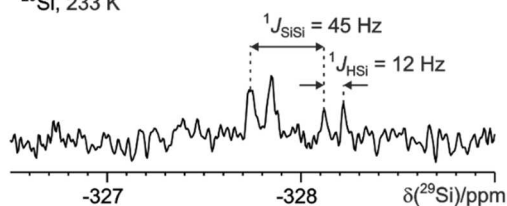
$K_6Rb_6Si_{17}$  + crypt (1:2), NS=1k, 4 months, TBI-F

$^1H^{29}Si$  DEPT, 203 K



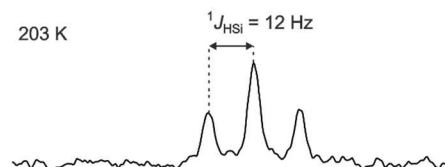
$K_6Rb_6Si_{17}$  + crypt (1:2), NS=1k, 2 months, CPP-BBO

$^{29}Si$ , 233 K



$K_6Rb_6Si_{17}$  + crypt (1:2), NS=64, 3 months  
TBI-F, ammonia presaturated  $^1H$  spectra

203 K



233 K

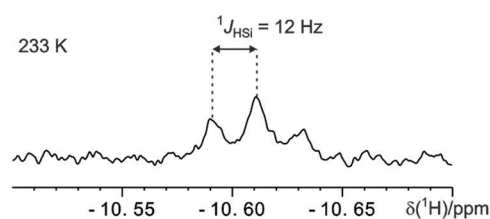
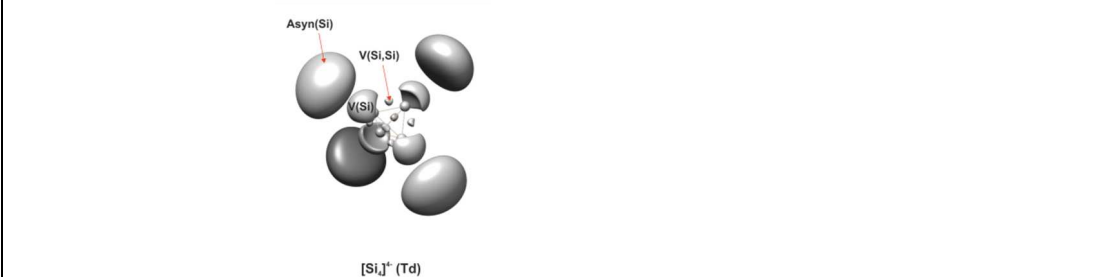


**Figure S10.**  $^{29}Si$  spectra (left) of two different samples of  $K_6Rb_6Si_{17}$  with crypt (1:2) in liquid ammonia at 203 K (top,  $^1H^{29}Si$  DEPT) and 233 K (bottom,  $^{29}Si$ ) and ammonia presaturated  $^1H$  spectra (right) of a third sample of  $K_6Rb_6Si_{17}$  with crypt (1:2) in liquid ammonia at 203 K (top) and 233 K (bottom), measured on 600 MHz spectrometers with TBI-F and CPP-BBO probe head respectively. The coupling constants  $^1J_{SiSi} = 45$  Hz and  $^1J_{HSi} = 12$  Hz of the resonances of the  $[\mu-HSi_4]^{3-}$  cluster at  $\delta(^{29}Si) = -327.8$  ppm and  $\delta(^{29}Si) = -10.61$  ppm are not affected by a change in temperature, thus suggesting a rigid  $[\mu-HSi_4]^{3-}$  silicide cluster in this temperature range.

### 3.5.3 Theoretical calculations

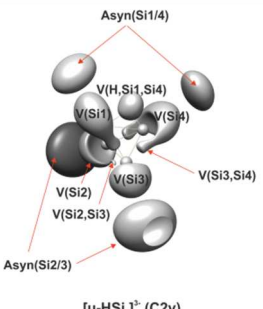
#### 3.5.3.1 ELI-D analysis

**Table S1.** ELI-D surface and analysis of [Si $_4$ ] $^{4-}$  cluster. Isovalue=1.49 was applied for the ELI-D surface.



[Si $_4$ ] $^{4-}$	avg. population	$\sigma^2$ (fluctuation)	$\lambda$ (relative fluctuation)	eccentricity
4 x C(Si)	10.060	0.390	0.039	---
6 x V(Si,Si)	1.195	0.819	0.685	0.902
4 x V(Si)	2.629	1.357	0.516	---
4 x Asyn(Si)	0.506	0.442	0.874	---
$\Sigma$ 18 Basins	$\Sigma$ 59.952			

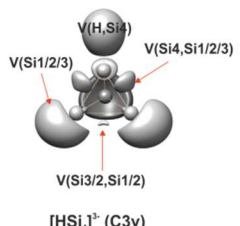
The ELI-D analysis of the [Si $_4$ ] $^{4-}$  cluster resulted in 18 basins; 4 core basins (C(Si)), 6 disynaptic Si-Si basins (V(Si-Si)) with high eccentricity, 4 monosynaptic Si valence basins (V(Si)) and 4 asynaptic basins (Asyn(Si)) (Table S1). Altogether no multicenter character, i.e. three-center bond, was found in the naked Si $_4$  $^{4-}$ . Integration over the basins yields 10.060 electrons for each C(Si) as expected. However, the disynaptic V(Si,Si) basin is irregularly low occupied ( $N(\Omega) = 1.195e^-$ ). On the other hand, the population of the monosynaptic basin V(Si) is significantly deviating from the classical lone pair population ( $N(\Omega) = 2.629e^-$ ). Additionally, the asynaptic basins (ASyn(Si)), which are located around 4.20 Å from the nuclei, are also noticeably populated by Rydberg electrons ( $N(\Omega) = 0.506e^-$ ). From the population analysis of the basin, a high relative fluctuation index is obtained for valence monosynaptic basin ( $\sigma^2 = 1.357e^-$ ;  $\lambda = 0.516$ ), disynaptic basin ( $\sigma^2 = 0.819e^-$ ;  $\lambda = 0.685$ ) and asynaptic basins ( $\sigma^2 = 0.442e^-$ ;  $\lambda = 0.874$ ). Especially, the relative fluctuation index of the disynaptic basin V(Si,Si) is very atypical for a classical 2c-2e bond, which would hint at high correlation degree with other basins. Indeed, the analysis of the delocalization index revealed a significant delocalization of disynaptic V(Si $M$ ,Si $N$ ) basin to both monosynaptic basins V(Si $M$ ) and V(Si $N$ ) ( $\delta(V(SiM/N),V(SiM,SiN)) = 0.1655$ ). In addition, the monosynaptic basins (V(Si $M$ )) exhibits a high delocalization index with the core basin (C(Si $M$ )) as well as with the asynaptic basin (Asyn(Si $M$ )).

**Table S2.** ELI-D surface and analysis of  $[\mu\text{-HSi}_4]^{3-}$ -cluster. Isovalue = 1.49 was applied for the ELI-D surface.


$[\mu\text{-HSi}_4]^{3-}$	avg. population	$\sigma^2$ (fluctuation)	$\lambda$ (relative fluctuation)	eccentricity
4 x C(Si)	10.060	0.392	0.037	---
4 x V(Si1/4,Si2/3)	1.412	0.918	0.650	1.043
1 x V(Si2,Si3)	1.014	0.730	0.720	0.887
1 x V(H,Si1,Si4)	1.988	0.789	0.397	---
2 x V(Si1/4)	2.460	1.198	0.487	---
2 x V(Si2/3)	2.734	1.321	0.483	---
2 x Asyn(Si1/4)	0.131	0.125	0.954	---
2 x Asyn(Si2/3)	0.213	0.198	0.930	---
$\Sigma$ 18 Basins	$\Sigma$ 59.965			

The ELI-D analysis of the protonated cluster with a shared H-atom ( $[\mu\text{-HSi}_4]^{3-}$ ) yields also in 18 basins (Table S2). Compared to the naked  $[\text{Si}_4]^{4-}$  cluster, the obvious difference found in ELI-D analysis of  $[\mu\text{-HSi}_4]^{3-}$  is the annihilation of one disynaptic  $V(\text{Si}1,\text{Si}4)$ , and the appearance of an additional polysynaptic basin  $V(\text{H},\text{Si}1,\text{Si}4)$ . The latter is populated by 1.988 electrons, which clearly indicates a 3c-2e bond. The relative fluctuation index of this basin is slightly pronounced ( $\sigma^2 = 0.789e^-$ ;  $\lambda = 0.397$ ), however, not as high as for the disynaptic basins  $V(\text{Si}1/4,\text{Si}2/3)$  ( $\sigma^2 = 0.918e^-$ ;  $\lambda = 0.650$ ) and  $V(\text{Si}2,\text{Si}3)$  ( $\sigma^2 = 0.730e^-$ ;  $\lambda = 0.720$ ). The evaluation of delocalization index demonstrates that the electrons in the polysynaptic basin  $V(\text{H},\text{Si}1,\text{Si}4)$  are delocalized into the two monosynaptic basins  $V(\text{Si}1)$  and  $V(\text{Si}4)$ . When  $[\text{Si}_4]^{4-}$  is protonated on one vertex (Table S3), all disynaptic basins between Si atoms were retained as in the naked cluster. As expected, one monosynaptic basin  $V(\text{Si})$  and one asynaptic basin  $\text{Asyn}(\text{Si})$  are now eliminated, while an additional disynaptic basin  $V(\text{H},\text{Si})$  appears. The latter basin ( $V(\text{H},\text{Si})$ ) is populated by 2.020 electrons with a low relative fluctuation index ( $\sigma^2 = 0.571$ ;  $\lambda = 0.283$ ), which is in line with the description of a classical two center two electrons bond.

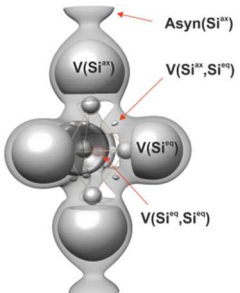
**Table S3.** ELI-D surface and analysis of [HSi<sub>4</sub>]<sup>3-</sup> cluster. Isovalue = 1.49 was applied for the ELI-D surface.



[HSi <sub>4</sub> ] <sup>3-</sup>	avg. population	$\sigma^2$ (fluctuation)	$\lambda$ (relative fluctuation)	eccentricity
4 x C(Si)	10.061	0.392	0.037	---
3 x V(Si <sub>3/2</sub> ,Si <sub>1/2</sub> )	0.985	0.715	0.650	0.920
3 x V(Si <sub>4</sub> ,Si <sub>1/2/3</sub> )	1.811	1.065	0.720	1.293
1 x V(H,Si <sub>4</sub> )	2.020	0.571	0.397	---
3 x V(Si <sub>1/2/3</sub> )	2.906	1.351	0.465	---
3 x Asyn(Si)*	0.128	0.122	0.953	---
3 x Asyn(H)*	0.069	0.068	0.986	---
$\Sigma$ 20 Basins	$\Sigma$ 59.962			

\*asynaptic basins are below the threshold and therefore are not shown.

**Table S4.** ELI-D surface and analysis of [Si<sub>5</sub>]<sup>2-</sup> cluster. Isovalue = 1.46 was applied for the solid ELI-D surface, whereas isovalue = 1.20 was used to show the disynaptic basin V(Si<sup>eq</sup>,Si<sup>eq</sup>).



[Si <sub>5</sub> ] <sup>2-</sup>	avg. population	$\sigma^2$ (fluctuation)	$\lambda$ (relative fluctuation)	eccentricity
5 x C(Si)	10.058	0.397	0.040	---
3 x V(Si <sup>eq</sup> ,Si <sup>eq</sup> )	0.514	0.431	0.839	0.705
6 x V(Si <sup>ax</sup> ,Si <sup>eq</sup> )	1.221	0.851	0.697	0.584
2 x V(Si <sup>ax</sup> )	2.497	1.078	0.432	---
3 x V(Si <sup>eq</sup> )	2.594	1.253	0.483	---
2 x Asyn(Si)	0.021	0.020	0.952	---
$\Sigma$ 21 Basins	$\Sigma$ 71.975			

The ELI-D analysis of the [Si<sub>5</sub>]<sup>2-</sup> showed a total of 21 basins (Table S4); five core basins C(Si) ( $N(\Omega) = 10.058e^-$ ), two monosynaptic valence basins V(Si<sup>ax</sup>) for the top and bottom silicon atoms ( $N(\Omega) = 2.497e^-$ ), three monosynaptic valence basins V(Si<sup>eq</sup>) for the three silicon atoms in the equatorial position ( $N(\Omega) = 2.594e^-$ ), six disynaptic valence basins V(Si<sup>ax</sup>,Si<sup>eq</sup>) between the top silicon atom and the silicon atom in the equatorial position ( $N(\Omega) = 1.221e^-$ ), three disynaptic valence basins V(Si<sup>eq</sup>,Si<sup>eq</sup>) between the silicon atom in the equatorial plane ( $N(\Omega) = 0.514e^-$ ), two asynaptic basins Asyn(Si<sup>ax</sup>) for the top/bottom silicon atoms ( $N(\Omega) = 0.021e^-$ ). As in the [Si<sub>4</sub>]<sup>4-</sup> naked cluster, monosynaptic basins are significantly higher populated by more than two electrons, while both disynaptic basins V(Si<sup>eq</sup>,Si<sup>eq</sup>) and V(Si<sup>ax</sup>,Si<sup>eq</sup>) are populated less than two. Especially the disynaptic basin

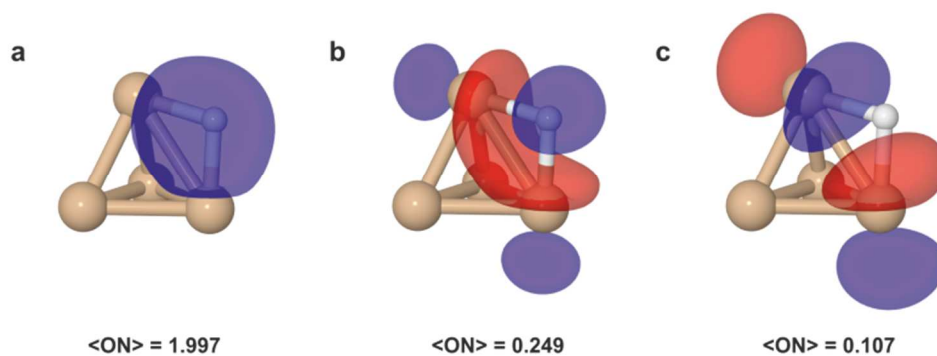
$V(\text{Si}^{\text{eq}}, \text{Si}^{\text{eq}})$  is very sparsely populated and shows a fluctuation index close to 1 ( $\sigma^2 = 0.431$ ;  $\lambda = 0.839$ ). These basins are delocalized almost completely over all other disynaptic basins and monosynaptic basins. The ELI-D analysis did not result directly a multicenter bond character as predicted by AdNDP analysis of its heavier analogue  $[\text{Ge}_5]^{2-}$ . However, the sum of electron population over two times  $\frac{1}{2} V(\text{Si}^{\text{ax}}, \text{Si}^{\text{eq}})$  and  $\frac{1}{2} V(\text{Si}^{\text{eq}}, \text{Si}^{\text{eq}})$  basins yield a population of 1.478 electrons, which corresponds to a electron deficit multicenter bond.

### 3.5.3.2 NBO analysis

#### $[\text{Si}_4]^{4-}$ , $[\mu\text{-HSi}_4]^{3-}$ and $[\text{HSi}_4]^{3-}$

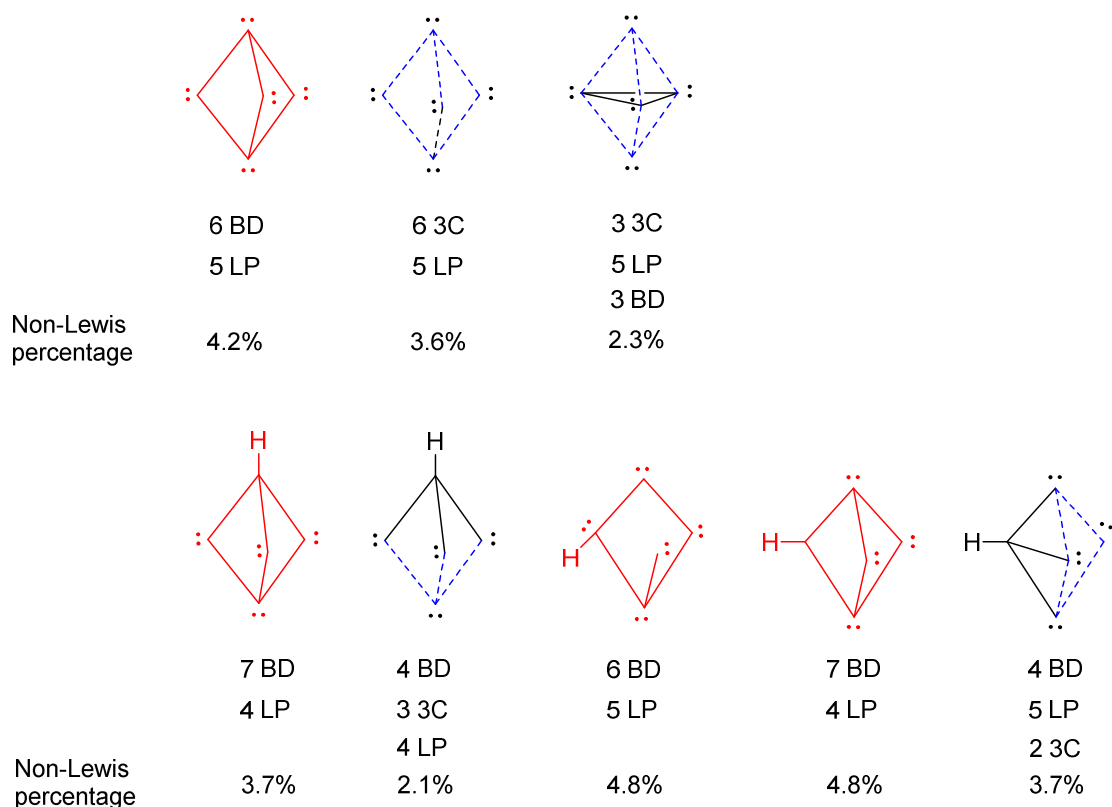
In line with the ELI-D analysis (Table S1-S2), the NBO analysis showed no multicenter character for the naked  $[\text{Si}_4]^{4-}$ , whereas for  $[\mu\text{-HSi}_4]^{3-}$  with shared H atom, an additional three center NBOs (3C) emerged (Figure S11). In the naked  $\text{Si}_4^{4-}$  cluster, the occupation number ( $\langle \text{ON} \rangle$ ) of bonding NBOs between the silicon atoms (BD Si-Si) and lone pair NBOs of the silicon atoms (LP Si) are slightly less than two electrons ( $\langle \text{ON} \rangle$  BD Si-Si =  $1.974e^-$ ;  $\langle \text{ON} \rangle$  LP Si-Si =  $1.988e^-$ ). Consequently, the antibonding orbital  $\text{BD}^*(\text{Si-Si})$  is marginally occupied ( $\langle \text{ON} \rangle$   $\text{BD}^* \text{Si-Si} = 0.0136e^-$ ). The deletion of the non-Lewis NBO contribution leads to a destabilization of  $299.4 \text{ kJ}\cdot\text{mol}^{-1}$ . The 3C NBO in the protonated cluster is properly occupied with  $1.997e^-$ , which is also in full agreement with the polysynaptic basin's population calculated from ELI-D. A significant occupation of a lesser 3-center NBO ( $\langle \text{ON} \rangle$   $3\text{Cn} = 0.249e^-$ ) and an antibonding 3-center NBO ( $\langle \text{ON} \rangle$   $3\text{C}^* = 0.107e^-$ ) was found (Figure S11). Since the 3C NBO is almost fully occupied, the source of the occupation of the respective non-Lewis NBOs is apparently other NBOs. Indeed, detailed inspection of the occupation of lone pair NBO of the vertex atom (LP Si) as well as the Si-Si bonding NBO (BD Si-Si) suggests an excitation from LP Si and BD Si-Si NBOs into the  $3\text{Cn}/3\text{C}^*$  NBO. This is further strengthened by the second order perturbation analysis revealing strong donor-acceptor interactions between the LP Si/BD-Si-Si NBOs and  $3\text{Cn}/3\text{C}^*$  NBO (up to  $32 \text{ kJ}\cdot\text{mol}^{-1}$ ). In contrast, no donor-acceptor interaction is found between the 3C and  $3\text{Cn}/3\text{C}^*$ , which is fully consistent with the occupation number of 3C NBO. The deletion of the non-Lewis NBOs matrix elements in  $[\mu\text{-HSi}_4]^{3-}$  leads to massive destabilization ( $499.2 \text{ kJ}\cdot\text{mol}^{-1}$ ) of the cluster. This suggests a more pronounced delocalization in  $[\mu\text{-HSi}_4]^{3-}$  than in the naked cluster. For the protonated cluster on the vertex ( $[\text{HSi}_4]^{3-}$ ), no 3C NBO was predicted and one LP NBO vanished, whereas a bonding NBO between Si and H (BD Si-H) appears. Apart from significant occupation of antibonding Si-H NBO ( $\langle \text{ON} \rangle$   $\text{BD}^* \text{Si-H} = 0.102e^-$ ), marginal occupation of antibonding NBO between Si-Si ( $\langle \text{ON} \rangle$   $\text{BD}^* \text{Si-Si} \sim 0.011e^-$ ) was observed. Deletion of non-Lewis

NBOs resulted in a destabilization of 386.0 kJ/mol. Hence, in general both protonated clusters showed a larger degree of delocalization to Non-Lewis NBOs. However, when the effect is discounted, the axial protonated cluster ( $[\text{HSi}_4]^{3-}$ ) is becoming more stable by 53.6 kJ/mol than the cluster with the shared proton ( $[\mu\text{-HSi}_4]^{3-}$ ).



**Figure S11.** Non-Lewis 3Cn and 3C\* NBOs of  $[\mu\text{-HSi}_4]^{3-}$  are significantly occupied.



$[\text{Si}_5]^{2-}$ ,  $[\mu\text{-HSi}_5]^-$ ,  $[\text{H}^{\text{ax}}\text{Si}_5]^-$  and  $[\text{H}^{\text{eq}}\text{Si}_5]^-$ 

**Figure S12.** Lewis Structures of  $[\text{Si}_5]^{2-}$ ,  $[\text{H}^{\text{ax}}\text{Si}_5]^-$ ,  $[\text{H}^{\text{eq}}\text{Si}_5]^-$ ,  $[\mu\text{-HSi}_5]^-$  obtained by automatic search algorithm from NBO6 (in red) and directed search (black). Blue dashed lines indicate bonds included in 3C-2e bond. The percentage of non-Lewis occupation is the qualitative measure of the suggested Lewis structures. All structures exhibit extremely high delocalization degree.

The construction of a proper Lewis structure of  $[\text{Si}_5]^{2-}$  for the NBO analysis is not as trivial as in  $[\text{Si}_4]^{4-}$ . In this case, the best Lewis structure exhibits three 3-center orbitals (Figure S12). These 3C NBOs consist of  $3s$ - ( $\sim 10\%$ ) and  $3p$ -type ( $\sim 90\%$ ) NAOs of the two axial Si atoms as well as  $3p$ -type NAO of the equatorial Si atom. The average occupation number for the 3C NBOs  $\langle \text{ON } 3\text{C} \rangle$  is ( $1.993e^-$ ), which indicates a localized 3C-2e bond. Furthermore, non-Lewis 3Cn NBOs are also occupied significantly (a situation similar to  $[\mu\text{-HSi}_4]^{3-}$ ), while the occupation of BD NBOs between  $\text{Si}^{\text{eq}}$  atoms as well as all LP NBOs deviate strongly from 2 electrons ( $\langle \text{ON } 3\text{Cn} \rangle = 0.481e^-$ ;  $\langle \text{ON BD } \text{Si}^{\text{eq}}\text{-Si}^{\text{eq}} \rangle = 1.619e^-$ ;  $\langle \text{ON LP } \text{Si}^{\text{eq}} \rangle = 1.874$ ;  $\langle \text{ON LP } \text{Si}^{\text{ax}} \rangle = 1.951$ ). Additionally, the second order perturbation analysis showed very strong donor-acceptor interaction from LP  $\text{Si}^{\text{eq}}$  and BD  $\text{Si}^{\text{eq}}\text{-Si}^{\text{eq}}$  to 3Cn NBOs ( $E^{(2)} = \sim 288.7 - 570 \text{ kJ}\cdot\text{mol}^{-1}$ ; in the sum a total of  $4738.9 \text{ kcal}\cdot\text{mol}^{-1}$ ). As in  $[\text{Si}_4]^{4-}$  cluster, when non-Lewis orbital contribution is turned off, the  $[\text{Si}_5]^{2-}$  is destabilized by  $2188.1 \text{ kJ}\cdot\text{mol}^{-1}$ . Note, that the amount of destabilization is by no means unique and is very dependent on the reference localized Lewis structure. As mentioned above, the best Lewis structure to describe  $[\text{Si}_5]^{2-}$  exhibits three 3C Lewis NBOs five lone pairs for each Si

atoms and 3 bonding NBOs between  $\text{Si}^{\text{eq}}$ . Other possible Lewis structure as proposed by the default search by NBO6 does not show 3C orbitals but rather six bonding Si-Si, with five lone pairs for each Si atoms. However, the suggested Lewis structure (Figure S12) is highly delocalized and possesses higher non-Lewis NBO occupation (4.2%). Hence, it is qualitatively worse than the presented Lewis structure in the manuscript (2.3%).

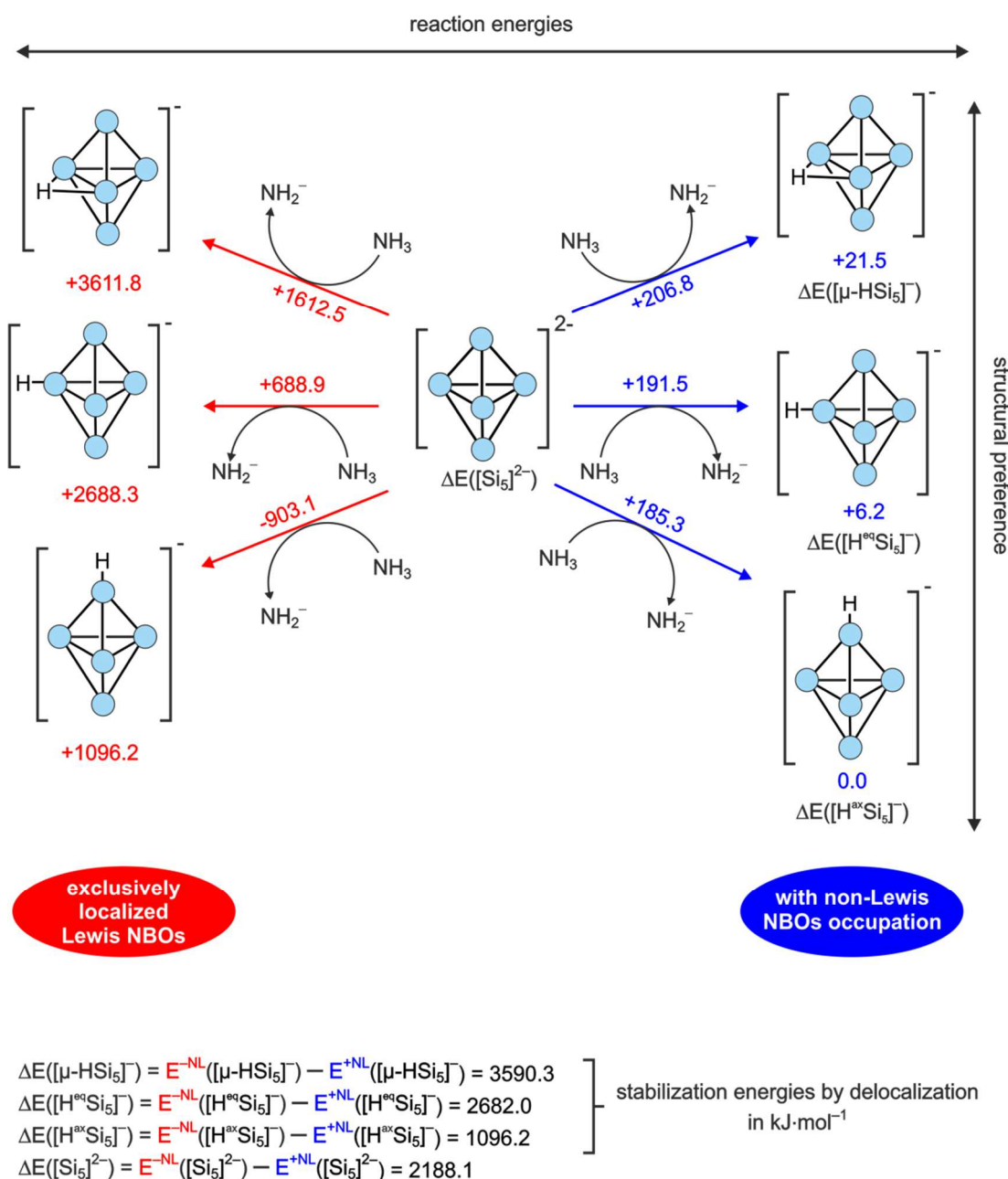


**Figure S13.** Protonation energies of  $[\text{Si}_5]^{2-}$  with non-Lewis contribution and without non-Lewis contribution.

In general, the protonation of  $[\text{Si}_5]^{2-}$  are thermodynamically not feasible in liquid ammonia (Figure S13). Nevertheless, to understand the protonation behavior, three possible protonation sites were calculated: axially protonated  $[\text{H}^{\text{ax}}\text{Si}_5]^-$ , equatorially  $[\text{H}^{\text{eq}}\text{Si}_5]^-$

and  $[\mu\text{-HSi}_5]^-$ . The most stable protonated cluster is  $[\text{H}^{\text{ax}}\text{Si}_5]^-$ . The terminally protonated cluster is more stable than the  $[\mu\text{-HSi}_5]^-$  by  $21.5 \text{ kJ}\cdot\text{mol}^{-1}$ ; an inverse situation as in  $[\text{HSi}_4]^{3-}$  and  $[\mu\text{-HSi}_4]^{3-}$ . The second most stable protonated cluster is also terminally protonated, however, at the equatorial Silicon atoms  $[\text{H}^{\text{eq}}\text{Si}_5]^-$ . This conformation is only  $6.2 \text{ kJ}\cdot\text{mol}^{-1}$  less stable than the global minimum. Overall, massive destabilization was predicted when the non-Lewis NBOs contribution is deleted. For  $[\text{H}^{\text{ax}}\text{Si}_5]^-$  ( $1096.2 \text{ kJ}\cdot\text{mol}^{-1}$ ), the amount of destabilization is less than in the naked  $[\text{Si}_5]^{2-}$ . Therefore, in the case the localized picture is considered, the protonation leading to the  $[\text{H}^{\text{ax}}\text{Si}_5]^-$  is highly favored, simply due to significant different in destabilization energies. E.g. For  $[\text{H}^{\text{ax}}\text{Si}_5]^-$ , a difference of  $1091.9 \text{ kJ}\cdot\text{mol}^{-1}$  in destabilization energy relative to the naked cluster  $[\text{Si}_5]^{2-}$  is obtained, i.e. reduced delocalization. In contrast, the protonation leading to  $[\text{H}^{\text{eq}}\text{Si}_5]^-$  and  $[\mu\text{-HSi}_5]^-$  increases the delocalization by  $494.0 \text{ kJ}\cdot\text{mol}^{-1}$  and  $1497.3 \text{ kJ}\cdot\text{mol}^{-1}$  compared to the naked cluster. This means, the stability of  $[\text{H}^{\text{eq}}\text{Si}_5]^-$  and  $[\mu\text{-HSi}_5]^-$  owes to the massive delocalization. Without delocalization such “weird” looking Lewis structure (Figure S13) is very unlikely.

### 3.5.3.3 Computational Details

All geometries are optimized at TPSSH/6-311+G(d,p) level of theory in the continuum of NH<sub>3</sub> (SMD).<sup>[43,44]</sup> The dielectric constant was increased to 22.63 to adapt the low temperature measurement. Thermochemical analysis was performed at the same level of theory. Single point energies were obtained at DLPNO-CCSD(T)/def2-TZVPP level of theory on top the optimized geometry.<sup>[45]</sup> NMR shift and coupling calculations were performed at TPSSH/pcSseg-4. The chemical shift of the silicon core in Zintl-ions were referenced to Si core in TMS. Problem with accuracy arises since NMR calculation of Si core are usually deviating more than protons. Hence, the chemical shielding of TMS is not computed as usual but rather a combination of experimental and theoretical values. The experimental chemical shift of H<sub>3</sub>Si<sup>-</sup> is known at -174.50 ppm (referenced to TMS). With the computed chemical shielding of this compound (550.28), the chemical shielding of TMS is simply estimated by the addition the calculated chemical shielding and experimental chemical shift of H<sub>3</sub>Si<sup>-</sup>, this yields to a shielding of 375.78 for the Si core in TMS. Compared to the directly calculated chemical shielding (345.82), the deviation equals approximately 30 ppm. When using the directly calculated shielding for the reference system, the deviation in calculated chemical shift of the Zintl-ions is systematic but may look odd in the manuscript, since it is always off by 30 ppm. Additionally, this may impede the assignment of the calculated values to experimental values because we may search for unknown signals in the wrong region. ELI-D<sup>[46]</sup> and NBO<sup>[47]</sup> analysis were conducted using the wavefunction from TPSSH/6-311+G(d,p) using DGRID5.0<sup>[48]</sup> and NBO6<sup>[49]</sup>. Gaussian09 D.01 was used for geometry optimization and NMR calculations.<sup>[50]</sup> For single point, ORCA 4.0 was used.<sup>[51]</sup>

## 3.5.3.4 Cartesian Coordinates

**[Si<sub>4</sub>]<sup>4-</sup>**

Si	0.87030500	0.87030500	0.87030500
Si	-0.87030500	-0.87030500	0.87030500
Si	0.87030500	-0.87030500	-0.87030500
Si	-0.87030500	0.87030500	-0.87030500

**[μ-HSi<sub>4</sub>]<sup>3-</sup>**

Si	1.30293413	0.00000000	0.76503101
Si	0.00000000	-1.24652541	-0.83224368
Si	0.00000000	1.24652541	-0.83224368
Si	-1.30293413	0.00000000	0.76503101
H	0.00000000	0.00000000	1.91349200

**[HSi<sub>4</sub>]<sup>3-</sup>**

Si	-0.00885105	1.47320259	-0.15409253
Si	0.00231001	-0.00264282	1.72840598
Si	1.27118155	-0.73411578	-0.16511671
Si	-1.28125003	-0.72973500	-0.15188690
H	0.01660952	-0.00670898	-1.24861685

**[Si<sub>5</sub>]<sup>2-</sup>**

Si	-1.86825800	-0.00000700	-0.00088000
Si	-0.00001900	-0.85251000	-1.19577100
Si	0.00001300	1.46292700	-0.13911900
Si	0.00001300	-0.61038800	1.33667000
Si	1.86825100	-0.00002200	-0.00090100

**[H<sup>ax</sup>Si<sub>5</sub>]<sup>-</sup>**

Si	-1.73875283	0.00006197	0.00007034
Si	0.03670073	-0.90203487	-1.26709172
Si	0.03724715	1.54800379	-0.14815405
Si	0.03693562	-0.64604442	1.41508066
Si	1.73634736	-0.00058346	-0.00006653
H	3.22977200	-0.00088909	0.00010489

**[H<sup>eq</sup>Si<sub>5</sub>]<sup>-</sup>**

Si	-1.90110700	0.00014900	-0.08975400
Si	0.00000000	1.34592400	-0.65708500
Si	0.00000000	-0.00088500	1.29649600
Si	0.00000000	-1.34523000	-0.65851700
Si	1.90110800	0.00014900	-0.08975400
H	-0.00000100	-0.00149400	2.78058000

**[μ-HSi<sub>5</sub>]<sup>-</sup>**

Si	-1.93234400	-0.00021000	0.14707500
Si	-0.00064200	1.31626100	-0.74621300
Si	0.00030900	-0.00207200	1.33123400
Si	0.00009800	-1.31451800	-0.74962700
Si	1.93249000	0.00029400	0.14672300
H	0.00123900	0.00341500	-1.80870200

### 3.6 Additional Findings

Here, the necessity of a 100%  $^{29}\text{Si}$  enrichment for the NMR spectroscopic investigations is addressed. The NMR properties of silicon – with  $^{29}\text{Si}$  being its only NMR active isotope with spin  $I = 1/2$  – are rather poor due to its low negative gyromagnetic ratio ( $\mu = -0.5548$ ) and low natural abundance (4.70%). Additionally, the solubility of silicon Zintl anions is even in liquid ammonia very low. Therefore, an enrichment of the NMR active isotope is highly desirable as it enables the detection of these elusive species. However, a degree of enrichment less than 100% becomes detrimental, as several overlapping coupling patterns are expected for each species. Their origin will be discussed in the following, exemplary for the trigonal bipyramidal [Si $_5$ ] $^{2-}$  cluster with 80%  $^{29}\text{Si}$  enrichment.

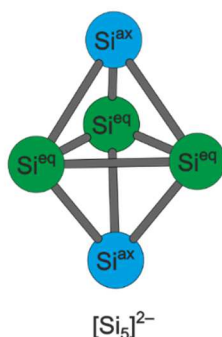


**Figure AF1.** Schematical representation of the trigonal bipyramidal cluster [Si $_5$ ] $^{2-}$  with two groups of chemically equivalent Si atoms in axial and equatorial position. The axial Si atoms are marked in blue, the equatorial Si atoms are marked in green.

The trigonal bipyramidal cluster [Si $_5$ ] $^{2-}$  exhibits two distinct groups of chemically equivalent Si atoms, i.e. two axial Si atoms (Si<sup>ax</sup>, Figure AF1 in blue) and three equatorial Si atoms (Si<sup>eq</sup>, Figure AF1 in green). At 100%  $^{29}\text{Si}$  enrichment, these Si atoms give rise to two separated NMR signals: a quartet at  $\delta = +348.7$  for the axial ones and a triplet at  $\delta = -347.8$  ppm for the equatorial ones in the  $^{29}\text{Si}$  NMR spectra (see manuscript).

However, a  $^{29}\text{Si}$  enrichment of 80% does not lead to a single cluster with four NMR active and one NMR inactive nuclei, but rather to a mixture of several conformations with  $n$   $^{29}\text{Si}$  atoms ( $0 < n < 5$ ). Additionally, the conformations with  $1 < n < 4$  result more than one single distribution, e.g. for  $n = 3$ : Either a) exclusively the three Si<sup>eq</sup>, b) two Si<sup>ax</sup> and one Si<sup>eq</sup>, or c) one Si<sup>ax</sup> and two Si<sup>eq</sup> are labeled with NMR active  $^{29}\text{Si}$ . Each distribution gives rise to a different pattern for both  $^{29}\text{Si}$  signals: a) no signal for Si<sup>ax</sup> and a singlet for Si<sup>eq</sup>, b) a doublet for Si<sup>ax</sup> and a triplet for Si<sup>eq</sup>, and c) a triplet for Si<sup>ax</sup> and a doublet for Si<sup>eq</sup>. All the possible cluster occupations with their respective distributions as well as the resulting theoretical NMR signals are summarized in Figure AF2.

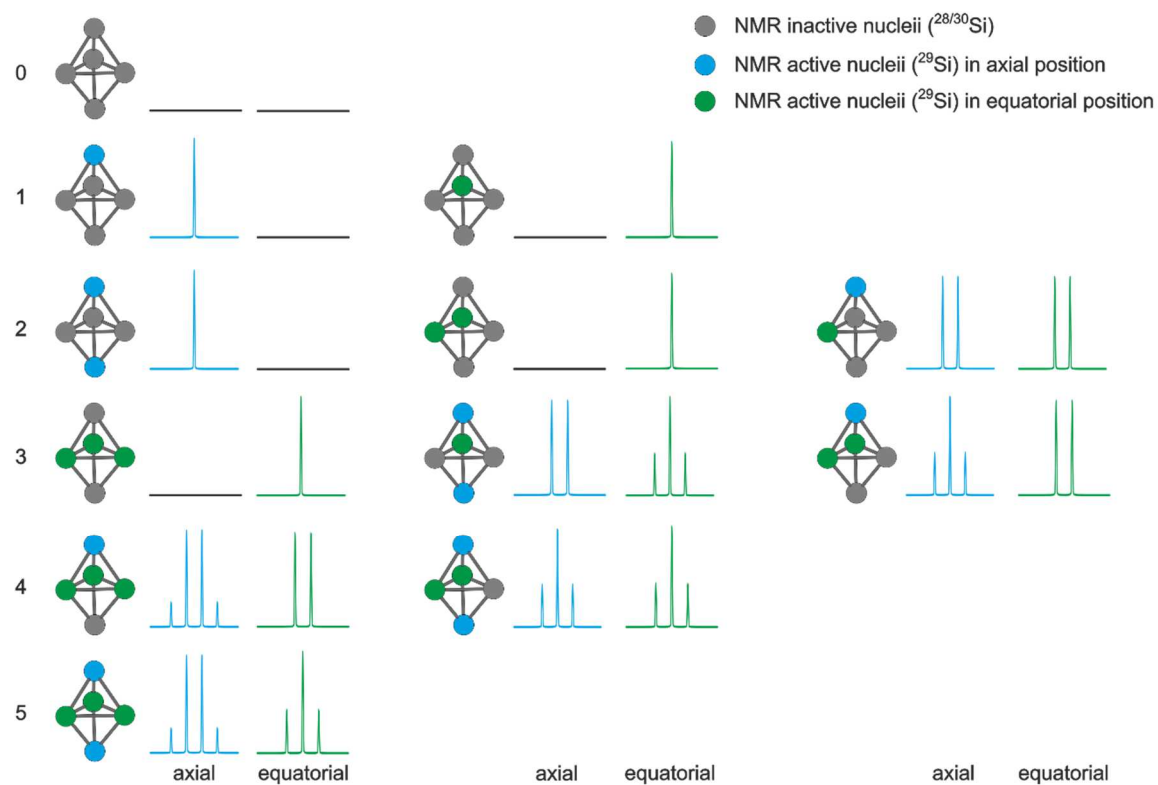


**Figure AF2.** All possible occupations ( $0 < n < 5$ ) for  $^{29}\text{Si}$  in  $[\text{Si}_5]^{2-}$  with their respective distributions and the resulting theoretical NMR signals for axial and equatorial Si atoms.

Furthermore, for most of the distributions (except for  $n = 0$  and  $n = 5$ , where only one combination is possible) their permutations must be considered as well, which result in identical NMR signals adding up to a total net signal. Exemplified for  $n = 3$  with one Si<sup>ax</sup> and two Si<sup>eq</sup>, three permutations in the equatorial plane (three over two) and two permutations in the axis (two over one) can be achieved (see Figure AF3). Thus, in total six different combinations can be realized, which are accounted for by a weighting factor  $f = 6$  in the net signals.

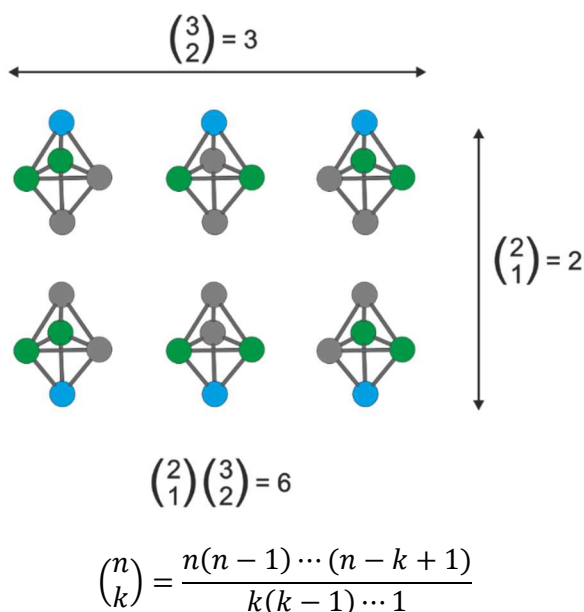


**Figure AF3.** Permutations for  $n = 3$  with one Si<sup>ax</sup> and two Si<sup>eq</sup> NMR active nuclei. Three permutations in the equatorial plane and two permutations in the axis are achieved. A total of six combinations must be accounted for the signals of the axial and equatorial Si atoms by a weighting factor  $f = 6$ .



The weighting factors for each distribution of all conformations (occupation  $0 < n < 5$ ) are summarized in Figure AF4. The superpositions of all signals for each conformation ( $0 < n < 5$ ) are shown on the right side, including their weighting factors  $f$ . The signals are normalized, and their integrals are noted above each signal for better visualization.

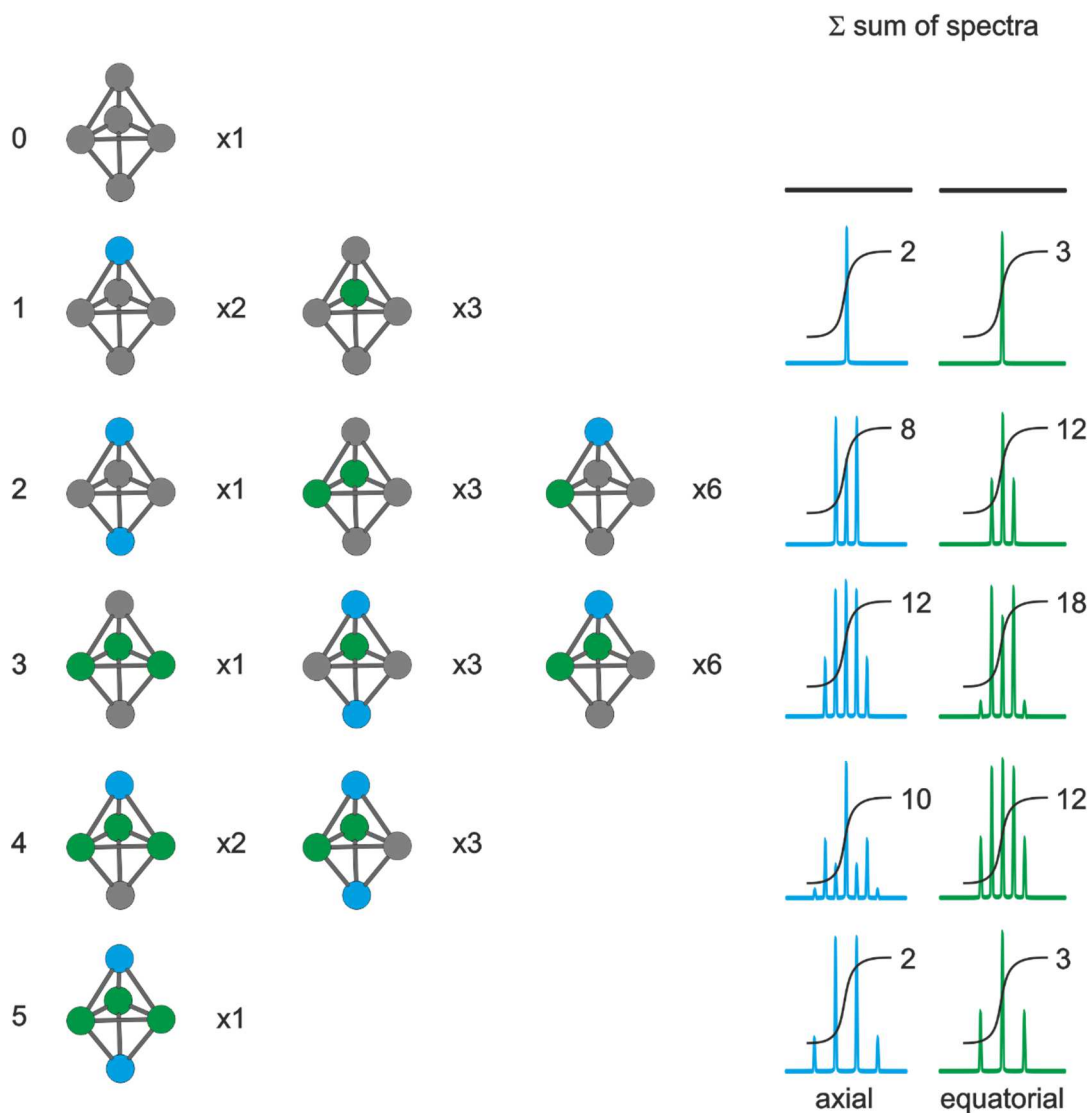


**Figure AF4.** Summary of all weighting factors for each distribution of all conformations ( $0 < n < 5$ ) on the left side. Weighted superpositions of all signals for each conformation ( $0 < n < 5$ ) on the right side. The sums of the spectra are normalized, and their integrals are noted above each signal for better visualization.

So far, all possible conformations, the different distributions and their permutations were regarded, but not the degree of <sup>29</sup>Si enrichment. The probability  $P(n)$  for a [Si<sub>5</sub>]<sup>2-</sup> cluster with exactly  $n$  NMR active <sup>29</sup>Si atoms at a degree of enrichment  $\omega$  can be calculated by Equation (1).

$$P_{\omega}(n) = \omega^n(1 - \omega)^{(5-n)} \quad \text{Eq (1)}$$

Each Si atom has a probability of  $\omega = 0.8$  to be NMR active (80% <sup>29</sup>Si labeled), and a probability of  $(1 - \omega) = 0.2$  to be NMR inactive (20% <sup>28/30</sup>Si). Exemplified for  $n = 3$ , there are three NMR active Si atoms (Figure AF5 either in blue or green) and two NMR inactive Si atoms (Figure AF5 in grey). The probability  $P_{80\%}(3)$  for exactly three Si atoms being NMR active and two being NMR inactive at 80% <sup>29</sup>Si enrichment, independent of their positions is calculated by the product of the degree of enrichment  $\omega$  (80%) to the power of the number of <sup>29</sup>Si atoms  $n$  ( $n = 3$ ) and the probability not being <sup>29</sup>Si labeled  $(1 - \omega)$  to the power of the number of <sup>28</sup>Si and <sup>30</sup>Si atoms  $(5 - n)$ , i.e.  $P_{80\%}(3) = 0.8^3 \cdot 0.2^2 = 0.02048$ . As aforementioned, for  $n = 3$ , a total of ten combinations was obtained, so the total probability for  $n = 3$  amounts to:  $P_{80\%}^{tot}(3) = f \cdot P_{80\%}(3) = 10 \cdot 0.02048 = 0.2048 = 20.48\%$ .

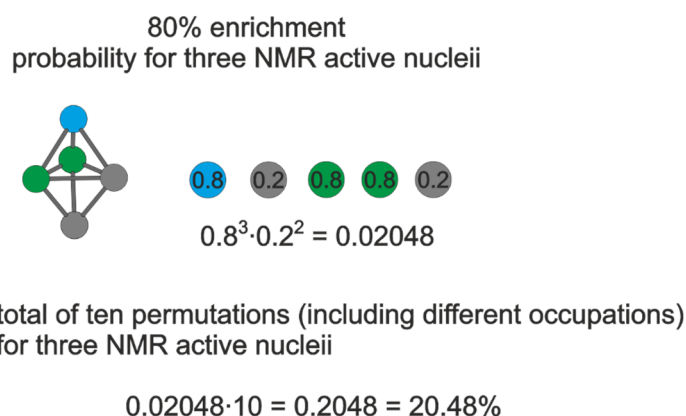


**Figure AF5.** Exemplified calculation for three NMR active Si atoms for a single permutation and for the total probability of three NMR active Si atoms in arbitrary order.

**Table AF1.** Summary of individual probabilities  $P_{80\%}(n)$  and total probabilities  $P_{80\%}^{tot}(n)$ .

$n$	$P_{80\%}(n)$	$f$	$P_{80\%}^{tot}(n)$
0	0.03%	1	0.03%
1	0.13%	5	0.64%
2	0.51%	10	5.12%
3	2.05%	10	20.48%
4	8.19%	5	40.96%
5	32.77%	1	32.77%
$\sum_{n=0}^5 (P_{80\%}^{tot}(n))$			100%

The single probabilities for each conformation ( $0 < n < 5$ ) are given in Table AF1. The weighted net signals for each conformation (see Figure AF4) must be adjusted by a factor of their single probabilities  $P_{80\%}(n)$ . Superposition of all possible weighted signals (for axial as well as for equatorial Si atoms) results in two net signals with complex coupling patterns shown in Figure AF6. Note, that only the single probabilities  $P_{80\%}(n)$  have to be accounted for, since the possible permutations are already considered in the total probabilities  $P_{80\%}^{tot}(n)$ .

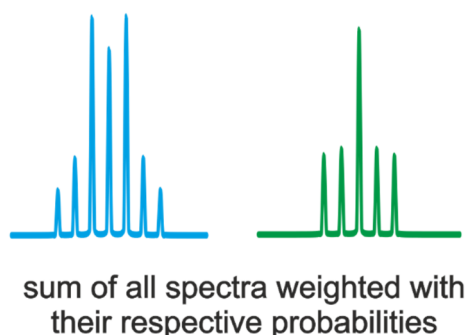


**Figure AF6.** Superposition of all possible weighted signals for axial and equatorial Si atoms in the  $[\text{Si}_5]^{2-}$  cluster including all conformations ( $0 < n < 5$ ), their distribution (axial or equatorial), feasible permutations ( $f$ ) and single probabilities  $P_{80\%}(n)$  of 80%  $^{29}\text{Si}$  enrichment.

In summary, an 80%  $^{29}\text{Si}$  enrichment entails highly complex coupling patterns in the NMR signals of the axial and equatorial Si atoms of the  $[\text{Si}_5]^{2-}$  cluster caused by a multitude of possible conformations, distributions and permutations. In addition, regarding the accompanied intensity decrease compared to the full  $^{29}\text{Si}$  enrichment (i.e. -20%), any lesser degree of  $^{29}\text{Si}$  enrichment can be assumed to be detrimental for the NMR spectroscopic investigation of silicon Zintl ions. Interestingly, 80% enrichment does not result exclusively in a single conformation with  $n = 4$ , but a considerable amount of  $n = 3$  (20.48%) and  $n = 5$  (32.77%) are predicted to be formed. With the help of this work other degrees of  $^{29}\text{Si}$  enrichment as well as other silicide cluster or even other Zintl anions (e.g. Sn or Pb) can be investigated further rather easily, as the coupling patterns can be a powerful tool for structural elucidation. Especially for nuclei with higher natural abundance, these investigations may give further insight into the rich world of anionic Zintl clusters.

### 3.7 References

- [1] W. Preetz, G. Peters, *Eur. J. Inorg. Chem.* **1999**, 1831–1846.
- [2] E. L. Muetterties, F. Klanberg, *Inorg. Chem.* **1966**, 5, 315–316; F. Klanberg, E. L. Muetterties, *Inorg. Chem.* **1966**, 5, 1955–1960.
- [3] A. R. Pitochelli, F. M. Hawthorne, *J. Am. Chem. Soc.* **1960**, 82, 4427–4428; H. C. Longuet-Higgins, M. d. V. Roberts, *Proc. R. Soc. London Ser. A* **1955**, 230, 110–119.
- [4] H. G. von Schnering, W. Hoenle, *Chem. Rev.* **1988**, 88, 243–273.
- [5] M. Scheer, G. Balazs, A. Seitz, *Chem. Rev.* **2010**, 110, 4236–4256.
- [6] A. F. Holleman, E. Wiberg, N. Wiberg, *Anorganische Chemie*, 103rd ed., de Gruyter, Berlin, **2017**.
- [7] A. Schnepf, *Chem. Soc. Rev.* **2007**, 36, 745–758; P. Willmes, K. Leszczynska, Y. Heider, K. Abersfelder, M. Zimmer, V. Huch, D. Scheschkewitz, *Angew. Chem. Int. Ed.* **2016**, 55, 2907–2910; *Angew. Chem.* **2016**, 128, 2959–2963; Y. Heider, D. Scheschkewitz, *Dalton Trans.* **2018**, 47, 7104–7112.
- [8] S. Gärtner, N. Korber in *Structure and Bonding*, Vol. 140 (Ed.: T. F. Fässler), Springer, Berlin, **2011**.
- [9] S. Scharfe, F. Kraus, S. Stegmaier, A. Schier, T. F. Fässler, *Angew. Chem. Int. Ed.* **2011**, 50, 3630–3670; *Angew. Chem.* **2011**, 123, 3712–3754.
- [10] K. Wiesler, K. Brandl, A. Fleischmann, N. Korber, *Z. Anorg. Allg. Chem.* **2009**, 635, 508–512.
- [11] C. Lorenz, S. Gärtner, N. Korber, *Crystals* **2018**, 8, 276.
- [12] J. D. Corbett, P. A. Edwards, *Chem. Commun.* **1975**, 984–985; M. Somer, W. Carrillo-Cabrera, E. M. Peters, K. Peters, M. Kaupp, H. G. von Schnering, *Z. Anorg. Allg. Chem.* **1999**, 625, 37–42.
- [13] M. Neumeier, F. Fendt, S. Gärtner, C. Koch, T. Gärtner, N. Korber, R. M. Gschwind, *Angew. Chem. Int. Ed.* **2013**, 52, 4483–4486; *Angew. Chem.* **2013**, 125, 4579–4582.
- [14] F. Fendt, C. Koch, M. Neumeier, S. Gärtner, R. M. Gschwind, N. Korber, *Chem. Eur. J.* **2015**, 21, 14539–14544.
- [15] F. S. Kocak, B. Eichhorn, *Structure and Bonding*, Vol. 140, Springer, Berlin, **2011**.
- [16] M. Baudler, K. Glinka, *Chem. Rev.* **1993**, 93, 1623–1667.
- [17] V. Quéneau, E. Todorov, S. C. Sevov, *J. Am. Chem. Soc.* **1998**, 120, 3263–3264.
- [18] S. Joseph, C. Suchentrunk, F. Kraus, N. Korber, *Eur. J. Inorg. Chem.* **2009**, 4641–4647.

- [19] S. Joseph, C. Suchentrunk, N. Korber, *Z. Naturforsch. B* **2010**, 65, 1059–1065; J. M. Goicoechea, S. C. Sevov, *J. Am. Chem. Soc.* **2004**, 126, 6860–6861.
- [20] J. M. Goicoechea, S. C. Sevov, *Inorg. Chem.* **2005**, 44, 2654 – 2658.
- [21] T. Henneberger, W. Klein, T. F. Fässler, *Z. Anorg. Allg. Chem.* **2018**, 644, 1018–1027.
- [22] T. F. Fässler, L. Schiegerl, A. Karttunen, J. Tillmann, S. Geier, G. Raudaschel-Sieber, M. Waibel, *Angew. Chem. Int. Ed.* **2018**, 57, 12950–12955; *Angew. Chem.* **2018**, 130, 13132–13137.
- [23] C. Lorenz, F. Hastreiter, J. Hioe, N. Lokesh, S. Gärtner, N. Korber, R. M. Gschwind, *Angew. Chem. Int. Ed.* **2018**, 57, 12956–12960; *Angew. Chem.* **2018**, 130, 13138–13142.
- [24] C. Lorenz, S. Gärtner, N. Korber, *Z. Anorg. Allg. Chem.* **2017**, 643, 141–145.
- [25] C. B. Benda, T. Henneberger, W. Klein, T. F. Fässler, *Z. Anorg. Allg. Chem.* **2017**, 643, 146–148.
- [26] W. Lu, C. M. Lieber, *Nat. Mater.* **2007**, 6, 841–850; M. L. Snedaker, Y. C. Zhang, C. S. Birkel, H. Wang, T. Day, Y. F. Shi, X. L. Ji, S. Kraemer, C. E. Mills, A. Moosazadeh, M. Moskovits, G. J. Snyder, G. D. Stucky, *Chem. Mater.* **2013**, 25, 4867–4873; B. K. Teo, X. H. Sun, *Chem. Rev.* **2007**, 107, 1454–1532.
- [27] F. S. Kocak, D. O. Downing, P. Zavalij, Y. F. Lam, A. N. Vedernikov, B. Eichhorn, *J. Am. Chem. Soc.* **2012**, 134, 9733 – 9740.
- [28] Fässler and co-workers refer, in a footnote, to the calculation and detection of CCSD(T) shifts (+225 ppm and –455 ppm) of  $[\text{Si}_5]^{2-}$  in Ref. [22].
- [29] A. Wiesner, S. Steinhauer, H. Beckers, C. Mglter, S. Riedel, *Chem. Sci.* **2018**, 9, 7169–7173.
- [30] Gaussian window function and zero filling gives minimal linewidths of circa 3 Hz.
- [31] N. Wiberg, G. Wagner, G. Muller, *Angew. Chem. Int. Ed. Engl.* **1985**, 24, 229–230; *Angew. Chem.* **1985**, 97, 220–222; K. M. Baines, A. G. Brook, R. R. Ford, P. D. Lickiss, A. K. Saxena, W. J. Chatterton, J. F. Sawyer, B. A. Behnam, *Organometallics* **1989**, 8, 693–709.
- [32] C. N. Smit, F. Bickelhaupt, *Organometallics* **1987**, 6, 1156–1163.
- [33] M. Driess, H. Pritzkow, S. Rell, *Organometallics* **1996**, 15, 1845 – 1855.
- [34] K. W. Klinkhammer, W. Schwarz, *Angew. Chem. Int. Ed. Engl.* **1995**, 34, 1334–1336; *Angew. Chem.* **1995**, 107, 1448–1451.
- [35] Uniform distribution of uncorrelated electrons over the number of vertex atoms/volume.
- [36] Recently, Fässler et al. published a communication on the compound  $[\text{K}([\text{18}]\text{crown-6})][\text{Rb}([\text{18}]\text{crown-6})]_2[\text{HGe}_4\text{ZnPh}_2] \cdot 8\text{NH}_3$ , which contains a protonated

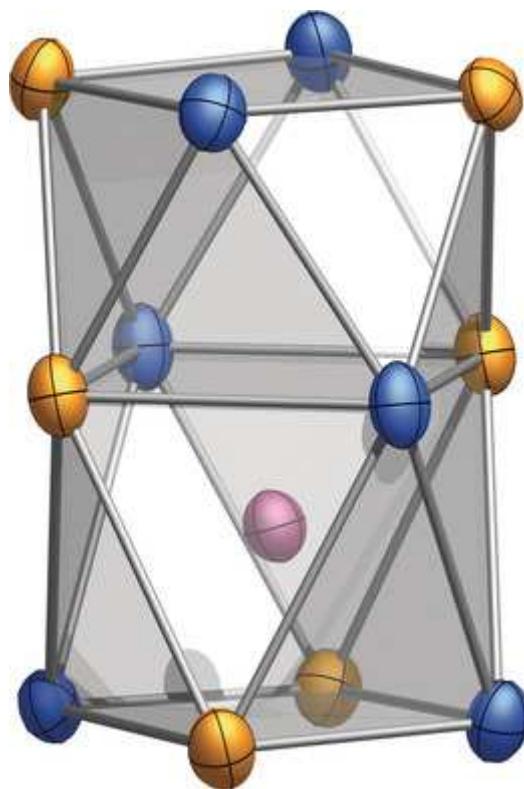
- tetragermanide cluster, in T. Henneberger, W. Klein, J. Dums, T. F. Fässler, *Chem. Commun.* **2018**, <https://doi.org/10.1039/C8CC06843G>. Here, the H atom also bridges the edge of the cluster.
- [37] The bridging H atom conformer [ $\mu$ -HSi<sub>9</sub>]<sup>3-</sup> was only predicted as a high-energy intermediate (+68.5 kJmol<sup>-1</sup>) in the H-hopping mechanism (see Ref. [23]).
- [38] F. Weinhold, C. R. Landis, *Valency and Bonding: A Natural Bond Orbital Donor-Acceptor Perspective*, Cambridge University Press, Cambridge, **2005**, p. 760.
- [39] A situation similar to the one reported for the heavier homologue [Ge<sub>5</sub>]<sup>2-</sup>, where six three-center two-electron bonds (3c-2e) were predicted by AdDNP analysis. In this case, much more localized 3c-2e bonds were obtained. C. Liu, L. J. Li, Q. J. Pan, Z. M. Sun, *Chem. Commun.* **2017**, 53, 6315–6318.
- [40] J. D. Corbett, *Struct. Bonding* (Berlin) **1997**, 87, 157.
- [41] T. F. Fässler, *Coord. Chem. Rev.* **2001**, 215, 347–377.
- [42] L. Hackspill, *Helv. Chim. Acta* **1928**, 11.
- [43] a) V. N. Staroverov, G. E. Scuseria, J. Tao and J. P. Perdew, “Comparative assessment of a new nonempirical density functional: Molecules and hydrogen-bonded complexes,” *J. Chem. Phys.* **2003**, 119, 12129; b) J. M. Tao, J. P. Perdew, V. N. Staroverov, and G. E. Scuseria, “Climbing the density functional ladder: Nonempirical meta-generalized gradient approximation designed for molecules and solids,” *Phys. Rev. Lett.* **2003**, 91, 146401.
- [44] A. V. Marenich, C. J. Cramer, and D. G. Truhlar, “Universal solvation model based on solute electron density and a continuum model of the solvent defined by the bulk dielectric constant and atomic surface tensions,” *J. Phys. Chem. B* **2009**, 113, 6378-96.
- [45] a) Riplinger, C.; Sandhoefer, B.; Hansen, A.; Neese, F. J. *Chem. Phys.* **2013**, 139, 134101; b) Riplinger, C.; Neese, F. J. *Chem. Phys.* **2013**, 138, 034106.
- [46] a) Kohout, M.: A measure of electron localizability. *Int. J. Quantum Chem.* **2004** 97, 651–658; b) Kohout, M.: Bonding indicators from electron pair density, *Faraday Discuss.* **2007**, 135, 43–54; c) Kohout, M.: Electron pairs in position space. *Struct. Bond.* **2016**, 170, 119–168; d). Kohout, M., Pernal, K., Wagner, F.R., Grin, Y.: Electron localizability indicator for correlated wavefunctions. I parallel-spin pairs. *Theor. Chem. Acc.* **2004**, 112, 453–459; e) Kohout, M., Pernal, K., Wagner, F.R., Grin, Y.: Electron localizability indicator for correlated wavefunctions. II antiparallel-spin pairs. *Theor. Chem. Acc.* **2005**, 113, 287–293.
- [47] F. Weinhold, C. R. Landis, *Valency and Bonding: A Natural Bond Orbital Donor-Acceptor Perspective* (Cambridge University Press, **2005**), 760pp.

- [48] NBO 6.0. E. D. Glendening, J. K. Badenhoop, A. E. Reed, J. E. Carpenter, J. A. Bohmann, C. M. Morales, C. R. Landis, and F. Weinhold, Theoretical Chemistry Institute, University of Wisconsin, Madison **2013**.
- [49] M. Kohout, DGrid, version 5.0, Dresden, **2017**.
- [50] Gaussian 09, Revision D.01, M. J. Frisch, G. W. Trucks, H. B. Schlegel, G. E. Scuseria, M. A. Robb, J. R. Cheeseman, G. Scalmani, V. Barone, G. A. Petersson, H. Nakatsuji, X. Li, M. Caricato, A. Marenich, J. Bloino, B. G. Janesko, R. Gomperts, B. Mennucci, H. P. Hratchian, J. V. Ortiz, A. F. Izmaylov, J. L. Sonnenberg, D. Williams-Young, F. Ding, F. Lipparini, F. Egidi, J. Goings, B. Peng, A. Petrone, T. Henderson, D. Ranasinghe, V. G. Zakrzewski, J. Gao, N. Rega, G. Zheng, W. Liang, M. Hada, M. Ehara, K. Toyota, R. Fukuda, J. Hasegawa, M. Ishida, T. Nakajima, Y. Honda, O. Kitao, H. Nakai, T. Vreven, K. Throssell, J. A. Montgomery, Jr., J. E. Peralta, F. Ogliaro, M. Bearpark, J. J. Heyd, E. Brothers, K. N. Kudin, V. N. Staroverov, T. Keith, R. Kobayashi, J. Normand, K. Raghavachari, A. Rendell, J. C. Burant, S. S. Iyengar, J. Tomasi, M. Cossi, J. M. Millam, M. Klene, C. Adamo, R. Cammi, J. W. Ochterski, R. L. Martin, K. Morokuma, O. Farkas, J. B. Foresman, and D. J. Fox, Gaussian, Inc., Wallingford CT, **2016**.
- [51] Neese, F.; "Software update: the ORCA program system, version 4.0" *WIREs Comput Mol Sci* **2017**, e1327.





## 4 [Co@Sn<sub>6</sub>Sb<sub>6</sub>]<sup>3-</sup>: An Off-Center Endohedral 12-Vertex Cluster



The NMR spectroscopic investigations were performed by Florian Hastreiter. The theoretical calculations were performed by Kevin Reiter and Florian Weigend. The synthesis and characterization of the solids were performed by Robert J. Wilson. The preparation of the organometallic cobalt precursor and of the samples were carried out by Phillip Büschelberger.

---

Robert J. Wilson,<sup>[a]</sup> Florian Hastreiter,<sup>[b]</sup> Kevin Reiter,<sup>[c]</sup> Philipp Büschelberger,<sup>[d]</sup> Robert Wolf,<sup>[d]</sup> Ruth M. Gschwind,<sup>[b]</sup> Florian Weigend,<sup>[c]</sup> and Stefanie Dehnen\*<sup>[a]</sup>

*Angew. Chem. Int. Ed.* **2018**, *57*, 15359-15363.

DOI:10.1002/anie.201807180

© 2018 Wiley-VCH Verlag GmbH & Co. KGaA. Reproduced with permission.

## 4.1 Abstract

We report on the asymmetric occupation of a 12-vertex cluster centered by a single metal atom. Three salts of related intermetalloid cluster anions, [Co@Sn<sub>6</sub>Sb<sub>6</sub>]<sup>3-</sup> (**1**), [Co<sub>2</sub>@Sn<sub>5</sub>Sb<sub>7</sub>]<sup>3-</sup> (**2**), and [Ni<sub>2</sub>@Sn<sub>7</sub>Sb<sub>5</sub>]<sup>3-</sup> (**3**) were synthesized, which have *pseudo-C*<sub>4v</sub>-symmetric or *pseudo-D*<sub>4h</sub>-symmetric 12-vertex Sn/Sb shells and interstitial Co<sup>-</sup> ions or Ni atoms. Anion **1** is a very unusual single-metal-“centered” 12-atom cluster, with the inner atom being clearly offset from the cluster center for energetic reasons. Quantum chemistry served to assign atom types to the atomic positions and relative stabilities of this cluster type. The studies indicate that the structures are strictly controlled by the total valence electron count – which is particularly variable in ternary intermetalloid cluster anions. Preliminary <sup>119</sup>Sn NMR studies in solution, supported by quantum-chemical calculations of the shifts, illustrate the complexity regarding Sn:Sb distributions of such ternary systems.

## 4.2 Introduction

The anion [Pt@Pb<sub>12</sub>]<sup>2-</sup> was the first fully characterized example of a ligand-free cluster composed of p-block element atoms with a transition-metal at its center.<sup>[1]</sup> This anion, and the subsequently isolated [M@Pb<sub>12</sub>]<sup>2-</sup> (M = Ni, Pd) and [Ir@Sn<sub>12</sub>]<sup>3-</sup>,<sup>[2]</sup> are in many ways the archetypes of so-called “endohedral intermetalloid clusters”. They have near-perfect icosahedral (*I*<sub>h</sub>) symmetry, the bonding within the clusters’ shells is electron deficient (< 2 e<sup>-</sup>/edge) and highly delocalized, and the inner transition metal atoms formally contribute no electron density to the p-block element shells, which have 50 total valence electrons (Figure 1, left). In stark contrast to [Pt@Pb<sub>12</sub>]<sup>2-</sup>, the 12-vertex intermetalloid clusters [Ru@Ge<sub>12</sub>]<sup>3-</sup> and [M@Ge<sub>8</sub>As<sub>4</sub>]<sup>3-</sup> (M = V, Ta) have much lower (*pseudo*-)*D*<sub>2d</sub> symmetry,<sup>[3]</sup> electron-precise (2 e<sup>-</sup>) cluster-shell bonds, and inner transition metal atoms that formally donate their valence electrons to the cluster shell orbitals.<sup>[4]</sup> Thus the cluster shells of [Ru@Ge<sub>12</sub>]<sup>3-</sup> and [M@Ge<sub>8</sub>As<sub>4</sub>]<sup>3-</sup> have 59 and 60 valence electrons, respectively (Figure 1, right). Between these two extremes is [Mn@Pb<sub>12</sub>]<sup>3-</sup>, in which the Mn atom formally transfers some, but not all, of its valence electrons to the 12-vertex shell, causing a distortion from *I*<sub>h</sub> to *D*<sub>2h</sub> (Figure 1, center).<sup>[5]</sup> The geometric variation in 12-vertex intermetalloid clusters was investigated by means of comprehensive theoretical studies, which showed a trend of increasing delocalization of d-orbital electron density onto the main group cluster shell going from late to early transition metals.<sup>[6]</sup>

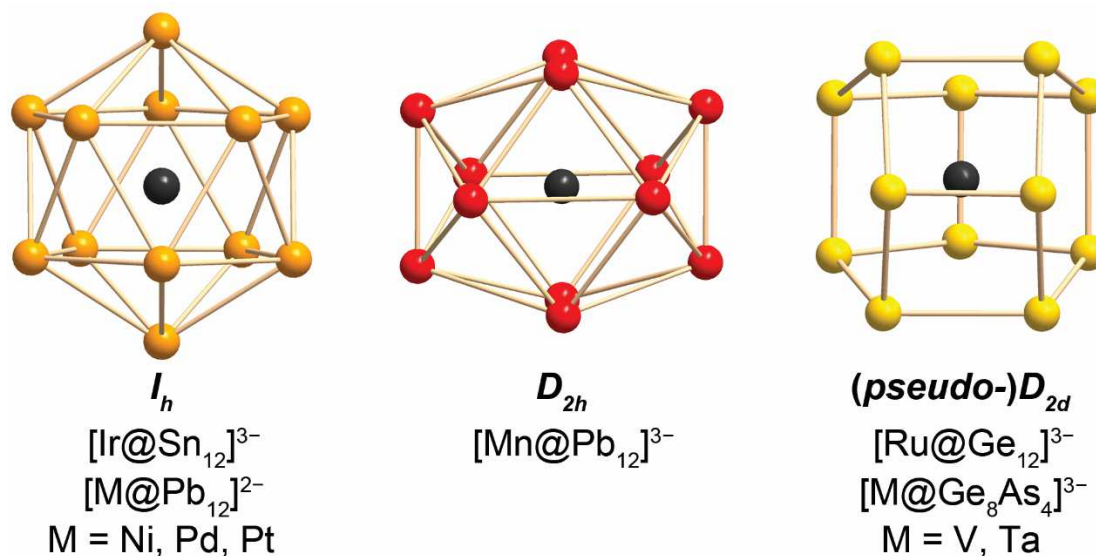


**Figure 1.** Examples of structurally characterized 12-vertex intermetalloid clusters with a single encapsulated transition metal atom, which have been identified with the point symmetries  $I_h$ ,<sup>[1-2]</sup>  $D_{2h}$ ,<sup>[5]</sup> and  $(\text{pseudo-})D_{2d}$ .<sup>[3, 4b,c]</sup>

Intermetalloid clusters with 12-vertices that contain two inner metal atoms have also been structurally characterized. The reactions of  $[\text{K}(\text{crypt-222})]_2(\text{E}_2\text{Bi}_2)$  ( $\text{E} = \text{Sn}, \text{Pb}$ ) with  $\text{Ni}(\text{cod})_2$  in *en* afforded  $[\text{K}(\text{crypt-222})]_3[\text{Ni}_2@\text{E}_7\text{Bi}_5]$ .<sup>[7]</sup> The anions in these salts have *pseudo- $D_{4h}$*  geometries, in which two (formal)  $\text{Ni}^0$  atoms occupy the centers of two square antiprisms that share a 4-atom face. The  $(\text{E}_7\text{Bi}_5)^{3-}$  cluster shells have a total of 56 valence electrons, and their bonding can be described as consisting of a combination of two-center and three-center bonds, while the inner Ni atoms achieve an 18 electron situation.<sup>[7b]</sup>

We recently reported that  $[\text{K}(\text{crypt-222})]_2(\text{Sn}_2\text{Sb}_2)$  reacts with  $[\text{LCu}(\text{NCMe})]$  ( $\text{L} = \text{nacnac} = [(\text{N}(\text{C}_6\text{H}_3\text{Pr}_{2-2,6})\text{C}(\text{Me}))_2\text{CH}]^-$ ) in either 1,2-diaminoethane (*en*) or dimethylformamide (DMF) to afford the dimer  $[(\text{CuSn}_5\text{Sb}_3)_2]^{4-}$  as the  $[\text{K}(\text{crypt-222})]^+$  salt.<sup>[8]</sup> In this anion, the  $\text{Cu}^+$  ions are not in endohedral positions, but rather are incorporated into the shells of the cluster monomers.  $\text{Cu}$ ,<sup>[8-9]</sup>  $\text{Ni}$ <sup>[2a, 7, 10]</sup> and  $\text{Co}$ <sup>[11]</sup> atoms generally have  $d^{10}$  electron configurations when incorporated into intermetalloid clusters. In light of this, we have now also probed the reactivity of  $[\text{K}(\text{crypt-222})]_2(\text{Sn}_2\text{Sb}_2)$  with  $\text{Ni}(\text{cod})_2$  and  $[\text{Co}(\text{cod})_2]^-$  to ascertain how the formal charges of the three  $d^{10}$  metal atoms or ions ( $\text{Cu}^+$ ,  $\text{Ni}^0$ ,  $\text{Co}^-$ ) affect the structures of the product  $\text{M}/\text{Sn}/\text{Sb}$  ternary clusters.

From these investigations, we can now report the syntheses, structural and spectroscopic characterization, and theoretical investigation of three new 12-vertex intermetalloid clusters,  $[\text{Co}@\text{Sn}_6\text{Sb}_6]^{3-}$  (**1**, CCDC 1850710),  $[\text{Co}_2@\text{Sn}_5\text{Sb}_7]^{3-}$  (**2**, CCDC 1850711), and  $[\text{Ni}_2@\text{Sn}_7\text{Sb}_5]^{3-}$  (**3**, CCDC 1850709) (Figure 2, Figures S2-S8). According to their compositions, which were rationalized by means of electrospray ionization mass spectrometry (ESI-MS) and micro-X-ray fluorescence spectroscopy ( $\mu$ -XFS) (see below

and Supporting Information), the Sn/Sb shells of all three clusters have valence electron counts of 56, but with different element ratios that reflect the formal charges of the inner transition metal atoms. A total cluster charge of  $-3$  appears to be favored owing to the requirements of crystallization with [K(crypt-222)]<sup>+</sup> cations. Anions **2** and **3** are isoelectronic and isostructural with both each other and the aforementioned Bi-containing clusters, [Ni<sub>2</sub>@E<sub>7</sub>Bi<sub>5</sub>]<sup>3-</sup> (E = Sn, Pb),<sup>[7]</sup> as well as a related polycation, [Ni<sub>2</sub>@Bi<sub>12</sub>]<sup>4+</sup>.<sup>[12]</sup> Anion **1**, however, possesses the same basic fused square-antiprism structure,<sup>[13]</sup> yet notably with only one 8-atom “pocket” occupied. It is therefore unprecedented, in that no other 12-vertex cluster with a single inner metal atom adopts an oblong geometry where the transition metal is offset from the center. Co-centered intermetaloid clusters with one or two inner transition metal atom(s), for example, [Co@Sn<sub>9</sub>]<sup>4-</sup> and [Co<sub>2</sub>@Ge<sub>16</sub>]<sup>4-</sup>, have been reported; however, all such examples have symmetrically centered geometries.<sup>[11]</sup> With **2** providing a convenient comparison, we explore here the unusual structure of cluster **1** using density functional theory (DFT) calculations (which also served to identify the most stable atom distribution within the structures) and attempt to probe its solution stability using <sup>119</sup>Sn NMR spectroscopy.

### 4.3 Results and Discussion

The [Co@Sn<sub>6</sub>Sb<sub>6</sub>]<sup>3-</sup> (**1**) and [Co<sub>2</sub>@Sn<sub>5</sub>Sb<sub>7</sub>]<sup>3-</sup> (**2**) anions co-crystallized in the salt [K(crypt-222)]<sub>3</sub>**1**<sub>0.83</sub>**2**<sub>0.17</sub>·2dmf·2tol, which formed over the course of several months from a solution of [K(crypt-222)]<sub>2</sub>(Sn<sub>2</sub>Sb<sub>2</sub>)·en, [K(thf)<sub>x</sub>][Co(cod)<sub>2</sub>],<sup>[14]</sup> and crypt-222 in DMF and toluene at 5 °C (note: the product crystallizes alongside some residual [K(crypt-222)]<sub>2</sub>(Sn<sub>2</sub>Sb<sub>2</sub>), see SI for details). The two anions are statistically disordered on the same position in the unit cell and the two possible orientations of anion **1** are evenly represented. This results in a partially occupied cobalt site ( $\approx 59\%$ ), an unreasonably short (virtual) Co–Co distance (2.246(4) Å), and disorder along the 4-atom ring, which makes up the cluster “waist” (Figure S2). The occupancy of the cobalt position was used to estimate the relative abundance of the anions. Analysis of a DMF solution of the salt by ESI-MS revealed mass envelopes for the monoanions [CoSn<sub>6</sub>Sb<sub>6</sub>]<sup>-</sup> and [Co<sub>2</sub>Sn<sub>5</sub>Sb<sub>7</sub>]<sup>-</sup>, with the former being notably more abundant than the latter in the mass spectrum (Figure 3a). Thus the mass spectrometric data perfectly confirms the compositions of both **1** and **2** and qualitatively supports that **1** is more abundant than **2**, assuming that these closely related cluster anions have similar ionization efficiencies.<sup>[15]</sup>

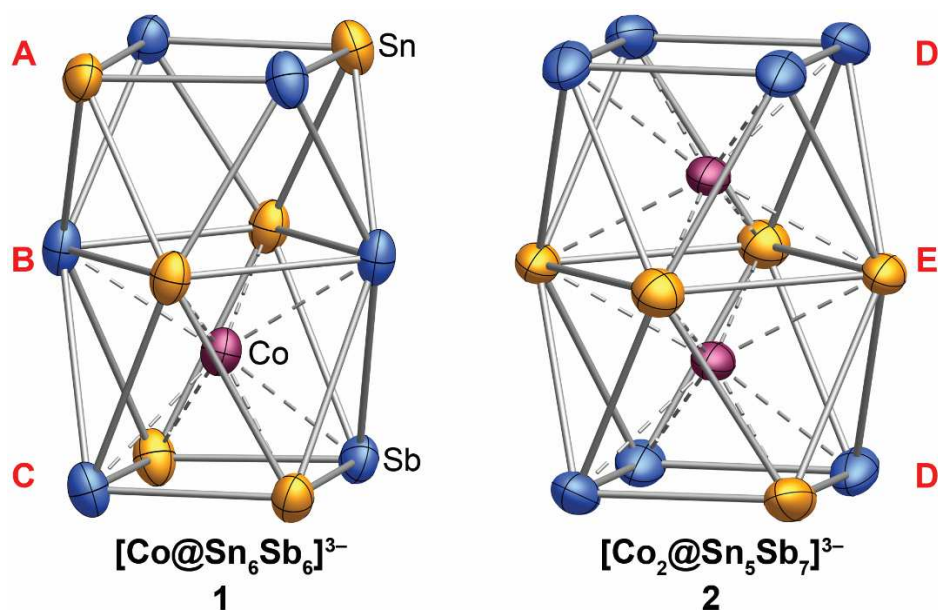


**Figure 2.** The structures of anion **1** in  $[\text{K}(\text{crypt-222})]_3\mathbf{1}_{0.83}\mathbf{2}_{0.17}\cdot 2\text{dmf}\cdot 2\text{tol}$  (left) and anion **2** in  $[\text{K}(\text{crypt-222})]_3\mathbf{2}$  (right). For clarity, the disorder in anion **1** has been omitted and atoms are colored to represent the most probable isomers deduced from comprehensive DFT calculations (see text and Supporting Information). Thermal ellipsoids are drawn at 50% probability. Atom colors are as follows: Co, violet; Sn, orange; Sb, blue. The letters A – E refer to the Sn/Sb atomic positions in the corresponding horizontal four-membered rings. Average interatomic distances for **1** and **2** [Å(std. dev.)]: A/C–A/C 2.867(4), B–B 3.144(35), A–B 3.065(20), B–C 3.450(17), Co–B 2.599(10), Co–C 2.640(11), D–D 2.885(3), E–E 3.298(10), D–E 3.253(14), Co–D 2.575(10), Co–E 2.626(11), Co–Co 2.411(2). Average interatomic distances for **3** (see Supporting Information for structure) [Å(std. dev.)]: D–D 2.897(4), E–E 3.264(27), D–E 3.275(19), Ni–D 2.595(12), Ni–E 2.609(5), Ni–Ni 2.432(2).

While the isolation of  $[\text{K}(\text{crypt-222})]_3\mathbf{1}_{0.83}\mathbf{2}_{0.17}\cdot 2\text{dmf}\cdot 2\text{tol}$  provided a reasonable crystallographic structure of **1** (Figure 2, left), it did not provide a satisfying structure of the minor component **2**. We were able to achieve the exclusive characterization of anion **2**, however, by carrying out the same reaction in a mixture of en and DMF at 60 °C. After less than 24 h, a black powder was precipitated by the fast addition of toluene. ESI-MS analysis of a filtered DMF solution of this powder indicated the presence of  $[\text{Co}_2\text{Sn}_5\text{Sb}_7]^-$  (Figure 3b) and  $[\text{CoSn}_6\text{Sb}_3]^-$  (Figure S15) as the overwhelming majority of the dissolved sample. Tandem MS suggested that the latter was derived from the former, as  $[\text{CoSn}_6\text{Sb}_3]^{2-}$  was the main fragmentation product of  $[\text{Co}_2\text{Sn}_5\text{Sb}_7]^-$  (Figures S16 and S17). A few black crystals of the salt  $[\text{K}(\text{crypt-222})]_3\mathbf{2}$  suitable for X-ray diffraction were grown from a filtered en solution of the powder (see Supporting Information for details), allowing us to structurally characterize **2** (Figure 2, right). The yields of these recrystallizations were, however, extremely poor. We have therefore used filtered DMF solutions of the powder product as a means of accessing  $[\text{K}(\text{crypt-222})]_3\mathbf{2}$  in the quantities required for  $^{119}\text{Sn}$  NMR analysis (see below).

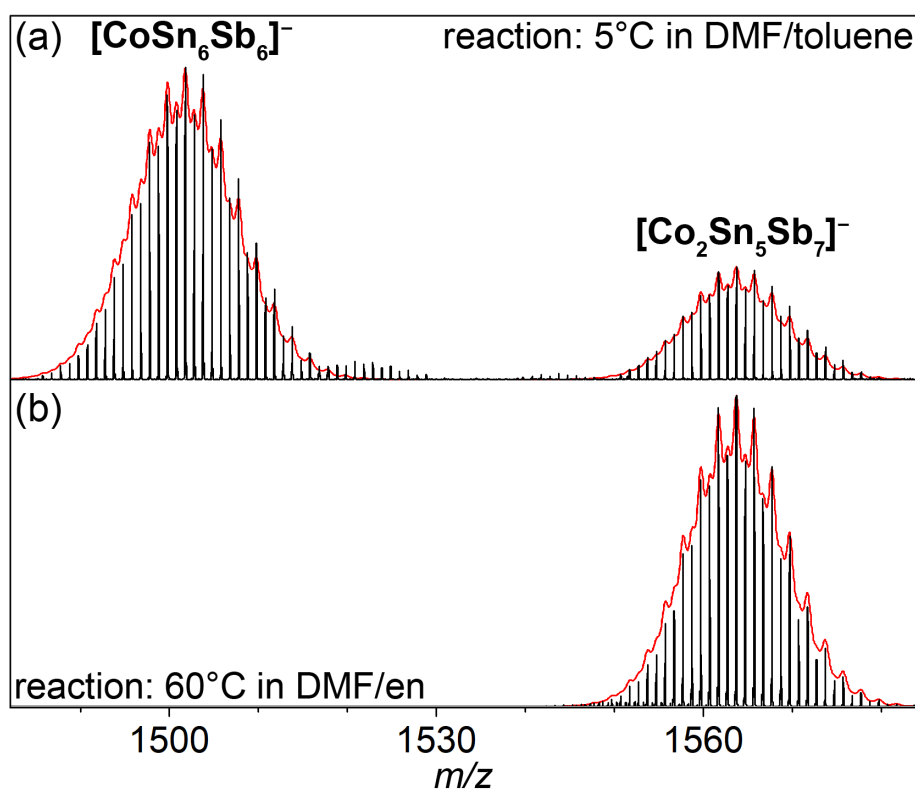


**Figure 3.** Segments of the high-resolution ESI mass spectra (negative ion mode; black lines) recorded from DMF solutions of (a)  $[\text{K}(\text{crypt-222})]_3[\text{Co@Sn}_6\text{Sb}_6]_{0.83}[\text{Co}_2\text{@Sn}_5\text{Sb}_7]_{0.17} \cdot 2\text{dmf} \cdot 2\text{tol}$  crystallized from DMF/toluene at 5 °C and (b) the crude powder obtained by heating the reactants at 60 °C in a mixture of en and DMF overnight and rapid addition of toluene (see Supporting Information for details). The red lines are simulated mass envelopes for  $[\text{CoSn}_6\text{Sb}_6]^-$  (left) and  $[\text{Co}_2\text{Sn}_5\text{Sb}_7]^-$  (right). Detailed analyses of mass spectra are contained in the Supporting Information.

A similar reaction performed with the known nickel precursor  $[\text{Ni}(\text{cod})_2]$  yielded  $[\text{Ni}_2\text{@Sn}_7\text{Sb}_5]^{3-}$  (**3**) as the  $[\text{K}(\text{crypt-222})]^+$  salt, structurally characterized as  $[\text{K}(\text{crypt-222})]_3\mathbf{3} \cdot 2\text{en} \cdot 2\text{tol}$ . It was isolated from a solution of the reactants in en and toluene at 5 °C (Figure S7 and S8). Despite the differences in composition, the structure of **3** is very similar to that of **2**, therefore details are not discussed here (see Supporting Information). However, the compound was important as a benchmark; notably, a high-temperature reaction, similar to that discussed above for **2**, produced a relatively clean powder of the compound (see Figures S21 and S30 for the ESI-MS and  $^{119}\text{Sn}$  NMR spectra) in high yield.

As noted above, the observed topology for **1** with the inner atom clearly offset from the cluster center is unusual at first glance; from previous investigations one might rather have expected one of the types shown in Figure 1. Thus, we first carried out a systematic search of energetically lowest lying minima for **1** in order to estimate the energetic distance from the observed to other topologies. This was done with a genetic algorithm extended by atom-type assignment via perturbation theory.<sup>[16]</sup> Within this algorithm, the individual optimizations were carried out at density functional level (the number of generations was

set to 30, the size of each generation to 25; in each generation the 13 energetically least favorable structures were replaced with newly generated ones; for further details see Supporting Information). The 25 isomers in the last generations of evolution all show the experimentally found *pseudo-C<sub>4v</sub>* topology of two fused square-antiprisms, distorted to various degrees for some of the energetically higher isomers. They differ only in the Sn/Sb distribution throughout. The same is observed for analogous treatments carried out for **2** and **3**. The energy ranges spanned by the respective 25 isomers of **1**, **2**, and **3** in the corresponding final populations amount to 37, 22, and 61 kJ·mol<sup>-1</sup>, respectively. The energetically most favorable isomers for the three compositions are shown in Figure 4a (for **1**, two almost isoenergetic isomers are found).

Calculated natural atomic charges<sup>[17]</sup> for the Co atoms in **1** and **2** are -1.32 to -1.35, respectively, whereas the value for the Ni atoms in **3** is -0.33. This supports the assumption that the cobalt atoms are formally Co<sup>-</sup> anions, isoelectronic with Ni<sup>0</sup>. Thus, all three observed Sn/Sb cages may be regarded as 56 valence electron species. We further note the excellent agreement between the measured and the geometry-optimized structures (Table S5, maximum deviations of calculated bond lengths from measured ones: -0.090/+0.048 Å for **1**, -0.004/+0.024 Å for **2**, -0.054/0.068 for **3**, the greater deviation in calculated and measured bond lengths for **1** may be a product of the whole cluster disorder in [K(crypt- 222)]<sub>3</sub>**1**<sub>0.83</sub>**2**<sub>0.17</sub>·2dmf·2tol). The external (Sn<sub>6±1</sub>Sb<sub>6±1</sub>)<sup>(2±1)-</sup> cages with *pseudo-D<sub>4h</sub>* topology are obviously very favorable, even if one “pocket” is not filled with a transition metal atom, as in **1** (→*pseudo-C<sub>4v</sub>* symmetry). This becomes even more evident when starting structure optimizations of **1** from typical representatives of centered 12-atomic species for all symmetry-distinct Sn/Sb distributions of each topology, like *pseudo-I<sub>h</sub>* (12 isomers), *pseudo-D<sub>5h</sub>* (58), *pseudo-D<sub>2d</sub>* (111), *pseudo-D<sub>6d</sub>* (35), *pseudo-D<sub>6h</sub>* (44) and *pseudo-O<sub>h</sub>* (15). The resulting most favorable structures (Figure 4b) are higher in energy than **1b** by 48 to 118 kJ·mol<sup>-1</sup>, and moreover strongly distorted in most cases. This underscores the point that it is the number of valence electrons, and not (only) the number of vertices, that determines cluster geometry, such as discussed in the recent study by Goicoechea and McGrady on related binary cluster anions.<sup>[6]</sup> To confirm this, we also investigated the effects of small changes in the valence electron count of **1** on its structure, which is detailed in the Supporting Information (Figure S33).

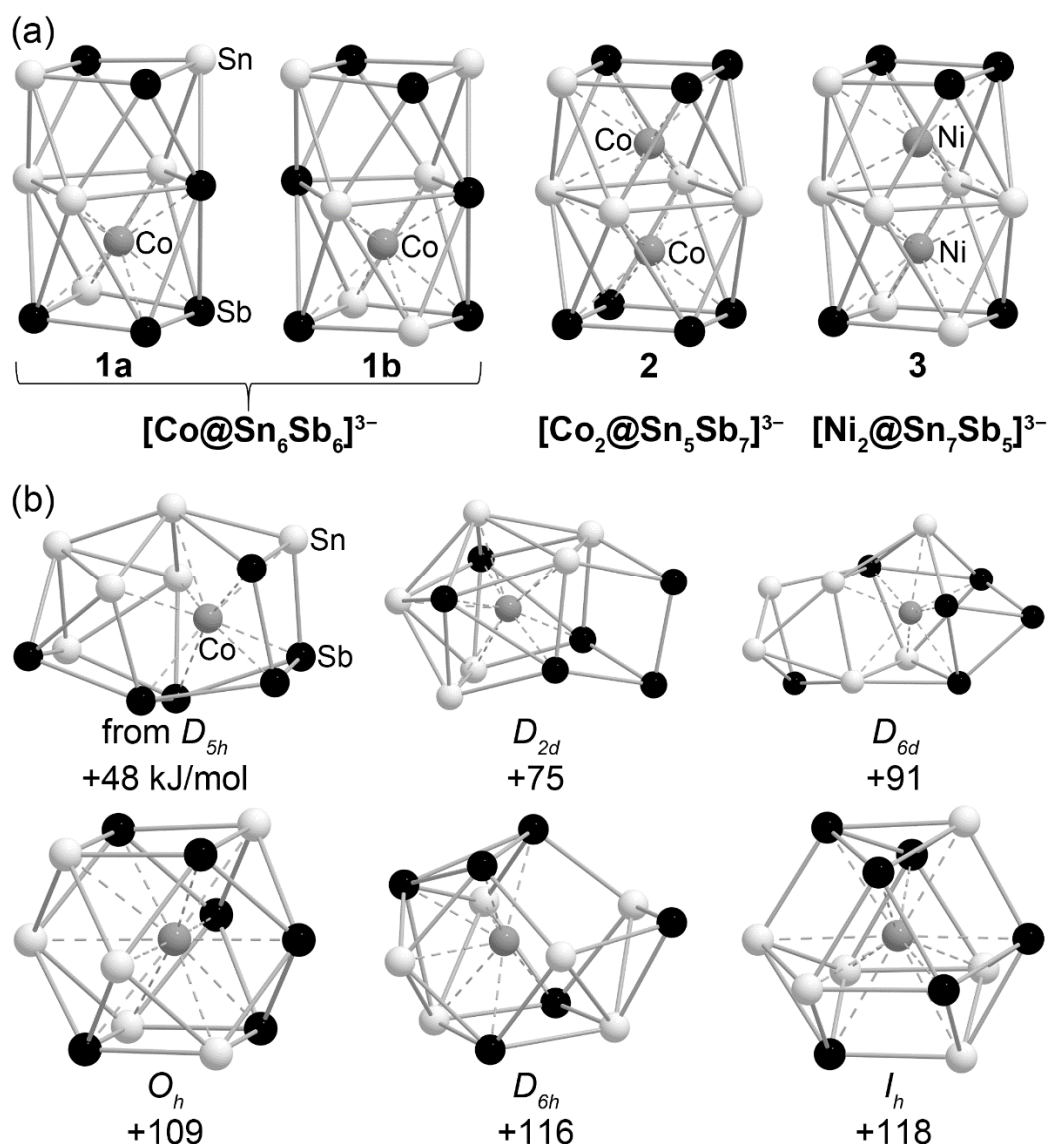


**Figure 4.** a) Lowest energy isomers of anions **1** – **3** (point group symmetry  $C_1$  for **1a**, **2**, **3**, and  $C_2$  for **1b**). Sb atoms are drawn as black, Sn as light gray, and Co as dark gray. **1b** and **1a** are almost isoenergetic ( $\Delta E = 2$  kJ·mol<sup>-1</sup> in favor of **1a**). b) Most stable structures of  $[\text{Co}@_{\text{Sn}_6\text{Sb}_6}]^{3-}$  resulting from optimizations starting from (*pseudo*-)symmetries  $D_{5h}$ ,  $D_{2d}$ ,  $D_{6d}$ ,  $O_h$ ,  $D_{6h}$ , and  $I_h$ . Energies are relative to **1b**.

According to the calculations, the uncommon and unexpected fused square-antiprism structure of **1**, with one occupied and one unoccupied “pocket”, is hence formed for two key reasons. 1) The total electron count needs to fit with a total charge of  $-3$ , such as found for most ternary intermetallic clusters of this size. 2) With 12 shell atoms around an interstitial Co atom, reasonably stable cages result with 50 ( $I_h$ -type topology), 54 (distorted  $C_{2v}$ -type topology), and 56 valence electrons ( $C_{4v}$ -type topology), which for a  $-3$  charge and even electron numbers are realized with Sn:Sb compositions of 12:0, 8:4, or 6:6, respectively (see Supporting Information for the former two); apparently, the maximization of heteroatomic bonds leads to a strong preference of the formation of the



6:6 variant, hence negating the (theoretical) possibility of forming a 50 electron *closo* cluster upon release of all Sb atoms from the system. This further illustrates the distinct difference of using a binary precursor, the decomposition of which is accompanied by a loss of heteroatomic bond energy, from to the use of a homoatomic precursor anion.

To gain further insight into the behavior and stability of clusters **1** and **2** in solution, we performed the first  $^{119}\text{Sn}$  NMR measurements on such ternary clusters, in combination with thorough DFT calculations of the chemical shifts.<sup>[18]</sup> For consistency, the NMR spectra were recorded on fresh solutions prepared analogously to those used for the ESI-MS studies – that is, from single crystals of  $[\text{K}(\text{crypt-222})]_3\mathbf{1}_{0.83}\mathbf{2}_{0.17}\cdot 2\text{dmf}\cdot 2\text{tol}$  along with the co-crystallizing precursor on one hand, and the precipitate comprising cluster **2** and the  $[\text{CoSn}_6\text{Sb}_3]^{9-}$  species mentioned above, on the other hand (see Figures S26-S29).

Indeed, we observe a set of resonances ( $\delta = -635, -857, -879$  ppm), which occurs in the spectra of both samples and is therefore most likely assigned to the different Sn positions in cluster **2**. This is further corroborated by the shift pattern calculated for all possible Sn:Sb distributions within  $[\text{Co}_2@\text{Sn}_5\text{Sb}_7]^{3-}$  (upon averaging shifts of Sn positions in the outer rings and the equatorial ring, respectively), which suggests that the signals for the outer ring atoms should appear significantly upfield of those of the inner ring (see Tables S8 and S9). The calculations on the other hand indicate that it is difficult to unambiguously assign the signals of cluster **1** owing to additional signals that we attribute either to species which form upon the oxidation of the co-crystallized precursor ( $\delta = -1606$  ppm, see Figure S26-S28), or to as-of-yet unidentified impurities or decomposition products. We note that the ESI-MS spectrum of the sample containing **1** (Figure S9) was significantly more complex than that of the powder containing **2** (Figure S15), and the NMR data suggests that some of these signals are the result of reactions prior to injection (and not just upon fragmentation by ionization). Because of this uncertainty, the present data is discussed here as preliminary results only, further illustrating the high complexity of the clusters with their different Sn positions, as well as the array of possible Sn:Sb distributions, which distinguishes these systems from known binary cases.<sup>[1,2,9-9,19-21]</sup> Further studies on ternary clusters are thus planned to augment our knowledge of their properties in solution with the goal of using NMR for fingerprint detection of these uncommon species.

#### 4.4 Conclusions

In conclusion, we have presented here the synthesis and characterization of three new ternary intermetalloid clusters, [Co@Sn<sub>6</sub>Sb<sub>6</sub>]<sup>3-</sup> (**1**), [Co<sub>2</sub>@Sn<sub>5</sub>Sb<sub>7</sub>]<sup>3-</sup> (**2**), and [Ni<sub>2</sub>@Sn<sub>7</sub>Sb<sub>5</sub>]<sup>3-</sup> (**3**), the first of which is an unusual case of an endohedral 12-vertex cage in which the single inner metal atom does not occupy a position at the center of the cluster. DFT calculations revealed no other viable structures with similar stoichiometries. The fact that **2** was obtained both in a mixture with **1**, and in an isolated form, along with high-level DFT calculations of the chemical shifts, prompted us to perform first <sup>119</sup>Sn NMR studies of this exceptionally complicated case, which will be intensified in future work.

## 4.5 Supporting Information

### 4.5.1 Experimental

#### 4.5.1.1 General considerations

All reactions were performed in an argon atmosphere using Schlenk techniques or a glovebox. Ethane-1,2-diamine (en) and N,N-dimethylformamide (DMF) (Aldrich, 99.8%) were distilled from CaH<sub>2</sub> and stored over 3 Å molecular sieves. Toluene (Acros Organics, 99%) was distilled from sodium-potassium alloy and stored over 3 Å molecular sieves. Crypt-222<sup>[21]</sup> (Merck) was dried under vacuum overnight. [K(crypt-222)]<sub>2</sub>(Sn<sub>2</sub>Sb<sub>2</sub>)·en was crystallized by concentration of a 2:1 en solution of crypt-222 and K<sub>2</sub>SnSb. K<sub>2</sub>SnSb was prepared by stoichiometric fusion of the elements at 950 °C for 48 hours in a niobium tube, sealed within an evacuated silica ampule. [K(thf)<sub>x</sub>][Co(cod)<sub>2</sub>] was prepared according to a modified literature procedure.<sup>[22]</sup>

#### 4.5.1.2 Synthesis of compounds

##### **[K(crypt-222)]<sub>3</sub>[Co@Sn<sub>6</sub>Sb<sub>6</sub>]<sub>0.825</sub>[Co<sub>2</sub>@Sn<sub>5</sub>Sb<sub>7</sub>]<sub>0.175</sub>·2dmf·2tol.**

[K(crypt-222)]<sub>2</sub>(Sn<sub>2</sub>Sb<sub>2</sub>)·en (100 mg, 73 μmol), [K(thf)<sub>0.15</sub>][Co(cod)<sub>2</sub>] (24 mg, 73 μmol), and crypt-222 (30 mg, 80 μmol) were combined in a Schlenk tube and dissolved in 2.5 ml of DMF. After stirring for 2 h, the dark red-brown solution was filtered through fritted glass and layered with 5 mL of toluene. The sample was stored at -5 °C. Red crystals of the precursor, [K(crypt-222)]<sub>2</sub>(Sn<sub>2</sub>Sb<sub>2</sub>)·en, were identified after 50 d by unit cell match (though they were visible much earlier), after which the sample was stored at 5 °C. After a further 100 d (150 d total), black crystals of [K(crypt-222)]<sub>3</sub>[Co@Sn<sub>6</sub>Sb<sub>6</sub>]<sub>0.825</sub>[Co<sub>2</sub>@Sn<sub>5</sub>Sb<sub>7</sub>]<sub>0.175</sub>·2dmf·2tol (Figure S1) had formed on the walls of the tube. After characterization by SC-XRD (Section 2.2), the remaining crystals were isolated and dried under high vacuum to afford 31 mg of product mixed with some residual [K(crypt-222)]<sub>2</sub>(Sn<sub>2</sub>Sb<sub>2</sub>)·en, as indicated by <sup>119</sup>Sn NMR (Figures S26-S28).

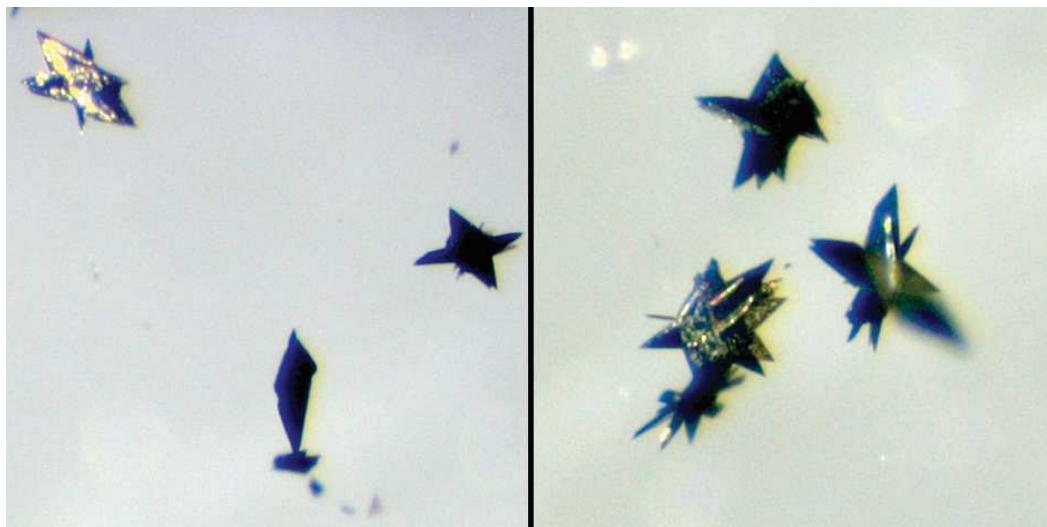


**Figure S1.** Crystals of [K(crypt-222)]<sub>3</sub>[Co@Sn<sub>6</sub>Sb<sub>6</sub>]<sub>0.825</sub>[Co<sub>2</sub>@Sn<sub>5</sub>Sb<sub>7</sub>]<sub>0.175</sub>·2dmf·2tol.

**[K(crypt-222)]<sub>3</sub>[Co@Sn<sub>6</sub>Sb<sub>6</sub>]<sub>0.825</sub>[Co<sub>2</sub>@Sn<sub>5</sub>Sb<sub>7</sub>]<sub>0.175</sub>·2dmf·2tol (2nd synthesis).**

[K(crypt-222)]<sub>2</sub>(Sn<sub>2</sub>Sb<sub>2</sub>)·en (100 mg, 73 μmol), [K(thf)<sub>0.15</sub>][Co(cod)<sub>2</sub>] (24 mg, 73 μmol), and crypt-222 (30 mg, 80 μmol) were combined in a Schlenk tube, dissolved in 2.5 ml of DMF, and stirred for 18 h. The resulting dark red-brown solution was heated to 60 °C for 3 h, filtered through fritted glass, layered with 5 mL of toluene, and then stored at 5 °C. Red crystals of the precursor salt, [K(crypt-222)]<sub>2</sub>(Sn<sub>2</sub>Sb<sub>2</sub>)·en, were identified visually after a week. After 135 d, some black crystals 4 of [K(crypt-222)]<sub>3</sub>[Co@Sn<sub>6</sub>Sb<sub>6</sub>]<sub>0.825</sub>[Co<sub>2</sub>@Sn<sub>5</sub>Sb<sub>7</sub>]<sub>0.175</sub>·2dmf·2tol had formed. A full SC-XRD dataset was collected and solved to ensure that the product was identical to the previous sample. The sample was stored at 5 °C for a further 60 d (185 d total) to allow for conversion of remaining [K(crypt-222)]<sub>2</sub>(Sn<sub>2</sub>Sb<sub>2</sub>)·en, after which the black crystals were isolated, washed with toluene (2 × 2.5 mL), and dried under high vacuum to afford 19 mg of product mixed with some residual crystals of [K(crypt-222)]<sub>2</sub>(Sn<sub>2</sub>Sb<sub>2</sub>)·en. That the two syntheses produced identical products was additionally confirmed by <sup>119</sup>Sn NMR (Figure S27).

**[K(crypt-222)]<sub>3</sub>[Co<sub>2</sub>@Sn<sub>5</sub>Sb<sub>7</sub>] (crude synthesis).**

[K(crypt-222)]<sub>2</sub>(Sn<sub>2</sub>Sb<sub>2</sub>)·en (206 mg, 150 μmol), [K(thf)<sub>0.15</sub>][Co(cod)<sub>2</sub>] (50 mg, 150 μmol), and crypt-222 (60 mg, 159 μmol) were combined in a Schlenk tube, dissolved in 2 ml of DMF and 2 mL of en, after which the dark red solution was stirred for 18 h at 60 °C. The resulting black solution was cooled for 1 h, after which 45 mL of toluene was added and the sample was stirred vigorously. The black precipitate was allowed to settle, and was then isolated and washed with successive aliquots of toluene (3 × 5 mL) and dried to afford 70 mg of a fine black powder. For subsequent analytical measurements, the powder was dissolved in DMF and filtered through a PTFE filter with a pore size of 0.45 μm to remove any elemental material. ESI(-) mass spectrometry (Section 3.3) showed only two significant mass envelopes for [Co<sub>2</sub>@Sn<sub>5</sub>Sb<sub>7</sub>]<sup>-</sup> and [Co@Sn<sub>6</sub>Sb<sub>3</sub>]<sup>-</sup>, the latter of which (after the loss of one electron) was shown by tandem mass spectrometry (Figure S16) to be the primary fragmentation product of the former. <sup>119</sup>Sn NMR (Figure S26) indicated that [K(crypt-222)]<sub>2</sub>[Co@Sn<sub>6</sub>Sb<sub>3</sub>] may also be present in the sample. Single crystals of [K(crypt-222)]<sub>3</sub>[Co<sub>2</sub>@Sn<sub>5</sub>Sb<sub>7</sub>] suitable for SC-XRD were obtained from a solution of the black powder in en, which was filtered and layered with toluene (section 2.3). However, possibly due to poor solubility in en, crystalline yields were too low to be determined.

**[K(crypt-222)]<sub>3</sub>[Ni<sub>2</sub>@Sn<sub>7</sub>Sb<sub>5</sub>]·2en·2tol.**

[K(crypt-222)]<sub>2</sub>(Sn<sub>2</sub>Sb<sub>2</sub>)·en (75 mg, 55 μmol) and [Ni(cod)<sub>2</sub>] (15 mg, 55 μmol) were combined in a Schlenk tube and dissolved in 2.5 ml of en. After stirring for 4 h, the dark red-brown solution was filtered through fritted glass, layered with 3 mL of toluene, and stored at 5 °C. After 24 d, it was noted that red crystals (possibly [K(crypt-222)]<sub>2</sub>(Sn<sub>2</sub>Sb<sub>2</sub>)·en) had formed on the walls of the tube. The sample was warmed to 35 °C for 20 h, then returned to storage at 5 °C. After a further 7 d, black crystals of [K(crypt-222)]<sub>3</sub>[Ni<sub>2</sub>@Sn<sub>7</sub>Sb<sub>5</sub>]·2en·2tol suitable for SC-XRD had formed on the wall of the tube.

**[K(crypt-222)]<sub>3</sub>[Ni<sub>2</sub>@Sn<sub>7</sub>Sb<sub>5</sub>] (crude synthesis).**

[K(crypt-222)]<sub>2</sub>(Sn<sub>2</sub>Sb<sub>2</sub>)·en (154 mg, 113 μmol) and [Ni(cod)<sub>2</sub>] (31 mg, 113 μmol) were combined in a Schlenk tube, dissolved in 1.5 ml of DMF and 1.5 mL of en, and stirred at 50 °C for 18 hours. The resulting black solution was cooled for 1 h, after which 35 mL of toluene was added and the sample stirred vigorously. The black precipitate was allowed to settle, and was then isolated and washed with successive aliquots of toluene (3 × 5 mL) and dried to afford 67 mg of a fine black powder. For subsequent analytical measurements,

the powder was dissolved in DMF and filtered through a PTFE filter with a pore size of 0.45 μm to remove any elemental material. ESI(-) mass spectrometry (Section 3.5) showed 5 four significant mass envelopes for [Ni@Sn<sub>4</sub>Sb<sub>4</sub>]<sup>-</sup>, [Ni<sub>2</sub>@Sn<sub>4</sub>Sb<sub>4</sub>]<sup>-</sup>, [HNi@Sn<sub>7</sub>Sb<sub>2</sub>]<sup>-</sup>, and [Ni<sub>2</sub>@Sn<sub>7</sub>Sb<sub>5</sub>]<sup>-</sup>. Repeated attempts to recrystallize [K(crypt-222)]<sub>3</sub> from the powder resulted in a large reduction in yield and only poor quality crystals, most likely as a result of cation and solvent disorder. The expected anion and three cations were, however, clearly visible. A filtered DMF solution of the powder was analyzed using <sup>119</sup>Sn NMR (see Figure S30).

## 4.5.2 Single Crystal X-Ray Diffraction

### 4.5.2.1 General considerations

The data sets for [K(crypt-222)]<sub>3</sub>[Co@Sn<sub>6</sub>Sb<sub>6</sub>]<sub>0.825</sub>[Co<sub>2</sub>@Sn<sub>5</sub>Sb<sub>7</sub>]<sub>0.175</sub>·2dmf·2tol, [K(crypt-222)]<sub>3</sub>[Ni<sub>2</sub>@Sn<sub>7</sub>Sb<sub>5</sub>]<sub>2en</sub>·2tol were collected at T = 100(2) K with Mo<sub>Kα</sub> radiation (λ = 0.71073 Å) on a STOE IPDS II with an image plate detector. The data set for [K(crypt-222)]<sub>3</sub>[Co<sub>2</sub>@Sn<sub>5</sub>Sb<sub>7</sub>] was collected at T = 100(2) K with Cu<sub>Kα</sub> radiation (λ = 1.5418 Å) on a STOE STADIVARI with an image plate detector. The structures were solved by direct methods and refined by full-matrix-least-squares methods against F<sup>2</sup> with Olex2.<sup>[23]</sup> CCDC 1850710, 1850711, and 1850709 contain the supplementary crystallographic data for this paper. These data are provided free of charge by The Cambridge Crystallographic Data Centre.

### 4.5.2.2 Structure refinement details for [K(crypt-222)]<sub>3</sub>[Co@Sn<sub>6</sub>Sb<sub>6</sub>]<sub>0.825</sub>[Co<sub>2</sub>@Sn<sub>5</sub>Sb<sub>7</sub>]<sub>0.175</sub>·2dmf·2tol.

General crystallographic data are listed in Table S1. Sb, Sn, Co, K, O, N, and C atoms were refined using anisotropic displacement parameters. The atomic occupation of Co1 was allowed to freely refine and converged on a value of 0.5876. As Sn and Sb are indistinguishable by single crystal X-ray diffraction, the refined occupation of Co1 was used to estimate the relative abundances of [Co@Sn<sub>6</sub>Sb<sub>6</sub>]<sup>3-</sup> and [Co<sub>2</sub>@Sn<sub>5</sub>Sb<sub>7</sub>]<sup>3-</sup>. The atomic coordinates and anisotropic displacement parameters of Sn3-6 and Sb3-6 were constrained to have the same values with the EXYZ and EADP commands, respectively; the ratio of Sn:Sb at these positions was fixed according to the estimated abundances of the two clusters. Hydrogen atoms were placed in idealized positions and their displacement parameters were fixed to be 20% larger than those of the attached carbon atoms. The highest peak and the deepest hole of the final difference Fourier map (1.90

$e^{-}\cdot\text{\AA}^{-3}/-1.00 e^{-}\cdot\text{\AA}^{-3}$ ) were located 1.20 Å from Sn1B and 0.69 Å from Sn3/Sb3 respectively (see the numbering scheme in Figure S2). Figure S3 shows the crystal packing in  $[\text{K}(\text{crypt-222})]_3[\text{Co}@\text{Sn}_6\text{Sb}_6]_{0.825}[\text{Co}_2@\text{Sn}_5\text{Sb}_7]_{0.175}\cdot 2\text{dmf}\cdot 2\text{tol}$ .

**Table S1.** X-ray measurement, structure solution, and refinement details of  $[\text{K}(\text{crypt-222})]_3[\text{Co}@\text{Sn}_6\text{Sb}_6]_{0.825}[\text{Co}_2@\text{Sn}_5\text{Sb}_7]_{0.175}\cdot 2\text{dmf}\cdot 2\text{tol}$ .

Compound	$[\text{K}(\text{crypt-222})]_3[\text{Co}@\text{Sn}_6\text{Sb}_6]_{0.825}[\text{Co}_2@\text{Sn}_5\text{Sb}_7]_{0.175}\cdot 2\text{dmf}\cdot 2\text{tol}$
CCDC number	1850710
Empirical formula	$\text{C}_{74}\text{H}_{138}\text{Co}_{1.18}\text{K}_3\text{N}_8\text{O}_{20}\text{Sb}_{6.17}\text{Sn}_{5.83}$
Formula weight /g·mol <sup>-1</sup>	3089.63
Crystal color, shape	black, plate
Crystal size /mm <sup>3</sup>	0.35 × 0.27 × 0.03
Crystal system	monoclinic
Space group	C2/c
<i>a</i> /Å	29.719(6)
<i>b</i> /Å	12.954(3)
<i>c</i> /Å	28.267(6)
$\alpha$ /°	90
$\beta$ /°	106.91(3)
$\gamma$ /°	90
<i>V</i> /Å <sup>3</sup>	10412(4)
<i>Z</i>	4
$\rho_{\text{calc}}$ /g·cm <sup>-3</sup>	1.971
$\mu(\text{MoK}\alpha)$ /mm <sup>-1</sup>	3.307
$\theta$ range /°	1.72 - 27.30
Reflections measured	41848
Independent reflections	10246
<i>R</i> (int)	0.0897
Restraints	1
Parameters	548
$R_1/wR_2$ ( $I > 2\sigma(I)$ )	0.0459/0.1053
$R_1/wR_2$ (all data)	0.0811/0.1175
Goodness-of-fit on $F_2$	0.901
Max. peak/hole /e <sup>-</sup> ·Å <sup>-3</sup>	1.90/-0.99
Absorption correction type	numerical
Min./Max. transmission	0.4331/0.9344

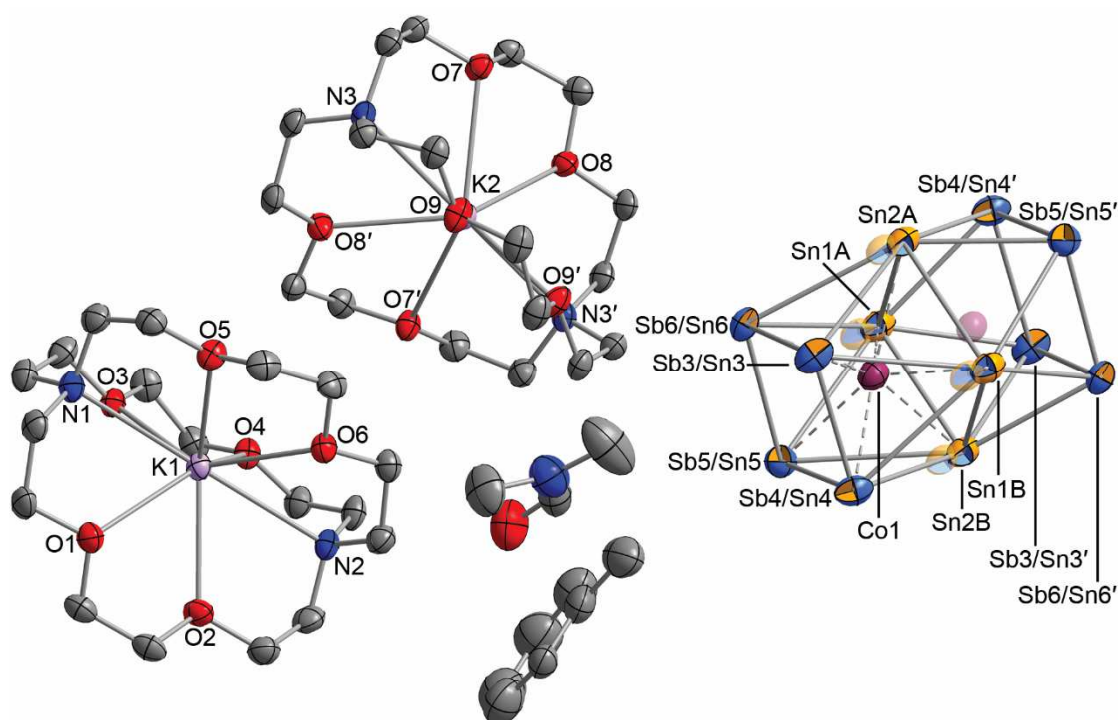


**Figure S2.** Asymmetric unit of  $[K(\text{crypt-222})]_3[\text{Co@Sn}_6\text{Sb}_6]_{0.825}[\text{Co}_2\text{@Sn}_5\text{Sb}_7]_{0.175}\cdot 2\text{dmf}\cdot 2\text{tol}$ . The cluster resides on a crystallographic inversion center and a twofold rotational axis passes through K2. These fragments have been grown to show the entirety of the molecules. The second component of the disordered anion is shown as 50% transparent. Thermal ellipsoids are drawn at 50% probability. Hydrogen atoms have been omitted for clarity. Elements are represented by the following colors: Sn, orange; Sb, blue; Co, purple; K, pink; O, red; N, green; C, gray.



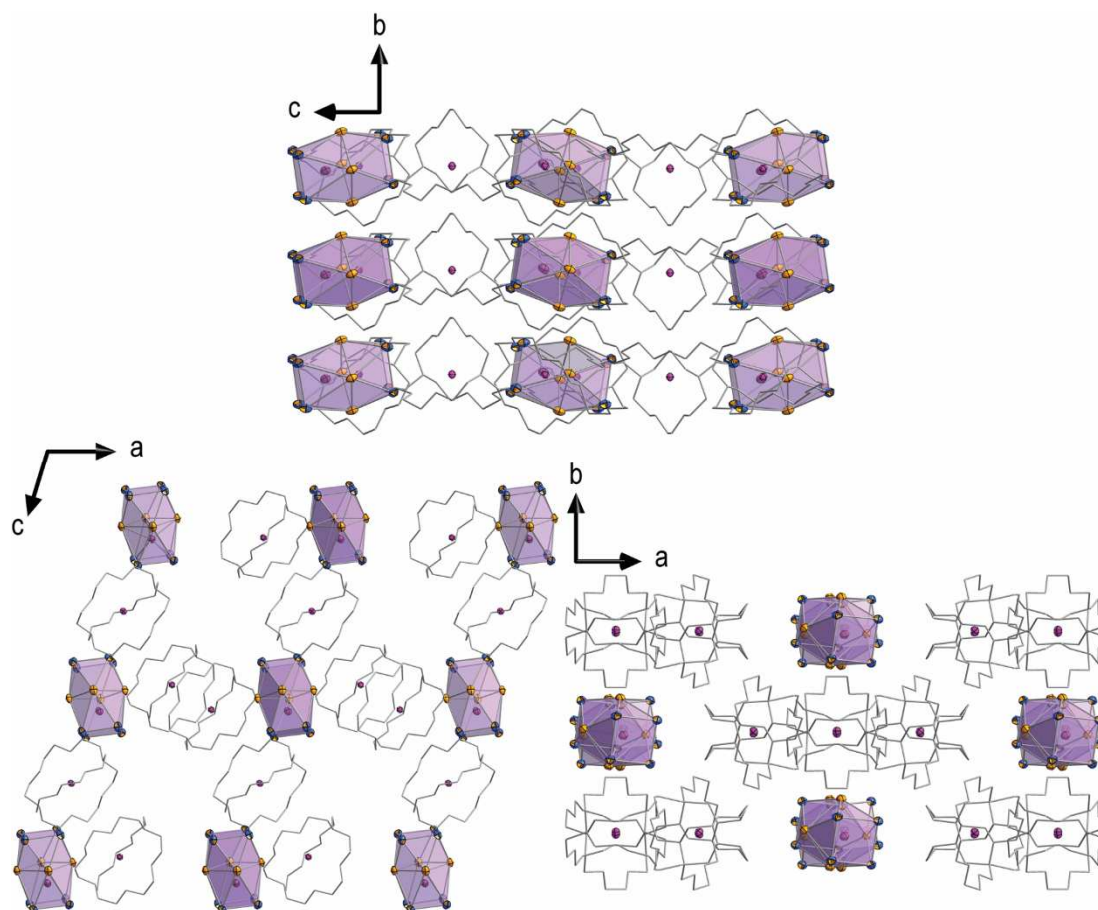


**Figure S3.** Packing of cations and anions in  $[K(\text{crypt-222})]_3[\text{Co@Sn}_6\text{Sb}_6]_{0.825}[\text{Co}_2\text{@Sn}_5\text{Sb}_7]_{0.175}\cdot 2\text{dmf}\cdot 2\text{tol}$  viewed down the a (top), b (bottom left), and c (bottom right) axes. Solvent molecules have been omitted and crypt-222 has been rendered as a stick model for clarity. Thermal ellipsoids are drawn at 50% probability. Elements are represented by the following colors: Sn, orange; Sb, blue; Co, purple; K, pink. The faces of the cluster anion are highlighted in light purple.

#### 4.5.2.3 Structure refinement details for [K(crypt-222)]<sub>3</sub>[Co<sub>2</sub>@Sn<sub>5</sub>Sb<sub>7</sub>]

General crystallographic data are listed in Table S2. Sb, Sn, Co, K, O, N, and C atoms were refined using anisotropic displacement parameters. The asymmetric unit contains a complete formula unit, however, there are two crystallographically independent half-clusters which reside on inversion centers at (0, 0, 0) and (1/2, 1/2, 1/2). The anion centered at (0, 0, 0) displays 3-fold disorder (Figure S4 and S5). The atomic occupations of the three orientations of this anion were constrained to have a sum of 1 with the SUMP command and all chemically equivalent bonds were restrained to have equal lengths with SADI. After refinement, the free variables of the three orientations converged to 0.664, 0.261, and 0.074. There is likely occupational disorder at all Sn and Sb positions, however, modelling this disorder had no effect on R values, and in the final stages of refinement the outer rings on the anions (Sn/Sb 1-4) were primarily assigned as Sb, while the inner rings (Sn 5-6) were assigned as Sn, according to calculated preferences (Section 6). Heavily disordered solvent molecules are present in the structure and a solvent mask was applied in the final stages of refinement, removing 143.7 e<sup>-</sup>/unit cell. This likely corresponds to 4 molecules of ethylenediamine (136 e<sup>-</sup>), or 2 per formula unit. Hydrogen atoms were placed in idealized positions and their displacement parameters were fixed to be 20% larger than those of the attached carbon atoms. The highest peak and the deepest hole of the final difference Fourier map (1.14 e<sup>-</sup>·Å<sup>-3</sup>/-1.66 e<sup>-</sup>·Å<sup>-3</sup>) were located 0.92 Å from Sb1A and 0.83 Å from Sb3A respectively (see the numbering scheme in Figure S4). Figure S6 shows the crystal packing in [K(crypt-222)]<sub>3</sub>[Co<sub>2</sub>@Sn<sub>5</sub>Sb<sub>7</sub>].

**Table S2.** X-ray measurement, structure solution, and refinement details of [K(crypt-222)]<sub>3</sub>[Co<sub>2</sub>@Sn<sub>5</sub>Sb<sub>7</sub>].

Compound	[K(crypt-222)] <sub>3</sub> [Co <sub>2</sub> @Sn <sub>5</sub> Sb <sub>7</sub> ]
CCDC number	1850711
Empirical formula	C <sub>54</sub> H <sub>108</sub> Co <sub>2</sub> K <sub>3</sub> N <sub>6</sub> O <sub>18</sub> Sb <sub>7</sub> Sn <sub>5</sub>
Formula weight /g·mol <sup>-1</sup>	2810.32
Crystal color, shape	black, block
Crystal size /mm <sup>3</sup>	0.13 × 0.11 × 0.09
Crystal system	Triclinic
Space group	P $\bar{1}$
<i>a</i> /Å	15.915(3)
<i>b</i> /Å	17.478(4)
<i>c</i> /Å	17.589(4)
$\alpha$ /°	93.18(3)
$\beta$ /°	93.84(3)
$\gamma$ /°	98.37(3)
<i>V</i> /Å <sup>3</sup>	4819.0(17)
<i>Z</i>	2
$\rho_{\text{calc}}$ /g·cm <sup>-3</sup>	1.937
$\mu(\text{CuK}\alpha)$ /mm <sup>-1</sup>	29.588
$\Theta$ range /°	2.52 to 74.25
Reflections measured	87727
Independent reflections	18152
<i>R</i> (int)	0.0910
Restraints	1872
Parameters	1173
<i>R</i> <sub>1</sub> / <i>wR</i> <sub>2</sub> ( <i>I</i> > 2σ( <i>I</i> ))	0.0456/0.0991
<i>R</i> <sub>1</sub> / <i>wR</i> <sub>2</sub> (all data)	0.0784/0.1079
Goodness-of-fit on <i>F</i> <sub>2</sub>	0.857
Max. peak/hole /e <sup>-</sup> ·Å <sup>-3</sup>	1.14/-1.66
Absorption correction type	multi-scan
Min./Max. transmission	0.0009/0.0147

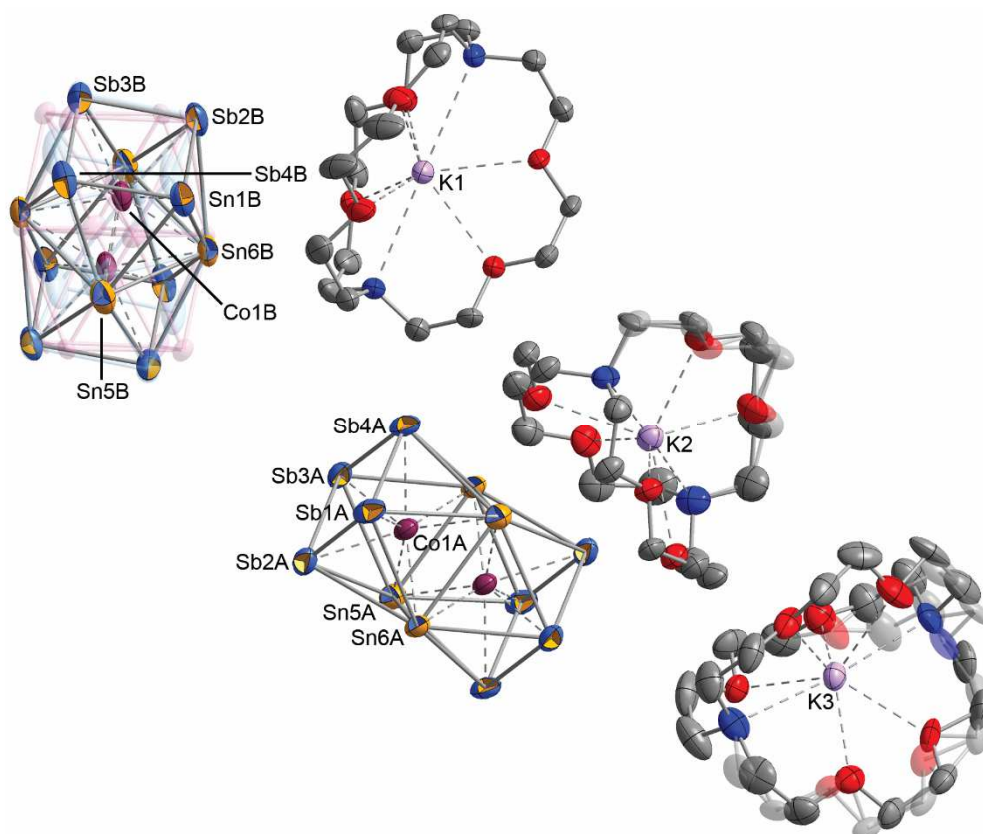


**Figure S4.** Asymmetric unit of  $[K(\text{crypt-222})]_3[\text{Co}_2@\text{Sn}_5\text{Sb}_7]$ . The clusters reside on crystallographic inversion centers. These fragments have been grown to show the entirety of the molecules. The anion in the upper-left corner is disordered over three different orientations (see Figure S5, minor components shown in pink and blue at 70% transparency). Thermal ellipsoids are drawn at 50% probability. Hydrogen atoms have been omitted for clarity. Elements are represented by the following colors: Sn, orange; Sb, blue; Co, purple; K, pink; O, red; N, green; C, gray. Dual-colored octants represent sights of mixed occupation according to DFT calculations, with the major component indicated by the outer color. For expediency, occupational disorder was not modeled in this structure, and Sn and Sb were assigned according to the most probable locations.

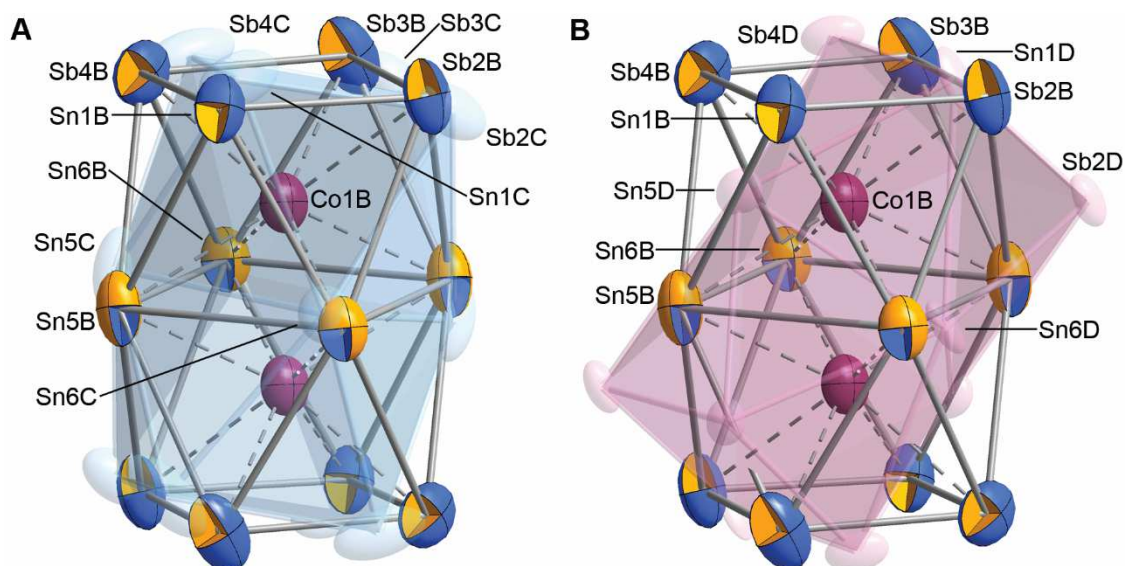


**Figure S5.** Close up of the disordered anion in the crystal structure of  $[K(\text{crypt-222})]_3[\text{Co}_2@\text{Sn}_5\text{Sb}_7]$ . The cluster with blue/orange ellipsoids is the primary orientation of the anion (66.4%). Shown in relation to this are the less abundant orientations in blue (A, 26.1%) and pink (B, 7.4%). The cluster resides on crystallographic inversion centers and the fragments have been grown to show the entirety of the molecules. Thermal ellipsoids are drawn at 50% probability. Cobalt atoms Co1C and Co1D have been omitted for clarity.

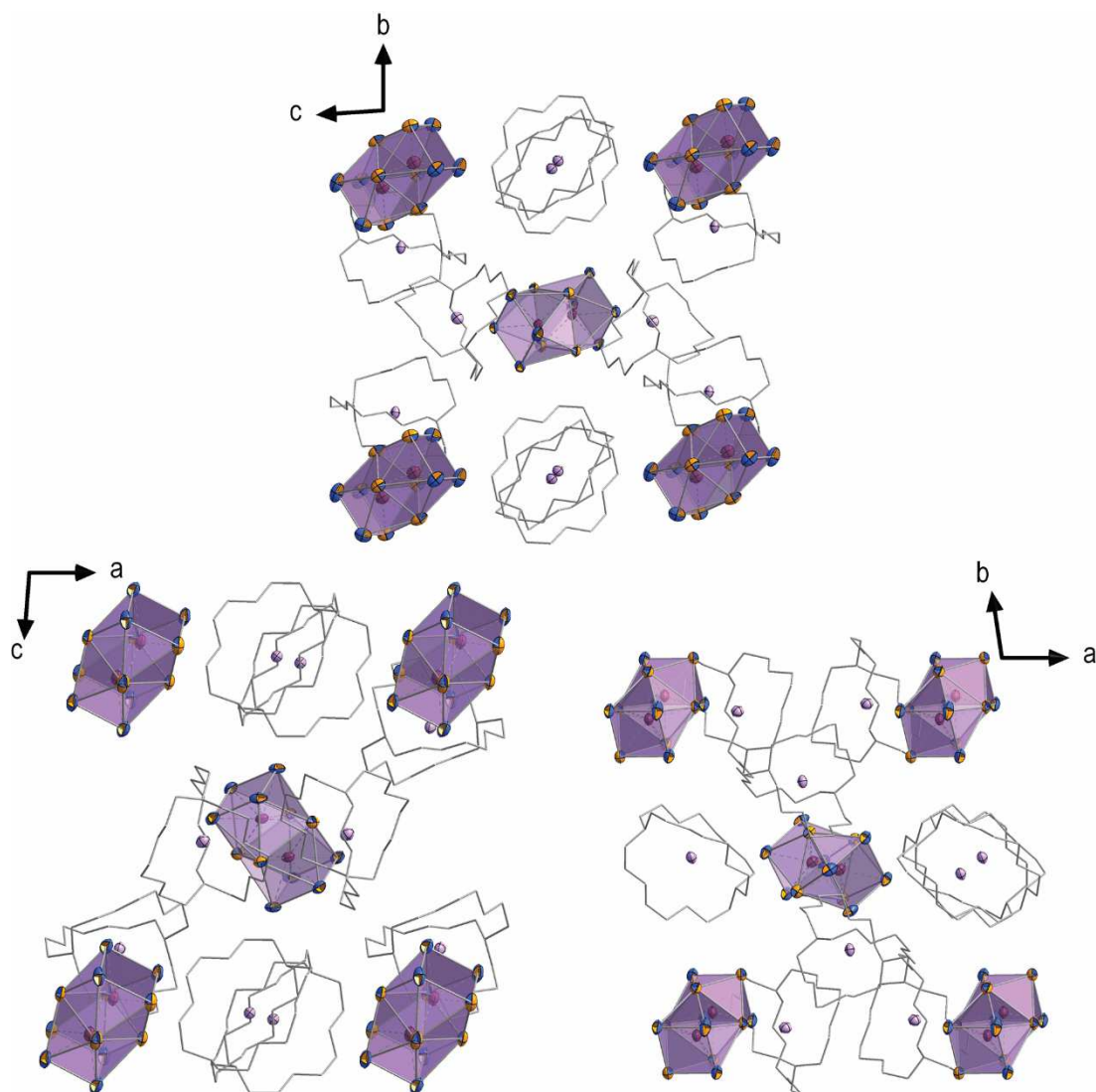


**Figure S6.** Packing of cations and anions in [K(crypt-222)]<sub>3</sub>[Co<sub>2</sub>@Sn<sub>5</sub>Sb<sub>7</sub>] viewed down the a (top), b (bottom left), and c (bottom right) axes. Crypt-222 has been rendered as a stick model for clarity. Thermal ellipsoids are drawn at 50% probability. Elements are represented by the following colors: Sn, orange; Sb, blue; Co, purple; K, pink. The faces of the cluster anion are highlighted in light purple.

4.5.2.4 Structure refinement details for  $[K(\text{crypt-222})]_3[\text{Ni}_2@\text{Sn}_7\text{Sb}_5]\cdot 2\text{en}\cdot 2\text{tol}$ 

General crystallographic data are listed in Table S3. Sb, Sn, Ni, K, O, N, and C atoms were refined using anisotropic displacement parameters. The atomic coordinates and anisotropic displacement parameters of Sn3-6 and Sb3-6 were constrained to have the same values with the EXYZ and EADP commands respectively; the ratio of Sn:Sb at these positions was fixed at 3:5. Hydrogen atoms were placed in idealized positions and their displacement parameters were fixed to be 20% larger than those of the attached carbon atoms. The highest peak and the deepest hole of the final difference Fourier map ( $2.81 \text{ e}^- \cdot \text{\AA}^{-3} / -1.61 \text{ e}^- \cdot \text{\AA}^{-3}$ ) were located  $1.52 \text{ \AA}$  from Sn6/Sb6 and  $0.37 \text{ \AA}$  from Sn6/Sb6 respectively (see the numbering scheme in Figure S7). Figure S8 shows the crystal packing in  $[K(\text{crypt-222})]_3[\text{Ni}_2@\text{Sn}_7\text{Sb}_5]\cdot 2\text{en}\cdot 2\text{tol}$ .

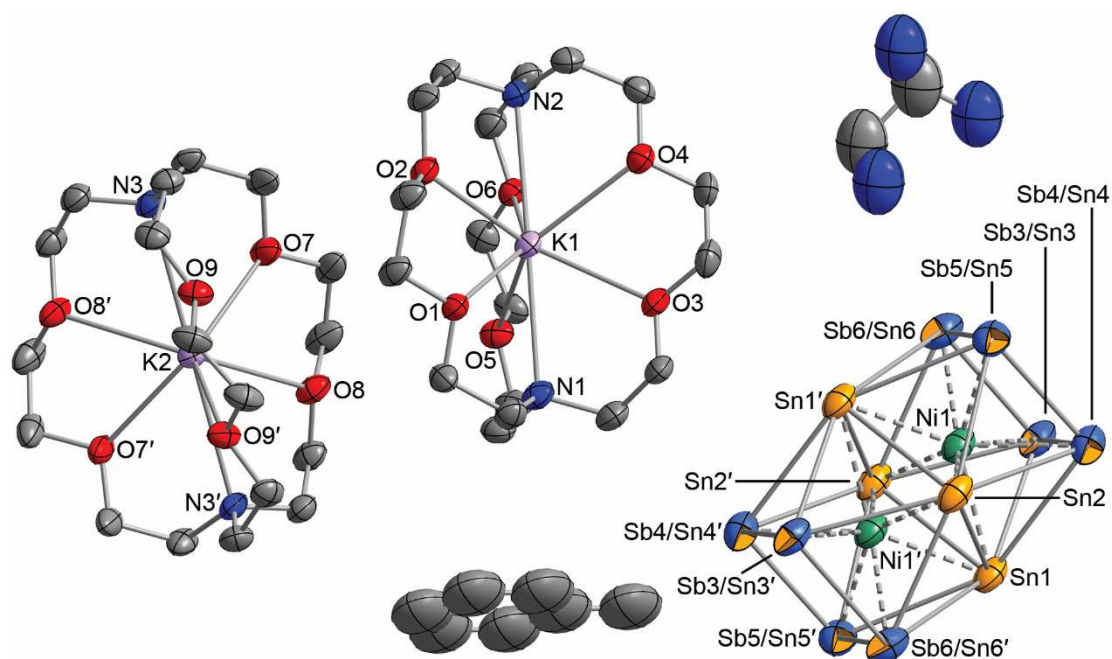


**Figure S7.** Asymmetric unit of  $[K(\text{crypt-222})]_3[\text{Ni}_2@\text{Sn}_7\text{Sb}_5]\cdot 2\text{en}\cdot 2\text{tol}$ . The cluster resides on crystallographic inversion center and a twofold rotational axis passes through K2 of the  $[K(\text{crypt-222})]^+$  cation on the left. These fragments have been grown to show the entirety of the molecules. Occupational disorder is shown with two-color ellipsoids where the outer color represents the major component. Thermal ellipsoids are drawn at 50% probability. Hydrogen atoms have been omitted for clarity. Elements are represented by the following colors: Sn, orange; Sb, blue; Ni, green; K, pink; O, red; N, blue; C, gray.

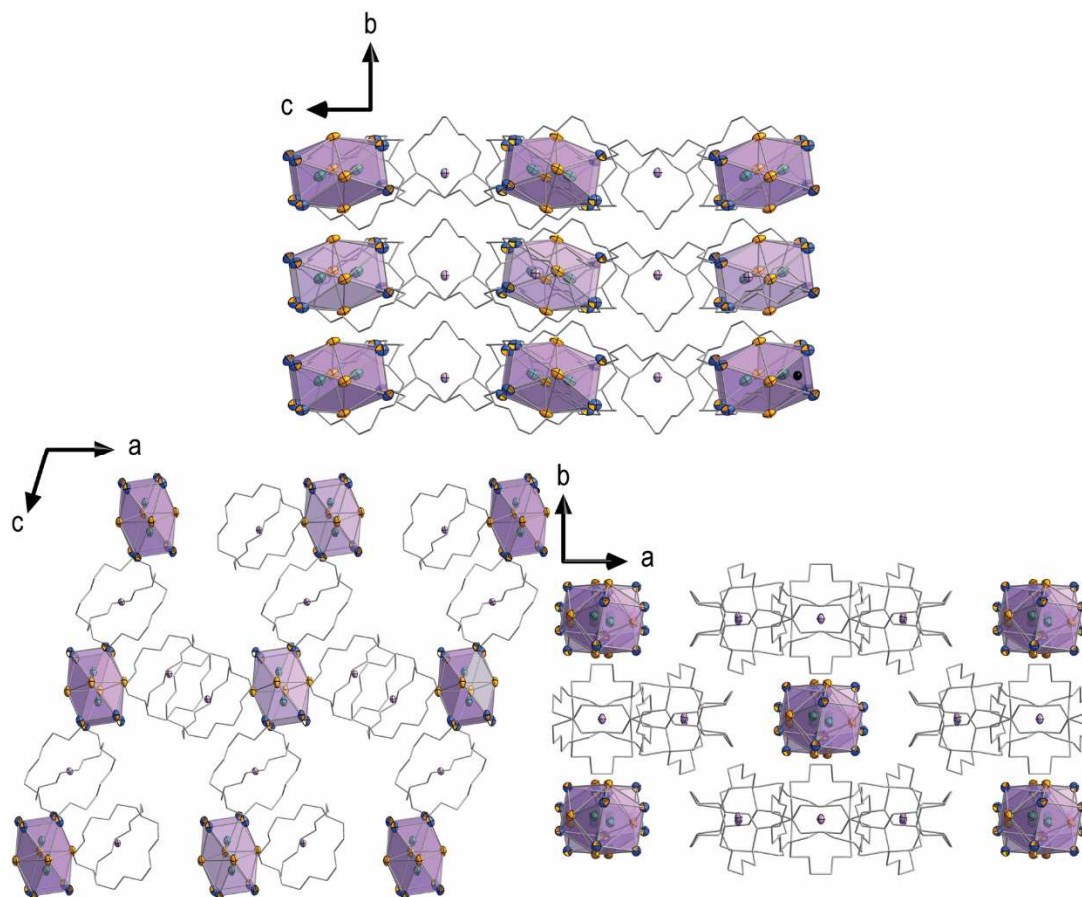


**Figure S8.** Packing of cations and anions in [K(crypt-222)]<sub>3</sub>[Ni<sub>2</sub>@Sn<sub>7</sub>Sb<sub>5</sub>]·2en·2tol viewed down the a (top), b (bottom left), and c (bottom right) axes. Solvent molecules have been omitted and crypt-222 has been rendered as a stick model for clarity. Thermal ellipsoids are drawn at 50% probability. Elements are represented by the following colors: Sn, orange; Sb, blue; Ni, green; K, pink. The faces of the cluster anion are highlighted in light purple.



**Table S3.** X-ray measurement, structure solution, and refinement details of [K(crypt-222)]<sub>3</sub>[Ni<sub>2</sub>@Sn<sub>7</sub>Sb<sub>5</sub>]·2en·2tol.

Compound	[K(crypt-222)] <sub>3</sub> [Ni <sub>2</sub> @Sn <sub>7</sub> Sb <sub>5</sub> ]·2en·2tol
CCDC number	1850709
Empirical formula	C <sub>72</sub> H <sub>140</sub> K <sub>3</sub> N <sub>10</sub> Ni <sub>2</sub> O <sub>18</sub> Sb <sub>5</sub> Sn <sub>7</sub>
Formula weight /g·mol <sup>-1</sup>	3108.4
Crystal color, shape	black, block
Crystal size /mm <sup>3</sup>	0.23 × 0.19 × 0.15
Crystal system	monoclinic
Space group	C2/c
<i>a</i> /Å	29.629(6)
<i>b</i> /Å	12.964(3)
<i>c</i> /Å	28.244(6)
$\alpha$ /°	90
$\beta$ /°	107.00(3)
$\gamma$ /°	90
<i>V</i> /Å <sup>3</sup>	10374(4)
<i>Z</i>	4
$\rho_{\text{calc}}$ /g·cm <sup>-3</sup>	1.989
$\mu(\text{MoK}\alpha)$ /mm <sup>-1</sup>	3.464
$\theta$ range /°	1.51 – 26.83
Reflections measured	45580
Independent reflections	11004
<i>R</i> (int)	0.0560
Restraints	51
Parameters	470
<i>R</i> <sub>1</sub> / <i>wR</i> <sub>2</sub> ( <i>I</i> > 2 $\sigma$ ( <i>I</i> ))	0.0675/0.1861
<i>R</i> <sub>1</sub> / <i>wR</i> <sub>2</sub> (all data)	0.1036/0.2020
Goodness-of-fit on <i>F</i> <sub>2</sub>	1.03
Max. peak/hole /e <sup>-</sup> ·Å <sup>-3</sup>	2.81/-1.61
Absorption correction type	numerical
Min./Max. transmission	0.499/0.637

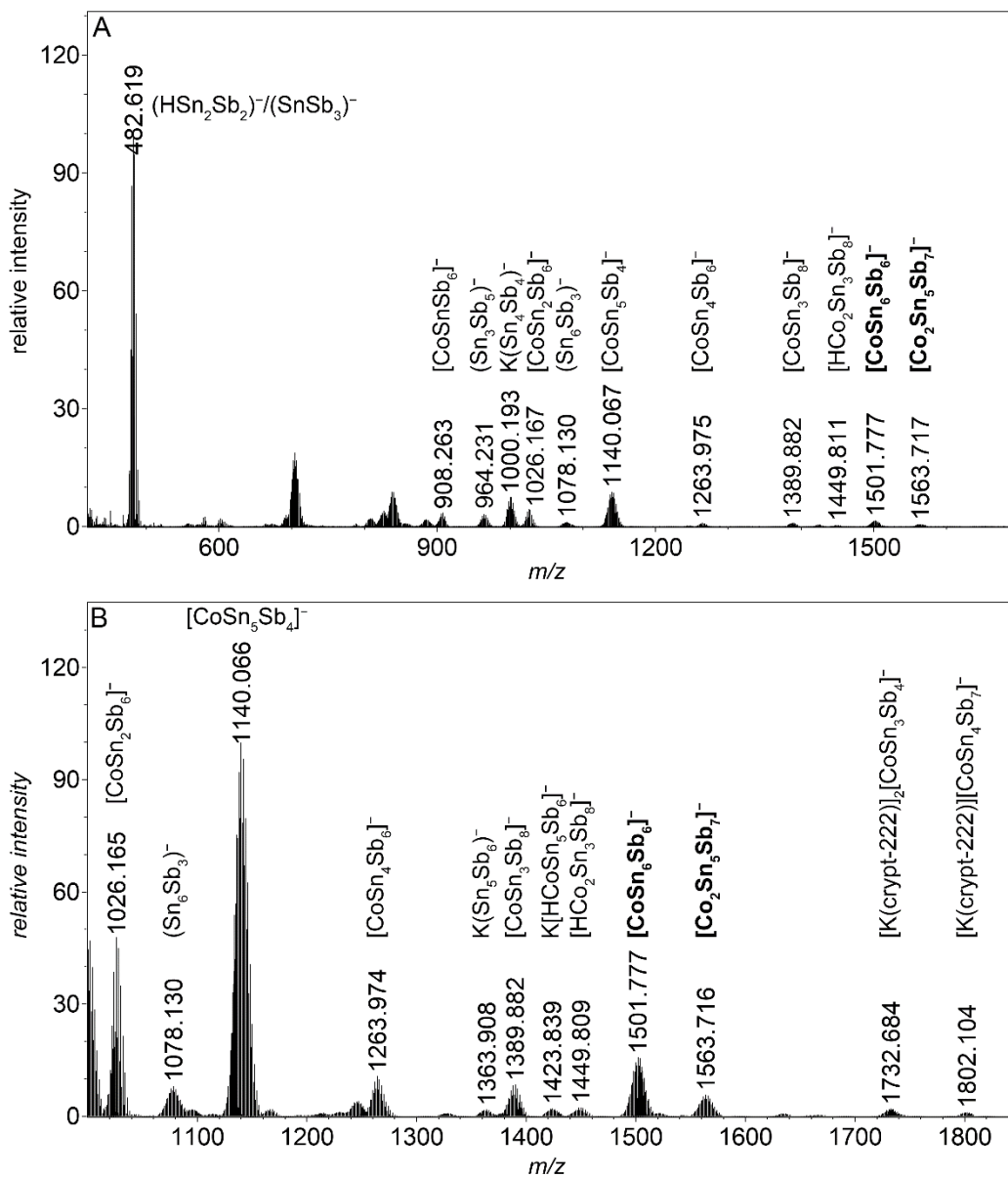
### 4.5.3 Mass Spectrometry

#### 4.5.3.1 Methods

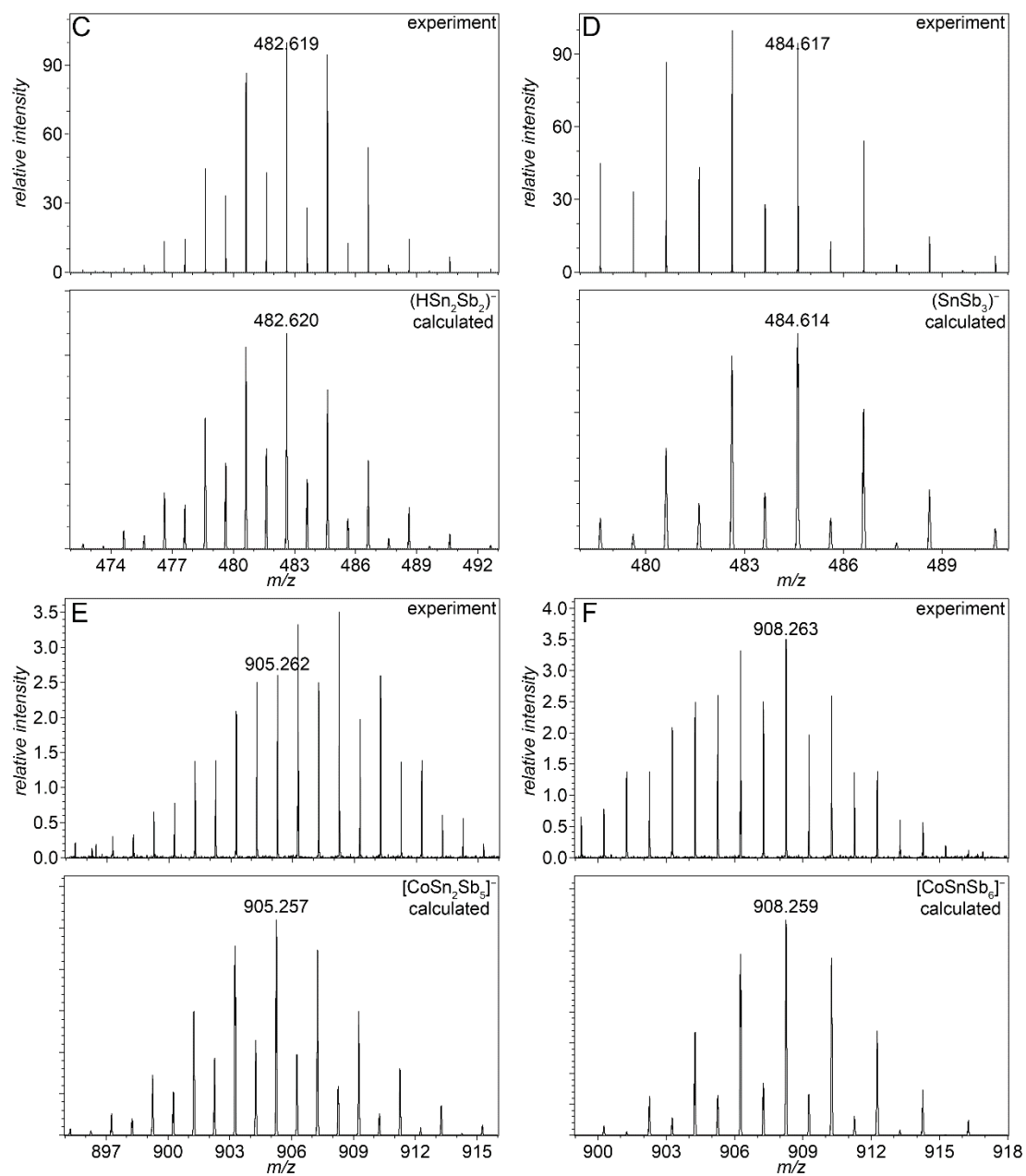
All mass spectra were recorded with a Thermo Fischer Scientific Finnigan LTQ-FT spectrometer in the negative ion mode. All samples were prepared inside of a glovebox, where they were dissolved in anhydrous DMF and filtered through Teflon syringe filters with a pore size of 0.45  $\mu\text{m}$ . The solutions were injected into the spectrometer with gastight 250  $\mu\text{L}$  Hamilton syringes by syringe pump infusion. All capillaries within the system were washed with dry DMF for 30 minutes before and at least 10 minutes in between measurements to avoid decomposition reactions and consequent clogging.

The following ESI parameters were used: spray voltage 3.6 kV, capillary temp 290 °C, capillary voltage -45, tube lens voltage -132.75, sheath gas 38, sweep gas 7, auxiliary gas 8.

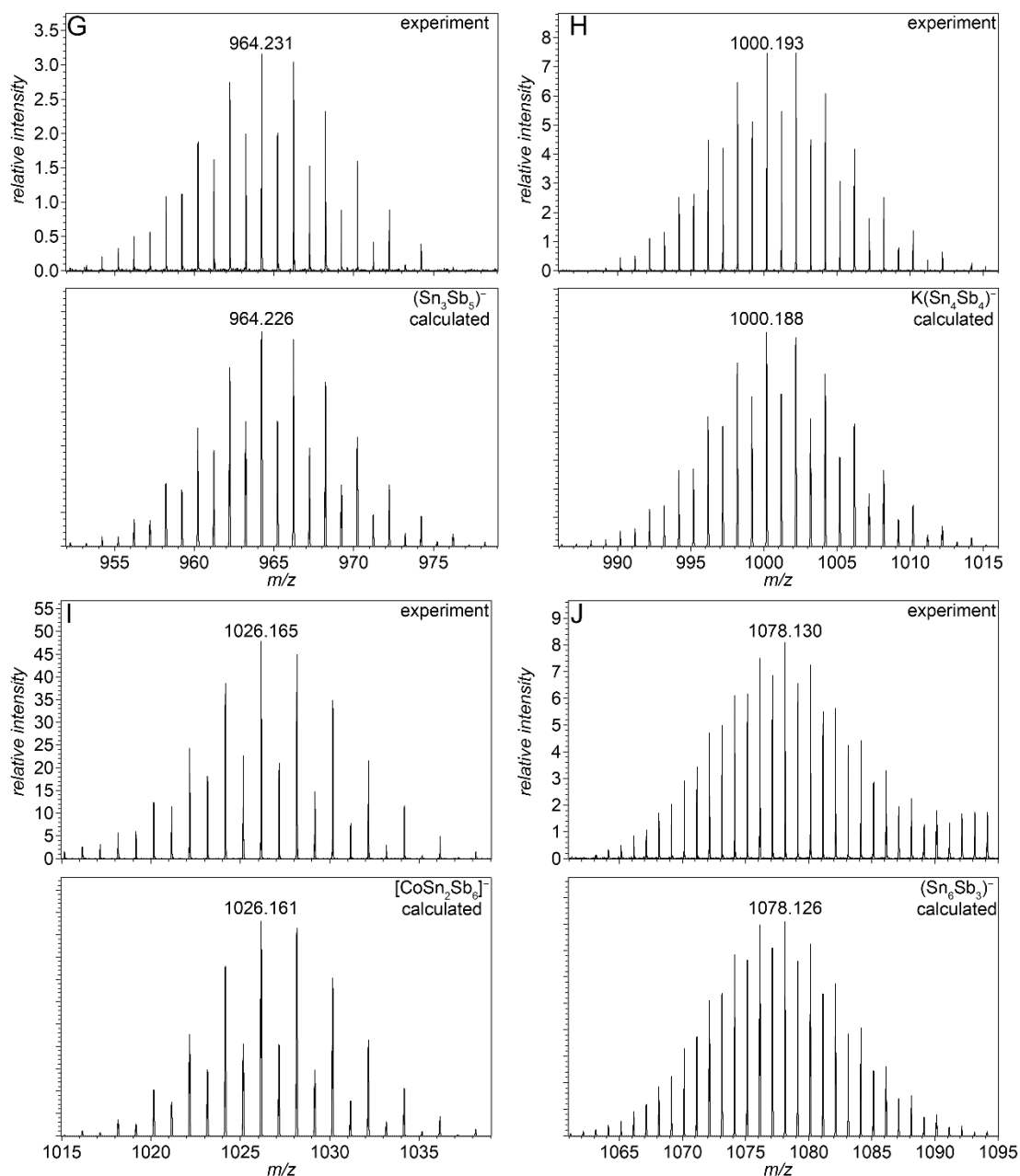
#### 4.5.3.2 High resolution mass signals obtained from crystals of [K(crypt-222)]<sub>3</sub>[Co@Sn<sub>6</sub>Sb<sub>6</sub>]<sub>0.825</sub>[Co<sub>2</sub>@Sn<sub>5</sub>Sb<sub>7</sub>]<sub>0.175</sub>·2dmf·2tol



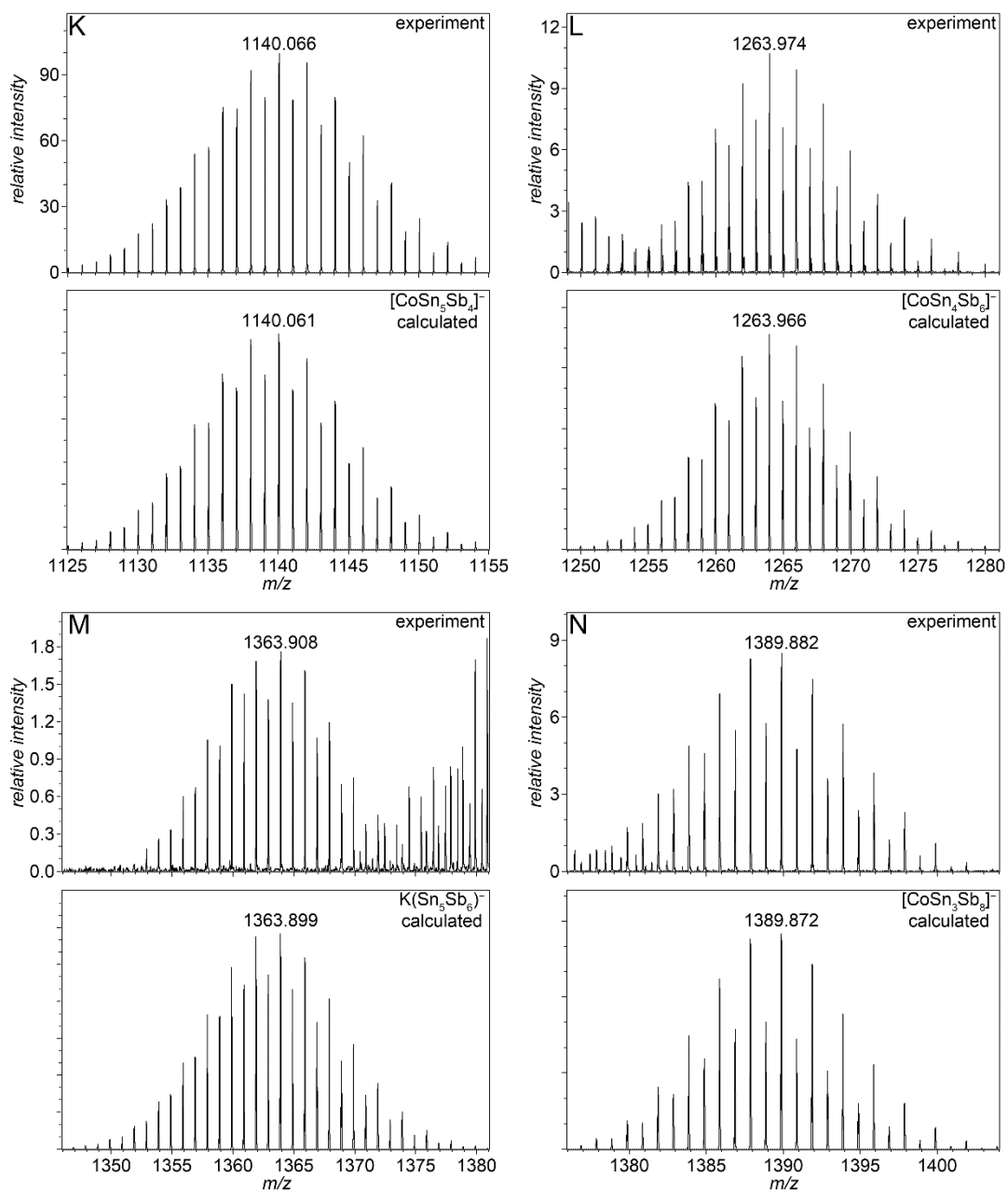
**Figure S9.** ESI(-) mass spectra of crystals of [K(crypt-222)]<sub>3</sub>[Co@Sn<sub>6</sub>Sb<sub>6</sub>]<sub>0.825</sub>[Co<sub>2</sub>@Sn<sub>5</sub>Sb<sub>7</sub>]<sub>0.175</sub>·2dmf·2tol dissolved in DMF.<sup>[24]</sup> Spectrum (A) is the average of data collected over the range of 400 – 2000 m/z (truncated). Spectrum (B) is the average of data accumulated over the range of 1000 – 1900 m/z, where most signals of interest are found.



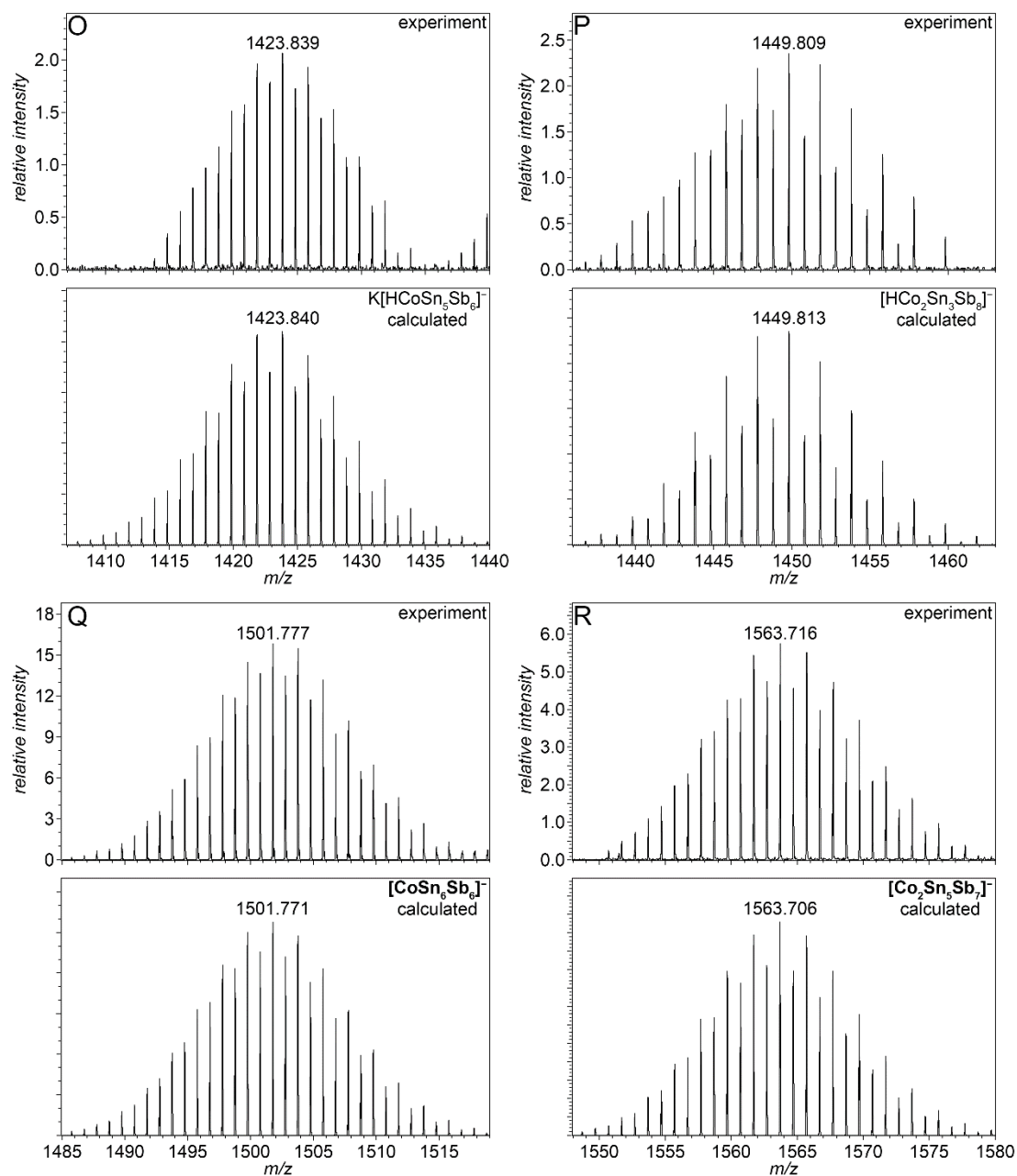
**Figure S10.** High resolution ESI(-) mass signals of (C)  $(\text{SnSb}_3)^-$ , (D)  $(\text{HSn}_2\text{Sb}_2)^-$ , (E)  $[\text{CoSn}_2\text{Sb}_5]^-$ , and (F)  $[\text{CoSnSb}_6]^-$ . Note that the mass envelopes of  $(\text{SnSb}_3)^-$  and  $(\text{HSn}_2\text{Sb}_2)^-$  overlap, as well as those of  $[\text{CoSn}_2\text{Sb}_5]^-$  and  $[\text{CoSnSb}_6]^-$ .



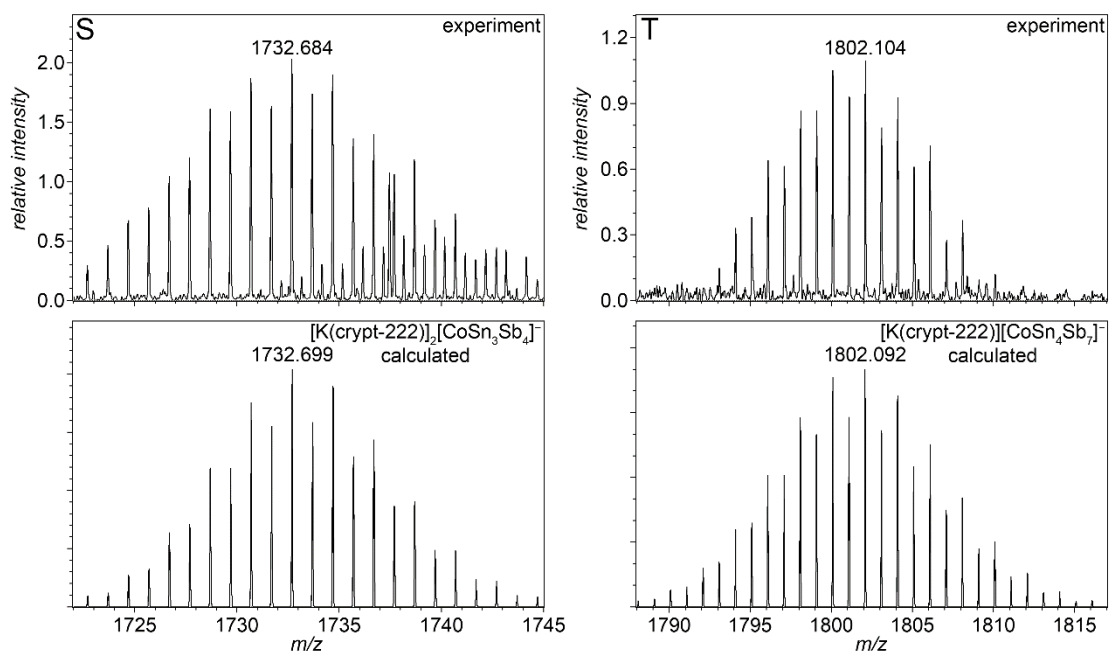
**Figure S11.** High resolution ESI(-) mass signals of (G)  $(\text{Sn}_3\text{Sb}_5)^-$ , (H)  $\text{K}(\text{Sn}_4\text{Sb}_4)^-$ , (I)  $[\text{CoSn}_2\text{Sb}_6]^-$ , and (G)  $(\text{Sn}_6\text{Sb}_3)^-$ .



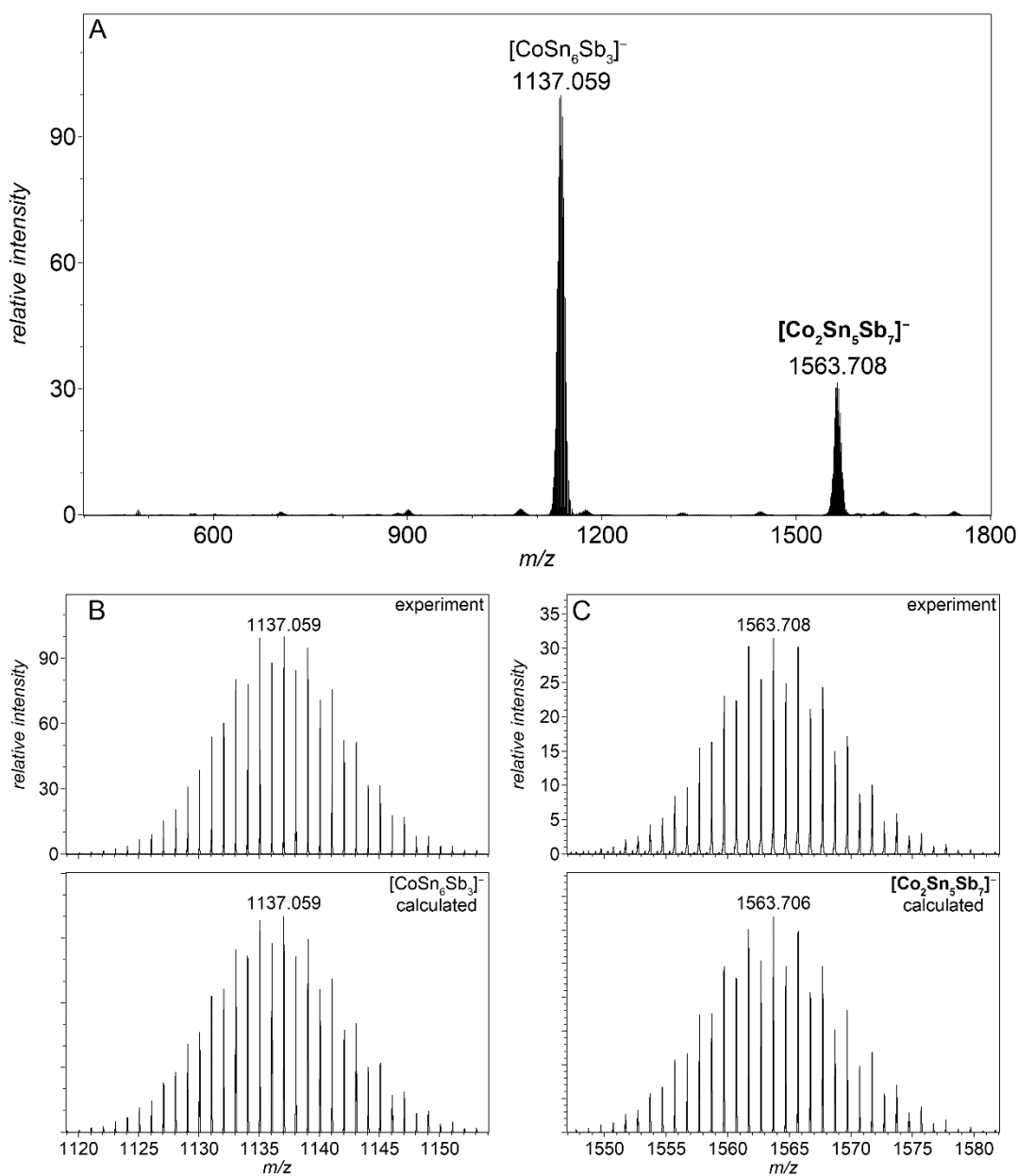
**Figure S12.** High resolution ESI(-) mass signals of (K)  $[\text{CoSn}_5\text{Sb}_4]^-$ , (L)  $[\text{CoSn}_4\text{Sb}_6]^-$ , (M)  $\text{K}(\text{Sn}_5\text{Sb}_6)^-$ , and (N)  $[\text{CoSn}_3\text{Sb}_8]^-$ .



**Figure S13.** High resolution ESI(-) mass signals of (O)  $K[HCoSn_5Sb_6]^-$ , (P)  $[HCo_2Sn_3Sb_8]^-$ , (Q)  $[CoSn_6Sb_6]^-$ , and (R)  $[Co_2Sn_5Sb_7]^-$ .

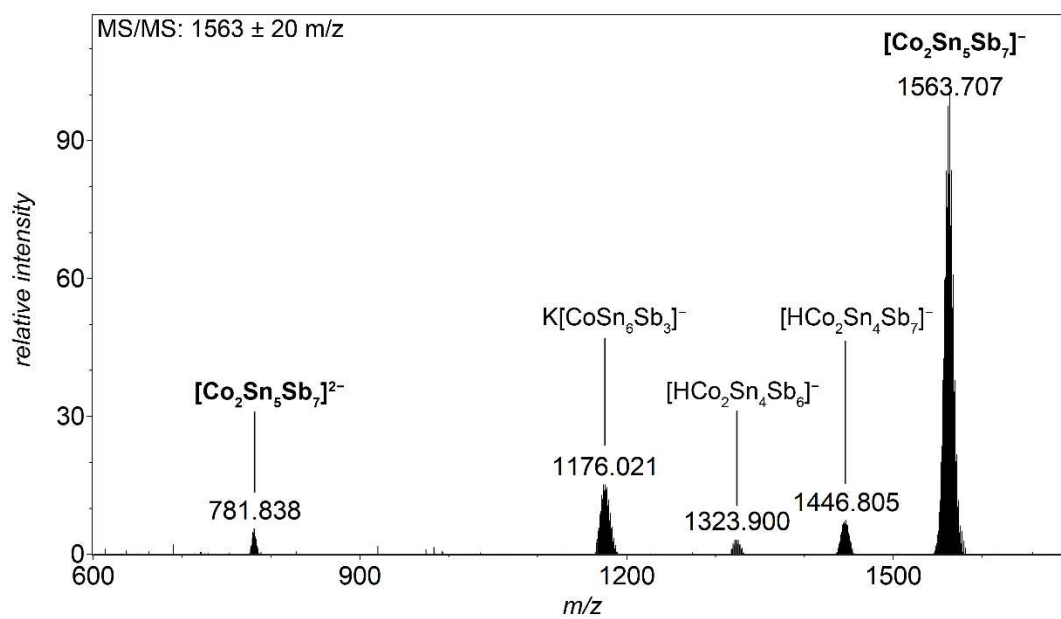


**Figure S14.** High resolution ESI(-) mass signals of (S)  $[\text{K}(\text{crypt-222})_2[\text{CoSn}_3\text{Sb}_4]^-]$  and (T)  $[\text{K}(\text{crypt-222})][\text{CoSn}_4\text{Sb}_7]^-]$ .

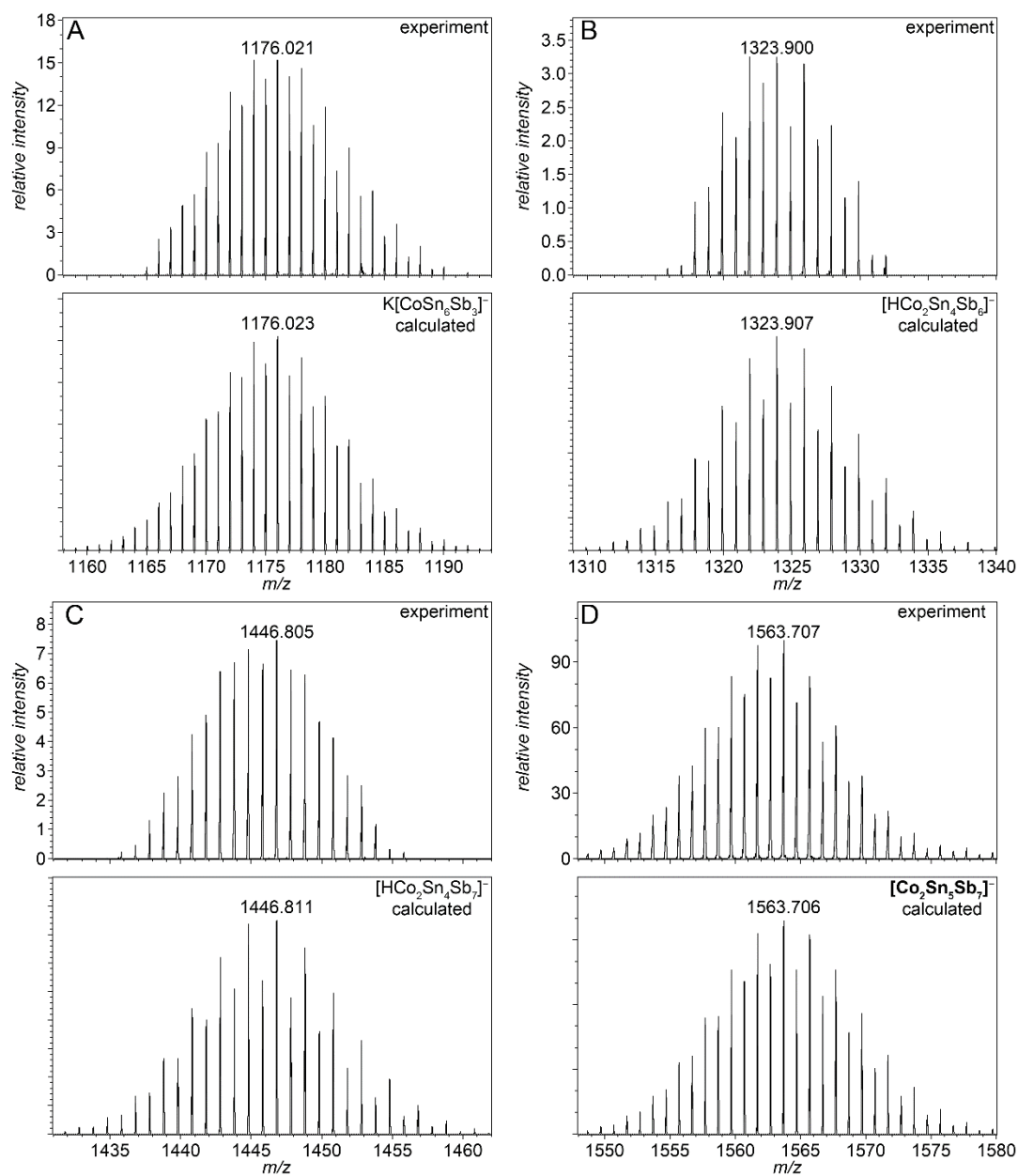
4.5.3.3 High resolution mass signals obtained from powder from crude synthesis of [K(crypt-222)]<sub>3</sub>[Co<sub>2</sub>@Sn<sub>5</sub>Sb<sub>7</sub>]

**Figure S15.** (A) ESI(-) mass spectrum of powder from crude synthesis of [K(crypt-222)]<sub>3</sub>[Co<sub>2</sub>@Sn<sub>5</sub>Sb<sub>7</sub>] dissolved in DMF (PTFE filter, 0.45 μm), and high resolution ESI(-) mass signals of (B) [CoSn<sub>6</sub>Sb<sub>3</sub>]<sup>-</sup> and (C) [Co<sub>2</sub>Sn<sub>5</sub>Sb<sub>7</sub>]<sup>-</sup>.

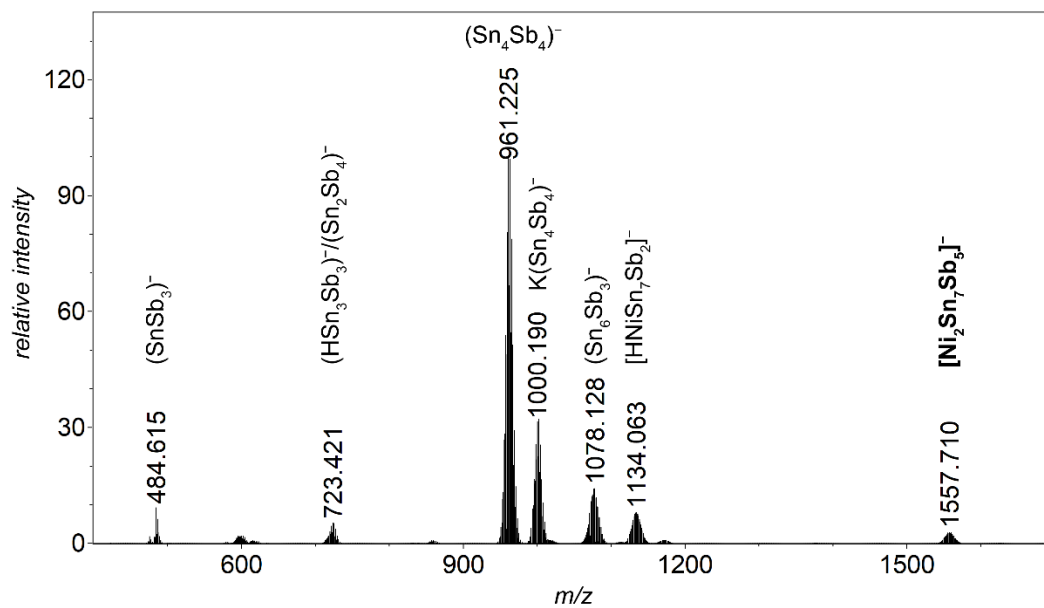




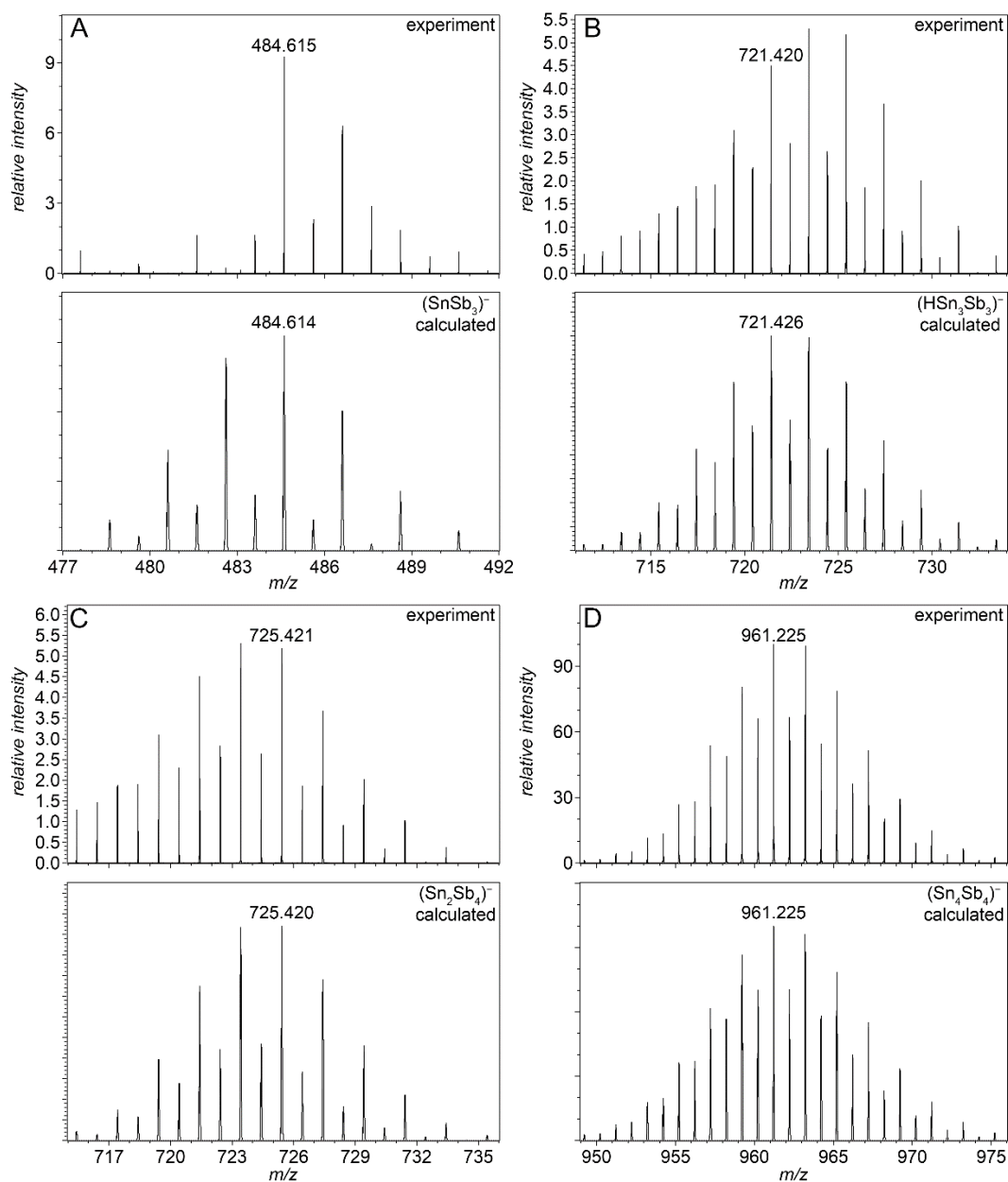
**Figure S16.** ESI(-) tandem mass spectrum derived from fragmentation of molecular ions in the region from 1543 to 1583 m/z.



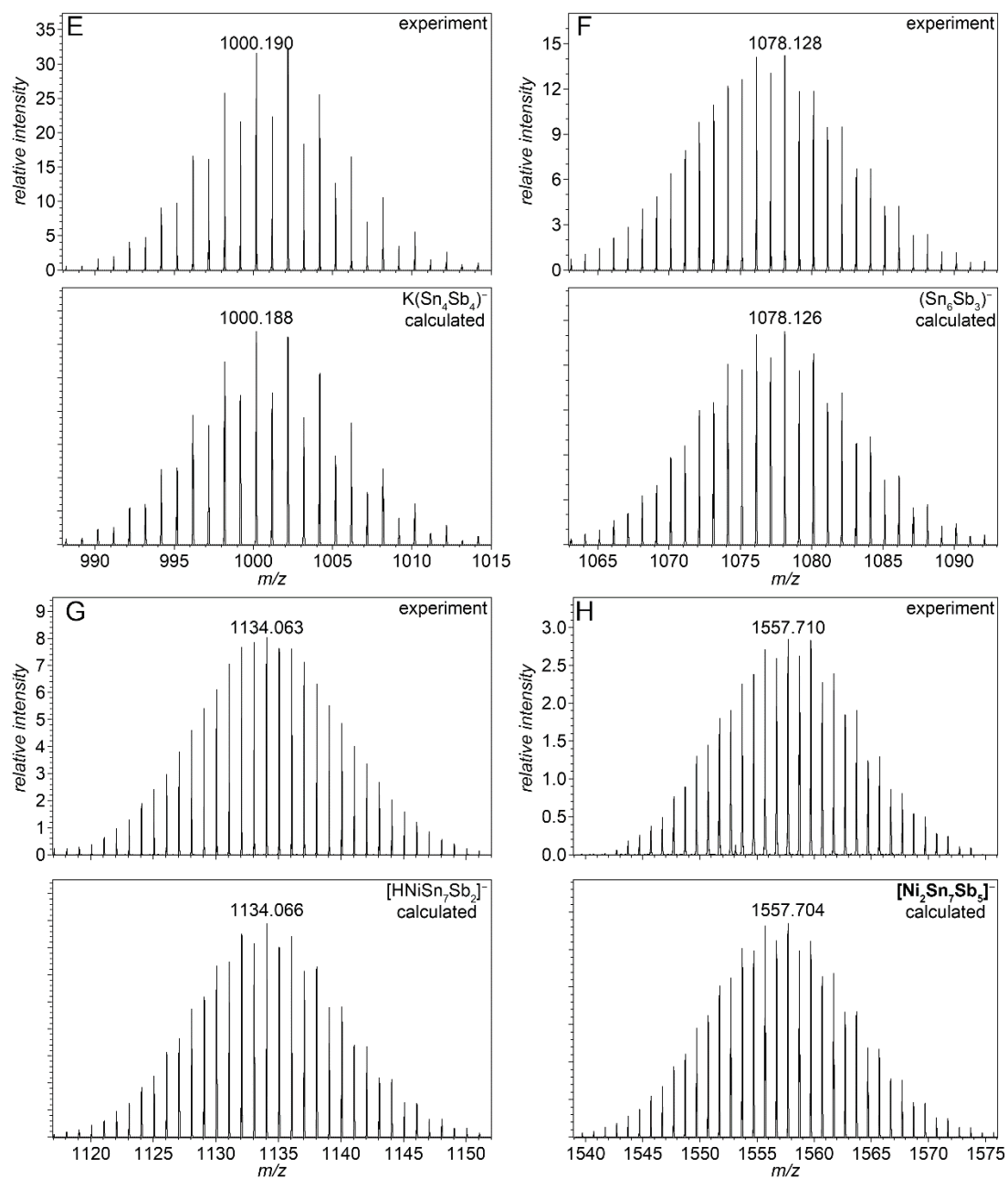
**Figure S17.** Individual high resolution ESI(-) mass signals obtained upon fragmentation of molecular ions in the region from 1543 to 1583  $m/z$ : (A)  $K[CoSn_6Sb_3]^-$ , (B)  $[HCo_2Sn_4Sb_6]^-$ , (C)  $[HCo_2Sn_4Sb_7]^-$ , and (D)  $[Co_2Sn_5Sb_7]^-$ .

4.5.3.4 High resolution mass signals obtained from single crystals of [K(crypt-222)]<sub>3</sub>[Ni<sub>2</sub>@Sn<sub>7</sub>Sb<sub>5</sub>]·2en·2tol

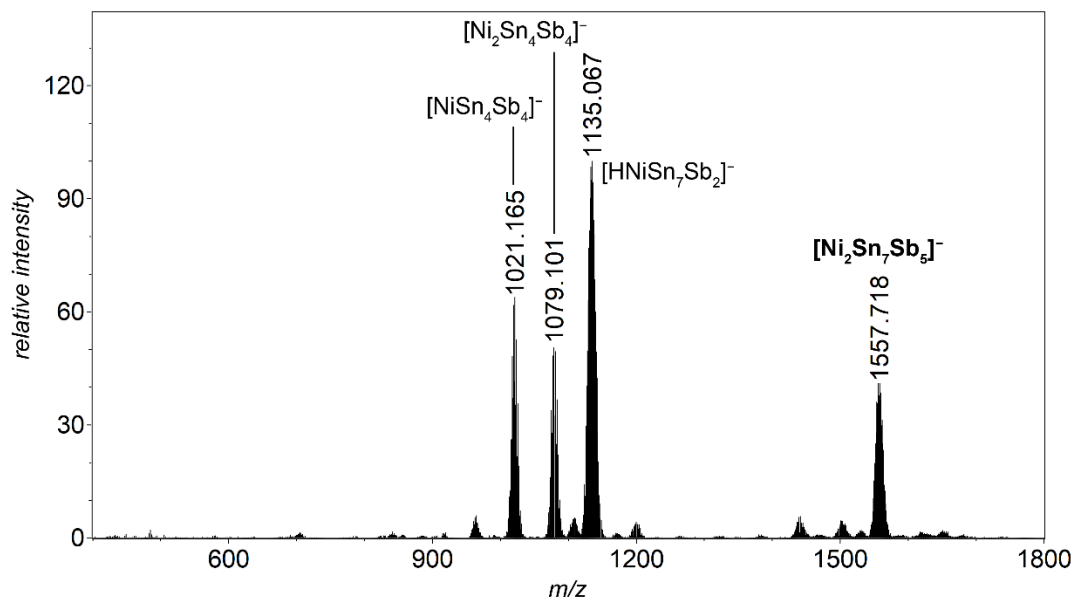
**Figure S18.** ESI(-) mass spectrum of a single crystal of [K(crypt-222)]<sub>3</sub>[Ni<sub>2</sub>@Sn<sub>7</sub>Sb<sub>5</sub>]·2en·2tol dissolved in DMF.



**Figure S19.** High resolution ESI(-) mass signals of (A)  $(\text{SnSb}_3)^-$  (weak), (B)  $(\text{HSn}_3\text{Sb}_3)^-$ , (C)  $(\text{Sn}_2\text{Sb}_4)^-$ , and (R)  $(\text{Sn}_4\text{Sb}_4)^-$ .



**Figure S20.** High resolution ESI(-) mass signals of (E)  $\text{K}(\text{Sn}_4\text{Sb}_4)^-$ , (F)  $(\text{Sn}_6\text{Sb}_3)^-$ , (G)  $[\text{HNiSn}_7\text{Sb}_2]^-$ , and (H)  $[\text{Ni}_2\text{Sn}_7\text{Sb}_5]^-$ .

4.5.3.5 High resolution mass signals obtained from powder from crude synthesis of [K(crypt-222)]<sub>3</sub>[Ni<sub>2</sub>Sn<sub>7</sub>Sb<sub>5</sub>]

**Figure S21.** ESI(-) mass spectrum of powder from crude synthesis of [K(crypt-222)]<sub>3</sub>[Ni<sub>2</sub>@Sn<sub>7</sub>Sb<sub>5</sub>] dissolved in DMF (PTFE filter, 0.45 μm).

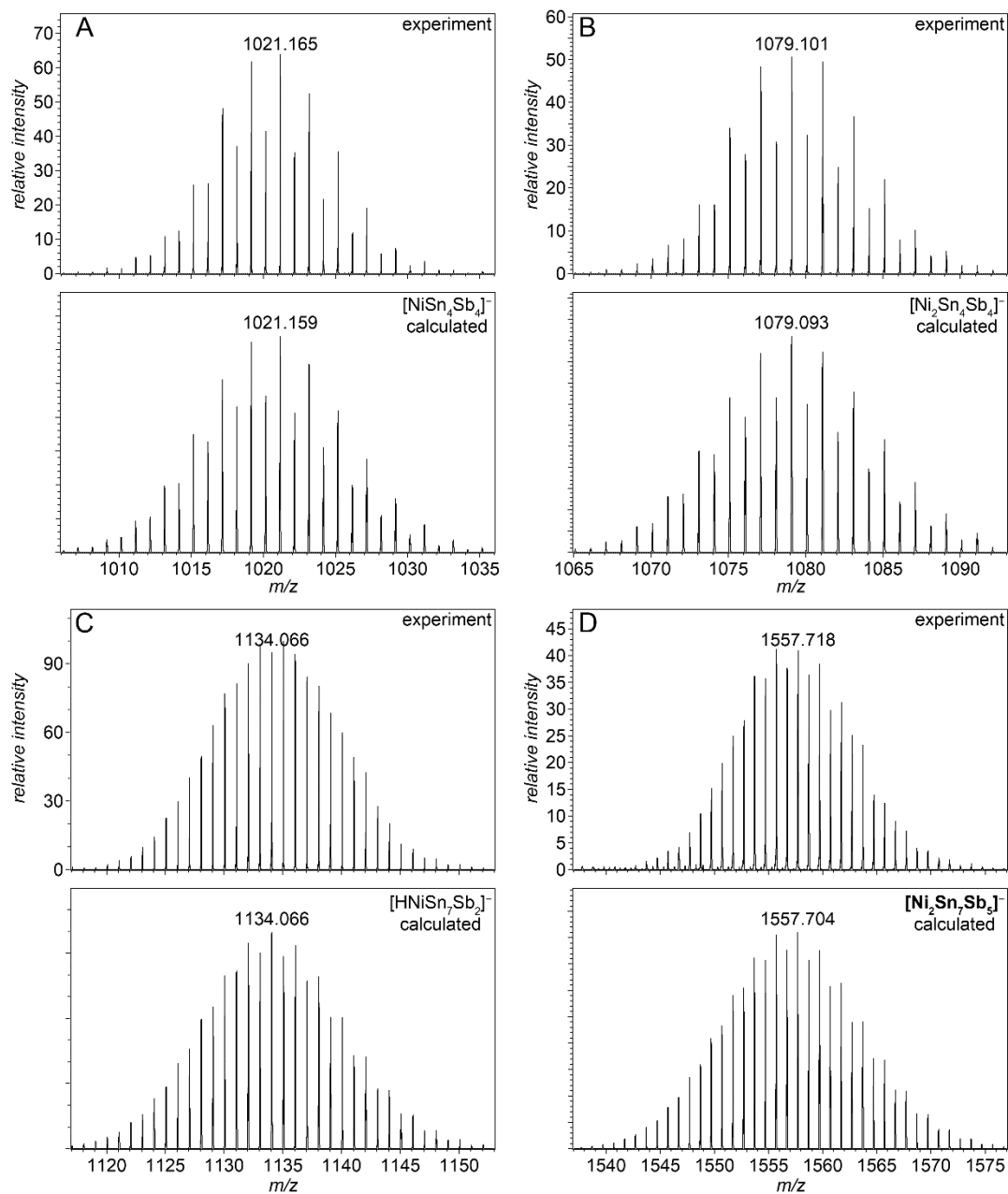


**Figure S22.** High resolution ESI(-) mass signals of (A)  $[\text{NiSn}_4\text{Sb}_4]^-$ , (B)  $[\text{Ni}_2\text{Sn}_4\text{Sb}_4]^-$ , (C)  $[\text{HNiSn}_7\text{Sb}_2]^-$ , and (D)  $[\text{Ni}_2\text{Sn}_7\text{Sb}_5]^-$ .

#### 4.5.4 Micro-X-ray Fluorescence Spectroscopy ( $\mu$ -XFS)

All  $\mu$ -XFS measurements were performed with a Bruker M4 Tornado, equipped with a Rh-target X-ray tube and a silicon drift detector. The emitted fluorescence photons are detected with an acquisition time of 100 s. Quantification of the elements is achieved through deconvolution of the spectra. Results are summarized in Table S4. K is omitted from the quantification results, as it is often overestimated with this technique. Figures S23-S25 present the measured spectra for single crystals of [K(crypt-222)]<sub>3</sub>[Co@Sn<sub>6</sub>Sb<sub>6</sub>]<sub>0.825</sub>[Co<sub>2</sub>@Sn<sub>5</sub>Sb<sub>7</sub>]<sub>0.175</sub>, [K(crypt-222)]<sub>3</sub>[Ni<sub>2</sub>@Sn<sub>7</sub>Sb<sub>5</sub>], and [K(crypt-222)]<sub>3</sub>[Co<sub>2</sub>@Sn<sub>5</sub>Sb<sub>7</sub>] along with the results of the deconvolution algorithm.

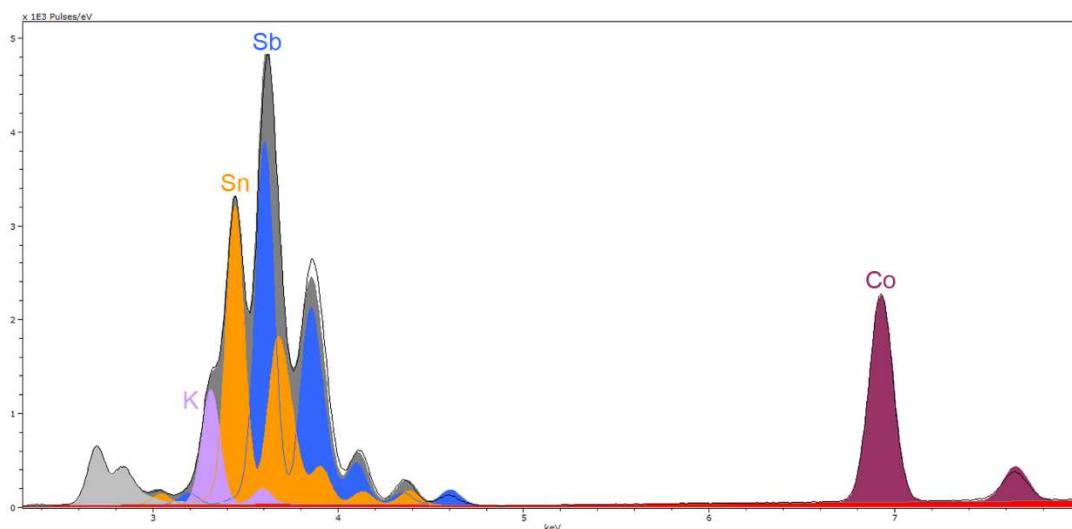


**Figure S23.**  $\mu$ -XF spectrum of [K(crypt-222)]<sub>3</sub>[Co@Sn<sub>6</sub>Sb<sub>6</sub>]<sub>0.825</sub>[Co<sub>2</sub>@Sn<sub>5</sub>Sb<sub>7</sub>]<sub>0.175</sub>·2dmf·2tol (line) with the results of the deconvolution algorithm (solid, colored). Element colors are as follows: K (pink), Sn (orange), Sb (blue), Co (purple).



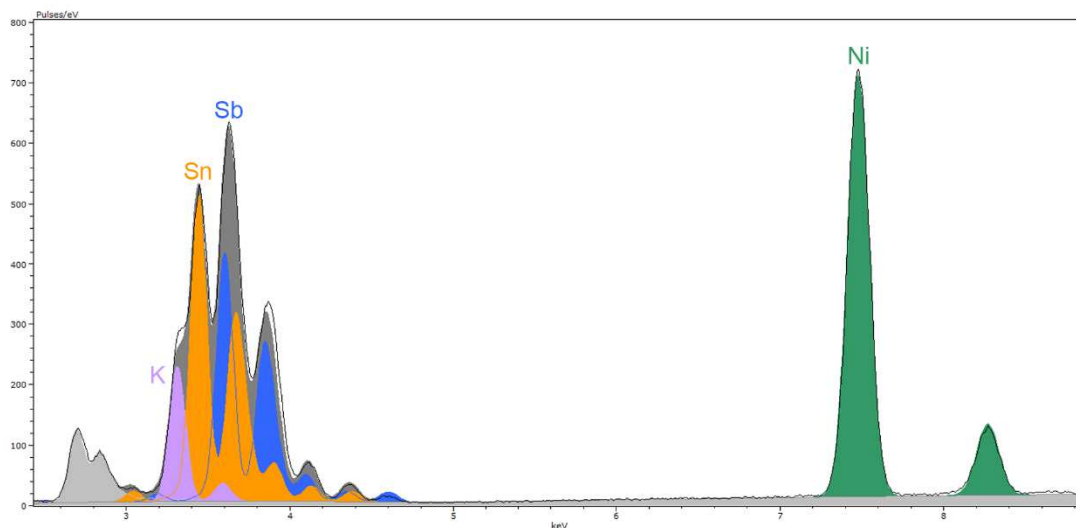


**Figure S24.**  $\mu$ -XF spectrum of  $[\text{K}(\text{crypt-222})]_3[\text{Ni}_2@ \text{Sn}_7\text{Sb}_5] \cdot 2\text{en} \cdot 2\text{tol}$  (line) with the results of the deconvolution algorithm (solid, colored). Element colors are as follows: K (pink), Sn (orange), Sb (blue), Ni (green).

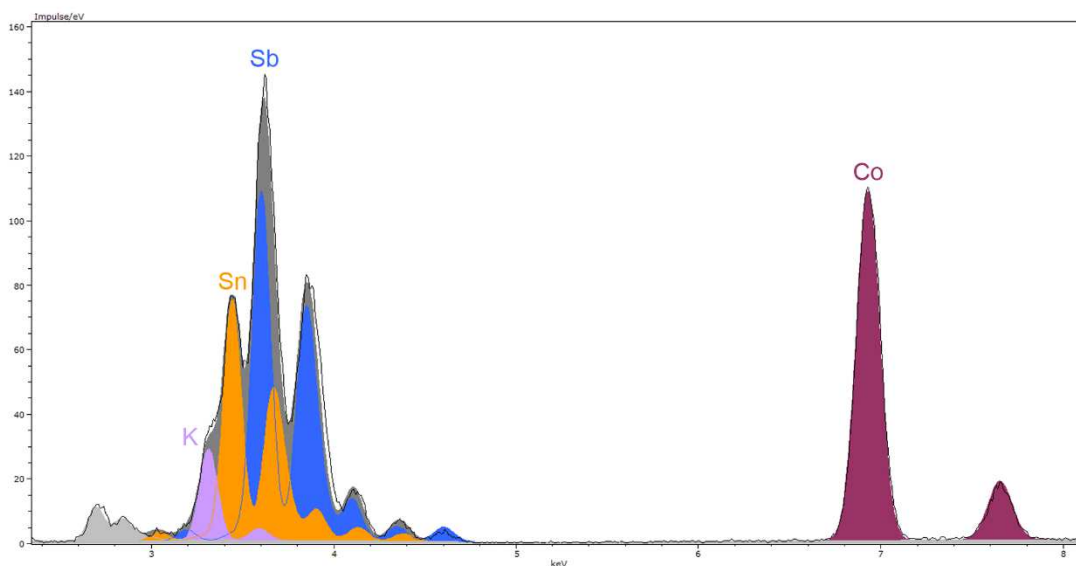


**Figure S25.**  $\mu$ -XF spectrum of  $[\text{K}(\text{crypt-222})]_3[\text{Co}_2@ \text{Sn}_5\text{Sb}_7]$  (line) with the results of the deconvolution algorithm (solid, colored). Element colors are as follows: K (pink), Sn (orange), Sb (blue), Co (purple).

**Table S4.** Results of semi-quantitative analysis of  $\mu$ -XFS for single crystals of [K(crypt-222)]<sub>3</sub>[Co@Sn<sub>6</sub>Sb<sub>6</sub>]<sub>0.825</sub>[Co<sub>2</sub>@Sn<sub>5</sub>Sb<sub>7</sub>]<sub>0.175</sub>·2dmf·2tol, [K(crypt-222)]<sub>3</sub>[Ni<sub>2</sub>@Sn<sub>7</sub>Sb<sub>5</sub>]·2en·2tol, and [K(crypt-222)]<sub>3</sub>[Co<sub>2</sub>@Sn<sub>5</sub>Sb<sub>7</sub>].

<b>[K(crypt-222)]<sub>3</sub>[Co@Sn<sub>6</sub>Sb<sub>6</sub>]<sub>0.825</sub>[Co<sub>2</sub>@Sn<sub>5</sub>Sb<sub>7</sub>]<sub>0.175</sub>·2dmf·2tol</b>				
	Experimental wt. %	Calculated wt. %	Experimental atom %	Calculated atom %
Sn - L	46.24	45.72	44.66	44.21
Sb - L	49.04	49.71	46.18	46.87
Co - K	4.72	4.58	9.17	8.92
<b>[K(crypt-222)]<sub>3</sub>[Ni<sub>2</sub>@Sn<sub>7</sub>Sb<sub>5</sub>]·2en·2tol</b>				
	Experimental wt. %	Calculated wt. %	Experimental atom %	Calculated atom %
Sn - L	53.46	53.36	50.14	50.00
Sb - L	39.10	39.10	35.76	35.71
Ni - K	7.44	7.54	14.12	14.29
<b>[K(crypt-222)]<sub>3</sub>[Co<sub>2</sub>@Sn<sub>5</sub>Sb<sub>7</sub>]</b>				
	Experimental wt. %	Calculated wt. %	Experimental atom %	Calculated atom %
Sn - L	40.24	37.96	38.04	35.71
Sb - L	52.80	54.51	48.69	50.00
Co - K	6.96	7.54	13.26	14.29

4.5.5  $^{119}\text{Sn}$  NMR

## 4.5.5.1 Methods

Samples were dissolved in  $d_7$ -DMF (Sigma Aldrich, 99.5%) and sealed in NMR tubes with J-Young valves in a glove box under a nitrogen atmosphere. Measurements were recorded on a Bruker Avance III 600 Spectrometer with a Cryoprobe Prodigy BBO probe head except for the spectrum of the pure precursor (Figure S30), which was done on a Bruker Avance III 300 Spectrometer. The temperatures for all measurements were controlled by a Bruker BCU II temperature unit. All measurements were carried out at 300 K. In order to optimize the sensitivity, a standard Bruker pulse program (zg,  $90^\circ$  pulse, 13.5  $\mu\text{s}$ ) with 10240 scans (approx. 4 h), a spectral width of 447 ppm, and relaxation delay of 1 s were used. The chemical shifts are reported in parts per million (ppm) relative to  $\text{SnMe}_4$  (90% in  $\text{C}_6\text{D}_6$ ) as an external standard. Data were processed with the Bruker TOPSPIN 3.2 and MestReNova 6.0 software. Note that each  $^{119}\text{Sn}$  spectrum consists of several spectra with a sweep width of 447 ppm to provide flat excitation profiles.

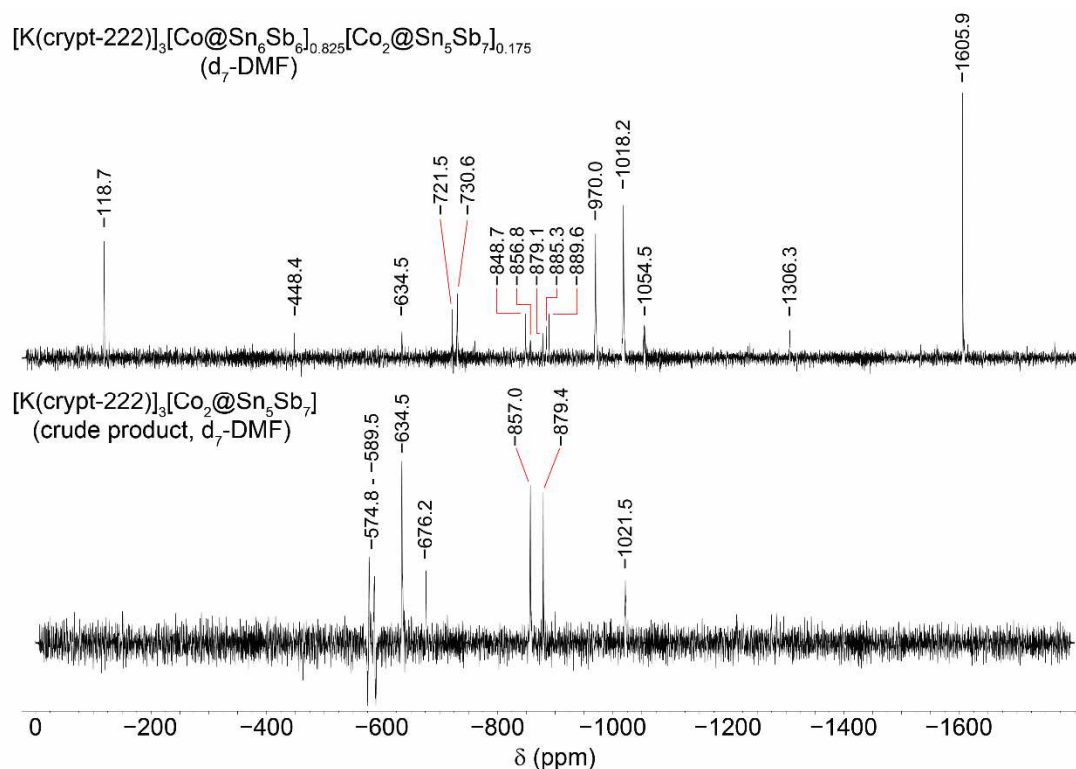


**Figure S26.** Comparison of  $^{119}\text{Sn}$  NMR spectra of Co/Sn/Sb cluster salts. Top: Spectra obtained from crystals of  $[\text{K}(\text{crypt-222})]_3[\text{Co}@\text{Sn}_6\text{Sb}_6]_{0.825}[\text{Co}_2@\text{Sn}_5\text{Sb}_7]_{0.175} \cdot 2\text{dmf} \cdot 2\text{tol}$  in dissolved in  $d_7$ -DMF. Bottom: spectrum obtained from  $[\text{K}(\text{crypt-222})]_3[\text{Co}_2@\text{Sn}_5\text{Sb}_7]$  (crude powder) dissolved in  $d_7$ -DMF and filtered through a PTFE filter with a 0.45  $\mu\text{m}$  pore size. Note: the peak at  $-1606$  ppm (top spectrum) can be confidently assigned to  $(\text{Sn}_2\text{Sb}_2)^{2-}$ ; [24] we tentatively assign the peak at  $-574.8 - -589.5$  ppm to  $[\text{Co}@\text{Sn}_6\text{Sb}_3]^{2-}$ . Note that this peak is distorted due to baseline correction.

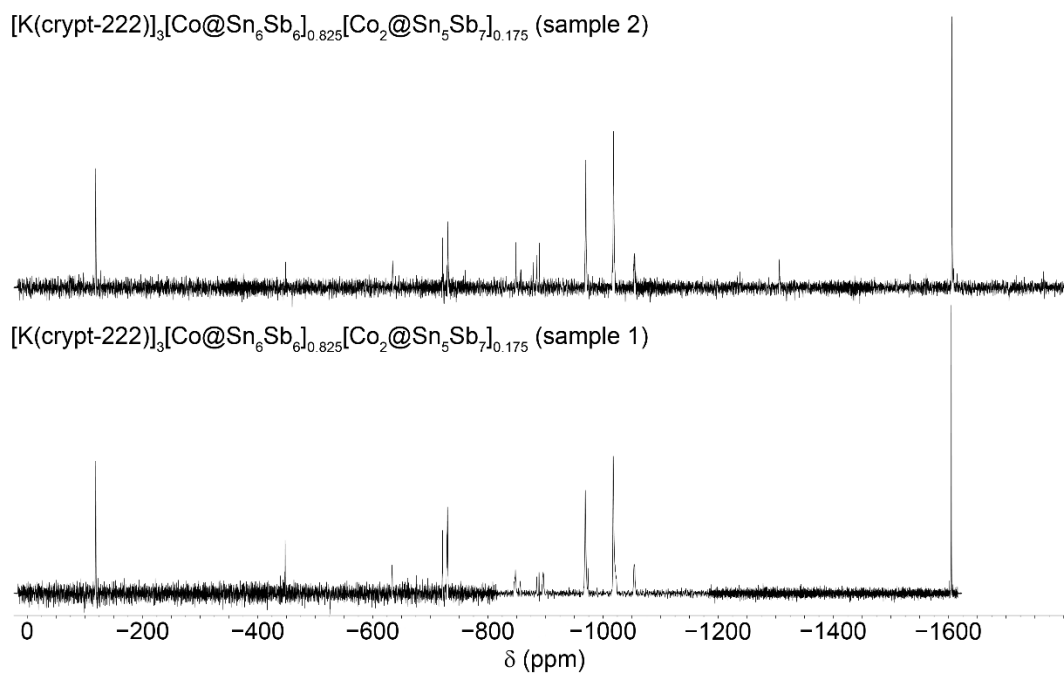


**Figure S27.**  $^{119}\text{Sn}$  NMR spectra of crystals of  $[\text{K}(\text{crypt-222})]_3[\text{Co@Sn}_6\text{Sb}_6]_{0.825}[\text{Co}_2\text{@Sn}_5\text{Sb}_7]_{0.175} \cdot 2\text{dmf} \cdot 2\text{tol}$  dissolved in  $\text{d}_7$ -DMF from two different syntheses. Note that the sharp signal  $-1606$  ppm is attributed to unreacted  $[\text{K}(\text{crypt-222})]_2(\text{Sn}_2\text{Sb}_2)$ .<sup>[24]</sup>

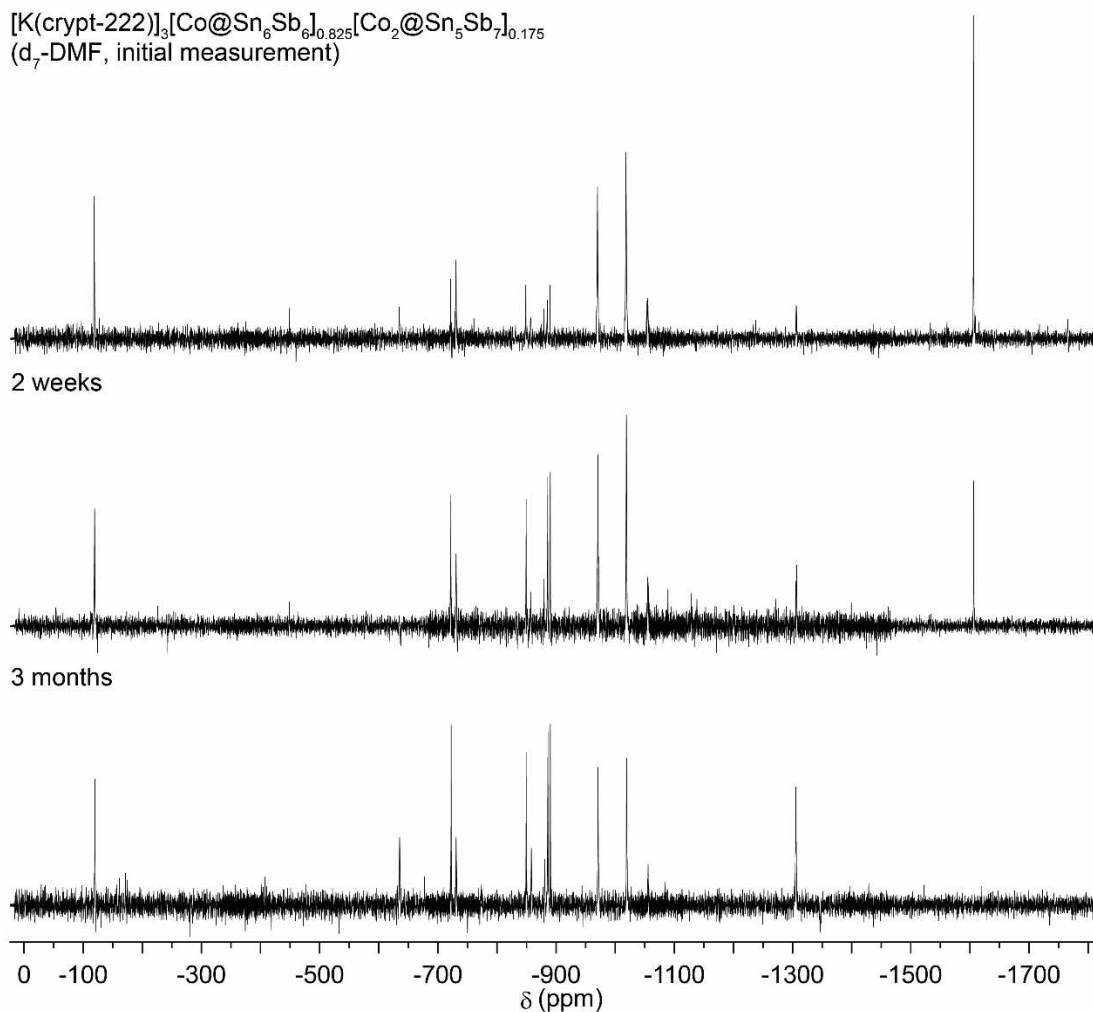


**Figure S28.**  $^{119}\text{Sn}$  NMR spectra of crystals of  $[\text{K}(\text{crypt-222})]_3[\text{Co@Sn}_6\text{Sb}_6]_{0.825}[\text{Co}_2@\text{Sn}_5\text{Sb}_7]_{0.175} \cdot 2\text{dmf} \cdot 2\text{tol}$  dissolved in  $d_7$ -DMF recorded (top) immediately, (middle) after 2 weeks, and (bottom) after 3 months in solution. The sample was stored in a sealed J-young tube under a nitrogen atmosphere between measurements. The signal at  $-1606$  ppm, unreacted  $[\text{K}(\text{crypt-222})]_2(\text{Sn}_2\text{Sb}_2)$ , disappears, while signals at  $-722$ ,  $-849$ ,  $-885$ ,  $-890$ , and  $-1306$  ppm increase in intensity.<sup>[24]</sup>

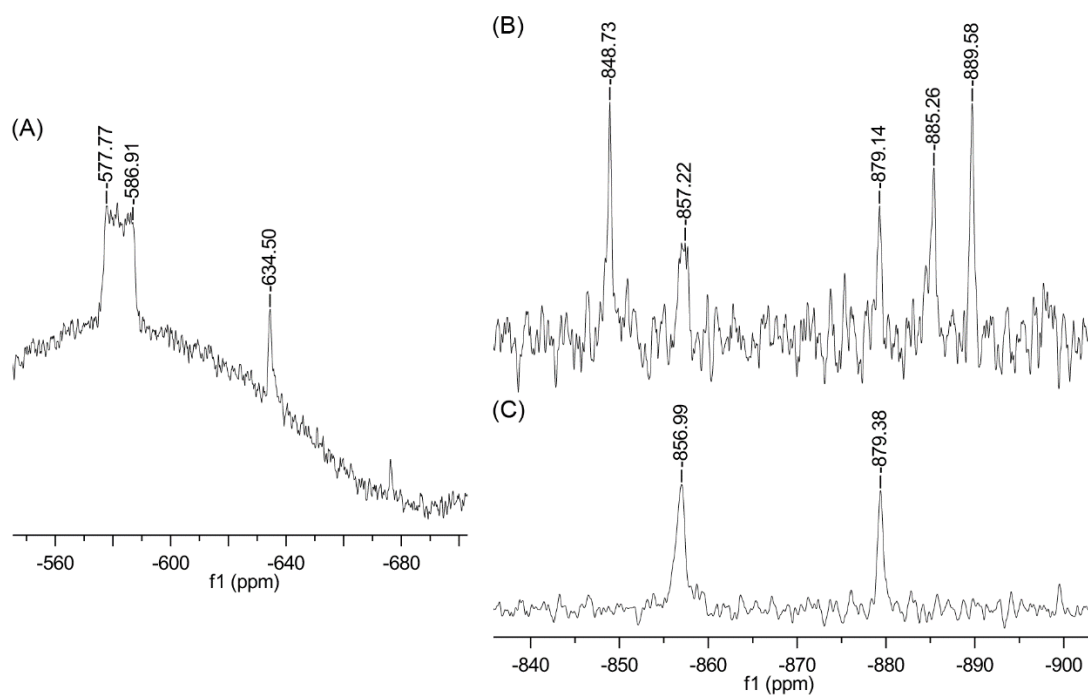


**Figure S29.** Close-up images of  $^{119}\text{Sn}$  NMR spectra recorded in  $d_7$ -DMF. (A) A section of the spectrum obtained from a filtered solution of the powder containing  $[\text{K}(\text{crypt-222})]_3[\text{Co}_2@\text{Sn}_5\text{Sb}_7]$ , shown without baseline correction. (B) A section of the spectrum obtained from  $[\text{K}(\text{crypt-222})]_3[\text{Co}@\text{Sn}_6\text{Sb}_6]_{0.825}[\text{Co}_2@\text{Sn}_5\text{Sb}_7]_{0.175}\cdot 2\text{dmf}\cdot 2\text{tol}$  and (C) the same region from the spectrum obtained from a filtered solution of the powder containing  $[\text{K}(\text{crypt-222})]_3[\text{Co}_2@\text{Sn}_5\text{Sb}_7]$  (not to scale).

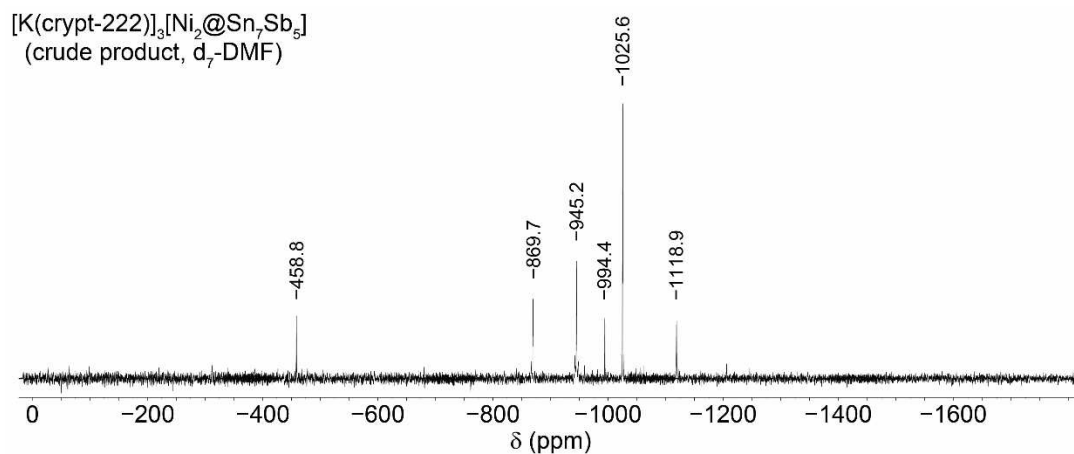


**Figure S30.**  $^{119}\text{Sn}$  NMR spectrum obtained from  $[\text{K}(\text{crypt-222})]_3[\text{Ni}_2@\text{Sn}_7\text{Sb}_5]$  (crude powder) dissolved in  $d_7$ -DMF and filtered through a PTFE filter with a  $0.45\ \mu\text{m}$  pore size.

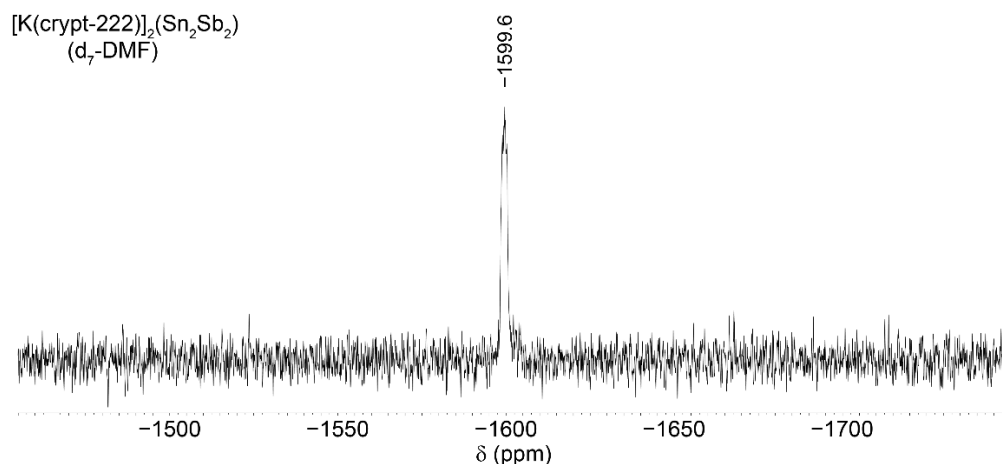


**Figure S31.**  $^{119}\text{Sn}$  NMR spectrum obtained from single crystals of  $[\text{K}(\text{crypt-222})]_2(\text{Sn}_2\text{Sb}_2)$  dissolved in  $d_7$ -DMF. Note that this spectrum was the only one measured on a Bruker Avance III 300 spectrometer.

## 4.5.6 Quantum Chemical Investigations

### 4.5.6.1 Quantum Chemical Methods and Comparison of Isomers

Calculations were done at DFT level with TURBOMOLE.<sup>[25]</sup> For a systematic investigation of the energy surfaces of  $(\text{CoSn}_6\text{Sb}_6)^{3-}$ ,  $(\text{Co}_2\text{Sn}_5\text{Sb}_7)^{3-}$ ,  $(\text{Ni}_2\text{Sn}_7\text{Sb}_5)^{3-}$ ,  $(\text{CoSn}_5\text{Sb}_7)^{3-}$  and  $(\text{CoSn}_7\text{Sb}_5)^{3-}$ , genetic algorithm procedures, extended by atom type assignment via perturbation theory,<sup>[26]</sup> were carried out. The number of generations was set to 30, the size of each generation to 25; in each generation the 13 energetically least favorable structures were replaced with newly generated ones. Within the genetic algorithm the BP86 functional<sup>[27]</sup> with def-SV(P) bases<sup>[28]</sup> was used. For the final populations, structure parameters were optimized using the TPSS functional<sup>[29]</sup> and basis sets of type dhf-TZVP<sup>[30]</sup> together with respective effective core potentials (for Sn and Sb).<sup>[31]</sup> The negative charge was compensated with the conductor-like screening model, COSMO,<sup>[32]</sup> used with default settings. The energetically most favorable structures are shown in Figure S32, comparison of average bond lengths of 1, 2, and 3 with those of their corresponding minimum energy isomers are provided in Table S5. NMR shielding constants for related, known compounds with experimentally measured NMR shifts (Table S6), for the ten most favorable isomers of  $(\text{CoSn}_6\text{Sb}_6)^{3-}$  (Table S7), and for the 15 most stable isomers of  $(\text{Co}_2\text{Sn}_5\text{Sb}_7)^{3-}$  (Table S8) were calculated at the same level, but using the all-electron basis TZVPall<sup>[33]</sup> for Sn. A statistical summary is given in Table S9. In Table S10 results with further functionals are shown for comparison. All isomers are of the same topology; for the numbering of atomic positions see Figure S34. Calculated shifts of additional compounds (for comparison) is given in Table S11.

## 4.5.6.2 Comparison of bond lengths

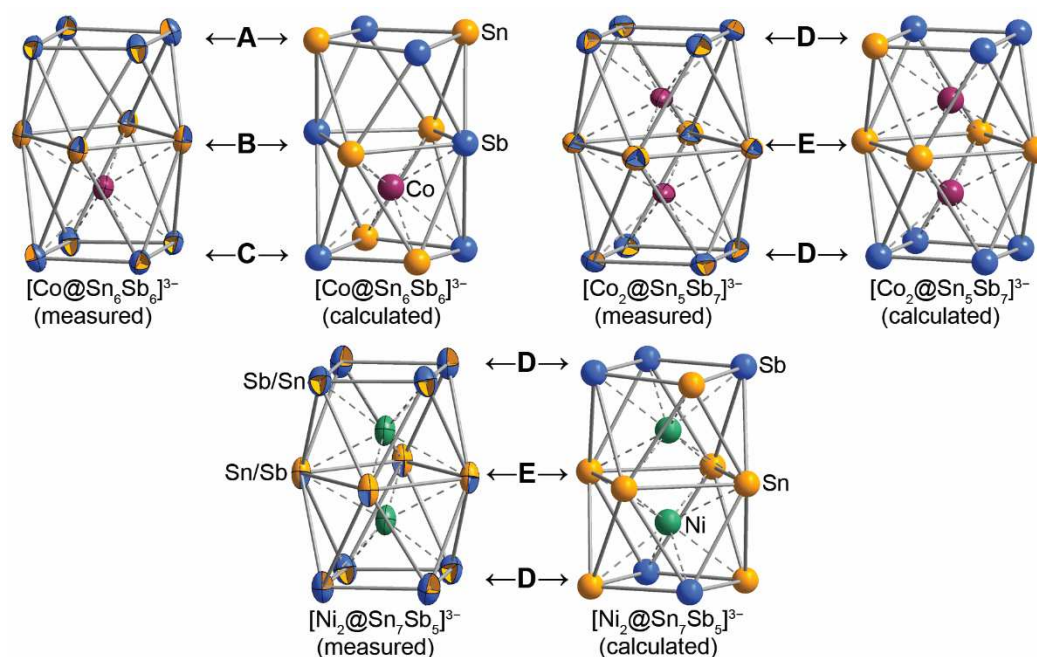


**Figure S32.** Comparison of experimental structures from diffraction data of 1, 2, and 3 with those of their corresponding minimum energy isomers.

**Table S5.** Comparison of average bond lengths of 1, 2, and 3 with those of their corresponding minimum energy isomers.

	[Co@Sn <sub>6</sub> Sb <sub>6</sub> ] <sup>3-</sup> (1)			[Co <sub>2</sub> @Sn <sub>5</sub> Sb <sub>7</sub> ] <sup>3-</sup> (2)			[Ni <sub>2</sub> @Sn <sub>7</sub> Sb <sub>5</sub> ] <sup>3-</sup> (3)		
	meas.	calcd.	diff.	meas.	calcd.	diff.	meas.	calcd.	diff.
A-A	2.867(4)	2.913(9)	0.046	2.885(3)	2.902(23)	0.017	2.897(4)	2.930(31)	0.033
D-D									
A-B	3.065(20)	3.113(70)	0.048	3.253(14)	3.260(25)	0.007	3.275(19)	3.282(34)	0.007
D-E									
B-B	3.144(35)	3.121(46)	-0.023	3.298(10)	3.294(29)	0.004	3.264(27)	3.306(28)	0.042
E-E									
B-C	3.450(17)	3.360(34)	-0.090	–	–	–	–	–	–
C-C	2.867(4)	2.895(6)	0.028	–	–	–	–	–	–
M-B	2.599(10)	2.535(49)	-0.064	2.626(11)	2.628(16)	0.002	2.609(5)	2.636(17)	0.027
M-E									
M-C	2.640(11)	2.651(15)	0.011	2.575(10)	2.582(37)	0.007	2.595(12)	2.609(37)	0.014
M-D									
M-M	–	–	–	2.411(2)	2.435	0.024	2.432(2)	2.435	0.003

M = Co or Ni



## 4.5.6.3 Study of the influence of electron numbers on the structures

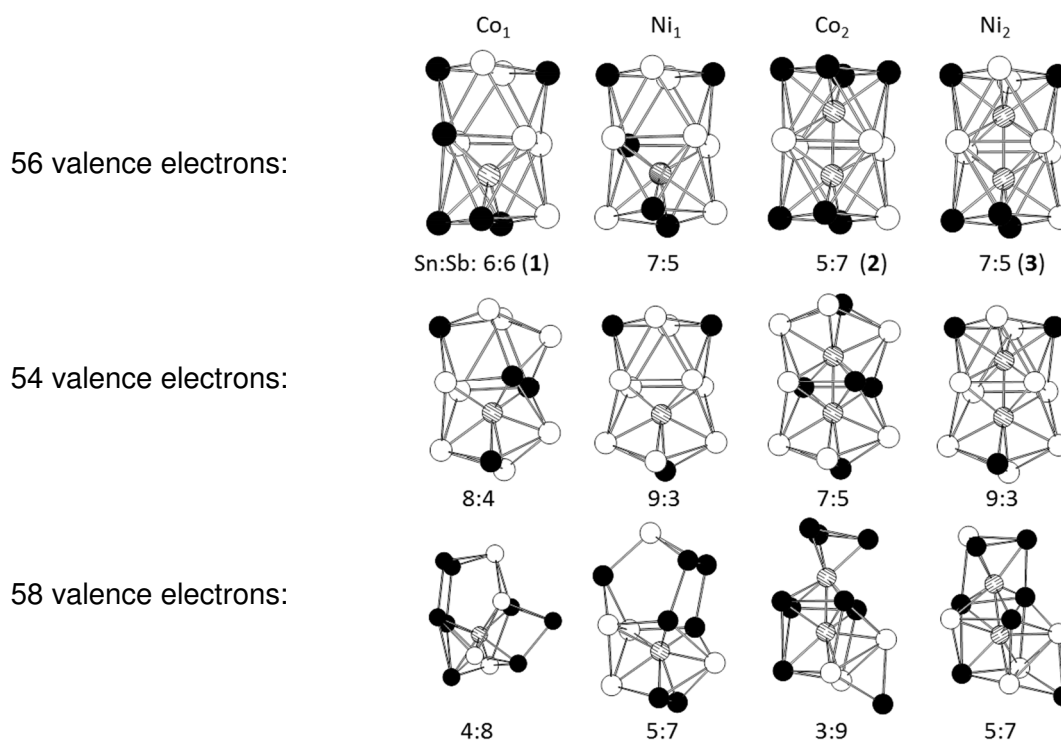


**Figure S33.** Global minimum structures of  $[Mx@(\text{Sn},\text{Sb})_{12}]$  ( $M = \text{Co}, \text{Ni}; x = 1, 2$ ; Sn:Sb ratio given in the graphic), running from  $[\text{Co}@(\text{Sn}_6\text{Sb}_6)]^{3-}$  (top left) to  $[\text{Ni}_2@(\text{Sn}_5\text{Sb}_7)]^{3-}$  (bottom right), comprising 56 (top row), 54 (middle row) or 58 valence electrons (bottom row), respectively, as obtained from a genetic algorithm. Sn atoms are drawn as empty, Sb atoms as black spheres. The addition of 2  $e^-$  causes extreme distortions away from the original structures, while the loss of 2  $e^-$  does not lead to the collapse of the fused antiprismatic structure, but rather to slight distortions into (near)  $C_{2v}$ -symmetric cages, independent of the nature and number of the interstitial atoms.

Two electrons were added or subtracted from the 56 electron clusters by swapping two Sb for two Sn atoms, and vice versa, while maintaining the  $-3$  charge, yielding 58 or 54 valence electron species, respectively. The lowest energy geometries of these hypothetical anions were then determined, again using the genetic algorithm. As shown in the figure, the addition of 2  $e^-$  causes extreme distortions away from the original structure, while the loss of 2  $e^-$  does not lead to the collapse of the fused antiprismatic structure, but the slight distortions only. For  $[\text{Co}_1@(\text{Sn}_6\text{Sb}_6)]$  (1), the latter yields a (near)  $C_{2v}$ -symmetric cage, which is similar to those found previously in a systematic study<sup>[34]</sup> of 12-atom (Co-free) Pb/Bi clusters for the range of 52 to 55 valence electrons. Very similar results are obtained for 2, 3, and the hypothetical species  $[\text{Ni}@(\text{Sn}_7\text{Sb}_5)]^{3-}$ . Further withdrawal of electrons from 1 by replacing Sb with Sn atoms inevitably ends at the icosahedral 50 valence electron structure of a hypothetical  $[\text{Co}@(\text{Sn}_{12})]^{3-}$ , which is very obviously not formed under the given experimental conditions. Interestingly, the hypothetical 60  $e^-$   $[\text{Co}@(\text{Sn}_2\text{Sb}_{10})]^{3-}$  does not seem to exist in a stable  $D_{2d}$ -type structure as a local minimum.

The genetic algorithm (GA) did not yield low-energy isomers with a structure such as found for [TaGe<sub>8</sub>As<sub>4</sub>]<sup>3–</sup>,<sup>[35]</sup> and separate calculations starting out from a corresponding D<sub>2d</sub>-type geometry, with all possible distributions of the Sn and Sb atoms, all end up with highly distorted cages with significantly higher energies than all of the structures of the final GA population (energy difference of the best D<sub>2d</sub>-type structure from the lowest energy isomer of the final GA population: +66 kJ·mol<sup>–1</sup>; energy difference from the highest energy isomer of the final GA population: +29 kJ·mol<sup>–1</sup>). This indicates that not only the total electron number, but also the nature and charge of the central atom controls the overall topology of the cluster.

#### 4.5.6.4 Calculation of chemical shifts

Validation of the method for calculating <sup>119</sup>Sn chemical shifts [ $\delta$  given in ppm relative to SnMe<sub>4</sub>] was done on the following experimentally observed species (X-ray, NMR and/or ESI-MS), highly related to the title compounds (Table S6). The shift values match within the expected error range of the method of  $\pm 200$  ppm (rightmost column) and reproduce well changes that are observed upon insertion of metal ions in a [Sn<sub>9</sub>]<sup>4–</sup> cage. It confirms that the sign of the deviation of the calculated shift value can vary in different systems, such as a slight upfield deviation observed for the (Sn<sub>2</sub>Sb<sub>2</sub>)<sup>2–</sup> anion versus a slight downfield deviation observed for [Sn<sub>9</sub>]<sup>4–</sup> and (somewhat more pronounced) upon insertion of Cu<sup>+</sup> or Co<sup>–</sup> to form [M@Sn<sub>9</sub>]<sup>3–</sup>. Finally, the study shows that massive charge overload at the Sn atoms, such as observed for [Sn<sub>4</sub>]<sup>4–</sup>, with one full negative charge per atom, leads to more dramatic deviations and therefore need to be handled with care.

**Table S6.** <sup>119</sup>Sn chemical shifts of known species (given in ppm relative to SnMe<sub>4</sub>), difference in chemical shifts upon inclusion of Cu<sup>+</sup> or Co<sup>–</sup> into [Sn<sub>9</sub>]<sup>4–</sup>. The calculated individual values – three for C<sub>4v</sub> or two for D<sub>3h</sub> (idealized) point group symmetries of the 9-atom cages – were averaged.

Species	Observation Method	Measured shift(s)	$\Delta\delta_{f-e}^g$	Ref.	Calculated shift(s)	$\Delta\delta_{f-e}^g$	$\Delta\delta_{exp-DFT}$
(Sn <sub>2</sub> Sb <sub>2</sub> ) <sup>2–</sup>	X-ray, NMR, ESI-MS	–1600	–	Fig. S30	–1683	–	–83
[Sn <sub>9</sub> ] <sup>4–</sup>	X-ray, NMR, ESI-MS	–1230 <sup>a</sup> –1149 <sup>b</sup>	0	[36]	–1149 <sup>d</sup>	0	+81 $\pm$ 0
[Cu@Sn <sub>9</sub> ] <sup>3–</sup>	X-ray, NMR	–1440	–210 –291	[37]	–1320 <sup>e</sup>	–171	+120
[CoSn <sub>9</sub> ] <sup>5–</sup>	X-ray, NMR	–776 <sup>c</sup>	+454 +373	[38]	–975 <sup>f</sup>	+174	–199
[Sn <sub>4</sub> ] <sup>4–</sup>	X-ray, NMR, ESI-MS	–1728	–	[39]	–2109	–	–381

<sup>a</sup> [Na(crypt-222)]<sup>+</sup> salt in en

<sup>b</sup> K<sup>+</sup> salt in DMF

<sup>c</sup> solid state <sup>119</sup>Sn MAS-NMR

<sup>d</sup> Average value in C<sub>4v</sub> symmetry: –1157, average value in D<sub>3h</sub> symmetry: –1141.

<sup>e</sup> Average value in C<sub>4v</sub> symmetry: –1332, average value in D<sub>3h</sub> symmetry: –1308.

<sup>f</sup> Average value in C<sub>4v</sub> and D<sub>3h</sub> symmetry: –975.

<sup>g</sup>  $\Delta\delta_{filled-empty}$

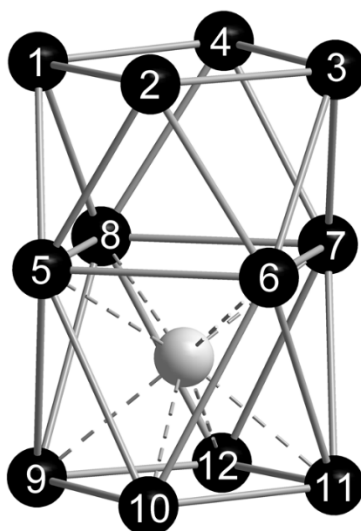


**Figure S34.** Numbering of Sn atoms in the cluster anions  $(\text{Co}_1\text{Sn}_6\text{Sb}_6)^{3-}$ , and  $(\text{Co}_2\text{Sn}_5\text{Sb}_7)^{3-}$ ; for the latter a second Co atom resides in the upper half of the molecule.

**Table S7.** Relative energy  $E$  and  $^{119}\text{Sn}$  chemical shifts relative to  $\text{SnMe}_4$  ( $\delta$  in ppm) at the 12 possible Sn positions for the ten most stable isomers A-J of  $(\text{Co}_1\text{Sn}_6\text{Sb}_6)^{3-}$  at level TPSS/COSMO (with default settings) with dhf-TZVP bases for Co and Sb (plus respective ECPs at Sb) and all-electron bases TZVPPall for Sn.

	$E$ (kJ/mol)	1	2	3	4	5	6	7	8	9	10	11	12
<b>A</b>	0		-1089		-1088		-538	-522	-404			-335	
<b>B</b>	2.6		-1122		-1125	-542		-539		-137		-132	
<b>C</b>	3.2		-1087	-1153		-337	-578		-462			-117	
<b>D</b>	3.9	-1194		-960		-413	-453	-463				-147	
<b>E</b>	4.2	-1185		-943			-436	-466	-426			-165	
<b>F</b>	8.1	-1131		-904		-447	-567		-349			40	
<b>G</b>	11.2	-1046		-1044			-517		-519	99		105	
<b>H</b>	14.1		-1020		-1289	-456	-456			-184		-184	
<b>I</b>	16.6			-1229	-1476	-241	-591		-523			148	
<b>J</b>	17.4	-996		-999		-407	-404			23		35	

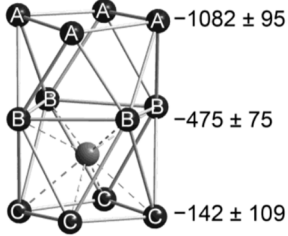
**Table S8.** Relative energy  $E$  and chemical shifts relative to SnMe<sub>4</sub> at the 12 possible Sn positions for the 15 most stable isomers A-O of (Co<sub>2</sub>Sn<sub>5</sub>Sb<sub>7</sub>)<sup>3-</sup>. See also Table S4.

	$E$ (kJ/mol)	1	2	3	4	5	6	7	8	9	10	11	12
<b>A</b>	0					-387	-527	-523	-383				-993
<b>B</b>	3.7			-715		-238	-628		-302				-715
<b>C</b>	6.5		-930			-373	-615		-305				-807
<b>D</b>	7.0		-853			-483		-482	-219				-852
<b>E</b>	8.9			-875			-567	-463	-347				-875
<b>F</b>	10.3					-467	-367	-455		-727			-777
<b>G</b>	10.6				-945		-475	-498	-481				-938
<b>H</b>	11.8		-619		-693		-635		-416				-764
<b>I</b>	12.0	-968				-493	-365	-422					-1026
<b>J</b>	15.1	-857		-537			-589		-439				-890
<b>K</b>	15.4		-670		-676		-488	-486					-837
<b>L</b>	15.7		-648		-648	-341			-341				-689
<b>M</b>	16.2	-850		-508		-342	-486						-902
<b>N</b>	17.7		-654		-723	-335	-527						-816
<b>O</b>	21.6		-616		-552				-497	-545			-624

**Table S9.** Statistical evaluation (minimum, maximum, average values and standard deviations) of chemical shifts for isomers of (Co<sub>1</sub>Sn<sub>6</sub>Sb<sub>6</sub>)<sup>3-</sup> and (Co<sub>2</sub>Sn<sub>5</sub>Sb<sub>7</sub>)<sup>3-</sup> with relative energies lower than 10 kJ·mol<sup>-1</sup>. A pictorial summary of the values is given below shifts (± standard deviation, caused by the different Sn/Sb distributions in the different isomers).

		1 - 4				5 - 8				9 - 12			
structures		min	max	avg	sig	min	max	avg	sig	min	max	avg	sig
(Co <sub>1</sub> Sn <sub>6</sub> Sb <sub>6</sub> ) <sup>3-</sup>	A-F	-1194	-904	-1082	95	-578	-357	-475	75	-335	40	-142	109
(Co <sub>2</sub> Sn <sub>5</sub> Sb <sub>7</sub> ) <sup>3-</sup>	A-E					5 - 8				1 - 4, 9 - 12			
						-628	-219	-428	127	-993	-715	-847	91

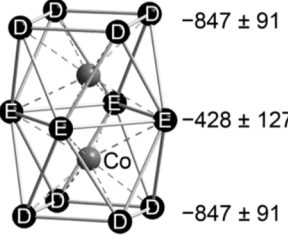
  



-1082 ± 95 ppm

-475 ± 75

-142 ± 109



-847 ± 91

-428 ± 127

-847 ± 91

## 4.5 Supporting Information

**Table S10.**  $^{119}\text{Sn}$  chemical shifts (in ppm relative to  $\text{SnMe}_4$ ) for the most favorable isomer of  $(\text{Co}_1\text{Sn}_6\text{Sb}_6)^{3-}$  calculated with different functionals and settings for the dielectric constant ( $\epsilon$ ). For Co the (all-electron) bases dhf-TZVP are used throughout, for Sn the TZVPPall all-electron basis.

Method		position					
functional	$\epsilon$	2	4	6	7	8	11
TPSS	$\infty$	-1088	-1089	-538	-522	-404	-335
TPSS	36.7	-1079	-1084	-538	-523	-406	-325
TPSSH	$\infty$	-1087	-1097	-545	-522	-423	-273
PBE	$\infty$	-1114	-1120	-522	-507	-385	-351
PBE0	$\infty$	-1130	-1127	-547	-507	-432	-200

**Table S11.**  $^{119}\text{Sn}$  chemical shifts (in ppm relative to  $\text{SnMe}_4$ ) of potential impurities to show up in the spectra shown in Section 5.1. For simplicity, the shifts of different positions have been averaged. Some of the values shown in Table S6 are repeated here for comparison.

Species	Observation Method	Calculated shift values (averaged for different positions)	Ref.
$[\text{Sn}_4]^{4-}$ ( $T_d$ )	X-Ray, ESI-MS, NMR	-2109	[39]
$(\text{SnSb}_3)^-$ ( $C_{3v}$ )	ESI-MS	-1655	this work
$(\text{Sn}_2\text{Sb}_2)^{2-}$ ( $C_{2v}$ )	X-Ray, ESI-MS, NMR	-1683	this work
$(\text{Sn}_3\text{Sb})^{3-}$ ( $C_{3v}$ )	hypothetic	-1854	this work
$[\text{Sn}_9]^{4-}$ ( $D_{3h}$ )	X-Ray, ESI-MS, NMR	-1141	[36]
$[\text{Sn}_9]^{4-}$ ( $C_{4v}$ )	X-Ray, ESI-MS, NMR	-1157	[36]
$[\text{Co}@\text{Sn}_9]^{5-}$ ( $D_{3h}$ )	X-Ray, NMR	-975	[38]
$[\text{Co}@\text{Sn}_9]^{5-}$ ( $C_{4v}$ )	X-Ray, NMR	-975	[38]
$(\text{Sn}_7\text{Sb}_2)^{2-}$ ( $C_{2v}$ )	hypothetic	-770	–
$[\text{Co}@\text{Sn}_7\text{Sb}_2]^{3-}$ ( $C_{2v}$ )	hypothetic	-628	–
$(\text{Sn}_6\text{Sb}_3)^-$ ( $D_{3h}$ )	ESI-MS	-507	this work
$[\text{Co}@\text{Sn}_6\text{Sb}_6]^{2-}$ ( $D_{3h}$ )	ESI-MS	-368	this work

The effect of a downfield shift of the  $^{119}\text{Sn}$  chemical shift upon insertion of  $\text{Co}^-$  into a 9-atom cage is consistent. The effect, however, decreases with an increasing number of Sb atoms involved in the 9-atom cage (hence, with a decrease in negative charge of the cluster).

## 4.6 References

- [1] E. N. Esenturk, J. Fettinger, Y.-F. Lam, B. Eichhorn, *Angew. Chem.* **2004**, *116*, 2184-2186; *Angew. Chem. Int. Ed.* **2004**, *43*, 2132-2134.
- [2] a) E. N. Esenturk, J. Fettinger, B. Eichhorn, *J. Am. Chem. Soc.* **2006**, *128*, 9178-9186; b) J.-Q. Wang, S. Stegmaier, B. Wahl, T. F. Fässler, *Chem. Eur. J.* **2010**, *16*, 1793-1798.
- [3] The prefix “pseudo” refers to an actual symmetry reduction by slight distortions and/or the presence of two different element types.
- [4] a) G. Espinoza-Quintero, J. C. A. Duckworth, W. K. Myers, J. E. McGrady, J. M. Goicoechea, *J. Am. Chem. Soc.* **2014**, *136*, 1210-1213; b) S. Mitzinger, L. Broeckaert, W. Massa, F. Weigend, S. Dehnen, *Chem. Commun.* **2015**, *51*, 3866-3869; c) S. Mitzinger, L. Broeckaert, W. Massa, F. Weigend, S. Dehnen, *Nat. Commun.* **2016**, *7*, 10480.
- [5] B. Zhou, T. Kramer, A. L. Thompson, J. E. McGrady, J. M. Goicoechea, *Inorg. Chem.* **2011**, *50*, 8028-8037.
- [6] J. M. Goicoechea, J. E. McGrady, *Dalton Trans.* **2015**, *44*, 6755-6766.
- [7] a) F. Lips, S. Dehnen, *Angew. Chem.* **2011**, *123*, 986-990; *Angew. Chem. Int. Ed.* **2011**, *50*, 955-959; b) R. Ababei, J. Heine, M. Holynska, G. Thiele, B. Weinert, X. Xie, F. Weigend, S. Dehnen, *Chem. Commun.* **2012**, *48*, 11295-11297.
- [8] R. J. Wilson, L. Broeckaert, F. Spitzer, F. Weigend, S. Dehnen, *Angew. Chem.* **2016**, *128*, 11950-11955; *Angew. Chem. Int. Ed.* **2016**, *55*, 11775-11780.
- [9] S. Scharfe, T. F. Fässler, S. Stegmaier, S. D. Hoffmann, K. Ruhland, *Chem. Eur. J.* **2008**, *14*, 4479-4483.
- [10] a) E. N. Esenturk, J. Fettinger, B. Eichhorn, *Chem. Commun.* **2005**, 247-249; b) E. N. Esenturk, J. C. Fettinger, B. W. Eichhorn, *J. Am. Chem. Soc.* **2006**, *128*, 12-13; c) M. M. Gillett-Kunnath, J. I. Paik, S. M. Jensen, J. D. Taylor, S. C. Sevov, *Inorg. Chem.* **2011**, *50*, 11695-11701.
- [11] a) J.-Q. Wang, S. Stegmaier, T. F. Fässler, *Angew. Chem. Int. Ed.* **2009**, *48*, 1998-2002; b) V. Hlukhyy, H. He, L.-A. Jantke, T. F. Fässler, *Chem. Eur. J.* **2012**, *18*, 12000-12007; c) H. He, W. Klein, L.-A. Jantke, T. F. Fässler, *Z. Anorg. Allg. Chem.* **2014**, *640*, 2864-2870; d) X. Jin, G. Espinoza-Quintero, B. Below, V. Arcisauskaite, J. M. Goicoechea, J. E. McGrady, *J. Organomet. Chem.* **2015**, *792*, 149-153; e) C. Liu, I. A. Popov, L. J. Li, N. Li, A. I. Boldyrev, Z. M. Sun, *Chem. Eur. J.* **2018**, *24*, 699-705.

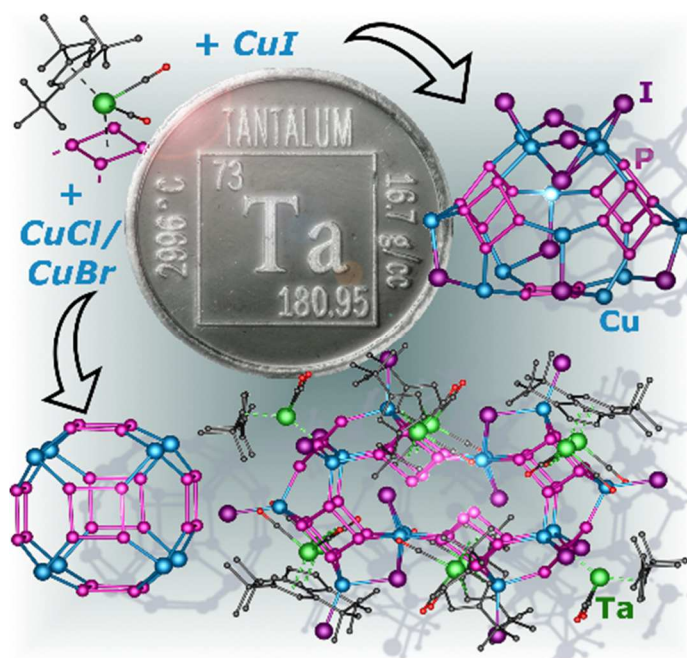
- [12] M. F. Groh, U. Müller, A. Isaeva, M. Ruck, *Z. Anorg. Allg. Chem.* **2017**, *643*, 1482-1490.
- [13] a) This geometry is also known to exist in a family of transition metal carbide clusters with the general formula  $[C_2@M_{10}M'_{2}(CO)_{22-24}]_4^-$  ( $M = M' = Rh$ ;  $M = Co$ ,  $M' = Pt$ ), as well as in  $[M_2E_{12}]$  units with topologically identical structural motifs in the extended solid state structures of Ir<sub>3</sub>Sn<sub>7</sub>- type phases and FeBi<sub>2</sub>. ; b) V. G. Albano, D. Braga, P. Chini, D. Strumolo, S. Martinengo, *J. Chem. Soc., Dalton Trans.* **1983**, 249-252; c) D. Strumolo, C. Seregni, S. Martinengo, V. G. Albano, D. Braga, *J. Organomet. Chem.* **1983**, *252*, C93-C96; d) V. G. Albano, D. Braga, D. Strumolo, C. Seregni, S. Martinengo, *J. Chem. Soc., Dalton Trans.* **1985**, 1309-1313; e) M. Schlüter, U. Häussermann, B. Heying, R. Pöttgen, *J. Solid State Chem.* **2003**, *173*, 418-424; f) C. Femoni, M. C. Iapalucci, G. Longoni, S. Zacchini, S. Fedi, F. F. de Biani, *Eur. J. Inorg. Chem.* **2012**, 2243-2250; g) V. J. Yannello, B. J. Kilduff, D. C. Fredrickson, *Inorg. Chem.* **2014**, *53*, 2730-2741; h) J. P. S. Walsh, S. M. Clarke, Y. Meng, S. D. Jacobsen, D. E. Freedman, *ACS Cent. Sci.* **2016**, *2*, 867-871.
- [14] a) K. Jonas, R. Mynott, C. Kruger, J. C. Sekutowski, Y. H. Tsay, *Angew. Chem.* **1976**, *88*, 808-809; *Angew. Chem. Int. Ed.* **1976**, *15*, 767-768; b) K. Jonas, US 4169845, **1979**.
- [15] R. Zadnand, A. Kraft, T. Schrader, U. Linne, *Chem. Eur. J.* **2004**, *10*, 4233-4239.
- [16] F. Weigend, *J. Chem. Phys.* **2014**, *141*, 134103.
- [17] A. E. Reed, R. B. Weinstock, F. Weinhold, *J. Chem. Phys.* **1985**, *83*, 735- 746.
- [18] a) F. Teixidor, M. L. Luetkens, R. W. Rudolph, *J. Am. Chem. Soc.* **1983**, *105*, 149-150; b) M. L. Luetkens, F. Teixidor, R. W. Rudolph, *Inorganica Chimica Acta* **1984**, *83*, L13-L15.
- [19] a) B. Kesanli, J. Fettinger, B. Eichhorn, *Chem. Eur. J.* **2001**, *7*, 5277- 5285; b) B. Kesanli, J. Fettinger, B. Eichhorn, *Angew. Chem.* **2001**, *113*, 2364-2366; *Angew. Chem. Int. Ed.* **2001**, *40*, 2300-2302; c) B. Kesanli, J. Fettinger, D. R. Gardner, B. Eichhorn, *J. Am. Chem. Soc.* **2002**, *124*, 4779-4786; d) B. Kesanli, J. E. Halsig, P. Zavalij, J. C. Fettinger, Y. F. Lam, B. W. Eichhorn, *J. Am. Chem. Soc.* **2007**, *129*, 4567-4574; e) F. S. Kocak, P. Zavalij, Y.-F. Lam, B. W. Eichhorn, *Inorg. Chem.* **2008**, *47*, 3515-3520; f) F. S. Kocak, P. Zavalij, B. Eichhorn, *Chem. Eur. J.* **2011**, *17*, 4858-4863; g) F. S. Kocak, D. O. Downing, P. Zavalij, Y. F. Lam, A. N. Vedernikov, B. Eichhorn, *J. Am. Chem. Soc.* **2012**, *134*, 9733-9740.
- [20] a) R. Ababei, W. Massa, K. Harms, X. L. Xie, F. Weigend, S. Dehnen, *Angew. Chem.* **2013**, *125*, 13786-13790; *Angew. Chem. Int. Ed.* **2013**, *52*, 13544-13548;

- b) R. Ababei, W. Massa, B. Weinert, P. Pollak, X. Xie, R. Clérac, F. Weigend, S. Dehnen, *Chem. Eur. J.* **2015**, *21*, 386-394.
- [21] crypt-222 = 4,7,13,16,21,24-hexaoxa-1,10-diazabicyclo[8.8.8]hexacosane
- [22] a) K. Jonas, R. Mynott, C. Kruger, J. C. Sekutowski, Y. H. Tsay, *Angew. Chem.* **1976**, *88*, 808-809; *Angew. Chem. Int. Ed.* **1976**, *15*, 767-768; b) K. Jonas, US 4169845, **1979**.
- [23] O. V. Dolomanov, L. J. Bourhis, R. J. Gildea, J. A. K. Howard, H. Puschmann, *J. Appl. Crystallogr.* **2009**, *42*, 339-341.
- [24] Note that [K(crypt-222)]<sub>3</sub>[Co@Sn<sub>6</sub>Sb<sub>6</sub>]0.83[Co<sub>2</sub>@Sn<sub>5</sub>Sb<sub>7</sub>]0.17 crystallizes alongside residual [K(crypt-222)]<sub>2</sub>(Sn<sub>2</sub>Sb<sub>2</sub>).
- [25] TURBOMOLE Version 7.2, TURBOMOLE GmbH 2017. TURBOMOLE is a development of University of Karlsruhe and Forschungszentrum Karlsruhe 1989–2007, TURBOMOLE GmbH since 2007.
- [26] F. Weigend, *J. Chem. Phys.* **2014**, *141*, 134103.
- [27] a) J. P. Perdew, *Phys. Rev. B* **1986**, *33*, 8822-8824; b) A. D. Becke, *Phys. Rev. A* **1988**, *38*, 3098-3100.
- [28] K. Eichkorn, F. Weigend, O. Treutler, R. Ahlrichs, *Theor. Chem. Acc.* **1997**, *97*, 119-124.
- [29] J. M. Tao, J. P. Perdew, V. N. Staroverov, G. E. Scuseria, *Phys. Rev. Lett.* **2003**, *91*, 146401.
- [30] F. Weigend, A. Baldes, *J. Chem. Phys.* **2010**, *133*, 174102.
- [31] B. Metz, H. Stoll, M. Dolg, *J. Chem. Phys.* **2000**, *113*, 2563-2569.
- [32] A. Klamt, G. Schüürmann, *J. Chem. Soc., Perkin Trans. 2* **1993**, 799-805.
- [33] R. Ahlrichs, K. May, *Phys. Chem. Chem. Phys.* **2000**, *2*, 943-945.
- [34] C. Seifried, L. Longo, P. Pollak, F. Weigend, *J. Chem. Phys.* **2017**, *146*, 034304.
- [35] S. Mitzinger, L. Broeckert, W. Massa, F. Weigend, S. Dehnen, *Nat. Commun.* **2016**, *7*, 10480–10490.
- [36] B. Eichhorn, S. Kocak, in *Struct. Bond.*, Vol. 140 (Ed.: T. Fässler), Springer, Heidelberg, **2011**, pp. 59-89.
- [37] S. Scharfe, T. F. Fässler, S. Stegmaier, S. D. Hoffmann, K. Ruhland, *Chem. Eur. J.* **2008**, *14*, 4479-4483.
- [38] V. Hlukhyy, S. Stegmaier, L. van Wüllen, T. F. Fässler, *Chem. Eur. J.* **2014**, *20*, 12157–12164.
- [39] M. Neumeier, F. Fendt, S. Gärtner, C. Koch, T. Gärtner, N. Korber, R. Gschwind, *Angew. Chem. Int. Ed.* **2013**, *52*, 4483–4486.



## 5 *cyclo*-P<sub>4</sub> Building Blocks: Achieving Non-Classical Fullerene Topology and Beyond

Full Paper



The diffusion-ordered NMR spectroscopic investigations were performed by Florian Hastreiter. The synthesis and characterization of the compounds as well as the sample preparation were performed by Fabian Dielmann, Barbara Krämer, Brian P. Johnson and Claudia Heindl. The analysis via X-ray crystallography was carried out by Eugenia V. Peresykina and Manfred Zabel.

---

Fabian Dielmann, Eugenia V. Peresykina, Barbara Krämer, Florian Hastreiter, Brian P. Johnson, Manfred Zabel, Claudia Heindl, and Manfred Scheer  
*Angew. Chem. Int. Ed.* **2016**, 55, 47, 14833-14837.

DOI:10.1002/anie.201606074

2016 Wiley-VCH Verlag GmbH & Co. KGaA. Open Access article.

## 5.1 Abstract

The cyclo-P<sub>4</sub> complexes [Cp<sup>R</sup>Ta(CO)<sub>2</sub>(η<sup>4</sup>-P<sub>4</sub>)] (Cp<sup>R</sup>: Cp<sup>''</sup> = 1,3-C<sub>5</sub>H<sub>3</sub>tBu<sub>2</sub>, Cp<sup>'''</sup> = 1,2,4-C<sub>5</sub>H<sub>2</sub>tBu<sub>3</sub>) turned out to be predestined for the formation of hollow spherical supramolecules with non-classical fullerene-like topology. The resulting assemblies constructed by CuX (X = Cl, Br) showed a highly symmetric 32-vertex core of solely four- and six-membered rings. In some supramolecules, the inner cavity was occupied by an additional CuX unit. On the other hand, using CuI, two different supramolecules with either peanut- or pear-like shapes and outer diameters in the range of 2-2.5 nm were isolated. Furthermore, the spherical supramolecules containing Cp<sup>'''</sup> ligands at tantalum are soluble in CH<sub>2</sub>Cl<sub>2</sub>. NMR spectroscopic investigations in solution revealed the formation of isomeric supramolecules owing to the steric hindrance caused by the third tBu group on the Cp<sup>'''</sup> ligand. In addition, a 2D coordination polymer was obtained and structurally characterized.

## 5.2 Introduction

Fullerenes, defined as spherical carbon clusters, are prime examples of discrete nanosized supramolecules. Owing to their unique optic and electronic properties, they have gained increasing attention in materials science and nanotechnology.<sup>[1]</sup> However, the majority of reports on fullerenes are restricted to the most stable derivatives such as C<sub>60</sub> and C<sub>70</sub>, which can be prepared on a reasonable scale. Consisting of solely five- and six-membered rings, they are so-called classical fullerenes. Some time ago, we succeeded in showing that [Cp<sup>\*</sup>Fe(η<sup>5</sup>-P<sub>5</sub>)] (Cp<sup>\*</sup> = C<sub>5</sub>Me<sub>5</sub>) containing a *cyclo*-P<sub>5</sub> ligand self-assembles with copper(I) halides to give supramolecules with a fullerene-like topology. These unprecedented carbon-free analogues of the I<sub>h</sub>-C<sub>80</sub> (Figure 1) and I-C<sub>140</sub> frameworks represent less stable fullerene-like congeners.<sup>[2]</sup>

Some time ago, we were interested to see whether non-classical fullerenes of various ring sizes<sup>[3]</sup> are also accessible using the metallasupramolecular approach. The *cyclo*-P<sub>4</sub> complex [Cp<sup>''</sup>Ta(CO)<sub>2</sub>(η<sup>4</sup>-P<sub>4</sub>)]<sup>[4]</sup> (**1a**; Cp<sup>''</sup> = 1,3-C<sub>5</sub>H<sub>3</sub>tBu<sub>2</sub>) seems to be predestined for the formation of spheres comprising the four-membered ring motif. First investigations of the reactivity of **1a** with CuCl revealed the formation of the spherical supramolecule [(Cp<sup>''</sup>Ta(CO)<sub>2</sub>(η<sup>4</sup>-P<sub>4</sub>))<sub>6</sub>{CuCl}<sub>8</sub>] (**2a**), which consists exclusively of four- and six-membered rings.<sup>[5]</sup> Its scaffold consists of 32 inorganic core atoms and exhibits O<sub>h</sub> symmetry; this non-classical fullerene framework has not been obtained in fullerene chemistry thus far.<sup>[6]</sup>

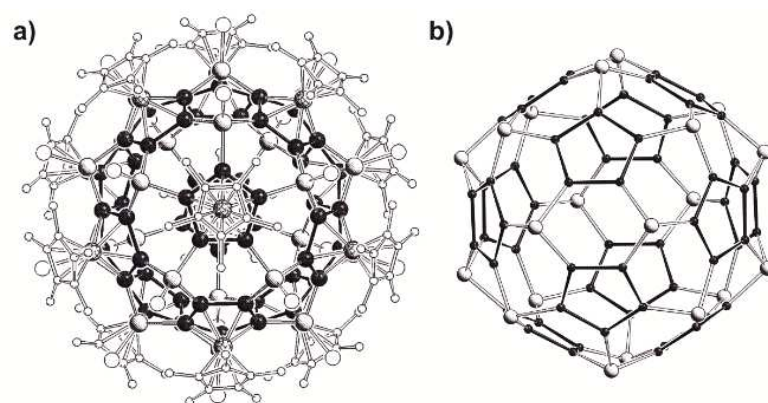


**Figure 1.** a) Supramolecule with 80 vertices based on  $[\text{Cp}^*\text{Fe}(\eta^5\text{-P}_5)]$  and  $\text{CuX}$  ( $X = \text{Cl}, \text{Br}$ ). b) The molecular scaffold illustrating the  $h\text{-C}_{80}$  fullerene topology.

This single result led to some decisive questions as to whether the concept of structural arrangements of four- and six-membered rings in supramolecules could be extended to unprecedented spherical structural motifs as it was possible for the five-membered ring of pentaphosphaferrocene.<sup>[2,7]</sup> Moreover, further information on the formation process and the structural stability in solution was required as the insolubility of the formerly obtained 32-vertex ball **2a** did not allow any investigations of its behaviour in solution. Thus, a third *tert*-butyl group was introduced into the cyclopentadienyl ring to increase the solubility, and the complex  $[\text{Cp}^{\text{tBu}}\text{Ta}(\text{CO})_2(\eta^4\text{-P}_4)]$  (**1b**;  $\text{Cp}^{\text{tBu}} = 1,2,4\text{-C}_5\text{H}_2\text{tBu}_3$ ) was synthesized, structurally characterized, and examined in terms of its reactivity towards copper(I) halides.

Herein, we report on a systematic investigation of the reactivity of the *cyclo*- $\text{P}_4$  ligand tantalum complexes **1a** and **1b** towards  $\text{CuX}$  ( $X = \text{Cl}, \text{Br}, \text{I}$ ), which led to the isolation and structural characterization of three novel representatives of spherical  $\text{C}_{32}$  analogues  $[\{\text{Cp}^{\text{R}}\text{Ta}(\text{CO})_2(\eta^4\text{-P}_4)\}_6\{\text{CuX}\}_8]$  (**2b**:  $\text{Cp}^{\text{R}} = \text{Cp}^{\text{tBu}}$ ,  $X = \text{Br}$ ; **2c**:  $\text{Cp}^{\text{R}} = \text{Cp}^{\text{tBu}}$ ,  $X = \text{Cl}$ ; **2d**:  $\text{Cp}^{\text{R}} = \text{Cp}^{\text{tBu}}$ ,  $X = \text{Br}$ ). For the first time, the solubility of the  $\text{Cp}^{\text{tBu}}$  derivatives (**2c** and **2d**) enabled a characterization in solution. Furthermore, we succeeded in the isolation of two spheres containing singular scaffolds,  $[\{\text{Cp}^{\text{tBu}}\text{Ta}(\text{CO})_2(\eta^4\text{-P}_4)\}_{10}\{\text{Cu}_{14}\text{I}_{10}(\mu\text{-I})_2(\mu_3\text{-I})_2\}]$  (**3**) and  $[\{\text{Cp}^{\text{tBu}}\text{Ta}(\text{CO})_2(\eta^4\text{-P}_4)\}_5\{\text{Cu}_{12}\text{I}_3(\mu\text{-I})_8(\mu_4\text{-I})(\text{CH}_3\text{CN})_5\}]$  (**4a**, **4b**). The unprecedented double sphere of **3** shows potential for subsequent aggregation according to the spherical building block concept. Their structures give insight into the formation pathway of the 32-vertex balls as the missing  $\text{TaP}_4$  unit is replaced by a  $\text{CuI}$  network to form **4** or is merged to a second incomplete ball via a  $(\text{CuI})_x$  moiety to form the “peanut”-shaped compound **3**.

### 5.3 Results and Discussion

A solution of CuBr in CH<sub>3</sub>CN/CH<sub>2</sub>Cl<sub>2</sub> was carefully layered on a solution of **1a** in CH<sub>2</sub>Cl<sub>2</sub> or in a CH<sub>2</sub>Cl<sub>2</sub>/DMF mixture whereupon the formation of orange crystals of **2b** at the phase boundary could be observed within one day (Figure 2). **2b** crystallizes in the trigonal space group R3̄ as CH<sub>2</sub>Cl<sub>2</sub> solvate, and its molecular structure was identified as the supramolecule  $[\{\text{Cp}^*\text{Ta}(\text{CO})_2(\eta^4\text{-P}_4)\}_6\{\text{CuBr}\}_8]$  (**2b**). Compound **2b** consists of six *cyclo*-P<sub>4</sub> complexes **1a** bound to eight copper(I) halide units in a 1,2,3,4-coordination mode, as in the Cl derivative **2a**. Each Cu atom is tetrahedrally coordinated by three P atoms and one terminal halide. The inorganic core consists of 32 non-carbon atoms and features a Cu<sub>8</sub> cube with *cyclo*-P<sub>4</sub> rings above its six faces. This results in a closed structure consisting exclusively of alternating four- and six-membered rings to give the topology of a truncated octahedron. Consequently, the tantalum atoms form a Ta<sub>6</sub> octahedron.<sup>[13]</sup> The P–P bond lengths of 2.1569(15)–2.1840(15) Å in **2b** are similar to those in the free complex **1a**<sup>[4]</sup> (2.157(2)–2.189(2) Å). The inner cavity of **2b** has a diameter<sup>[8]</sup> of 0.6 nm and possesses a cuboidal shape, with the Cu atoms in the corners and the P<sub>4</sub> rings forming the faces. The outer diameter is 2.17 nm, which is similar to **2a**.

A change of the used halide to iodide did not result in the formation of the isostructural C<sub>32</sub> analogue as CuI, unlike copper(I) halides, tends to form extended CuI aggregates.<sup>[9]</sup> By carefully layering a solution of CuI in CH<sub>3</sub>CN over a solution of **1a** in toluene, orange prisms of  $[\{\text{Cp}^*\text{Ta}(\text{CO})_2(\eta^4\text{-P}_4)\}_{10}\{\text{Cu}_{14}\text{I}_{10}(\mu\text{-I})_2(\mu_3\text{-I})_2\}]$  (**3**) were formed within four days (Figure 2). After approximately two weeks, a new crop of yellow prisms appeared as the second fraction, representing another spherical cluster, namely  $[\{\text{Cp}^*\text{Ta}(\text{CO})_2(\eta^4\text{-P}_4)\}_5\{\text{Cu}_{12}\text{I}_3(\mu\text{-I})_8(\mu_4\text{-I})(\text{CH}_3\text{CN})_5\}]$  (**4**; Figure 2). The crystallization of cluster **4** was delayed during the synthesis of **3** owing to its higher solubility, which was concluded from an optical examination of the crystalline material and the unit cells of dozens of different crystals. The formation of **3** and **4** in the same reaction is due to the very similar ratios of **1a**/CuI in the composition of both products (**3**: 1:2.33; **4**: 1:2.40). Interestingly, the direct synthesis of compound **4** was possible under similar reaction conditions in the presence of [Cp\*Fe(η<sup>5</sup>-P<sub>5</sub>)]. The formation of **4**, albeit as another solvatomorph (**4a**), was accompanied by the formation of brown needles of the earlier reported 2D coordination polymer  $[\{\text{Cp}^*\text{Fe}(\eta^5\text{-P}_5)\}(\text{CuI})]_n$ .<sup>[10]</sup> Apparently, the presence of [Cp\*Fe(η<sup>5</sup>-P<sub>5</sub>)] in the reaction mixture inhibits the preliminary formation of **3** and favors the formation of **4**.

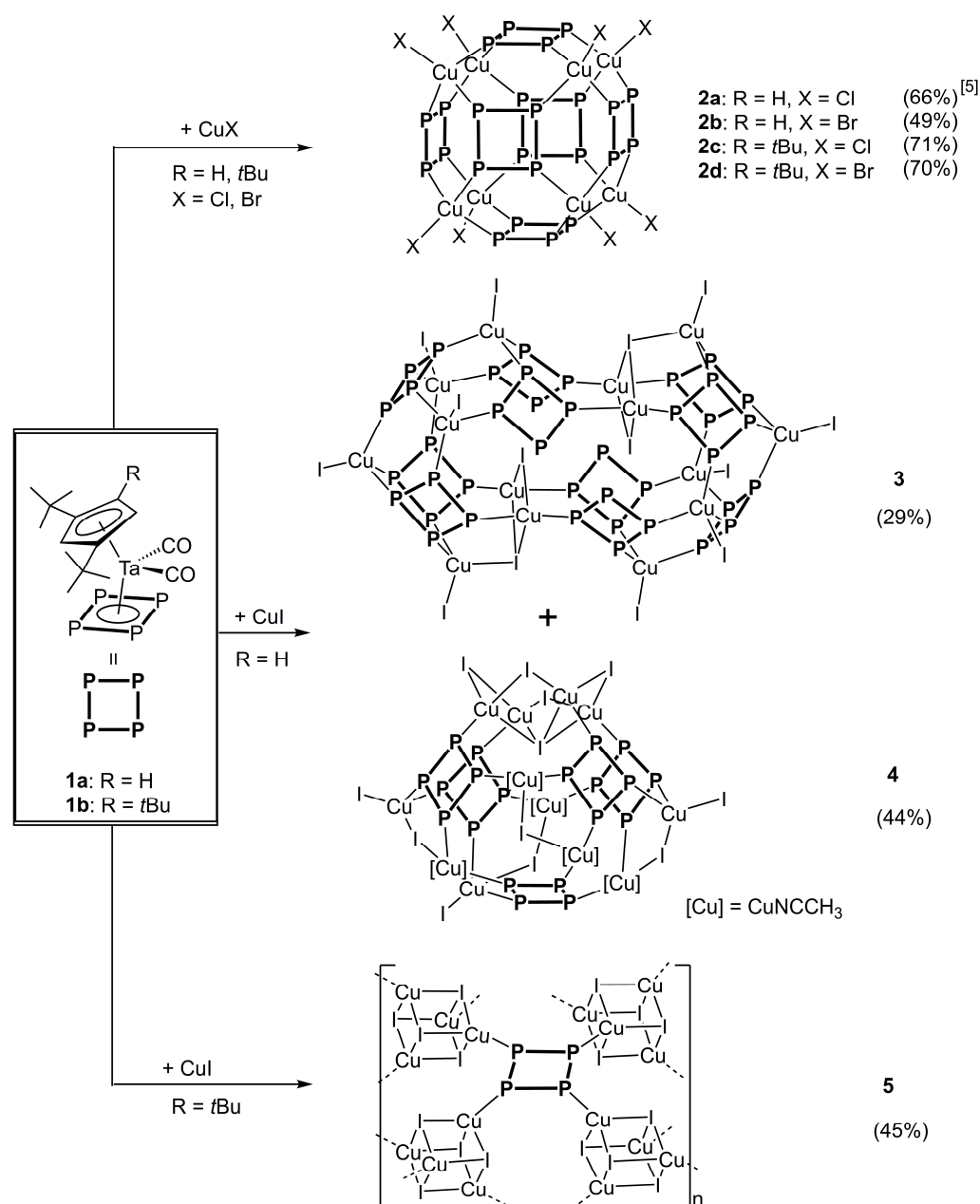


**Figure 2.** Reaction of  $[\text{Cp}^{\text{R}}\text{Ta}(\text{CO})_2(\eta^4\text{-P}_4)]$  (**1a**:  $\text{Cp}^{\text{R}} = \text{Cp}''$ ; **1b**:  $\text{Cp}^{\text{R}} = \text{Cp}'''$ ) with copper(I) halides yield the supramolecules **2-4** and the coordination polymer **5** (yields in parentheses).

Compound **3** crystallizes in the monoclinic space group  $C2/m$ , and structural analysis revealed an unprecedented nanocapsule that consisted of ten *cyclo*- $\text{P}_4$  complexes **1a** bound to eight  $\text{CuI}$  units and two  $\text{Cu}_3\text{I}_3$  units (Figure 3b). Six complexes **1a** bind in a 1,2,3,4- and four in an 1,2,3-Coordination mode. The whole supramolecule **3** can be described in terms of two  $[(\text{Cp}''\text{Ta}(\text{CO})_2(\eta^4\text{-P}_4))_5(\text{CuI})_5]$  fragments connected by two  $\text{Cu}_2\text{I}_2$  units. The two cluster fragments have similar inorganic frameworks, which can be derived from those of **2a** and **2b** by removing one *cyclo*- $\text{P}_4$  complex **1a** and coordinating four  $\text{CuX}$  units to it. Therefore, it seems that on the way to the formation of the regular 32-vertex spheres of **2**,

two incomplete spheres were fused by two  $\text{Cu}_2\text{I}_2$  units to give a double sphere **3**. The resulting inner scaffold of **3** has a peanut-like shape and consists of 58 inorganic core atoms, 40 P, 14 Cu, and 4 I atoms (Figure 3). The iodine atoms only support the scaffold as its connectivity can be achieved with Cu-P bonds. As expected, the Cu-I bonds with terminal iodide (average: 2.53(1) Å) are shorter than to  $\mu$ -I (2.598(3) Å) and  $\mu_3$ -I (average: 2.69(2) Å) atoms. The P-P bond lengths of 2.138(5)-2.191(5) Å in **3** are in a wider range than in the free complex **1a**.<sup>[4]</sup> The supramolecule **3** has a long axis<sup>[8]</sup> of 2.81 nm and a short axis of 2.28 nm. The inner cavity of **3** is completely blocked by the  $\mu$ -I atoms of the  $\text{Cu}_3\text{I}_3$  units.<sup>[13]</sup>

Compound **4** crystallizes as two solvatomorphic forms, the orthorhombic (space group *Pbca*, **4a**) and the monoclinic (space group *P2<sub>1</sub>/n*, **4b**) form. Single-crystal X-ray diffraction manifested the presence of a hollow shell in both cases, which consisted of five *cyclo*-P<sub>4</sub> complexes **1a** bound to three neutral  $\{\text{Cu}_2\text{I}_2\text{CH}_3\text{CN}\}$  units, one cationic  $\{\text{Cu}_2\text{I}(\text{CH}_3\text{CN})_2\}^+$ , and one anionic  $\{\text{Cu}_4\text{I}_5\}^-$  unit (Figure 3c). Complex **1a** features a 1,2,3,4-coordination mode just like clusters **2a** and **2b**, but the different nature of the copper halide units leads to a completely new framework. The inorganic scaffold of **4** can be described as an open shell of five *cyclo*-P<sub>4</sub> rings connected via eight  $\text{Cu}_2(\mu\text{-I})$  units, which form four five-membered  $\text{P}_2\text{Cu}_2\text{I}$  and four eight-membered  $\text{P}_4\text{Cu}_3\text{I}$  rings. The open shell is capped by a bowl-like  $\{\text{Cu}_4\text{I}_5\}^-$  unit (Figure 3g), a common building unit in CuBr- and CuI-based supramolecules.<sup>[2d,f,7]</sup> In **4**, in contrast to **3**, iodide becomes a part of the inorganic scaffold of **4** that consists of 41 core atoms (20 P, 12 Cu, 9 I) and has  $C_2$  symmetry. Each Cu atom in **4** is tetracoordinated, and the Cu-I bond lengths of terminal iodides (average: 2.55(1) Å in **4a**, 2.56(1) Å in **4b**) are typically shorter than to  $\mu$ -I atoms (2.6(1) Å in **4a**, 2.64(8) Å in **4b**). The P-P bonds in **4a** (2.129(3)-2.168(3) Å) and **4b** (2.128(4)-2.166(4) Å) are shorter than in **1a** and **3**, respectively. The spherical cluster **4** has an outer diameter<sup>[8]</sup> of 2.35 nm. Like in **3**, the inner cavity of **4** is occupied by iodide, which here belongs to the  $\{\text{Cu}_4\text{I}_5\}^-$  unit. Interestingly, the supramolecules in **4a** and **4b** are isomers: The structural difference between their scaffolds was traced back to two positions occupied by either an iodide or a  $\text{CH}_3\text{CN}$  molecule.<sup>[13]</sup>

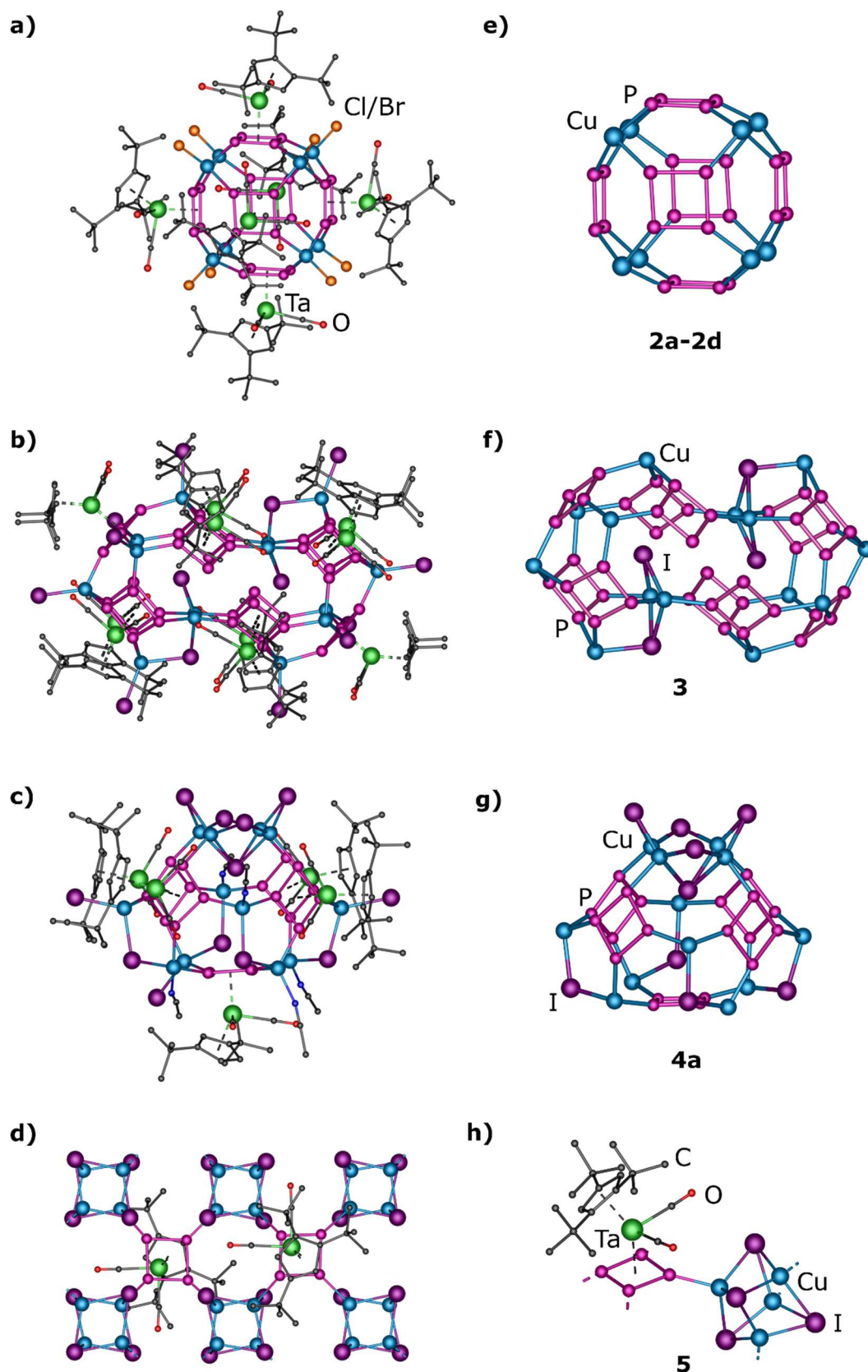


**Figure 3.** a–c) Molecular structures of **2c** (a), **3** (b), and **4a** (c). d) Section of the 2D polymeric network in **5**. Hydrogen atoms omitted for clarity. e–g) Scaffolds of the supramolecules **2a-d** (e), **3** (f), and **4a** (g). h) Repeating unit of **5**.

In the IR spectra of all products, the two CO stretching vibrations (**2a**: 2040 cm<sup>-1</sup>, 1974 cm<sup>-1</sup>; **2b**: 2042 cm<sup>-1</sup>, 1972 cm<sup>-1</sup>; **3**: 2011 cm<sup>-1</sup>, 1969 cm<sup>-1</sup>; and **4**: 2017 cm<sup>-1</sup>, 1976 cm<sup>-1</sup>) all display a significant shift to higher wavenumbers compared to those of **1a** (1983 cm<sup>-1</sup>, 1952 cm<sup>-1</sup>). Furthermore, all compounds obtained from the Cp<sup>''</sup> derivative **1a** were completely insoluble in *n*-hexane, toluene, CH<sub>2</sub>Cl<sub>2</sub>, and THF.

Certainly, NMR spectroscopic characterization would be desirable to confirm the existence of the superspheres in solution. A promising approach for this is based on increasing the steric demand on the Cp<sup>R</sup> ligand by introducing a third *tert*-butyl group on the Cp<sup>R</sup> ring. For this reason, [Cp<sup>'''</sup>Ta(CO)<sub>2</sub>(η<sup>4</sup>-P<sub>4</sub>)] (**1b**) was synthesized in analogy to the preparation of **1a**<sup>[4]</sup> in good yields (73%). The comprehensive characterization of **1b** in solution as well as in the solid state by X-ray crystallography showed almost identical structural features to those of **1a**.<sup>[13]</sup>

The reactivity of **1b** towards CuX (X = Cl, Br) was investigated by adding a solution of CuX in CH<sub>3</sub>CN to a solution of **1b** in toluene or benzene and stirring it for ten minutes. Subsequently, the red solution was layered with Et<sub>2</sub>O, and after three weeks red prisms of **2c** and **2d** had been formed (Figure 2). These products were also formed when **1b**/CuX ratios ranging from 1:1 to 1:2 were used.

Both **2c** and **2d**, crystallized in the monoclinic space group *P*2<sub>1</sub>/*n*, and X-ray structural analysis revealed the supramolecules [(Cp<sup>'''</sup>Ta(CO)<sub>2</sub>(η<sup>4</sup>-P<sub>4</sub>))<sub>6</sub>{CuX}<sub>8-x</sub>] (**2c**: X = Cl, *x* = 0.6; **2d**: X = Br, *x* = 0.3; Figure 3a). The molecular structures of **2a-2d** are similar; with the exception of the additional *tert*-butyl group, they exhibit the same spherical supramolecules and alternating patterns of four- and six-membered rings in the 32-vertex core (Figure 3e). The O<sub>h</sub> symmetry of the inorganic scaffold is violated by the organic substituents at the Ta atoms, which leads to overall C<sub>3i</sub> (**2b**) or C<sub>i</sub> symmetry (**2c**, **2d**) for the supramolecules in the solid state. The P–P bonds of 2.144(3)-2.176(3) Å in **2d** are only slightly shorter than those in the free complex **1b**<sup>[4]</sup> and supramolecule **2a** (2.156(2)-2.180(2) Å).<sup>[5]</sup> The inner cavities of **2c** and **2d** have the same size (d<sub>inner</sub> = 0.6 nm) whereas the maximum outer diameters of 2.50 nm (**2c**) and 2.54 nm (**2d**) are larger by about 0.35 nm than those of the Cp<sup>''</sup> derivatives **2a** and **2b**<sup>[5]</sup>, which is due to the third *t*Bu group in the Cp<sup>'''</sup> ligands.

Attention needs to be drawn to the co-existence of the supramolecules **2b-2d** with isomeric and slightly incomplete inorganic scaffolds in the solid state. One CuX unit is missing in the 32-vertex scaffold for 20-50% of the supramolecules. In 10% of the spheres, an additional CuX unit is present, which points into the cavity. In this case, the Cu ion is coordinated to two *cyclo*-P<sub>4</sub> in η<sup>2</sup>-mode while the terminal X ion is located at the center of the cavity. This CuX unit can either co-exist with adjacent Cu ions σ-coordinated to the



*cyclo*-P<sub>4</sub> unit or neighbor a CuX vacancy in the 32-vertex scaffold.<sup>[13]</sup> It thereby forms two or one Cu···Cu contacts of 2.81-2.95 Å.

Apparently, the single *t*Bu group also supports the formation of the spherical clusters. However, it induces the formation of even more isomeric forms in addition to the structural variation in the inorganic core. In the free complex **1b**, the Cp<sup>'''</sup> ligand can rotate freely. However, upon coordination to the copper halide units, the rotation is hindered as the halides are now situated in between the *t*Bu groups. With increasing halide size, this immobilization becomes more pronounced. As a consequence, every molecule of complex **1b** can appear in two enantiomeric conformations that differ in the orientation of the single *t*Bu group, which again leads to isomeric clusters. In the crystal structure of **2c**, only one isomer is observed. However, the crystal structure of **2d** consists of co-crystallized epimeric clusters as indicated by the disorder of one *t*Bu group.<sup>[13]</sup> As the formation of the spherical clusters in solution should not be influenced by the orientation of the single *t*Bu group, a freshly prepared solution of **2c** and **2d** should contain several isomeric clusters, which might inhibit the crystallization of the macromolecules. This specific property is in accordance with the experimental observation that even from concentrated mixtures of **1b** with CuX (X = Cl, Br), single crystals of **2c** and **2d** are formed within several weeks, whereas **2a** and **2b** crystallized within one day.

Compounds **2c** and **2d** are orange, air-sensitive solids, and are insoluble in hexane and Et<sub>2</sub>O. As anticipated, they are sparingly soluble in toluene and have moderate solubility in CH<sub>2</sub>Cl<sub>2</sub>. In the <sup>1</sup>H NMR spectra of **2c** and **2d** in CD<sub>2</sub>Cl<sub>2</sub>, six broad resonances appear between 1 and 2 ppm for the *t*Bu groups and two broad resonances at 6.4 and 7.4 ppm for the methine H atoms. The presence of two resonances for the methine protons indicates the inhibited rotation of the Cp<sup>'''</sup> ligand. The distinct downfield shift of the resonance at 7.4 ppm was attributed to the proximity of the halide ligand. The presence of several broad resonances for the *t*Bu groups is in accordance with a slow isomerization of the clusters in solution. In the <sup>31</sup>P{<sup>1</sup>H} NMR spectrum, very broad resonances were observed between -50 and -90 ppm, which were shifted upfield by approximately 100 ppm to the free complex **1b**. This indicates that the P<sub>4</sub> cycle interacts with the Lewis acidic copper(I) halides. Furthermore, resonances of the free complex **1b** could be detected neither in the <sup>1</sup>H nor in the <sup>31</sup>P{<sup>1</sup>H} NMR spectrum. The same observations were made in NMR spectroscopic investigations of a freshly prepared reaction mixture of **1b** and CuX (X = Cl, Br). These results indicate that the spherical aggregates, such as **2c** and **2d**, are formed immediately and remain intact in solution. This hypothesis was also confirmed by diffusion ordered spectroscopy (DOSY) experiments. The hydrodynamic radii thus determined correlate well with the radii derived from the crystal structure in the solid state.<sup>[13]</sup>

In the ESI mass spectra of **2c** and **2d**, only fragments of the clusters were detected. In CH<sub>2</sub>Cl<sub>2</sub> solutions, the cation  $[(\text{Cp}^*\text{Ta}(\text{CO})_2\text{P}_4)_2\text{Cu}]^+$  was observed. In CH<sub>2</sub>Cl<sub>2</sub>/CH<sub>3</sub>CN mixtures, larger cluster fragments up to  $[(\text{Cp}^*\text{Ta}(\text{CO})_2\text{P}_4)_3\text{Cu}_2\text{Cl}]^+$  could be detected. The IR spectra show two CO stretching vibrations (**2c**: 2019 cm<sup>-1</sup>, 1979 cm<sup>-1</sup>; **2d**: 2015 cm<sup>-1</sup>, 1973 cm<sup>-1</sup>), which are located at significantly higher wavenumbers than those of **1b** (1982 cm<sup>-1</sup>, 1939 cm<sup>-1</sup>); similar observations were made for the analogous Cp\* clusters **2a** and **2b**.

Upon addition of a solution of CuI in CH<sub>3</sub>CN to a stirred solution of **1b** in CH<sub>2</sub>Cl<sub>2</sub>, an orange solution was obtained. After stirring the mixture for 4 hours, the <sup>31</sup>P{<sup>1</sup>H} NMR spectrum of the reaction mixture displayed no resonances corresponding to **1b**, but very broad resonances appeared between -30 to -90 ppm, just like in the spectra of the CuCl/Br clusters **2c** and **2d**. However, the corresponding DOSY NMR experiment indicated that the spheres formed in solution have a smaller radius than the derivatives **2c** and **2d**.<sup>[13]</sup> In the ESI mass spectrum of the reaction mixture, the cation  $[(\text{Cp}^*\text{Ta}(\text{CO})_2\text{P}_4)_2\text{Cu}_2\text{I}]^+$  represents the largest fragment, as found for isolated **2c**. After removal of the solvent, two carbonyl bands (2013 cm<sup>-1</sup>, 1971 cm<sup>-1</sup>) appear in the IR spectrum of the obtained solid, which are similar to those of the clusters **2c** (2019 cm<sup>-1</sup>, 1979 cm<sup>-1</sup>) and **2d** (2015 cm<sup>-1</sup>, 1973 cm<sup>-1</sup>), but also correspond to those of **3** (2011 cm<sup>-1</sup>, 1969 cm<sup>-1</sup>) and **4** (2017 cm<sup>-1</sup>, 1976 cm<sup>-1</sup>). Both the solubility of these species and the analytical data indicate the presence of spherical aggregates in solution with structures similar to, but smaller than, those of the clusters **2c** and **2d**. Incomplete spheres thus seem to exist in solution that might be structurally comparable to fragments of **4** after CuI release or sections of **3**. However, upon layering diethyl ether over the reaction mixture, yellow plates of the 2D polymer **5** were formed (Figure 2d), which were insoluble in hexane, Et<sub>2</sub>O, toluene, CH<sub>2</sub>Cl<sub>2</sub>, and THF.

X-ray structure analysis of **5** revealed the 2D coordination polymer  $[\text{Cp}^*\text{Ta}(\text{CO})_2(\eta^4\text{-P}_4)\{\text{Cu}_4(\mu_3\text{-I})_4\}]_n$ , in which the *cyclo*-P<sub>4</sub> ligand complexes **1b** link  $\{\text{Cu}_4(\mu_3\text{-I})_4\}$  heterocubane units in a 1,2,3,4-coordination mode (Figure 3h). Even though these complexes **1b** feature the same coordination mode as in the spherical molecule **2c** and **2d**, the Cu<sub>4</sub>I<sub>4</sub> units induce the formation of the layered structure in **5**. Therefore, every second complex **1b** is located on the opposite side of the polymeric layer.<sup>[13]</sup> Compared with the free complex **1b**, the average P-P bond is also shorter in **5** (2.150(6) Å). The Cu<sub>4</sub>I<sub>4</sub> heterocubane structural motif is known in the coordination chemistry.<sup>[11]</sup> In **5**, each iodine atom bridges three copper atoms with an average Cu-I distance of 2.66(4) Å, which lies in the typical range for such bonds.<sup>[12]</sup> The resulting layers of Cu<sub>4</sub>I<sub>4</sub> and *cyclo*-P<sub>4</sub> units are separated by the bulky Cp\* ligands and the carbonyl ligands at the Ta atoms as well as co-crystallized CH<sub>3</sub>CN solvent molecules.

## 5.4 Conclusions

In summary, a systematic study towards spherical supramolecules starting from the *cyclo*-P<sub>4</sub>-containing tantalum complexes **1a** and **1b** as building blocks has yielded fascinating supramolecular assemblies with a non-classical fullerene topology. The CuX-based superspheres (X = Cl, Br; **2b-d**) thus obtained mostly exhibit hollow 32-vertex scaffolds in the shape of a truncated octahedron that exclusively consists of alternating P<sub>4</sub> four- and Cu<sub>2</sub>P<sub>4</sub> six-membered rings. In the solid state, isomeric and slightly incomplete supramolecules with lower symmetry were also observed. The higher steric demand in Cp<sup>'''</sup> derivative **1b** compared to **1a** improved the solubility of these 2.5 nm large molecules. NMR spectroscopic studies confirmed that **1b**-based spherical aggregates are immediately assembled and remain intact in solution. Although **1b** did not give rise to molecular clusters in the reaction with CuI, **1a** enabled the synthesis of the previously unknown supramolecules **3** and **4** with sizes of up to 2.2-2.8 nm. Cluster **3** consists of two open shells similar to those in **2** that are fused together by two Cu<sub>3</sub>I<sub>3</sub> units to give an unprecedented peanut-shaped scaffold of 58 non-carbon atoms. The 41-vertex supramolecule **4** exhibits a completely new topology. A hemisphere of five *cyclo*-P<sub>4</sub> and four {Cu<sub>2</sub>}<sup>+</sup> units closed by a Cu<sub>4</sub>I<sub>5</sub><sup>-</sup> bowl results in a pear-shaped inorganic framework, where, in contrast to **3**, the iodides are also involved in the scaffold construction. However, both structures can be viewed as snapshots of the formation of the 32-vertex balls as the missing TaP<sub>4</sub> unit of the 32-vertex ball can be replaced by a CuI network to form **4** or merged to a second incomplete ball via a (CuI)<sub>x</sub> moiety to form peanut-shaped compound **3**.

## 5.5 Supporting Information

### 5.5.1 Experimental Part

All reactions were performed under an inert atmosphere of dry nitrogen or argon with standard vacuum, Schlenk, and glove-box techniques. Solvents were purified, dried and degassed prior to use by standard procedures.  $[\text{Cp}^*\text{Ta}(\text{CO})_2(\eta^4\text{-P}_4)]^{[21]}$  and  $[\text{Cp}^*\text{Fe}(\eta^5\text{-P}_5)]^{[22]}$  was synthesized following reported procedures. Commercially available chemicals were used without further purification. Solution NMR spectra were recorded on either Bruker Avance 300 or 400 spectrometer. The corresponding ESI-MS spectra were acquired on a ThermoQuest Finnigan MAT TSQ 7000 mass spectrometer, while elemental analyses were performed on a Vario EL III apparatus. IR spectra were recorded on a VARIAN FTS-800 FT-IR spectrometer in the form of KBr discs.

#### 5.5.1.1 Synthesis of $[\text{Cp}^*\text{Ta}(\text{CO})_2(\eta^4\text{-P}_4)]$ (**1b**)

A solution of  $[\text{Cp}^*\text{Ta}(\text{CO})_4]$  (0.961 g, 1.83 mmol) and  $\text{P}_4$  (739 mg, 5.96 mmol) in 40 mL toluene are irradiated for 8 hours, while a color change from red to brown can be observed. Afterwards the solvent is removed in vacuo, the residue pre-absorbed on silica and separated by column chromatography (hexane,  $34 \times 3.8$  cm). **1b** is eluted as a yellow band using a hexane/toluene mixture (15:1). The solvent is removed in vacuo to give pure **1b** as a yellow solid. Single crystals of **1b** can be obtained by cooling of a saturated solution of **1b** in hexane.

Analytical data of **1b**:

**Yield:** 785 mg (1.32 mmol, 73%)

**$^1\text{H}$  NMR** ( $\text{C}_6\text{D}_6$ ):  $\delta$  [ppm] = 0.87 (s,  $^t\text{Bu}$ , 9 H), 1.33 (s,  $^t\text{Bu}$ , 18 H), 6.16 (s,  $-\text{CH}=\text{}$ , 2 H).

**$^{31}\text{P}\{^1\text{H}\}$  NMR** ( $\text{C}_6\text{D}_6$ ):  $\delta$  [ppm] = 50.6 (t,  $^1J_{\text{PP}} = 297$  Hz, 1 P), 21.0 (t,  $^1J_{\text{PP}} = 242$  Hz, 1 P), 1.2 (dd,  $^1J_{\text{PP}} = 297$  Hz,  $^1J_{\text{PP}} = 242$  Hz, 2 P).

**IR** (KBr)  $\tilde{\nu}_{\text{CO}}$  [ $\text{cm}^{-1}$ ] = 1982 (vs), 1939 (vs).

**FDI-MS** ( $\text{CH}_2\text{Cl}_2$ )  $m/z = 594.4$   $[\text{Cp}^*\text{Ta}(\text{CO})_2\text{P}_4]^+$

#### 5.5.1.2 Synthesis of $[\{\text{Cp}^*\text{Ta}(\text{CO})_2(\mu_5\text{-}\eta^4\text{:}\eta^1\text{:}\eta^1\text{:}\eta^1\text{-P}_4)\}_6\{\text{CuBr}\}_{7.6}]$ (**2b**)

A thin Schlenk tube was charged with a solution of **1a** (52 mg, 0.095 mmol) in 2 mL  $\text{CH}_2\text{Cl}_2$ . Onto this solution was carefully layered a mixture of 4 mL  $\text{CH}_2\text{Cl}_2$  and 2 mL  $\text{CH}_3\text{CN}$ , followed by a solution of  $\text{CuBr}$  (18 mg, 0.13 mmol) in  $\text{CH}_3\text{CN}/\text{CH}_2\text{Cl}_2$  (1 mL / 1 mL). The doubly layered system was allowed to stand in an undisturbed area and orange crystals of **2b** formed within 24 hours. The mixture was allowed to stand a total of 5 days

to ensure thorough diffusion, and the mother liquor was decanted away. The crystals were washed once with 2 mL CH<sub>3</sub>CN and twice with 2 mL CH<sub>2</sub>Cl<sub>2</sub> and dried under vacuum.

Analytical data for **2b**:

**Yield:** 34 mg (49% based on **1a**)

**IR** (KBr):  $\tilde{\nu}_{\text{CO}}$  [cm<sup>-1</sup>] = 2042 (vs, br), 1972 (sh)

**Elemental analysis:** Calculated (%) for C<sub>90</sub>H<sub>126</sub>Br<sub>7.60</sub>Cu<sub>7.60</sub>O<sub>12</sub>P<sub>24</sub>Ta<sub>6</sub>·0.5(CH<sub>2</sub>Cl<sub>2</sub>)(CH<sub>3</sub>CN)<sub>2</sub> (4429.1 g/mol): C 24.92, H 2.94, N 0.13; found: C 25.22, H 3.00; N 0.12.

### 5.5.1.3 Synthesis of $[\{\text{Cp}^{\text{***}}\text{Ta}(\text{CO})_2(\mu_5\text{-}\eta^4\text{:}\eta^1\text{:}\eta^1\text{:}\eta^1\text{-P}_4)\}_6\{\text{CuCl}\}_{7.4}]$ (**2c**)

A mixture of CuCl (6.7 mg, 0.067 mmol) and **1b** (30 mg, 0.051 mmol) in CH<sub>2</sub>Cl<sub>2</sub> (2.5 mL) was stirred for 5 hours at room temperature. The resulting red solution was transferred into a thin Schlenk tube and carefully layered with Et<sub>2</sub>O (2.5 mL). The mixture was stored at room temperature in the dark. Within two weeks tiny red prisms deposited in the vessel. The microcrystalline material was isolated, washed with CH<sub>2</sub>Cl<sub>2</sub> (1 mL) and Et<sub>2</sub>O (3 × 2 mL) and dried under vacuum at room temperature to yield 26 mg (71 %) of **2c**.

Single crystals suitable for an X-ray structure analysis were obtained by the following procedure: A solution of CuCl (7 mg, 0.071 mmol) in CH<sub>3</sub>CN (1 mL) was added to a stirred solution of **1b** (30 mg, 0.051 mmol) in toluene (2 mL) at room temperature. After stirring the resulting orange solution over 10 minutes it was transferred into a thin Schlenk tube and carefully layered with Et<sub>2</sub>O (1.5 mL). The mixture was left at room temperature in the dark. Within one month red prisms of **2c** were formed. The crystalline material was isolated, washed with toluene (1 mL) and Et<sub>2</sub>O (2 × 2 mL) and dried under vacuum at room temperature to yield 19 mg (52 %) of **2c**.

Analytical data of  $[\{\text{Cp}^{\text{***}}\text{Ta}(\text{CO})_2(\mu_5\text{-}\eta^4\text{:}\eta^1\text{:}\eta^1\text{:}\eta^1\text{-P}_4)\}_6\{\text{CuCl}\}_{7.4}]$  (**2c**):

**Yield:** 26 mg (71 %, based on **1b**)

**<sup>1</sup>H NMR** (CD<sub>2</sub>Cl<sub>2</sub>, 400.13 MHz, 300 K):  $\delta$  [ppm] = 7.46 (s {br}; CH), 6.39 (s {br}; CH), 1.81 (s {br}; *t*Bu), 1.53 (s {br}; *t*Bu), 1.19 (s {br}; *t*Bu), 1.15 (s {br}; *t*Bu), 1.05 (s {br}; *t*Bu), 1.01 (s {br}; *t*Bu)

**<sup>31</sup>P{<sup>1</sup>H} NMR** (CD<sub>2</sub>Cl<sub>2</sub>, 161.98 MHz, 300 K):  $\delta$  [ppm] = -50.6 (s {br}), -81.0 (s {br})

**ESI-MS** (CH<sub>2</sub>Cl<sub>2</sub>/CH<sub>3</sub>CN):  $m/z$  (%) = 1944.6 (3)  $[\{\text{Cp}^{\text{***}}\text{Ta}(\text{CO})_2\text{P}_4\}_3\text{Cu}_2\text{Cl}]^+$ , 1845.6 (60)  $[\{\text{Cp}^{\text{***}}\text{Ta}(\text{CO})_2\text{P}_4\}_3\text{Cu}]^+$ , 1251.2 (100)  $[\{\text{Cp}^{\text{***}}\text{Ta}(\text{CO})_2\text{P}_4\}_2\text{Cu}]^+$ , 657.0 (9)  $[\{\text{Cp}^{\text{***}}\text{Ta}(\text{CO})_2\text{P}_4\}\text{Cu}]^+$

**IR** (KBr):  $\tilde{\nu}$  [ $\text{cm}^{-1}$ ] = 3095 (vw; CH), 3021 (vw; CH), 2962 (m; CH), 2922 (w; CH), 2869 (w; CH), 2019 (vs, CO), 1979 (s; CO), 1486 (w), 1463 (m), 1405 (w), 1367 (m), 1242 (m), 1168 (m), 508 (w), 464 (w)

**Elemental analysis:** Calculated (%) for  $(\text{C}_{19}\text{H}_{29}\text{O}_2\text{TaP}_4)_6(\text{CuCl})_{7.4}$  (4298.3 g/mol): C 31.89, H 4.08, N 0.0; found: C 32.32, H 4.38, N 0.0

#### 5.5.1.4 Synthesis of $[(\text{Cp}^*\text{Ta}(\text{CO})_2(\mu_5\text{-}\eta^4\text{:}\eta^1\text{:}\eta^1\text{:}\eta^1\text{-P}_4))_6\{\text{CuBr}\}_{7.7}]$ (**2d**)

A mixture of CuBr (18 mg, 0.126 mmol) and **1b** (25 mg, 0.042 mmol) in  $\text{CH}_2\text{Cl}_2$  (3 mL) was stirred for 5 hours at room temperature. The resulting red solution was transferred into a thin Schlenk tube and carefully layered with  $\text{Et}_2\text{O}$  (4 mL). The mixture was left at room temperature in the dark. Within two weeks a red, microcrystalline material was formed. It was isolated, washed with  $\text{CH}_2\text{Cl}_2$  (1 mL) and  $\text{Et}_2\text{O}$  ( $3 \times 2$  mL) and dried under vacuum at room temperature to yield 23 mg (70 %) of **2d**.

Single crystals suitable for an X-ray structure analysis were obtained by the following procedure: A solution of CuBr (7 mg, 0.049 mmol) in  $\text{CH}_3\text{CN}$  (0.4 mL) was added to a stirred solution of **1b** (15 mg, 0.025 mmol) in benzene (0.8 mL) at room temperature. After stirring the resulting orange solution over 10 minutes the mixture was left at room temperature in the dark. Within three weeks red prisms of **2d** were formed. The crystalline material was isolated, washed with toluene (1 mL) and  $\text{Et}_2\text{O}$  ( $2 \times 2$  mL) and dried under vacuum at room temperature to yield 5 mg (25 %) of **2d**.

Analytical data of  $[(\text{Cp}^*\text{Ta}(\text{CO})_2(\mu_5\text{-}\eta^4\text{:}\eta^1\text{:}\eta^1\text{:}\eta^1\text{-P}_4))_6\{\text{CuBr}\}_{7.7}]$  (**2d**):

**Yield:** 23 mg (70 %, based on **1b**)

**$^1\text{H}$  NMR** ( $\text{CD}_2\text{Cl}_2$ , 400.13 MHz, 300 K):  $\delta$  [ppm] = 7.39 (s {br}; CH), 6.37 (s {br}; CH), 1.79 (s {br}; tBu), 1.523 (s {br}; tBu), 1.21 (s {br}; tBu), 1.17 (s {br}; tBu), 1.08 (s {br}; tBu), 1.03 (s {br}; tBu),

**$^{31}\text{P}\{^1\text{H}\}$  NMR** ( $\text{C}_6\text{D}_6$ , 161.98 MHz, 300 K):  $\delta$  [ppm] = -60.7(s {br}), -79.7 (s {br}), -91.0 (s {br})

**ESI-MS** ( $\text{CH}_2\text{Cl}_2$ ):  $m/z$  (%) = 1251.2  $[(\text{Cp}^*\text{Ta}(\text{CO})_2\text{P}_4)_2\text{Cu}]^+$

**IR** (KBr):  $\tilde{\nu}$  [ $\text{cm}^{-1}$ ] = 3095 (vw; CH), 3021 (vw; CH), 2963 (m; CH), 2922 (w; CH), 2869 (w; CH), 2015 (vs, CO), 1973 (s; CO), 1489 (w), 1463 (w), 1404 (w), 1367 (w), 1241 (w), 1168 (w), 512 (w), 465 (w)

**5.5.1.5 Synthesis of  $[\{\text{Cp}''\text{Ta}(\text{CO})_2(\mu_5\text{-}\eta^4\text{:}\eta^1\text{:}\eta^1\text{:}\eta^1\text{-P}_4)\}_6\{\text{Cp}''\text{Ta}(\text{CO})_2(\mu_4\text{-}\eta^4\text{:}\eta^1\text{:}\eta^1\text{-P}_4)\}_4\{\text{Cu}_{14}\text{I}_{10}(\mu\text{-I})_2(\mu_3\text{-I})_2\}]$  (**3**) and  $[\{\text{Cp}''\text{Ta}(\text{CO})_2(\mu_5\text{-}\eta^4\text{:}\eta^1\text{:}\eta^1\text{:}\eta^1\text{-P}_4)\}_5\{\text{Cu}_{12}\text{I}_3(\mu\text{-I})_8(\mu_4\text{-I})(\text{MeCN})_5\}]$  (**4**)**

A solution of CuI (26 mg, 0.134 mmol) in CH<sub>3</sub>CN (3 mL) was carefully layered over a solution of **1a** (30 mg, 0.0557 mmol) and in toluene (3 mL) at room temperature. The mixture was left at room temperature in the dark. Within three days orange crystals of **3** were formed at the phase boundary. After 10 days also yellow crystals of **4** formed. The mother liquor was decanted and the crystals were washed with Diethylether (3 × 4 mL) and dried for 5 hours under vacuum at room temperature. Thereby, the orange crystals completely decomposed to give a bright orange powder, due to loss of solvent molecules included in the crystal lattice. The yellow crystals were separated manually.

Analytical data of  $[\{\text{Cp}''\text{Ta}(\text{CO})_2(\mu_5\text{-}\eta^4\text{:}\eta^1\text{:}\eta^1\text{:}\eta^1\text{-P}_4)\}_6\{\text{Cp}''\text{Ta}(\text{CO})_2(\mu_4\text{-}\eta^4\text{:}\eta^1\text{:}\eta^1\text{-P}_4)\}_4\{\text{Cu}_{14}\text{I}_{10}(\mu\text{-I})_2(\mu_3\text{-I})_2\}]$  (**3**):

**Yield:** 13 mg (29 % based on **1a**)

Elementary Analysis: Calculated (%) for (C<sub>13</sub>H<sub>23</sub>O<sub>2</sub>TaP<sub>4</sub>)<sub>10</sub>(CuI)<sub>14</sub>(C<sub>7</sub>H<sub>8</sub>)<sub>3</sub> (8324.4 g/mol): C 24.67, H 3.02, N 0.0; found: C 24.55, H 3.02, N 0.0

**IR** (KBr):  $\tilde{\nu}$  [cm<sup>-1</sup>] = 3078 (w; CH), 2960 (m; CH), 2905 (w; CH), 2865 (w; CH), 2011 (vs; CO), 1969 (vs; CO), 1486 (m), 1463 (m), 1445 (w), 1396 (w), 1364 (m), 1249 (m), 1164 (m), 1057 (w), 1024 (w), 919 (w), 871 (w), 858 (w), 512 (w), 463 (m)

Analytical data of  $[\{\text{Cp}''\text{Ta}(\text{CO})_2(\mu_5\text{-}\eta^4\text{:}\eta^1\text{:}\eta^1\text{:}\eta^1\text{-P}_4)\}_5\{\text{Cu}_{12}\text{I}_3(\mu\text{-I})_8(\mu_4\text{-I})(\text{MeCN})_5\}]$  (**4**)

**Yield:** 25 mg (44 % based on **1a**)

Elementary Analysis: Calculated (%) for (C<sub>13</sub>H<sub>23</sub>O<sub>2</sub>TaP<sub>4</sub>)<sub>5</sub>(CuI)<sub>12</sub>(C<sub>7</sub>H<sub>8</sub>) (5068.4 g/mol): C 19.43, H 2.25, N 0.0; found: C 19.84, H 2.28, N 0.0

**IR** (KBr):  $\tilde{\nu}$  [cm<sup>-1</sup>] = 2961 (w; CH), 2927 (w; CH), 2017 (s; CO), 1976 (s; CO)

**5.5.1.6 Selective synthesis of  $[\{\text{Cp}''\text{Ta}(\text{CO})_2(\mu_5\text{-}\eta^4\text{:}\eta^1\text{:}\eta^1\text{:}\eta^1\text{-P}_4)\}_5\{\text{Cu}_{12}\text{I}_3(\mu\text{-I})_8(\mu_4\text{-I})(\text{MeCN})_5\}]$  (**4**)**

A solution of CuI (81 mg, 0.423 mmol) in CH<sub>3</sub>CN (5 mL) was carefully layered over a solution of **1a** (30 mg, 0.056 mmol) and [Cp\*Fe(η<sup>5</sup>-P<sub>5</sub>)] (58 mg, 0.168 mmol) in toluene (8 mL) at room temperature. The mixture was left at room temperature in the dark. Within one month brown needles of a 2D coordination polymer<sup>[23]</sup> containing [Cp\*Fe(η<sup>5</sup>-P<sub>5</sub>)] and CuI in a 1:1 stoichiometry and yellow blocks of the spherical cluster **4** were deposited in the vessel. The crystalline material was isolated, washed with CH<sub>2</sub>Cl<sub>2</sub> (3 × 2 mL) and Et<sub>2</sub>O

(4 mL) and dried under vacuum at room temperature. Crystals of **4** were separated mechanically.

Analytical data of  $[(\text{Cp}^*\text{Ta}(\text{CO})_2(\mu_5\text{-}\eta^4\text{:}\eta^1\text{:}\eta^1\text{:}\eta^1\text{-P}_4))_5\{\text{Cu}_{12}\text{I}_3(\mu\text{-I})_8(\mu_4\text{-I})(\text{MeCN})_5\}]$  (**4**):

**Yield:** 10 mg (15 % based on **1a**)

**IR** (KBr):  $\tilde{\nu}$  [ $\text{cm}^{-1}$ ] = 2961 (w; CH), 2927 (w; CH), 2017 (s; CO), 1976 (s; CO)

### 5.5.1.7 Synthesis of $[(\text{Cp}^*\text{Ta}(\text{CO})_2(\mu_5\text{-}\eta^4\text{:}\eta^1\text{:}\eta^1\text{:}\eta^1\text{-P}_4))\{\text{Cu}_4(\mu_3\text{-I})_4\}]_n$ (**5**)

A solution of CuI (15 mg, 0.079 mmol) in  $\text{CH}_3\text{CN}$  (4 mL) was added to a stirred solution of **1b** (35 mg, 0.059 mmol) in toluene (10 mL) at room temperature. After stirring the resulting orange solution over 10 minutes it was transferred into a thin Schlenk tube and carefully layered with  $\text{Et}_2\text{O}$  (18 mL). The mixture was left at room temperature in the dark. Within three weeks yellow plates of **5** were formed, which were isolated, washed with toluene (1 mL) and  $\text{Et}_2\text{O}$  (2 × 2 mL) and dried under vacuum at room temperature.

Analytical data of the reaction mixture obtained by stirring **1b** and CuI in a ratio of 2:1 in  $\text{CH}_2\text{Cl}_2/\text{MeCN}$  mixtures over 4 hours:

**$^1\text{H}$  NMR** ( $\text{CD}_2\text{Cl}_2$ , 400.13 MHz, 300 K):  $\delta$  [ppm] = 7.30–7.00 (m {br}; CH), 6.44–6.06 (m {br}; CH), 1.72 (s {br}; *t*Bu), 1.51 (m {br}; *t*Bu), 1.33 (s {br}; *t*Bu), 1.29 (s {br}; *t*Bu), 1.25 (s {br}; *t*Bu), 1.18 (s {br}; *t*Bu), 1.15 (s {br}; *t*Bu), 1.11 (s {br}; *t*Bu),

**$^{31}\text{P}\{^1\text{H}\}$  NMR** ( $\text{C}_6\text{D}_6$ , 161.98 MHz, 300 K):  $\delta$  [ppm] = broad signals between –27 and –92 ppm

**Positive ion ESI-MS** ( $\text{CH}_2\text{Cl}_2$ ):  $m/z$  (%) = 1441.2 (20)  $[(\text{Cp}^*\text{Ta}(\text{CO})_2\text{P}_4)_2\text{Cu}_2\text{I}]^+$ , 1251.2 (100)  $[(\text{Cp}^*\text{Ta}(\text{CO})_2\text{P}_4)_2\text{Cu}]^+$ , 698.1 (35)  $[(\text{Cp}^*\text{Ta}(\text{CO})_2\text{P}_4)\text{Cu}(\text{CH}_3\text{CN})]^+$

**Negative ion ESI-MS** ( $\text{CH}_2\text{Cl}_2$ ):  $m/z$  (%) = 888.5 (0.5)  $[\text{Cu}_4\text{I}_5]^-$ , 698.7 (1)  $[\text{Cu}_3\text{I}_4]^-$ , 506.8 (3)  $[\text{Cu}_2\text{I}_3]^-$ , 316.8 (100)  $[\text{CuI}_2]^-$ , 127.1 (31)  $[\text{I}]^-$

**IR** (KBr):  $\tilde{\nu}$  [ $\text{cm}^{-1}$ ] = 2961 (m), 2921 (w), 2868 (w), 2013 (s; CO), 1971 (s; CO), 1485 (w), 1460 (m), 1404 (w), 1366 (m), 1261 (m), 1240 (m), 1167 (m), 1097 (m {br}), 1023 (m {br}), 803 (m {br}), 511 (w), 465 (m)

Analytical data of  $[(\text{Cp}^*\text{Ta}(\text{CO})_2(\mu_5\text{-}\eta^4\text{:}\eta^1\text{:}\eta^1\text{:}\eta^1\text{-P}_4))\{\text{Cu}_4(\mu_3\text{-I})_4\}]_n$  (**5**):

**Yield:** 12 mg (45 % based on CuI)

**IR** (KBr):  $\tilde{\nu}$  [ $\text{cm}^{-1}$ ] = 2961 (m), 2920 (w), 2868 (w), 2014 (s; CO), 1973 (s; CO), 1485 (w), 1460 (m), 1404 (w), 1366 (m), 1262 (m), 1240 (m), 1167 (m), 1101 (m {br}), 1024 (m {br}), 803 (w), 511 (w), 465 (m)



**Elemental analysis:** Calculated (%) for  $(C_{19}H_{29}TaO_2P_4)_4(CuI)_{16}(CH_3CN)_2(C_7H_8)_3$  (5782.9 g/mol): C 20.98, H 2.55, N 0.48; found: C 21.01, H 2.79, N 0.37.

## 5.5.2 X-ray Structure Analysis

### 5.5.2.1 General remarks

Crystals of were taken from a Schlenk flask under a stream of argon and immediately covered with mineral oil or perfluorinated Fomblin® mineral oil to prevent both decomposition and a loss of solvent. The quickly chosen single crystals covered by a drop of the oil were taken to the pre-centered goniometer head with CryoMount® and directly placed on diffractometer into a stream of cold nitrogen. X-ray diffraction studies faced many challenges, since the crystals have relatively small size and decompose rapidly losing solvent molecules. The data for **1b**, **2d**, **4a** and **5** were collected on an Agilent Technologies Gemini R-Ultra diffractometer equipped with Ruby CCD detector and an Enhanced Ultra  $CuK_{\alpha}$  sealed tube ( $\lambda = 1.54178 \text{ \AA}$ ) using  $1^\circ \omega$  scans. The data for **2b** were collected on a STOE IPDS equipped with STOE image plate detector and  $MoK_{\alpha}$  sealed tube ( $\lambda = 0.71073 \text{ \AA}$ ) using  $0.5^\circ \phi$  scans. The data for **3** and **4b** were collected on a Rigaku SuperNova diffractometer equipped with Titan<sup>S2</sup> CCD detector and a SuperNova  $CuK_{\alpha}$  microfocus source using  $0.5^\circ \omega$  scans. All measurements were performed at 150 (**1b**) or 123 K (the rest). Preliminary data were collected for **2c** (see Sect. 2.4 for detail)

**The following composition was established for structurally investigated compounds** (see corresponding sections):

<b>1b:</b>	$[Cp''Ta(CO)_2(\eta^4-P_4)]$
<b>2b:</b>	$\{[Cp''Ta(CO)_2(\mu_5-\eta^4:\eta^1:\eta^1:\eta^1-P_4)]_6\{CuBr\}_{7.6}\} \cdot 0.5(CH_2Cl_2)$
<b>2c:</b>	$\{[Cp''Ta(CO)_2(\mu_5-\eta^4:\eta^1:\eta^1:\eta^1-P_4)]_6\{CuCl\}_{7.3}\} \cdot nC_7H_8 \cdot mMeCN$ , $n$ and $m$ are unidentified (see Sect. 2.4)
<b>2d:</b>	$\{[Cp''Ta(CO)_2(\mu_5-\eta^4:\eta^1:\eta^1:\eta^1-P_4)]_6\{CuBr\}_{7.7}\} \cdot 3C_6H_6$
<b>3:</b>	$\{[Cp''Ta(CO)_2(\mu_5-\eta^4:\eta^1:\eta^1:\eta^1-P_4)]_6\{Cp''Ta(CO)_2(\mu_4-\eta^4:\eta^1:\eta^1-P_4)\}_4\{Cu_{14}I_{10}(\mu-I)_2(\mu_3-I)_2\}\} \cdot 2.3C_7H_8 \cdot 4.9MeCN$
<b>4a,</b> <b>4b:</b>	$\{[Cp''Ta(CO)_2(\mu_5-\eta^4:\eta^1:\eta^1:\eta^1-P_4)]_5\{Cu_{12}I_3(\mu-I)_8(\mu_4-I)(MeCN)_5\}\} \cdot nC_7H_8 \cdot mMeCN$ , for <b>4a</b> : $n=4.3$ , $m=2.4$ , for <b>4b</b> : $n=2.35$ , $m=3.5$
<b>5:</b>	$\{[Cp''Ta(CO)_2(\mu_5-\eta^4:\eta^1:\eta^1:\eta^1-P_4)]\{Cu_4(\mu_3-I)_4\}\}_n \cdot nC_2H_3N$

The structures of **1b-5** were solved by either charge flipping or direct methods with *SUPERFLIP*,<sup>[24]</sup> *SIR97*,<sup>[25]</sup> or *SHELX97*.<sup>[26]</sup> The structures were refined by full-matrix least-

squares method against  $|F|^2$  in anisotropic approximation using *SHELXL97* or the multiprocessor and variable memory version *SHELXL2013*. All non-hydrogen atoms were refined anisotropically, while the hydrogen atoms were set in calculated positions and refined riding on pivot atoms. Compound **2b** is isostructural to previously reported **2a**. In the crystal structures of **2b-2d**, partly vacant positions of one CuX unit in the scaffold are indicated by high displacement parameters. In addition, one CuX unit appears inside the cavity of the supramolecules. The displacement parameters of these heavy atoms were set equal to  $U_{\text{iso}} = 0.03 \text{ \AA}^{-2}$ , and the occupancy factors were refined. Their resulting values were fixed, and the refinement of the displacement parameters was performed. The solvent molecules in **2b-4** are disordered.

X-ray structure analysis of the compound **3** has proven to be a complicated task. The crystals of **3** are very unstable towards loss of the solvent and show quick amorphization out of mother solution even being protected by Fomblin<sup>®</sup> oil. The crystals slowly decay when irradiated. The unit cell determined from very quickly mounted crystal is monoclinic *C*-centered with  $a=32.91$ ,  $b= 26.31$ ,  $c= 34.63 \text{ \AA}$ ,  $\beta=103.4^\circ$ ,  $V=29171 \text{ \AA}^3$ , while crystals that were kept longer demonstrate twice smaller monoclinic *C*-centered unit cell  $a= 20.94$ ,  $b= 26.32$ ,  $c=26.51 \text{ \AA}$ ,  $\beta=93.0^\circ$ ,  $V= 14588 \text{ \AA}^3$ . Both unit cells are related as structure-superstructure (Fig. S1a). Our experiments show that the intensity of superstructural reflections fades in the series of consequent structural determinations performed from the same single crystal (Fig. S1b-d). Depending on the crystal size, these reflections disappear within 1 or 2 days of irradiation that together with small crystal size means that diffraction data of only a limited quality can be collected. In addition, the quality of the crystals is also limited by strong tendency to twinning, which is not systematic as follows from the five diffraction experiments from different crystals. The structural models in bigger unit cell (space group *C2/c*) feature high residual density (up to  $8 \text{ e} \cdot \text{\AA}^{-3}$ ) at heavy atoms, which can be assigned as the second position ( $\sim 15\%$ ) of the entire supramolecule, which lie in an inversion center  $\bar{1}$  (site symmetry  $C_i$ ). Together with systematically observed higher intensity of the observed reflections compared to calculated ones, the structure **3** demonstrates typical signs of allotwinning. When this electron density is described as the second position (refined portion 0.14), the quality factors ( $R_1$ ,  $wR_2$  and weighting scheme) decrease from  $R_1 = 0.155$  to 0.069,  $wR_2 = 0.355$  to 0.212, etc.

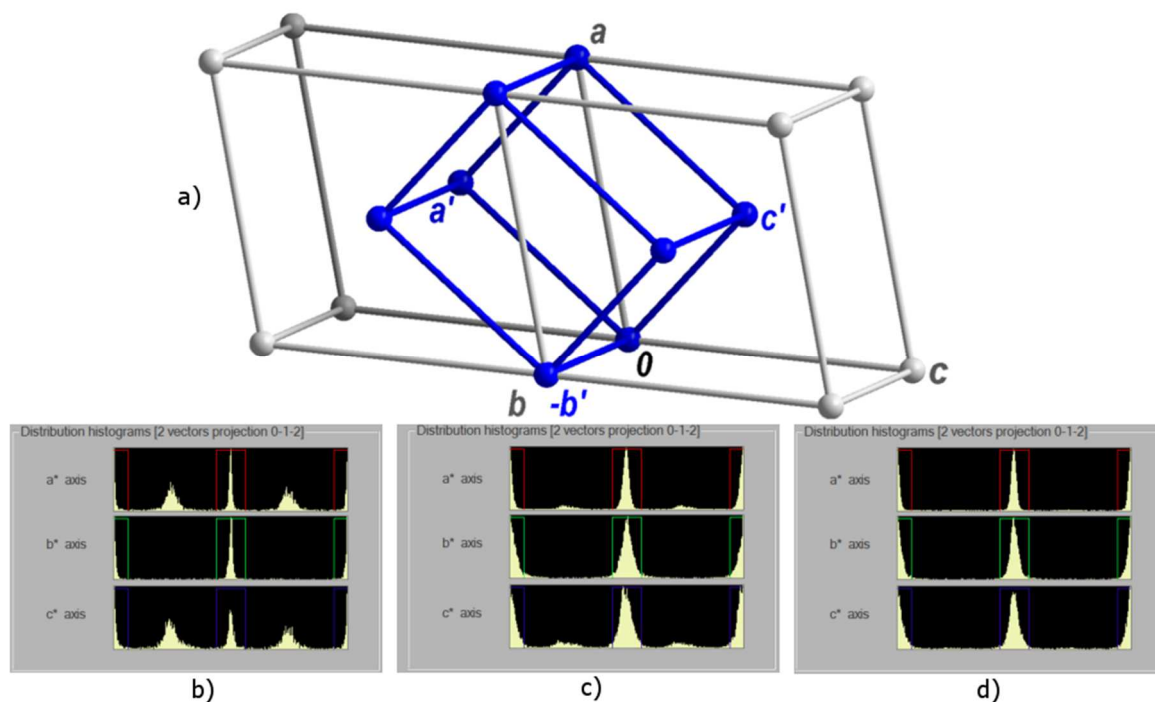


**Figure S1.** (a) Unit cells determined from fresh and aged crystal of **3** related as structure-superstructure. The unit cell relation is  $\mathbf{a}' = 1/2\mathbf{a} + 1/2\mathbf{c}$ ,  $\mathbf{b} = -\mathbf{b}'$ ,  $\mathbf{c}' = 1/2\mathbf{a} - 1/2\mathbf{c}$ , where  $\mathbf{a}$ ,  $\mathbf{b}$ ,  $\mathbf{c}$  and  $\mathbf{a}'$ ,  $\mathbf{b}'$ ,  $\mathbf{c}'$  are primitive vectors in super- and substructural cells, respectively. (b-d) The decrease of intensity of superstructural reflections in the series of consequent structural determinations performed from the same single crystal.

When weak superstructural reflections are ignored, the structure solution in smaller unit cell and  $C2/m$  space group gives the supramolecule lying in  $2/m$  position ( $C_{2h}$  site symmetry). In contrast, this model does not demonstrate significant electron density peaks at heavy atoms, and the displacement parameters of all the heavy atoms are significantly larger giving an impression of a structure averaged by symmetry. If this model is refined over the data collected from the crystal that showed no superstructural effect, it shows the a.d.p. ellipsoids systematically elongated in the direction perpendicular to the  $m_y$  plane. For this reason, the model in larger unit cell is preferred.

For **4**, two structures had been obtained, **4a** as a bulk product of the reaction in presence of  $\text{Cp}^*\text{FeP}_5$ , and **4b** as a 2<sup>nd</sup> phase in a fractional crystallization in the synthesis of **3**. The crystals of **4b** showed radiolysis that complicated the structure determination. Initially yellow crystals turned brown after several attempts to determine their crystal structure (Fig. S2) accompanied by gradual weakening of the diffraction pattern.

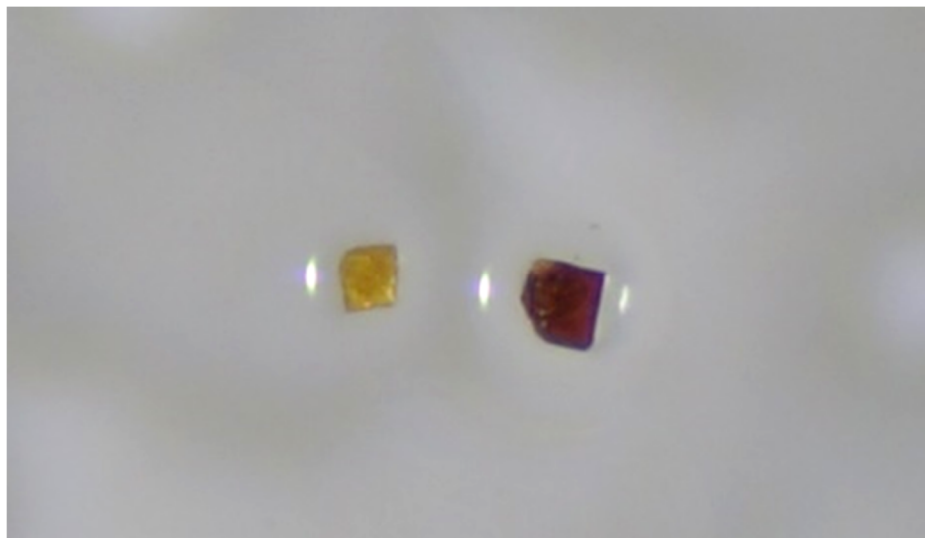


**Figure S2.** The crystal of **4b** before (left) and after irradiation with X-rays (right). The color change takes place after about 1 day irradiation. In case of **4a** the degradation of the crystal was not observed most probably due to its large size (Table S2) that allowed relatively fast X-ray diffraction experiment.

CIF files with comprehensive information on the details of the diffraction experiments and full tables of bond lengths and angles for **1b-5** are deposited in Cambridge Crystallographic Data Centre under the deposition codes CCDC-1482592 - CCDC-1482598, respectively. Crystallographic data and details of the diffraction experiments are given in Tables S1 and S2. The figures are generated with Olex<sup>[27]</sup> and ToposPro.<sup>[28]</sup>

Table S1. Experimental details for 1b-3

	1b	2b	2d	3
CCDC Code	1482592	1482593	1482594	1482595
Crystal data				
Chemical formula	C <sub>19</sub> H <sub>29</sub> O <sub>2</sub> P <sub>4</sub> Ta	C <sub>90</sub> H <sub>126</sub> Br <sub>7.60</sub> Cu <sub>7.60</sub> O <sub>12</sub> P <sub>24</sub> Ta <sub>6</sub> ·0.5(CH <sub>2</sub> Cl <sub>2</sub> )	C <sub>132</sub> H <sub>192</sub> Br <sub>7.70</sub> Cu <sub>7.70</sub> O <sub>12</sub> P <sub>24</sub> Ta <sub>6</sub>	C <sub>175.90</sub> H <sub>243.10</sub> Cu <sub>14.14</sub> N <sub>4.90</sub> O <sub>20</sub> P <sub>40</sub> Ta <sub>10</sub>
<i>M</i> <sub>r</sub>	594.25	4361.56	4904.39	8460.70
Crystal system, space group	Monoclinic, <i>P</i> 2 <sub>1</sub> / <i>n</i>	Trigonal, <i>R</i> 3: <i>H</i>	Monoclinic, <i>P</i> 2 <sub>1</sub> / <i>n</i>	Monoclinic, <i>C</i> 2/ <i>c</i>
Temperature (K)	150	123	123	123
<i>a</i> , <i>b</i> , <i>c</i> (Å)	16.3097(4), 8.4189(1), 18.4362(4)	23.1232(15), 22.5841(18)	17.3683(4), 18.9520(3), 26.5452(4)	32.9105(7), 26.3272(5), 34.6595(8)
β (°)	114.727 (3)	90	97.595 (2)	103.477(2)
<i>V</i> (Å <sup>3</sup> )	2299.36 (10)	10457.5 (16)	8661.1 (3)	29203.5(11)
<i>Z</i>	4	3	2	4
<i>F</i> (000)	1168	6202	4742	15883
<i>D</i> <sub>x</sub> (Mg m <sup>-3</sup> )	1.717	2.078	1.881	1.924
Radiation type	Cu Kα	Mo Kα	Cu Kα	Cu Kα
μ (mm <sup>-1</sup> )	11.54	8.34	12.29	21.84
Crystal habit and colour	yellow plate	red prism	brown plate	orange prism
Crystal size (mm)	0.25 × 0.09 × 0.02	0.09 × 0.08 × 0.06	0.13 × 0.08 × 0.02	0.09 × 0.08 × 0.05
Data collection				
Diffractometer	Xcalibur, Ruby, Gemini ultra	STOE-IPDS diffractometer	Xcalibur, Ruby, Gemini ultra	SuperNova, TitanS2
Absorption correction	Multi-scan	Numerical	Gaussian	Gaussian
<i>T</i> <sub>min</sub> , <i>T</i> <sub>max</sub>	0.317, 1.419	0.474, 0.664	0.361, 0.801	0.314, 0.538
No. of measured, independent and observed [ <i>I</i> > 2σ( <i>I</i> )] reflections	47006, 3686, 2802	27008, 4989, 4172	28998, 13244, 9306	49327, 27041, 17500
<i>R</i> <sub>int</sub>	0.058	0.081	0.050	0.051
(sin Θ/λ) <sub>max</sub> (Å <sup>-1</sup> )	0.578	0.636	0.572	0.623
Range of <i>h</i> , <i>k</i> , <i>l</i>	<i>h</i> = -18→18, <i>k</i> = -9→9, <i>l</i> = -20→21	<i>h</i> = -25→29, <i>k</i> = -29→27, <i>l</i> = -28→28	<i>h</i> = -19→19, <i>k</i> = -21→20, <i>l</i> = -20→30	<i>h</i> = -34→40, <i>k</i> = -20→32, <i>l</i> = -41→43
Refinement				
<i>R</i> [ <i>F</i> <sup>2</sup> > 2σ( <i>F</i> <sup>2</sup> )], <i>wR</i> ( <i>F</i> <sup>2</sup> ), <i>S</i>	0.024, 0.058, 0.95	0.028, 0.064, 0.96	0.042, 0.117, 0.95	0.070, 0.212, 1.04
No. of reflections	3686	4989	13244	27041
No. of parameters	244	245	1004	1478
No. of restraints	0	0	55	16
H-atom treatment	H-atom parameters constrained	H-atom parameters constrained	H-atom parameters constrained	H-atom parameters constrained
Δ <sub>max</sub> , Δ <sub>min</sub> (e Å <sup>-3</sup> )	1.43, -0.58	1.63, -0.65	1.81, -2.01	4.27, -2.72

Computer programs: *CrysAlis CCD*, Oxford Diffraction, *CrysAlis RED*, *SIR97* (Altomare, 1993), *SHELXL97* (Sheldrick, 1997), *PLATON* (Spek, 2003), *STOE* (1998), *SHELXL2013* (Sheldrick, 2013), *PLATON* (Spek, 2003), *SUPERFLIP* (Palatinus, 2007).

Table S2. Experimental details for 4-5

	4a	4b	5
CCDC Code	1482596	1482597	1482598
Crystal data			
Chemical formula	C <sub>86</sub> H <sub>161.60</sub> Cu <sub>12</sub> I <sub>12</sub> N <sub>7.40</sub> O <sub>10</sub> P <sub>20</sub> Ta <sub>5</sub>	C <sub>106.45</sub> H <sub>146.30</sub> Cu <sub>12</sub> I <sub>12</sub> N <sub>7.50</sub> O <sub>10</sub> P <sub>20</sub> Ta <sub>5</sub>	C <sub>21</sub> H <sub>32</sub> NCu <sub>4</sub> I <sub>4</sub> O <sub>2</sub> P <sub>4</sub> Ta
<i>M<sub>r</sub></i>	5675.99	5500.43	1397.06
Crystal system, space group	Orthorhombic, <i>Pbca</i>	Monoclinic, <i>P2<sub>1</sub>/n</i>	Monoclinic, <i>P2<sub>1</sub>/c</i>
Temperature (K)	123	123	123
<i>a</i> , <i>b</i> , <i>c</i> (Å)	31.1708(4), 31.9398(5), 35.6999(5)	20.9613 (5), 32.1655 (6), 30.1770 (6)	17.6897(4), 14.1142(4), 14.2011(3)
β (°)	90	108.513 (2)	94.870 (2)
<i>V</i> (Å <sup>3</sup> )	35542.4 (9)	19293.4 (7)	3532.87 (15)
<i>Z</i>	8	4	4
<i>F</i> (000)	21294	10266	2568
<i>D<sub>x</sub></i> (Mg m <sup>-3</sup> )	2.121	1.894	2.627
Radiation type	Cu Kα	Cu Kα	Cu Kα
μ (mm <sup>-1</sup> )	25.41	23.40	37.67
Crystal habit and colour	yellow prism	yellow prism	yellow plate
Crystal size (mm)	0.32 × 0.30 × 0.23	0.09 × 0.07 × 0.04	0.25 × 0.13 × 0.01
Data collection			
Diffractometer	Xcalibur, Ruby, Gemini ultra	Rigaku SuperNova, Titan <sup>S2</sup>	Xcalibur, Ruby, Gemini ultra
Absorption correction	For a sphere	Gaussian	Gaussian
<i>T<sub>min</sub></i> , <i>T<sub>max</sub></i>	0.014, 0.077	0.239, 0.527	0.057, 0.827
No. of measured, independent and observed [ <i>I</i> > 2σ( <i>I</i> )] reflections	69945, 27585, 23733	70458, 37049, 21383	12538, 5449, 4072
<i>R<sub>int</sub></i>	0.058	0.054	0.051
(sin θ/λ) <sub>max</sub> (Å <sup>-1</sup> )	0.574	0.623	0.573
Range of <i>h</i> , <i>k</i> , <i>l</i>	<i>h</i> = -35→34, <i>k</i> = -35→36, <i>l</i> = -40→37	<i>h</i> = -25→21, <i>k</i> = -29→38, <i>l</i> = -36→36	<i>h</i> = -12→20, <i>k</i> = -15→16, <i>l</i> = -15→16
Refinement			
<i>R</i> [ <i>F</i> <sup>2</sup> > 2σ( <i>F</i> <sup>2</sup> )], <i>wR</i> ( <i>F</i> <sup>2</sup> ), <i>S</i>	0.050, 0.131, 1.03	0.053, 0.138, 0.88	0.043, 0.104, 0.93
No. of reflections	27585	37049	5449
No. of parameters	1748	1638	344
No. of restraints	12	22	0
H-atom treatment	H-atom parameters constrained	H-atom parameters constrained	H-atom parameters constrained
Δ <sub>max</sub> , Δ <sub>min</sub> (e Å <sup>-3</sup> )	2.37, -1.43	4.92, -2.90	2.43, -1.14

Computer programs: *CrysAlis PRO* 1.171.38.41 (Rigaku OD, 2015), *SIR97* (Altomare, 1999), *SHELXL97* (Sheldrick, 1997), *SHELXL2013* (Sheldrick, 2013), *SUPERFLIP* (Palatinus, 2007).

5.5.2.2 Crystal structure of **1b**

Compound **1b** crystallizes as yellow plates from hexane solution.

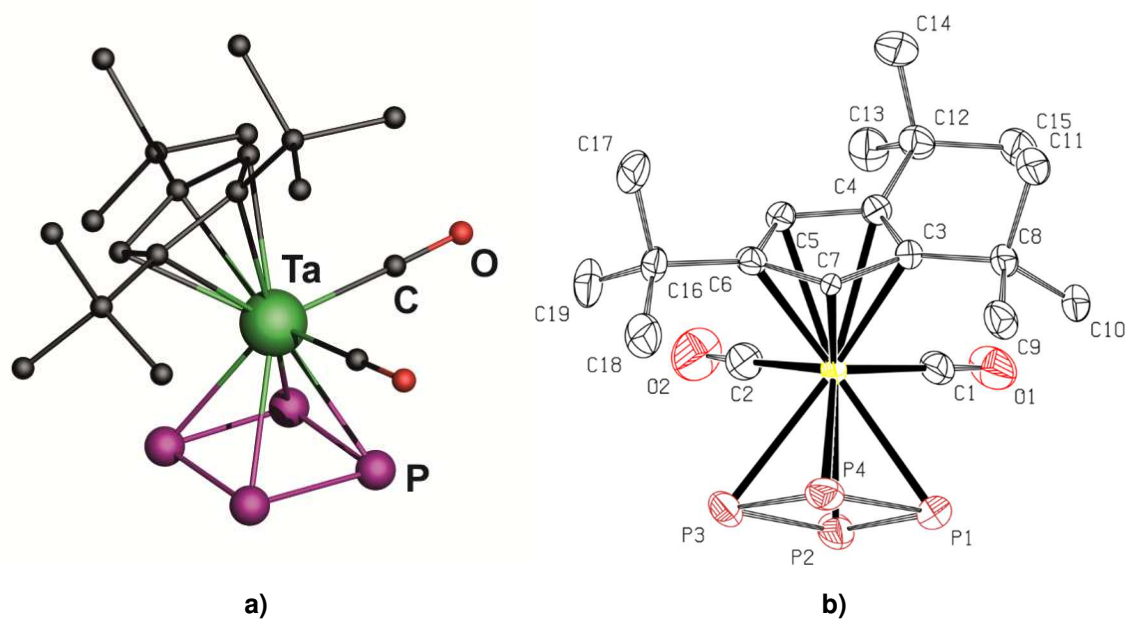


**Figure S3.** Molecular structure of **1b** in (a) ball-and-stick and (b) a.d.p. ellipsoid (50%) representation. Hydrogen atoms are omitted for clarity.

**Table S3.** Selected geometric parameters ( $\text{\AA}$ ,  $^\circ$ ) for **1b**.

Ta1—P1	2.6410 (12)	Ta1—C6	2.406 (3)
Ta1—P2	2.6495 (10)	Ta1—C7	2.386 (3)
Ta1—P3	2.6385 (10)	P1—P2	2.1729 (17)
Ta1—P4	2.6200 (11)	P1—P4	2.1555 (15)
Ta1—C1	2.078 (4)	P2—P3	2.1800 (15)
Ta1—C2	2.082 (5)	P3—P4	2.1624 (17)
Ta1—C3	2.415 (3)	O1—C1	1.138 (5)
Ta1—C4	2.464 (3)	O2—C2	1.134 (6)
Ta1—C5	2.414 (3)		
P2—P1—P4	88.64 (6)	P1—P4—P3	92.00 (6)
P1—P2—P3	91.06 (6)	Ta1—C1—O1	178.7 (3)
P2—P3—P4	88.28 (6)	Ta1—C2—O2	177.8 (4)

5.5.2.3 Crystal structure of **2b**

Compound  $[(Cp^*Ta(CO)_2P_4)_6(CuBr)_{7.6}] \cdot 0.5(CH_2Cl_2)$  (**2b**) crystallizes as orange blocks from  $CH_2Cl_2/CH_3CN/dmf-d_7$  mixtures. **2b** crystallizes with half of the molecule  $CH_2Cl_2$  per formula unit. The electron density at the center of the core of **2b** was assigned as minor position of bromide, which is coordinated to  $\eta_2$ -coordinated to *cyclo*-P<sub>4</sub> Cu(I) ion.

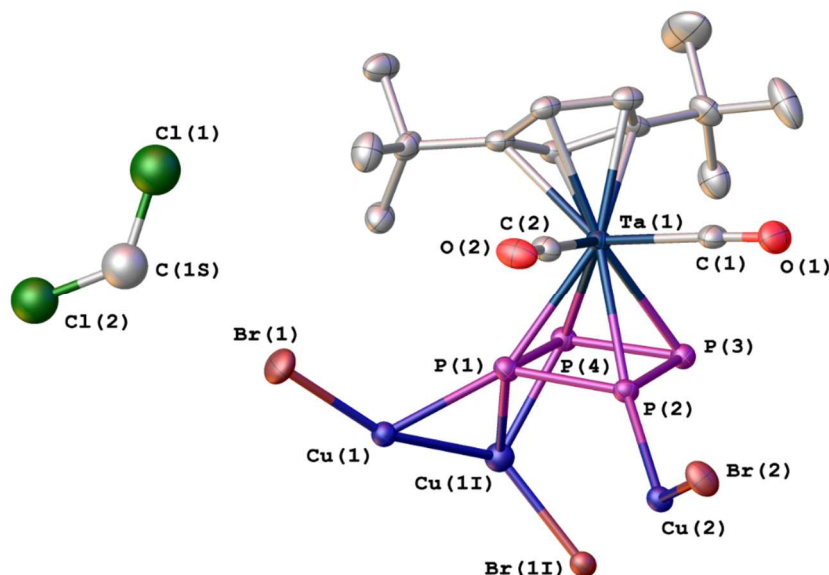
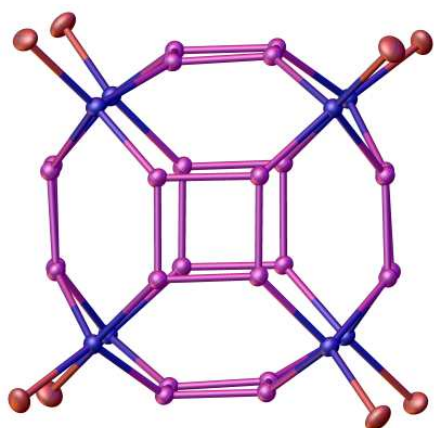


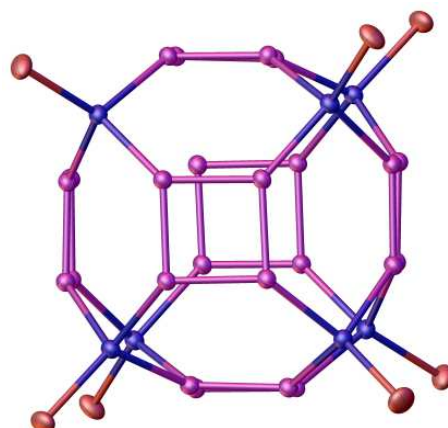
**Figure S4.** The independent part of supramolecule **2b**: (a) the disorder and (b) the enumeration scheme (cf. Table S4).

The inorganic scaffold of **2b** contains partly occupied Cu and Br positions, (Cu(1), Br(1) with occupancies 0.75; Cu(1i), Br(1i) with occupancies 0.1). They always have complementary occupancies, so that the CuBr unit is present or absent as a whole. These partial occupancies give rise to a disorder in the inorganic core similar to those in **2b**. The disorder can be only interpreted as a number of co-crystallizing supramolecules of similar but different inorganic scaffolds. Some of the co-crystallizing species are depicted in Fig. S5.

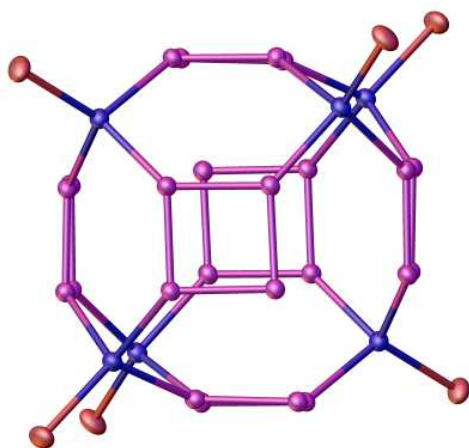




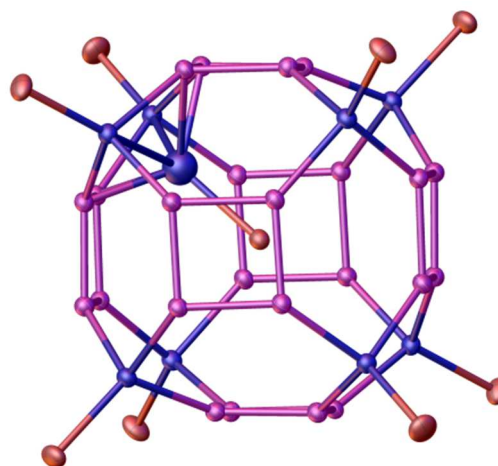
**Moiety 1:** max 0.75  
[[Cp<sup>'''</sup>Ta(CO)<sub>2</sub>P<sub>4</sub>]<sub>6</sub>(CuBr)<sub>8</sub>]



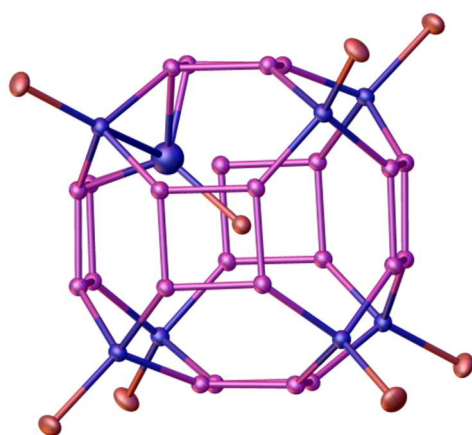
**Moiety 2:** max 0.875  
[[Cp<sup>'''</sup>Ta(CO)<sub>2</sub>P<sub>4</sub>]<sub>6</sub>(CuBr)<sub>7</sub>]



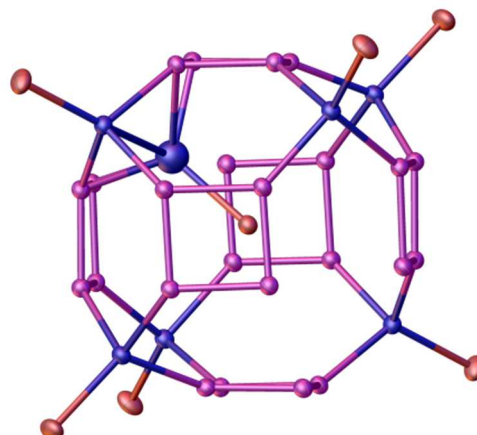
**Moiety 3:** max 1  
[[Cp<sup>'''</sup>Ta(CO)<sub>2</sub>P<sub>4</sub>]<sub>6</sub>(CuBr)<sub>6</sub>]



**Moiety 4:** max 0.1 probability  
[[Cp<sup>'''</sup>Ta(CO)<sub>2</sub>P<sub>4</sub>]<sub>6</sub>(CuBr)<sub>8</sub>(CuBr)]



**Moiety 5:** max 0.1 probability  
[[Cp<sup>'''</sup>Ta(CO)<sub>2</sub>P<sub>4</sub>]<sub>6</sub>(CuBr)<sub>7</sub>(CuBr)]



**Moiety 6:** max 0.1 probability  
[[Cp<sup>'''</sup>Ta(CO)<sub>2</sub>P<sub>4</sub>]<sub>6</sub>(CuBr)<sub>6</sub>(CuBr)]

**Figure S5.** Some co-crystallizing supramolecules of **2b** of similar but different inorganic scaffolds.

**Table S4.** Selected geometric parameters (Å, °) for **2b**.

Br1I—Cu1I <sup>i</sup>	2.25 (5)	Ta1—P4	2.6177 (10)
Br1I—Cu1I <sup>ii</sup>	2.25 (5)	Ta1—P3	2.6385 (10)
Br1I—Cu1I <sup>iii</sup>	2.25 (5)	Ta1—P1	2.6405 (11)
Br1I—Cu1I <sup>iv</sup>	2.25 (5)	Ta1—P2	2.6609 (11)
Br1I—Cu1I <sup>v</sup>	2.25 (5)	P1—P4	2.1595 (15)
Br1I—Cu1I	2.25 (5)	P1—P2	2.1828 (15)
Cu1I—P4	2.23 (6)	P2—P3	2.1840 (15)
Cu1I—P1 <sup>iv</sup>	2.28 (6)	P3—P4	2.1569 (15)
Cu1I—P1	2.34 (6)	Cu1—Br1	2.3281 (14)
Cu1I—P2 <sup>iv</sup>	2.47 (6)	Cu2—Br2	2.3635 (7)
Cu1—P1 <sup>i</sup>	2.3072 (12)	P1—Cu1I <sup>ii</sup>	2.28 (6)
Cu1—P1	2.3073 (12)	P2—Cu1I <sup>ii</sup>	2.47 (6)
Cu1—P1 <sup>iv</sup>	2.3074 (12)	P3—Cu2 <sup>i</sup>	2.3113 (11)
Cu2—P3 <sup>v</sup>	2.3113 (11)	P4—Cu2 <sup>iv</sup>	2.3152 (12)
Cu2—P4 <sup>ii</sup>	2.3152 (12)	C1—O1	1.141 (6)
Cu2—P2	2.3312 (12)	C2—O2	1.137 (6)
Cu1I <sup>i</sup> —Br1I—Cu1I <sup>ii</sup>	180 (3)	P3 <sup>v</sup> —Cu2—P4 <sup>ii</sup>	98.77 (4)
Cu1I <sup>ii</sup> —Br1I—Cu1I <sup>iii</sup>	124 (2)	P3 <sup>v</sup> —Cu2—P2	101.27 (4)
P4—Cu1I—P2 <sup>iv</sup>	97 (2)	P4 <sup>ii</sup> —Cu2—P2	98.84 (4)
P1—Cu1I—P2 <sup>iv</sup>	126 (2)	P3 <sup>v</sup> —Cu2—Br2	114.72 (4)
P1 <sup>ii</sup> —Cu1—P1	99.71 (4)	P4 <sup>ii</sup> —Cu2—Br2	118.18 (3)
P1 <sup>ii</sup> —Cu1—P1 <sup>iv</sup>	99.71 (4)	P2—Cu2—Br2	121.29 (3)
P1—Cu1—P1 <sup>iv</sup>	99.71 (4)	P4—P1—P2	88.18 (5)
P1 <sup>ii</sup> —Cu1—Br1	118.04 (3)	P1—P2—P3	91.09 (6)
P1—Cu1—Br1	118.04 (3)	P4—P3—P2	88.22 (5)
P1 <sup>iv</sup> —Cu1—Br1	118.04 (3)	P3—P4—P1	92.46 (6)

Symmetry code(s): (i)  $x-y, x, -z$ ; (ii)  $-x+y, -x, z$ ; (iii)  $-x, -y, -z$ ; (iv)  $-y, x-y, z$ ; (v)  $y, -x+y, -z$ .

5.5.2.4 Preliminary data on the crystal structure of **2c**

Compound **2c** crystallizes as very small orange blocks from toluene/MeCN mixtures. The dataset was collected on a synchrotron from a small and twinned crystal. The data were collected only up to the minimal resolution of 1 Å. The limited quality of the resulting dataset and lack of data allowed however to establish the major features of the crystal structure but did not allow its proper refinement. The compound is not isostructural to **2d** probably because of the differences in a solvate portion.

**Table S5.** Preliminary data for X-ray diffraction experiment for **2c**.

Empirical formula	$C_{114}H_{174}Cl_{7.4}Cu_{7.4}O_{12}P_{24}Ta_6 \cdot n C_7H_8 \cdot m$
Measurement device type	STOE IPDS 2
Wavelength	synchrotron ( $\lambda = 0.80000 \text{ \AA}$ )
Temperature	100 K
Crystal system	monoclinic
Space group	$P2_1/n$
Unit cell dimensions	$a = 18.358(4) \text{ \AA}$
	$b = 18.145(4) \text{ \AA}$
	$c = 29.282(6) \text{ \AA}$
	$\beta = 107.31(3)^\circ$
	$V = 9312(4) \text{ \AA}^3$
Formula units per unit cell	2
Crystal size [mm]	$0.05 \times 0.05 \times 0.02$
$R_{\text{int}}$	0.1162

The scaffold of the supramolecule **2c** is constituted similarly to **2b** and **2d**. The CuCl vacancy in the inorganic core is also proved, and the disorder revealing CuCl group pointing inside the inner cavity of the supramolecule is confirmed in analogy to the crystal structures of **2b** and **2d**. Nevertheless, the weight of two copper positions that was localized in the cavity do not suffice to compensate the occupancy of the central Cl atom. Therefore, charge balance cannot be achieved for this structure. The  $(CuCl)_{7.4}$  composition was determined according to the chloride content solely can be criticized. Three positions of a toluene and one position of a MeCN solvate molecules were also localized. The resulting quality factors are  $R_1 = 0.0780$ ,  $wR_2 = 0.2274$ ,  $GooF = 1.049$  that is high for low-resolution dataset. The largest difference peak and hole are 2.17 and  $-1.64 \text{ e} \cdot \text{\AA}^{-3}$ , while r.m.s. of the electron density is very high ( $0.29 \text{ e} \cdot \text{\AA}^{-3}$ ) and does not allow to recognize the missing low-occupied positions of Cu and solvent molecules. Even if 150 peaks of electron density are constructed in the difference Fourier map. For this reason, the refinement of

**2c** crystal structure cannot be accomplished. For the same reason the bond distances and other details are not further discussed.

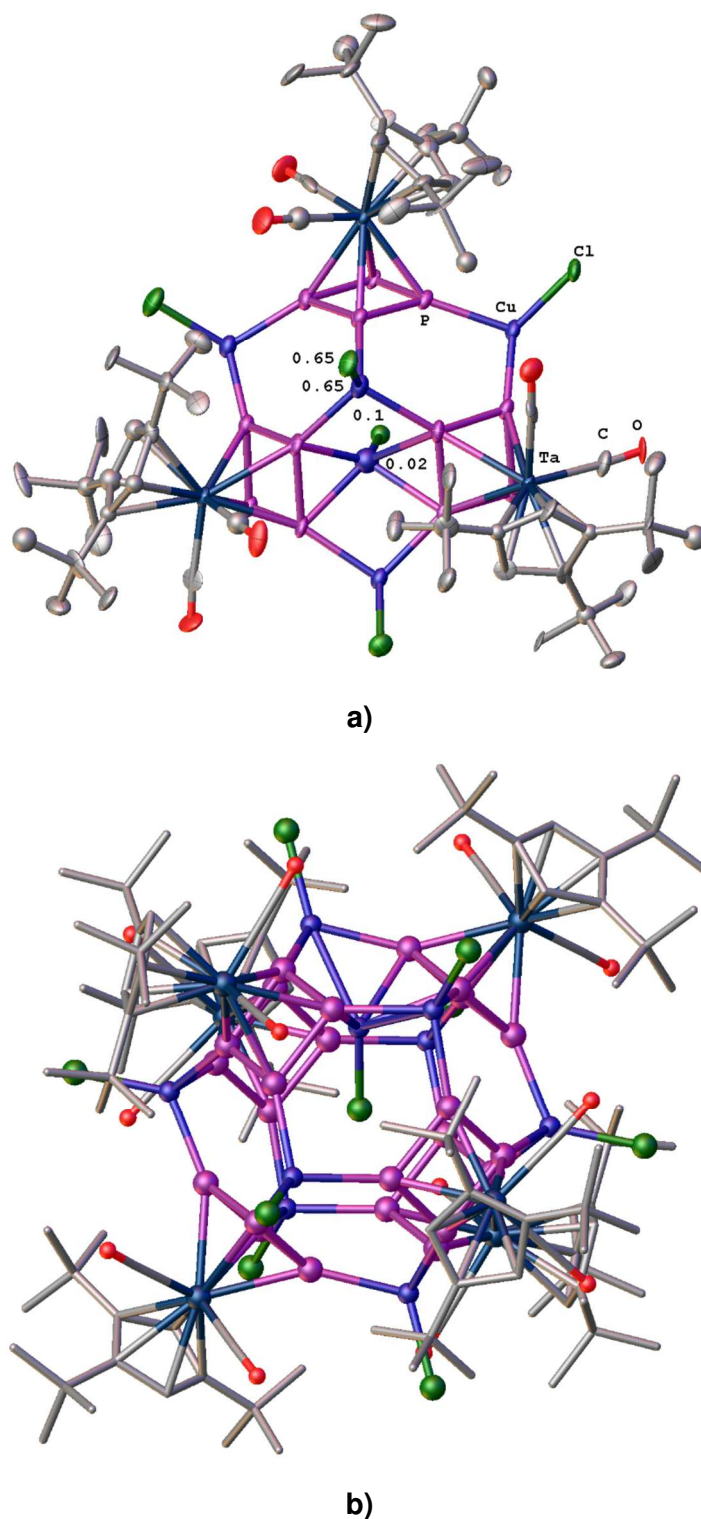


**Figure S6.** The supramolecule **2c**: (a) the independent part (ellipsoids of 50% probability). The occupancies of partly occupied Cu and Cl atoms are depicted; (b) ball-and-stick representation.

5.5.2.5 Crystal structure of **2d**

Compound  $[(\text{Cp}^*\text{Ta}(\text{CO})_2\text{P}_4)_6(\text{CuBr})_{7.6}(\text{CuBr})_{0.1}]\cdot 3(\text{C}_6\text{H}_6)$  (**2d**) crystallizes as orange blocks from benzene/MeCN mixtures. The asymmetric unit (Fig. S7) contains half a molecule of **2d** and two benzene solvent molecules. The terminal bromide group, *t*Bu groups of the  $\text{Cp}^*$  ligands, one entire  $\text{Cp}^*$  groups, and one benzene molecule are disordered over two positions.

The inorganic scaffold of **2d** contains partly occupied Cu and Br positions, (Cu(2v), Br(2a)+Br(2b) with occupancies 0.8; Cu(1i), Br(1i) with occupancies 0.1). They always have complimentary occupancies, so that the CuBr unit is present or absent as a whole. These partial occupancies give rise to a disorder in the inorganic core similar to those in **2b**. The disorder can be only interpreted as a number of co-crystallizing supramolecules of similar but different inorganic scaffolds. Some of the isomers are depicted in Fig. S8.

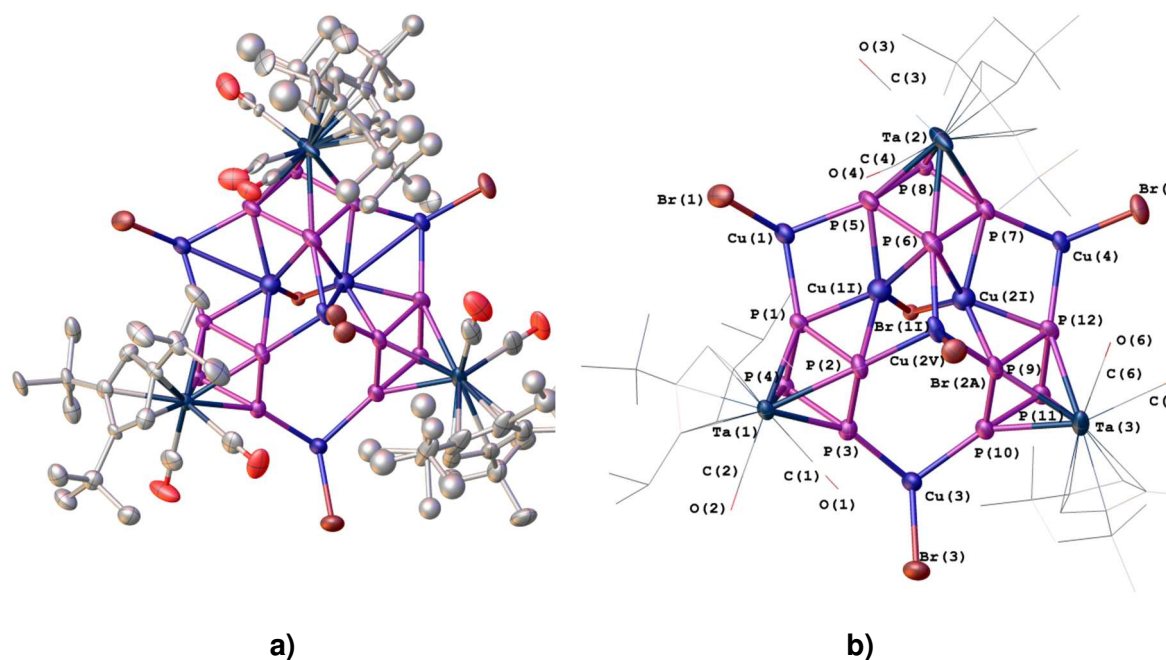
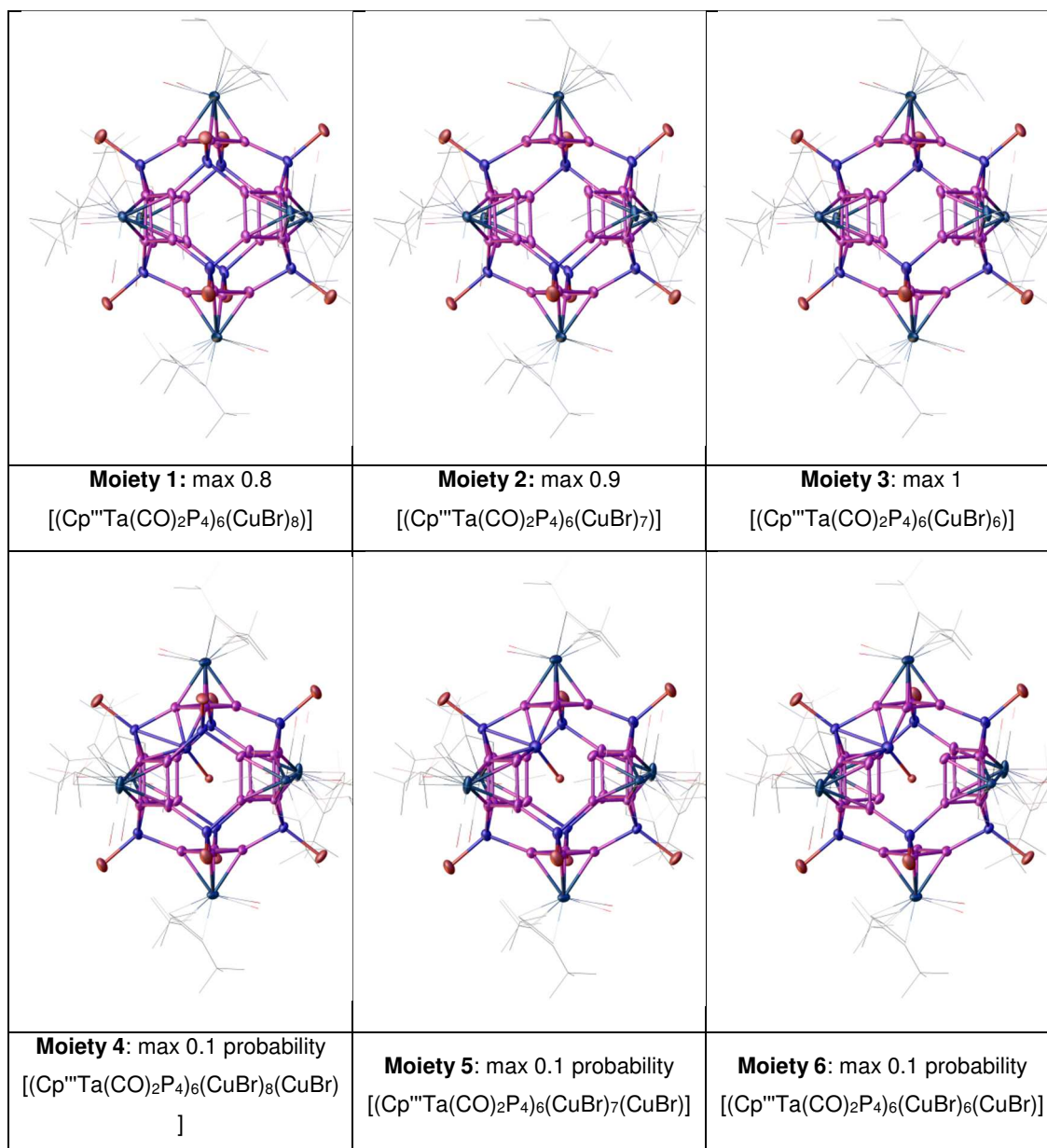


**Figure S7.** The independent part of supramolecule **2d**: (a) the disorder and (b) the enumeration scheme (cf. Table S6).

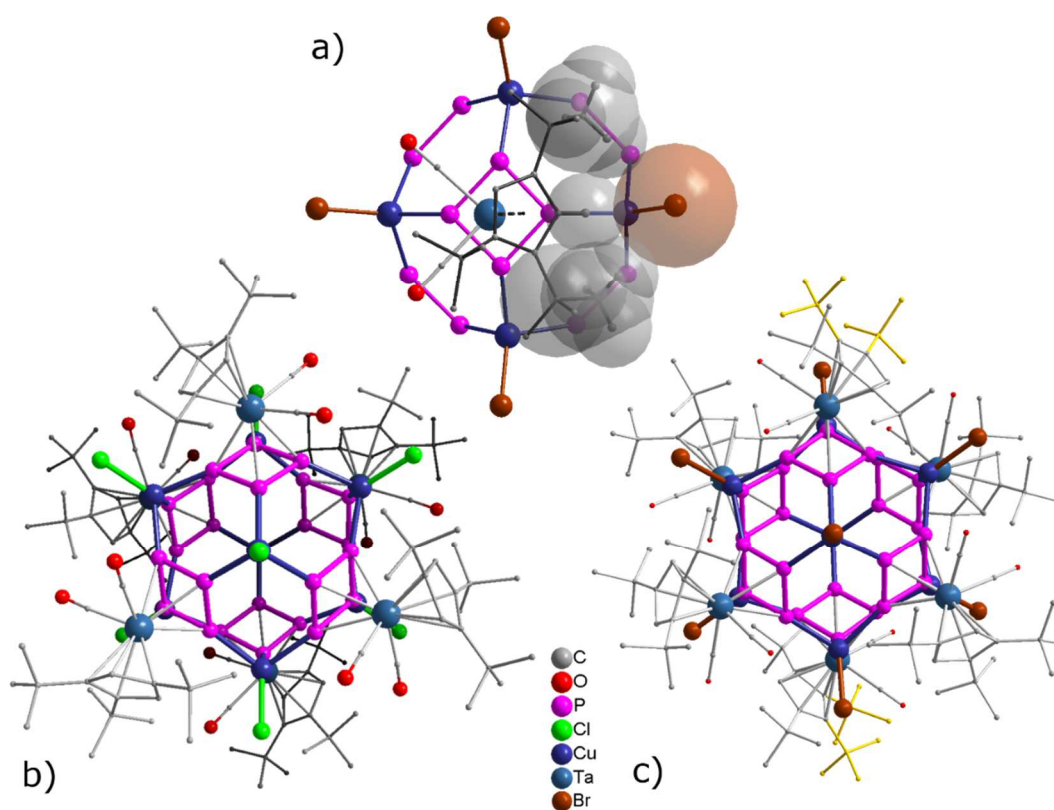
**Table S6.** Selected geometric parameters (Å) for **2d**.

Br1I—Cu2I	2.26 (6)	Cu3—Br3	2.3473 (16)
Br1I—Cu2I <sup>i</sup>	2.26 (6)	Cu4—Br4	2.3431 (13)
Br1I—Cu1I	2.33 (4)	Ta1—P1	2.620 (2)
Br1I—Cu1I <sup>i</sup>	2.33 (4)	Ta1—P2	2.631 (2)
Cu1I—P1	2.23 (4)	Ta1—P4	2.6434 (19)
Cu1I—P6	2.31 (4)	Ta1—P3	2.657 (2)
Cu1I—P5	2.33 (5)	Ta3—P10	2.622 (2)
Cu1I—P2	2.42 (5)	Ta3—P11	2.633 (2)
Cu1I—Cu1	2.81 (4)	Ta3—P12	2.637 (2)
Cu1I—Cu2V	2.83 (4)	Ta3—P9	2.638 (2)
Cu2I—P9	2.21 (6)	P1—P4	2.149 (3)
Cu2I—P12	2.33 (6)	P1—P2	2.149 (3)
Cu2I—P7	2.36 (7)	P2—P3	2.176 (3)
Cu2I—P6	2.41 (7)	P3—P4	2.168 (3)
Cu2I—Cu2V	2.77 (6)	P5—P6	2.170 (3)
Cu2I—Cu4	2.92 (7)	P5—P8	2.174 (3)
Br2A—Cu2V	2.357 (6)	P6—P7	2.150 (3)
Br2B—Cu2V	2.338 (7)	P7—P8	2.148 (3)
Cu2V—P9	2.307 (3)	P9—P10	2.144 (3)
Cu2V—P2	2.325 (2)	P9—P12	2.168 (3)
Cu2V—P6	2.326 (3)	P10—P11	2.155 (3)
Cu1—P1	2.314 (2)	P11—P12	2.161 (3)
Cu1—P11 <sup>i</sup>	2.316 (2)	P4—Cu4 <sup>i</sup>	2.312 (2)
Cu1—P5	2.326 (2)	P8—Cu3 <sup>i</sup>	2.301 (3)
Cu3—P8 <sup>i</sup>	2.301 (3)	P11—Cu1 <sup>i</sup>	2.316 (2)
Cu3—P10	2.319 (2)	C1—O1	1.120 (11)
Cu3—P3	2.322 (2)	C2—O2	1.121 (12)
Cu4—P12	2.298 (2)	C5—O5	1.098 (11)
Cu4—P7	2.306 (2)	C6—O6	1.130 (14)
Cu4—P4 <sup>i</sup>	2.312 (2)	C3—O3	1.16 (3)
Cu1—Br1	2.3406 (15)	C4—O4	1.18 (3)

Symmetry code(s): (i) -x+1, -y, -z.



**Figure S8.** Some supramolecules co-crystallizing in **2d** possessing similar but different inorganic scaffolds.

5.5.2.6 A comparison of the supramolecules in **2b** and **2d**

**Figure S9.** Steric hindrance of Cp''' ligand at **1b** when coordinating CuX to form supramolecule **2**. View along the threefold axis of the major isomer in **2b** and **2d**. The disordered *t*Bu groups (in 0.6/0.4 ratio), which positions cause isomerism are marked in yellow.

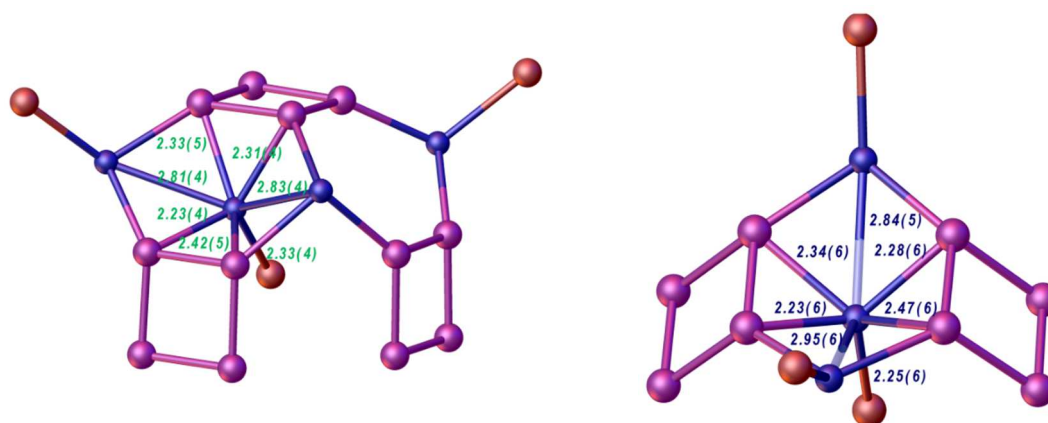


**Figure S10.** The geometry of the disordered fragments in (left) **2b** and (right) **2d**.



5.5.2.7 Crystal structure of **3**

Compound **3** crystallizes as orange blocks from toluene/MeCN mixtures. The solvent molecules occupy the vacancy between the clusters **3** and are strongly positionally disordered. The inorganic scaffold of **3** contains no vacant or disordered positions (Fig. S11). The solvent toluene and MeCN molecule occupy their positions with low probability. To refine them, a number of restraints was applied.

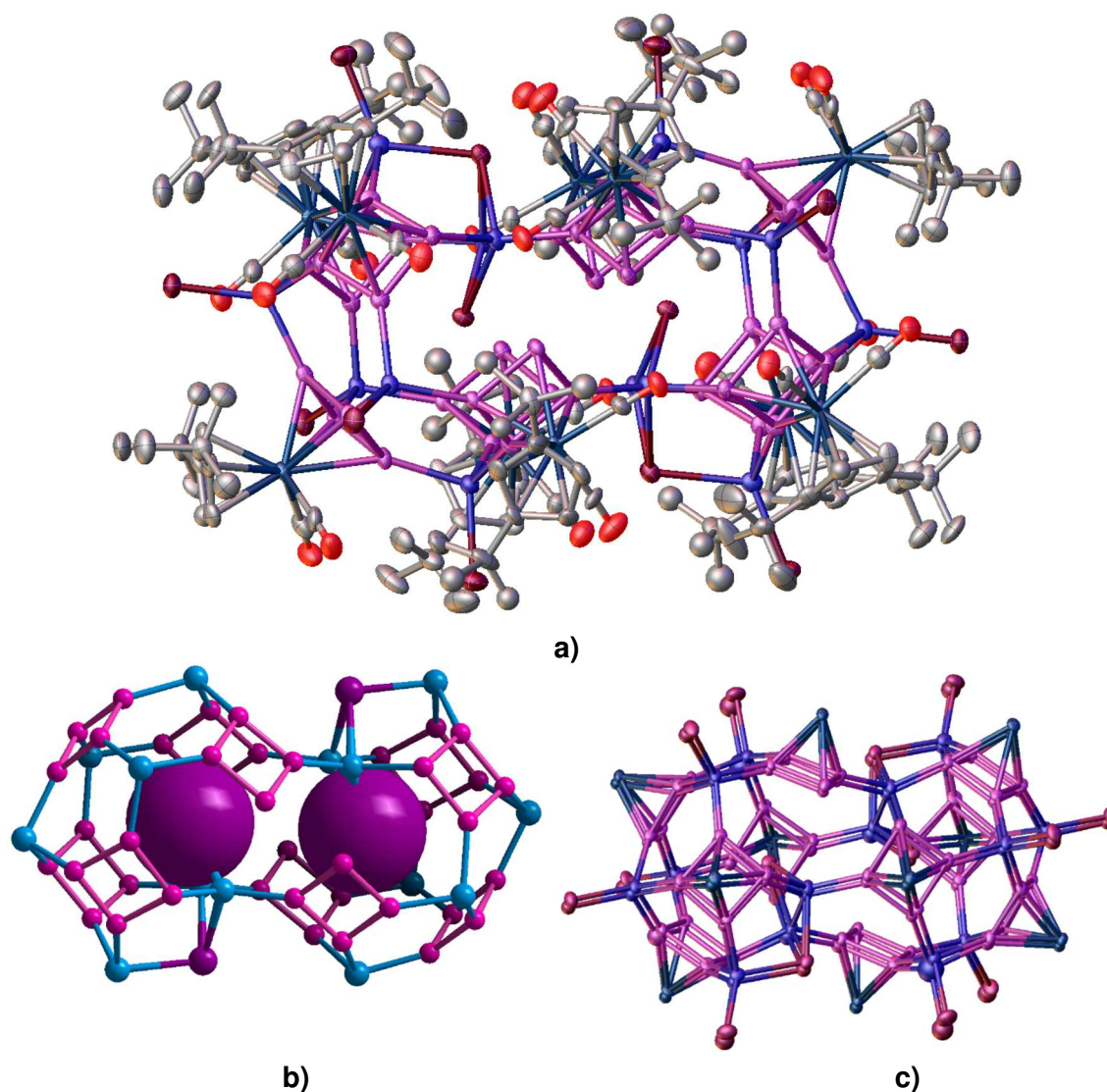


**Figure S11.** (a) The supramolecule in **3** (a.d.p. ellipsoids at 50% probability). Hydrogen atoms are not shown for clarity. (b) The  $\mu$ -I ions blocking the cavity in the scaffold of the supramolecule **3** are shown as van der Waals spheres. (c) allotwinning in **3** described in the structural model as a second component of the inorganic core, which refined portion is about 14%.

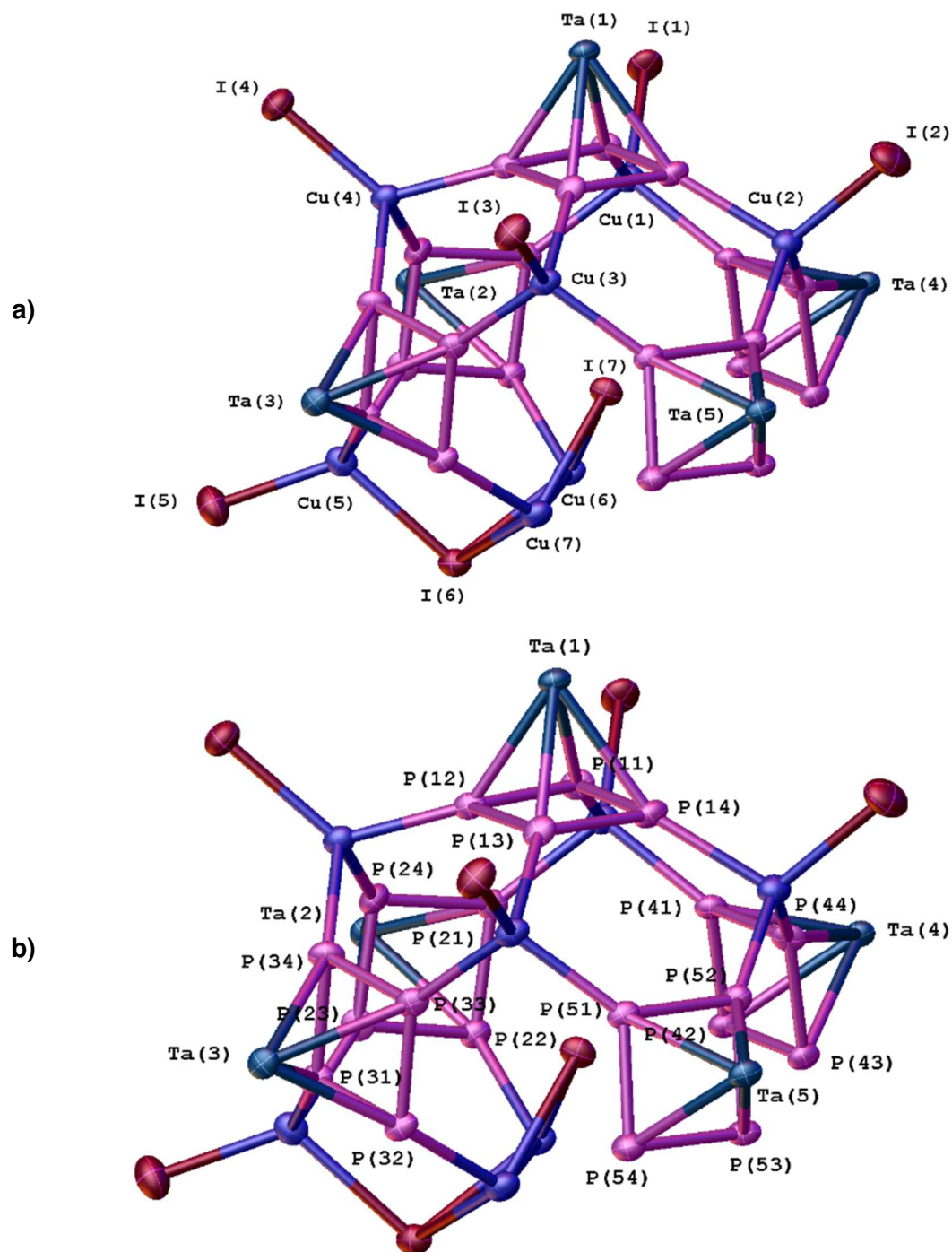


**Figure S12.** (a,b) The enumeration scheme in the inorganic scaffold of the supramolecule 4a (independent part is shown of the scaffold only).

**Table S7.** Selected geometric parameters (Å, °) for **3** and enumerating scheme.

	Major part	Minor part*		Major part	Minor part*
Cu1—I1	2.532 (2)	2.51 (2)	Ta1—P12	2.605 (3)	2.619 (18)
Cu2—I2	2.540 (2)	2.53 (3)	Ta1—P11	2.631 (4)	2.61 (3)
Cu3—I3	2.519 (3)	2.558 (17)	Ta1—P13	2.638 (4)	2.68 (2)
Cu4—I4	2.532 (2)	2.514 (17)	Ta1—P14	2.696 (4)	2.70 (3)
Cu5—I5	2.515 (2)	2.490 (17)	Ta2—P23	2.590 (4)	2.60 (3)
Cu5—I6	2.704 (2)	2.731 (16)	Ta2—P24	2.634 (5)	2.66 (4)
Cu6—I6	2.682 (2)	2.71 (2)	Ta2—P21	2.656 (4)	2.60 (2)
Cu6—I7	2.596 (2)	2.698 (17)	Ta2—P22	2.683 (4)	2.62 (3)
Cu7—I7	2.600 (3)	2.592 (17)	Ta3—P31	2.599 (4)	2.63 (3)
Cu7—I6	2.675 (3)	2.61 (2)	Ta3—P33	2.639 (4)	2.71 (2)
Cu1—P41	2.286 (4)	2.30 (3)	Ta3—P34	2.654 (5)	2.58 (3)
Cu1—P21	2.307 (4)	2.30 (3)	Ta3—P32	2.674 (4)	2.71 (3)
Cu1—P11	2.310 (4)	2.32 (3)	Ta4—P41	2.590 (4)	2.55 (3)
Cu2—P44	2.335 (4)	2.18 (4)	Ta4—P43	2.657 (4)	2.67 (3)
Cu2—P52	2.367 (5)	2.60 (4)	Ta4—P44	2.667 (4)	2.66 (2)
Cu2—P14	2.373 (4)	2.38 (5)	Ta4—P42	2.672 (4)	2.72 (3)
Cu3—P51	2.279 (4)	2.27 (3)	Ta5—P51	2.596 (4)	2.59 (3)
Cu3—P33	2.308 (4)	2.28 (3)	Ta5—P53	2.669 (4)	2.63 (3)
Cu3—P13	2.309 (5)	2.30 (2)	Ta5—P54	2.673 (4)	2.68 (3)
Cu4—P12	2.301 (4)	2.28 (2)	Ta5—P52	2.681 (4)	2.65 (3)
Cu4—P34	2.339 (5)	2.45 (3)	P11—P12	2.140 (5)	2.12 (3)
Cu4—P24	2.347 (5)	2.28 (5)	P11—P14	2.157 (6)	2.21 (4)
Cu5—P31	2.278 (4)	2.25 (3)	P12—P13	2.144 (6)	2.18 (3)
Cu5—P23	2.283 (4)	2.26 (3)	P13—P14	2.190 (6)	2.11 (4)
Cu6—P43 <sup>i</sup>	2.251 (4)	2.30 (4)	P21—P24	2.165 (6)	2.19 (5)
Cu6—P22	2.444 (4)	2.46 (3)	P21—P22	2.191 (5)	2.12 (3)
Cu7—P53 <sup>i</sup>	2.255 (4)	2.28 (3)	P22—P23	2.167 (6)	2.17 (3)
Cu7—P32	2.433 (5)	2.43 (3)	P23—P24	2.138 (5)	2.23 (5)
P53—Cu7 <sup>i</sup>	2.255 (4)	2.28 (3)	P31—P32	2.149 (6)	2.20 (3)
			P31—P34	2.155 (5)	2.17 (4)
C11C—O11C	1.135 (17)	-	P32—P33	2.163 (5)	2.24 (3)
C12C—O12C	1.100 (17)	-	P33—P34	2.167 (6)	2.15 (4)
C21C—O21C	1.134 (17)	-	P41—P44	2.150 (5)	2.16 (4)
C22C—O22C	1.098 (15)	-	P41—P42	2.154 (5)	2.12 (4)
C31C—O31C	1.123 (16)	-	P42—P43	2.164 (6)	2.15 (5)
C32C—O32C	1.153 (18)	-	P43—P44	2.169 (5)	2.21 (3)
C41C—O41C	1.081 (16)	-	P51—P52	2.144 (6)	2.22 (4)
C42C—O42C	1.159 (15)	-	P51—P54	2.159 (5)	2.18 (4)
C51C—O51C	1.147 (17)	-	P52—P53	2.183 (5)	2.07 (3)
C52C—O52C	1.142 (15)	-	P53—P54	2.174 (6)	2.19 (4)

\* the second position of the disordered inorganic scaffold has the same atom names with a suffix A.

### 5.5.2.8 Topological interrelation between inorganic scaffolds of the supramolecules **2** and **3**

The supramolecules **2** and **3** contain similar fragments with topology of a truncated octahedron also known as non-classical fullerene topology.

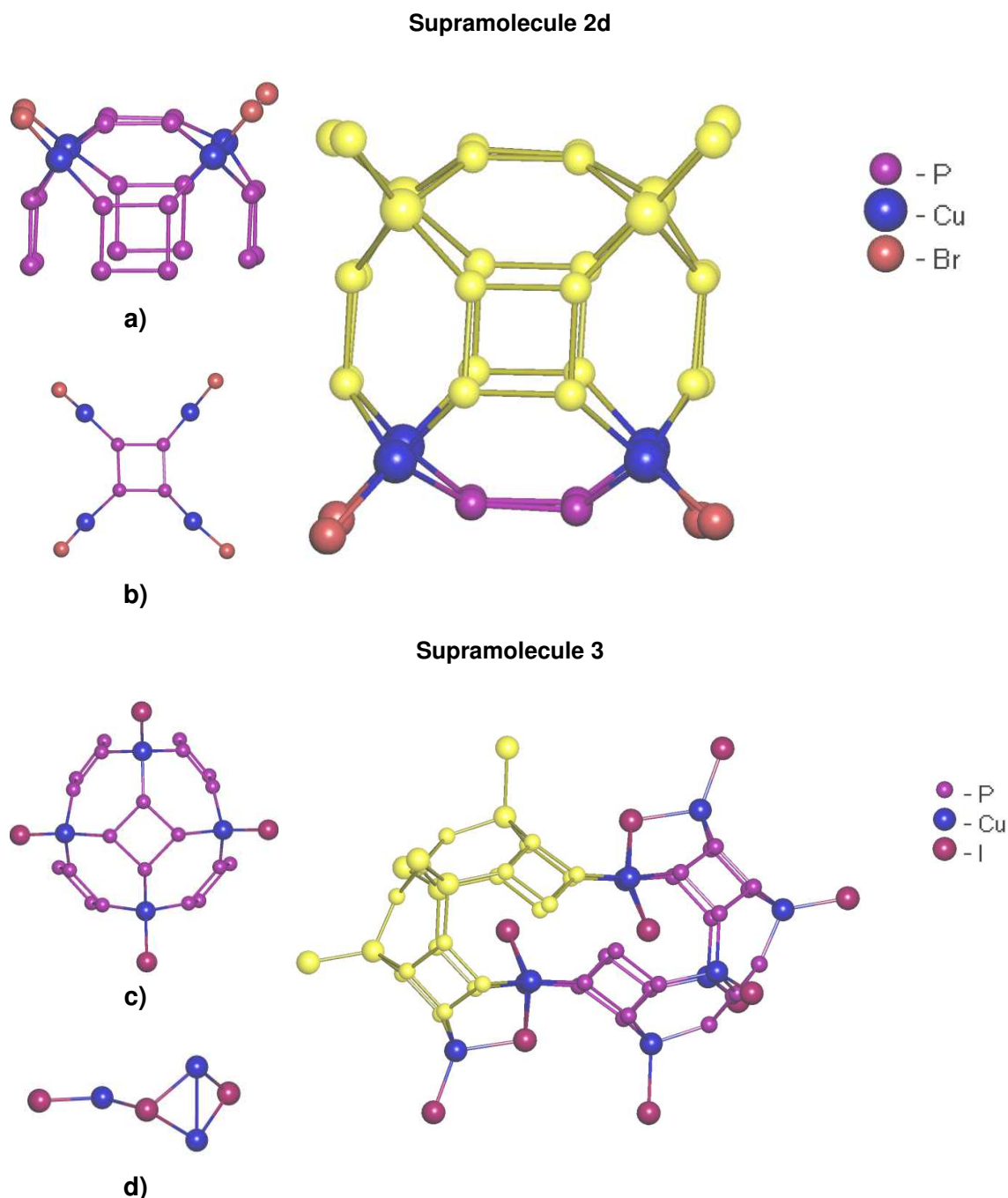


**Figure S13.** The interrelation of the fragments with non-classical fullerene-like topology (a and c, yellow highlighted) in supramolecules **2** and **3**. (b) The fragment  $(cyclo-P_4)(CuX)_4$  to be removed from **2d** structure of fullerene-like topology to afford construction of supramolecule **3**. (d) The fragment  $Cu_3I_3$  that in combination with fragment (c) gives the nanocapsule **3**.

## 5.5.2.9 Crystal structures and isomerism in compound 4

Compound **4** crystallizes as yellow blocks from toluene/MeCN mixtures as two crystalline phases. In **4a** the asymmetric unit contains one supramolecule in general position next to five and four positions of toluene and acetonitrile solvent molecules, respectively. In **4b** the asymmetric unit also contains one supramolecule in general position and another portion of the same solvent molecules. In both cases the inorganic scaffold of **4** contains no vacant positions (Fig. S12). Essential that in **4a** and **4b** the inorganic scaffold is isomeric. The isomerism between these scaffolds is traced back to only two different positions occupied either by iodide or MeCN molecule (Fig. S14).

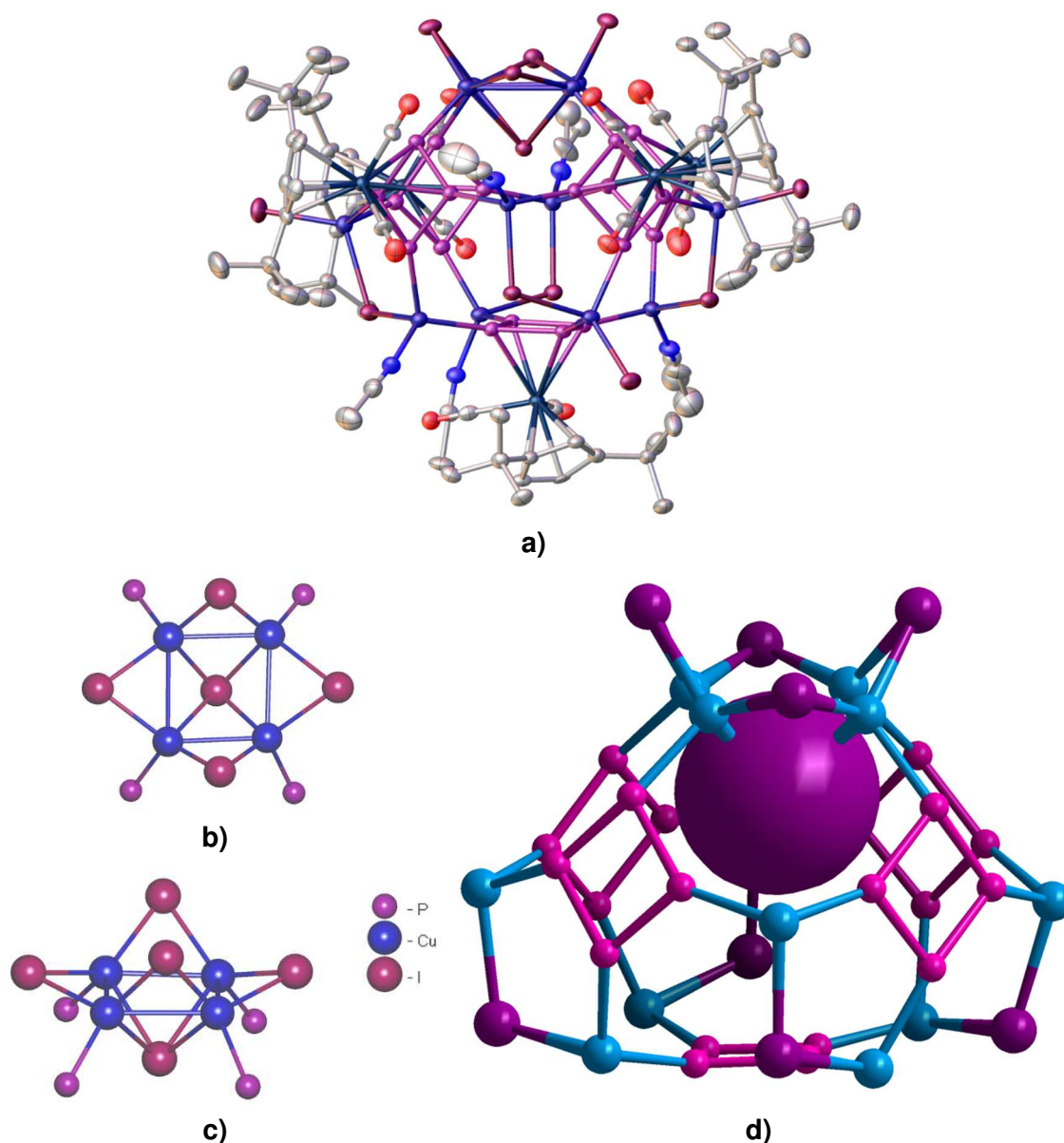


**Figure S14.** (a) The supramolecule **4a** (a.d.p. ellipsoids at 50% probability). Hydrogen atoms are not shown for clarity. (b, c) {Cu<sub>4</sub>I<sub>5</sub>}<sup>-</sup> capping fragment in the scaffold (d). The μ<sub>4</sub>-I ion belonging to the {Cu<sub>4</sub>I<sub>5</sub>}<sup>-</sup> unit and occupying the cavity is shown in van der Waals spheres.

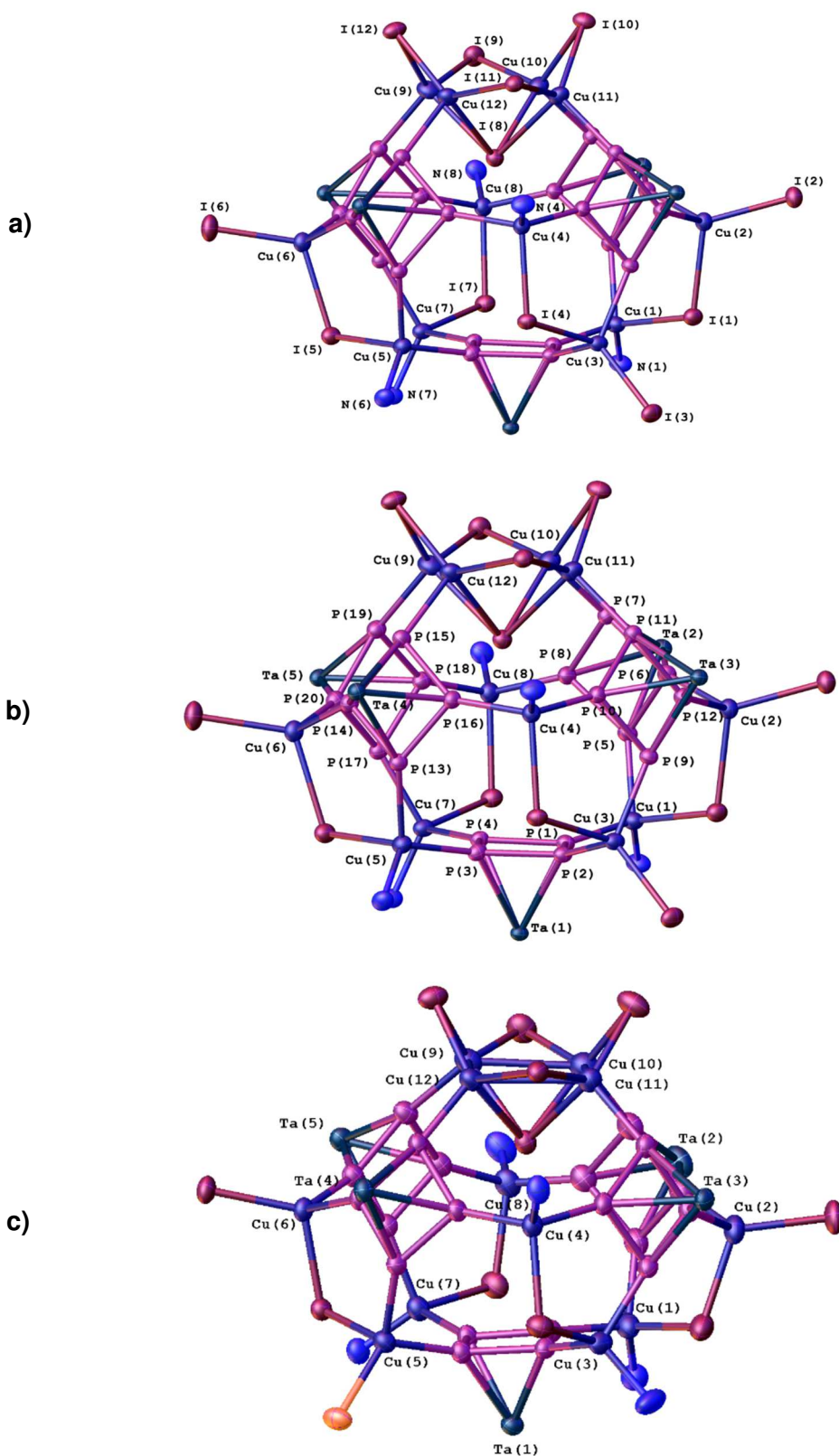


**Figure S15.** (a,b) The enumeration scheme in the inorganic scaffold of the supramolecule **4a**. Carbon and hydrogen atoms are not shown. Structurally isomeric supramolecules **4a** (b) and **4b** (c). Atom I(3) coordinated to Cu(5) in **4b** (not to Cu(3) as in **4a**) is highlighted in orange.

**Table S8.** Bond lengths in the inorganic scaffold (Å, °) for **4a** and **4b**. The enumeration scheme is the same except for the isomeric part (orange highlight).

	<b>4a</b>	<b>4b</b>		<b>4a</b>	<b>4b</b>
Ta1—P1	2.6414 (19)	2.661 (3)	Cu6—I5	2.6651 (13)	2.6330 (17)
Ta1—P2	2.6289 (19)	2.639 (3)	Cu6—I6	2.5593 (13)	2.5433 (17)
Ta1—P3	2.6480 (19)	2.633 (3)	Cu7—I7	2.6443 (13)	2.6379 (19)
Ta1—P4	2.6677 (19)	2.640 (3)	Cu8—I7	2.6290 (13)	2.641 (2)
Ta2—P5	2.668 (2)	2.653(4)	Cu9—I8	2.8066 (15)	2.758 (2)
Ta2—P6	2.612 (2)	2.623(3)	Cu9—I9	2.6089 (15)	2.597 (2)
Ta2—P7	2.620 (2)	2.609(3)	Cu9—I12	2.5643 (14)	2.553 (2)
Ta2—P8	2.644 (2)	2.632(4)	Cu10—I8	2.7253 (14)	2.781 (2)
Ta3—P9	2.654 (2)	2.656 (3)	Cu10—I9	2.5917 (14)	2.602 (2)
Ta3—P10	2.637 (2)	2.635 (3)	Cu10—I10	2.5676 (13)	2.577 (2)
Ta3—P11	2.641 (2)	2.632 (3)	Cu11—I8	2.7780 (14)	2.754 (2)
Ta3—P12	2.616 (2)	2.619 (3)	Cu11—I10	2.5722 (13)	2.556 (2)
Ta4—P13	2.643 (2)	2.663 (3)	Cu11—I11	2.6047 (13)	2.6083 (19)
Ta4—P14	2.627 (2)	2.607 (3)	Cu12—I8	2.7551 (14)	2.7754 (19)
Ta4—P15	2.632 (2)	2.638 (3)	Cu12—I11	2.6065 (14)	2.6151 (19)
Ta4—P16	2.644 (2)	2.648 (3)	Cu12—I12	2.5664 (14)	2.5689 (19)
Ta5—P17	2.629 (2)	2.657 (3)	P1—P4	2.159 (3)	2.156 (4)
Ta5—P18	2.637 (2)	2.628 (3)	P1—P2	2.161 (3)	2.161 (4)
Ta5—P19	2.647 (2)	2.626 (3)	P2—P3	2.151 (3)	2.152 (4)
Ta5—P20	2.629 (2)	2.618 (3)	P3—P4	2.162 (3)	2.147 (4)
Cu1—P1	2.284 (2)	2.284 (3)	P5—P6	2.129 (3)	2.128 (4)
Cu1—P5	2.296 (2)	2.286 (4)	P5—P8	2.142 (3)	2.145 (5)
Cu2—P12	2.268 (2)	2.287 (3)	P6—P7	2.160 (3)	2.160 (5)
Cu2—P6	2.302 (2)	2.283 (4)	P7—P8	2.148 (3)	2.158 (5)
Cu3—P2	2.299 (2)	2.284 (3)	P9—P10	2.148 (3)	2.140 (4)
Cu3—P9	2.303 (2)	2.300 (3)	P9—P12	2.149 (3)	2.132 (4)
Cu4—P10	2.239 (2)	2.274 (3)	P10—P11	2.158 (3)	2.153 (4)
Cu4—P16	2.257 (2)	2.254 (3)	P11—P12	2.159 (3)	2.161 (4)
Cu5—P3	2.266 (2)	2.310 (3)	P13—P14	2.138 (3)	2.141 (4)
Cu5—P13	2.285 (2)	2.339 (3)	P13—P16	2.142 (3)	2.166 (4)
Cu6—P14	2.298 (2)	2.281 (3)	P14—P15	2.162 (3)	2.148 (4)
Cu6—P20	2.292 (2)	2.289 (3)	P15—P16	2.160 (3)	2.155 (4)
Cu7—P4	2.297 (2)	2.302 (3)	P17—P20	2.145 (3)	2.135 (4)
Cu7—P17	2.261 (2)	2.310 (3)	P17—P18	2.146 (3)	2.146 (4)
Cu8—P8	2.253 (2)	2.239 (4)	P18—P19	2.168 (3)	2.151 (4)
Cu8—P18	2.262 (2)	2.259 (4)	P19—P20	2.157 (3)	2.159 (4)
Cu9—P19	2.306 (2)	2.299 (3)	C11C—O11	1.144 (10)	1.144 (15)
Cu10—P7	2.293 (2)	2.304 (4)	C12C—O12	1.151 (11)	1.128 (15)
Cu11—P11	2.301 (2)	2.313 (3)	C21C—O21	1.132 (12)	1.13 (2)

Cu12—P15	2.309 (2)	2.288 (3)	C22C—O22	1.169 (12)	1.132 (16)
Cu1—I1	2.6033 (13)	2.629 (2)	C31C—O31	1.152 (11)	1.132 (15)
Cu2—I1	2.6395 (13)	2.649 (2)	C32C—O32	1.131 (10)	1.115 (13)
Cu2—I2	2.5434 (13)	2.573 (6)	C41C—O41	1.165 (11)	1.116 (16)
Cu3—I3*	2.5390 (13)	2.5553 (18) (for Cu3—I5)	C42C—O42	1.146 (11)	1.114 (14)
Cu3—I4	2.6873 (13)	2.635 (2)	C51C—O51	1.130 (11)	1.108 (14)
Cu4—I4	2.6144 (12)	2.5964 (18)	C52C—O52	1.117 (11)	1.127 (15)
Cu5—I5	2.6209 (13)	2.6612 (18)			

\* The difference between structural isomers in **4a** and **4b**.

### 5.5.2.10 Crystal structure of **5**

Compound **5** crystallizes as yellow plates from toluene/CH<sub>3</sub>CN/Et<sub>2</sub>O mixtures. The asymmetric unit contains one unit of **1b** bound to a Cu<sub>4</sub>I<sub>4</sub> unit and an acetonitrile solvent molecule.

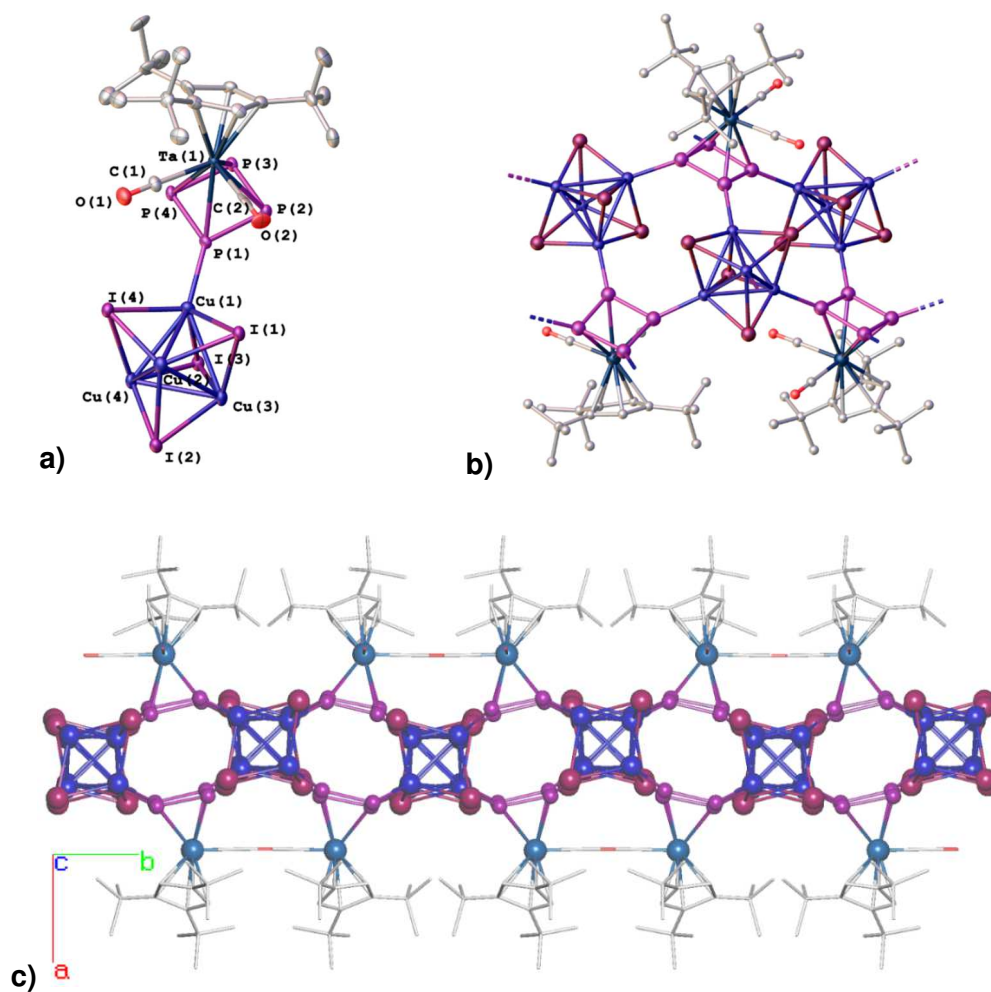


**Figure S16.** The enumeration scheme (up left) and the structure of a layer (up right) in **5**. The side view of the layer (bottom).



**Table S9.** Selected geometric parameters (Å, °) for **5**.

Ta1—P2	2.639 (2)	Cu4—P4 <sup>iii</sup>	2.260 (3)
Ta1—P3	2.641 (2)	P4—Cu4 <sup>iii</sup>	2.260 (3)
Ta1—P4	2.644 (2)	Cu2—I1	2.6273 (14)
Ta1—P1	2.665 (2)	Cu2—I4	2.6439 (17)
Cu1—P1	2.254 (3)	Cu2—I2	2.7130 (14)
Cu1—I1	2.6373 (17)	Cu3—I3	2.6289 (17)
Cu1—I4	2.6407 (15)	Cu3—I2	2.6340 (14)
Cu1—I3	2.7169 (15)	Cu3—I1	2.7106 (14)
Cu1—Cu2	2.837 (2)	Cu4—I2	2.6279 (16)
Cu1—Cu4	2.8666 (18)	Cu4—I3	2.6425 (15)
Cu1—Cu3	2.926 (2)	Cu4—I4	2.6963 (15)
Cu2—Cu4	2.814 (2)	P1—P4	2.153 (4)
Cu2—Cu3	2.858 (2)	P1—P2	2.157 (3)
Cu3—Cu4	2.927 (2)	P2—P3	2.146 (4)
P2—Cu2 <sup>iv</sup>	2.261 (3)	P3—P4	2.145 (3)
P3—Cu3 <sup>v</sup>	2.277 (3)	O1—C1	1.129 (11)
Cu2—P2 <sup>i</sup>	2.261 (3)	O2—C2	1.129 (14)
Cu3—P3 <sup>ii</sup>	2.278 (3)		
I1—Cu1—I4	108.38 (6)	Cu2—I1—Cu3	64.73 (4)
I1—Cu1—I3	109.42 (5)	Cu1—I1—Cu3	66.31 (5)
I4—Cu1—I3	110.96 (5)	Cu4—I2—Cu3	67.58 (5)
I1—Cu2—I2	111.50 (5)	Cu4—I2—Cu2	63.56 (5)
I1—Cu2—I4	108.59 (5)	Cu3—I2—Cu2	64.61 (4)
I4—Cu2—I2	111.61 (5)	Cu3—I3—Cu4	67.45 (5)
I3—Cu3—I2	106.03 (5)	Cu3—I3—Cu1	66.34 (5)
I2—Cu4—I3	105.81 (5)	Cu4—I3—Cu1	64.65 (4)
I3—Cu4—I4	111.55 (5)	Cu1—I4—Cu2	64.94 (5)
P4—P1—P2	90.93 (12)	Cu1—I4—Cu4	64.97 (4)
P3—P2—P1	88.70 (12)	Cu2—I4—Cu4	63.58 (5)
P4—P3—P2	91.47 (13)		
P3—P4—P1	88.82 (12)		

Symmetry code(s): (i)  $x, -y+1/2, z+1/2$ ; (ii)  $-x+1, y+1/2, -z+1/2$ ; (iii)  $-x+1, -y, -z+1$ ; (iv)  $x, -y+1/2, z-1/2$ ; (v)  $-x+1, y-1/2, -z+1/2$ .

### 5.5.3 Size Estimation from DOSY Experiments

#### 5.5.3.1 Spectroscopic Details

The DOSY spectra were recorded on an Avance III HD 600 (600.25 MHz) spectrometer equipped with a z gradient (53.5 Gauss/cm), 5 mm TCI cryo probe and BVT 3000 unit at 298 K. The NMR data was processed with the Bruker program TopSpin® 3.2 and the diffusion coefficient was calculated with the Bruker software T1/T2 relaxation package.

For the calibration of the  $^1\text{H}$  chemical shifts and for the temperature- and viscosity-correction of the diffusion coefficients, TMS (tetramethylsilane) was added. The  $^1\text{H}$ -diffusion measurement was performed with the convection suppressing DSTE (double stimulated echo) pulse sequence, developed by Mueller and Jerschow<sup>[22a]</sup> in a pseudo 2D mode. 120 dummy scans and 16 scans were used with a relaxation delay of 2 s. Sinusoidal shapes were used for the gradient and a linear gradient ramp with 20 or 5 increments between 5 and 95 % of the maximum gradient strength was applied for the diffusion relevant gradients. For the homospoil gradients, -13.7, 20 and 17.13 G  $\text{cm}^{-1}$  were applied. The length of the gradient pulse  $\delta$  was adjusted for every species in the sample to achieve appropriate signal attenuation curves, giving values for  $\delta$  of 2.0 ms for TMS and 3.4 or 3.6 ms for the supramolecules. A diffusion time  $\Delta$  of 45 ms was used.

#### 5.5.3.2 Size Estimation

From crystallographic data the diameter of the two clusters were estimated to be  $d = 25.0 \text{ \AA}$  (**2c**),  $25.4 \text{ \AA}$  (**2d**) from the maximum H-H distance plus twice the Van-der-Waals radius of a proton. From diffusion-ordered spectroscopy (DOSY) experiments<sup>[22b-c]</sup> the translational self-diffusion coefficient  $D$  of molecules in solution can be calculated according to the Stejskal-Tanner equation.<sup>[22]</sup> With the diffusion coefficients  $D$  of the analyte and of TMS (acting as viscosity reference), the hydrodynamic radius  $r_{\text{H}}$  of the analyte can be estimated following the Stokes-Einstein equation<sup>[23]</sup> to be  $r_{\text{H}} = 10.73 \text{ \AA}$  (**2c**),  $9.45 \text{ \AA}$  (**2d**). These are in good agreement with the crystal-derived radii of  $12.5 \text{ \AA}$  (**2c**) and  $12.7 \text{ \AA}$  (**2d**) in the solid state. Therefore, these results indicate the presence of the intact spherical supramolecules in solution. For the reaction of  $\{\text{Cp}^{\text{'''}}\text{Ta}(\text{CO})_2(\mu_5\text{-}\eta^4\text{:}\eta^1\text{:}\eta^1\text{:}\eta^1\text{:}\eta^1\text{-P}_4)\}$  with 2 eq.  $\text{CuI}$  a hydrodynamic radius of the species in solutions of  $r_{\text{H}} = 7.32 \text{ \AA}$  could be derived from the DOSY experiment, which is smaller than those obtained in the case of the  $\text{CuCl}$  and  $\text{CuBr}$  constructed spheres.

### 5.5.4 Additional Figures

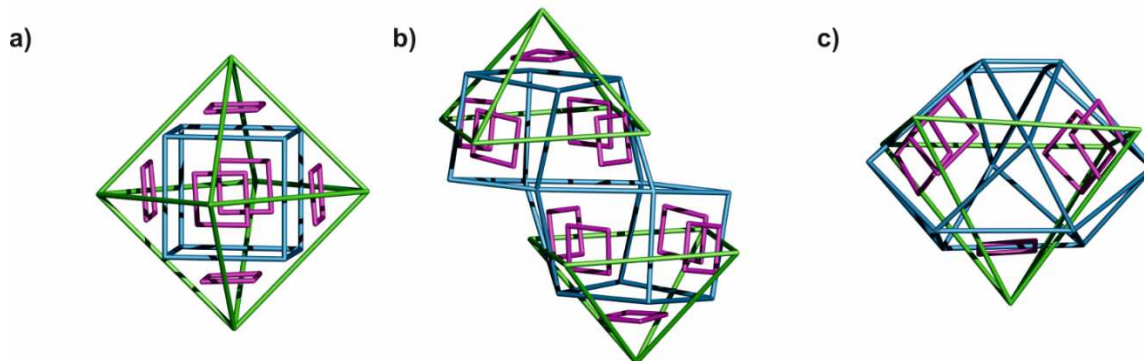


**Figure S17.** Polyhedra built by Ta (green), Cu (blue) and P (pink) in a) **2a-d**; b) **3**; c) **4**.

## 5.6 References

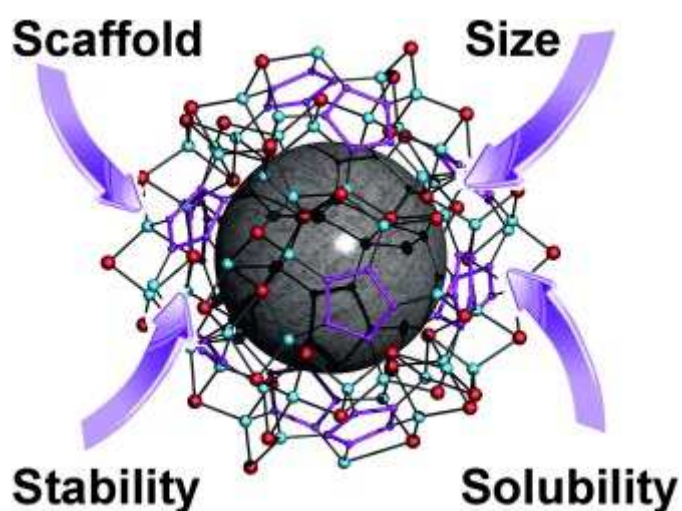
- [1] a) A. Popov, S. Yang, L. Dunsch, *Chem. Rev.* **2013**, *113*, 5989-6113; b) D. Jariwala, V. K. Sangwan, L. J. Lauhon, T. J. Marks, M. C. Hersam, *Chem. Soc. Rev.* **2013**, *42*, 2824-2860; c) C.-Z. Li, H.-L. Yip, A. K. Y. Jen, *J. Mater. Chem.* **2012**, *22*, 4161-4177; d) F. D'Souza, O. Ito, *Chem. Soc. Rev.* **2012**, *41*, 86-96; e) R. W. Sallfrank, A. Scheurer, *Top. Curr. Chem.* **2012**, *134*, 125-170; f) M. S. Dresselhaus, G. Dresselhaus, P. C. Eklund, *Science of Fullerenes and Carbon Nanotubes*, Academic Press, **1996**; g) P. W. Fowler, D. E. Manolopoulos, *An Atlas of Fullerenes*, Clarendon Press, **1995**; h) H. W. Kroto, J. R. Heath, S. C. O'Brien, R. F. Curl, R. E. Smalley, *Nature* **1985**, *318*, 162-163.
- [2] a) A. Schindler, C. Heindl, G. Balazs, C. Groeger, A. V. Virovets, E. V. Peresyphkina, M. Scheer, *Chem. Eur. J.* **2012**, *18*, 829-835; b) M. Scheer, A. Schindler, C. Gröger, A. V. Virovets, E. V. Peresyphkina, *Angew. Chem. Int. Ed.* **2009**, *48*, 5046-5049; c) J. Bai, A. V. Virovets, M. Scheer, *Science* **2003**, *300*, 781-783; d) F. Dielmann, M. Fleischmann, C. Heindl, E. V. Peresyphkina, A. V. Virovets, R. M. Gschwind, M. Scheer, *Chem. Eur. J.* **2015**, *21*, 6208-6214; e) E. V. Peresyphkina, C. Heindl, A. Schindler, M. Bodensteiner, A. V. Virovets, M. Scheer, *Z. Kristallogr. – Cryst. Mater.* **2014**, *229*, 735-740; f) S. Heintl, E. Peresyphkina, J. Sutter, M. Scheer, *Angew. Chem. Int. Ed.* **2015**, *54*, 13431-13435.
- [3] a) R. L. Murry, D. L. Strout, G. K. Odom, G. E. Scuseria, *Nature* **1993**, *366*, 665-667; b) Bharat, R. Bholá, T. Bally, A. Valente, M. K. Cyranski, L. Dobrzycki, S. M. Spain, P. Rempala, M. R. Chin, B. T. King, *Angew. Chem. Int. Ed.* **2010**, *49*, 399-402; c) W. Qian, S.-C. Chuang, R. B. Amador, T. Jarrosson, M. Sander, S. Pieniazek, S. I. Khan, Y. Rubin, *J. Am. Chem. Soc.* **2003**, *125*, 2066-2067.
- [4] O. J. Scherer, R. Winter, G. Wolmershäuser, *Z. Anorg. Allg. Chem.* **1993**, *619*, 827-835.
- [5] B. P. Johnson, F. Dielmann, G. Balazs, M. Sierka, M. Scheer, *Angew. Chem. Int. Ed.* **2006**, *45*, 2473-2475.
- [6] a) Y. D. Gao, W. C. Herndon, *J. Am. Chem. Soc.* **1993**, *115*, 8459-8460; b) H. W. Kroto, *Nature* **1987**, *329*, 529-531.
- [7] C. Heindl, E. V. Peresyphkina, A. V. Virovets, W. Kremer, M. Scheer, *J. Am. Chem. Soc.* **2015**, *137*, 10938-10941.
- [8] The diameters  $d$  of the inner cavities were calculated as the minimum distances between geometrically opposed atoms minus the van der Waals radii of the respective atoms (P: 0.180 nm, Cu: 0.140 nm, I: 0.198 nm). The  $d$  value was

- defined as the diameter of the largest sphere that can be inscribed in the cavity formed by the atoms. The outer diameter was taken as the maximum distance between two atoms the most distant from the center, plus twice the van der Waals radius for the H atom (0.12 nm).
- [9] a) C. Schwarzmaier, A. Schindler, C. Heindl, S. Scheuermayer, E. V. Peresyphkina, A. V. Virovets, M. Neumeier, R. Gschwind, M. Scheer, *Angew. Chem. Int. Ed.* **2013**, *52*, 10896-10899; b) F. Dielmann, A. Schindler, S. Scheuermayer, J. Bai, R. Merkle, M. Zabel, A. V. Virovets, E. V. Peresyphkina, G. Brunklaus, H. Eckert, M. Scheer, *Chem. Eur. J.* **2012**, *18*, 1168-1179.
- [10] J. Bai, A. V. Virovets, M. Scheer, *Angew. Chem., Int. Ed.* **2002**, *41*, 1737-1740.
- [11] R. Peng, M. Li, D. Li, *Coord. Chem. Rev.* **2010**, *254*, 1-18.
- [12] A. Vega, J.-Y. Saillard, *Inorg. Chem.* **2004**, *43*, 4012-4018.
- [13] See the Supporting Information.
- [14] O. J. Scherer, R. Winter, G. Wolmershäuser, *Z. Anorg. Allg. Chem.* **1993**, *619*, 827-835.
- [15] O. J. Scherer, T. Brück, *Angew. Chem.* **1987**, *99*, 59-59.
- [16] J. Bai, A. V. Virovets, M. Scheer, *Angew. Chem., Int. Ed.* **2002**, *41*, 1737-1740.
- [17] L. Palatinus, G. Chapuis, *J. Appl. Cryst.* **2007**, *40*, 786-790.
- [18] G. Scheldrick, *Acta Cryst. ser. A.*, **2008**, *64*, 112-122.
- [19] A. Altomare, M. C. Burla, M. Camalli, G. L. Casciarano, C. Giacovazzo, A. Guagliardi, A. G. G. Moliterni, G. Polidori, R. Spagna, *J. Appl. Cryst.* **1999**, *32*, 115-119.
- [20] O. V. Dolomanov, L. J. Bourhis, R. J. Gildea, J. A. K. Howard, H. Puschmann, *J. Appl. Cryst.* **2009**, *42*, 339-341.
- [21] V. A. Blatov, A. P. Shevchenko, D. M. Proserpio, *Cryst. Growth Des.* **2014**, *14*, 3576-3586.
- [22] a) A. Jerschow, N. Müller, *J. Magn. Reson.* **1997**, *125*, 372-375. b) C. S. Johnson, *Prog. Nucl. Magn. Reson. Spectrosc.* **1999**, *34*, 203-256; c) W. S. Price, *Concepts Magn. Reson.* **1998**, *10*, 197-237; d) E. O. Stejskal, J. E. Tanner, *The Journal of Chemical Physics* **1965**, *42*, 288-292.
- [23] A. Macchioni, G. Ciancaleoni, C. Zuccaccia, D. Zuccaccia, *Chem. Soc. Rev.* **2008**, *37*, 479-489.



## 6 A Nano-sized Supramolecule Beyond the Fullerene Topology

Full Paper



The diffusion-ordered NMR spectroscopic investigations were performed by Florian Hastreiter. The synthesis and characterization of the compounds as well as the sample preparation were performed by Fabian Dielmann, and Claudia Heindl. The analysis via X-ray crystallography was carried out by Eugenia V. Peresyphina and Alexander V. Virovets.

---

Fabian Dielmann, Claudia Heindl, Florian Hastreiter, Eugenia V. Peresyphina, Alexander V. Virovets, Ruth M. Gschwind, and Manfred Scheer  
*Angew. Chem. Int. Ed.* **2014**, 53,49, 13605-13608.

DOI: 10.1002/anie.201407120

© 2014 Wiley-VCH Verlag GmbH & Co. KGaA. Reproduced with permission.

## 6.1 Abstract

The reaction of  $[\text{Cp}^{\text{Bn}}\text{Fe}(\eta^5\text{-P}_5)]$  (**1**) ( $\text{Cp}^{\text{Bn}} = \eta^5\text{-C}_5(\text{CH}_2\text{Ph})_5$ ) with  $\text{CuI}$  selectively yields a novel spherical supramolecule  $(\text{CH}_2\text{Cl}_2)_{3.4}@[ (\text{Cp}^{\text{Bn}}\text{FeP}_5)_{12}\{\text{CuI}\}_{54}(\text{MeCN})_{1.46}]$  (**2**) showing a linkage of the scaffold atoms which is beyond the Fullerene topology. Its extended  $\text{CuI}$  framework reveals an outer diameter of 3.7 nm - a size that has not been reached before using five-fold symmetric building blocks. Furthermore, **2** shows a remarkable solubility in  $\text{CH}_2\text{Cl}_2$ , and NMR spectroscopy reveals that the scaffold of the supramolecule remains intact in solution. In addition, a novel 2D polymer  $\{[\text{Cp}^{\text{Bn}}\text{Fe}(\eta^5\text{-P}_5)]_2\{\text{Cu}_6(\mu\text{-I})_2(\mu_3\text{-I})_4\}\}_n$  (**3**) with an uncommon structural motif was isolated. Its formation can be avoided by using a large excess of  $\text{CuI}$  in the reaction with **1**.

## 6.2 Introduction

The chemistry of supramolecular aggregates is one of the most interesting and fascinating fields in current research.<sup>[1]</sup> Based on self-assembly, the formation of discrete nano-sized supramolecules is enabled.<sup>[2]</sup> In contrast to weak interactions, which mostly are non-directional, the formation of ligand-metal dative bonds allows the rational design of novel structural motifs.<sup>[3]</sup> Special attention has been paid to the design of spherical containers with defined inner cavities.<sup>[4]</sup> Recently, we have shown that the pentaphosphaferrocene  $[\text{Cp}^*\text{Fe}(\eta^5\text{-P}_5)]$  (**1a**) ( $\text{Cp}^* = \eta^5\text{-C}_5\text{Me}_5$ ) acts with  $\text{CuX}$  ( $\text{X} = \text{Cl}, \text{Br}$ ) as a building block for the formation of spherical supramolecules with  $I_h\text{-C}_{80}$  fullerene-like topology consisting of 12 five-membered rings and 30 six-membered units (Figure 1, left).<sup>[5a,b]</sup> However, their synthesis is accompanied by polymeric products and special synthetic conditions have to be applied to avoid these products.<sup>[5c-f]</sup> In addition, most of the products are barely soluble in common solvents. Also a series of 90-vertex balls has been isolated which have a slightly better solubility (Figure 1, right).<sup>[5c-f]</sup> It is of note that almost all attempts to obtain spherical supramolecules from  $\text{CuI}$  and pentaphosphaferrocene failed to date.<sup>[6]</sup>



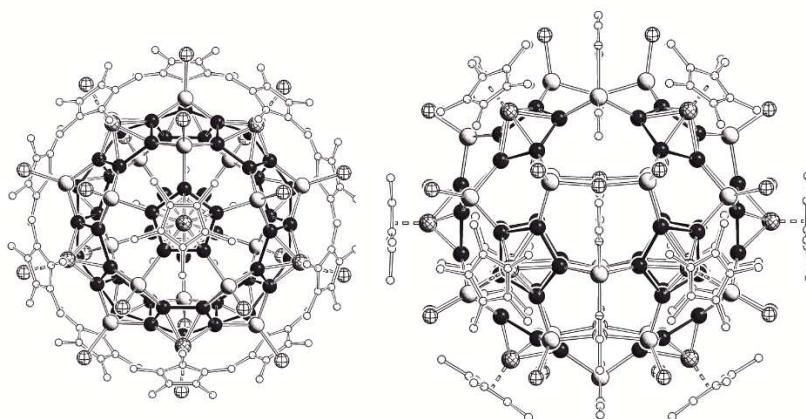
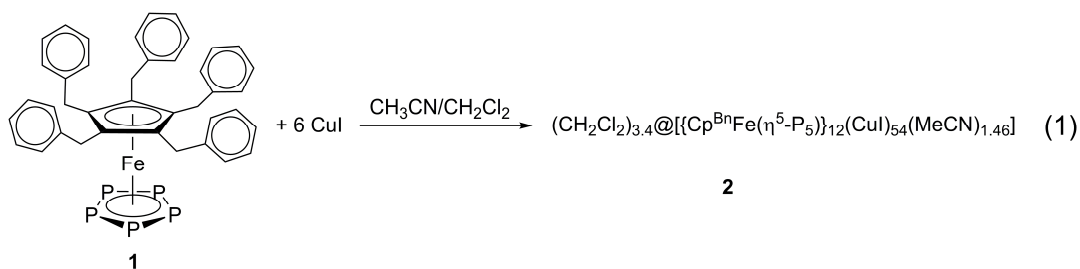


**Figure 1.** Examples of spherical supramolecules with fullerene-like topology self-assembled by **1a** and CuX (X = Cl, Br; incorporated templates are not shown). Left: 80-vertex ball, right: 90-vertex ball.

Herein we report the synthesis and characterization of a nano-sized spherical supramolecule, obtained by the self-assembly of  $[\text{Cp}^{\text{Bn}}\text{Fe}(\eta^5\text{-P}_5)]$  (**1**) ( $\text{Cp}^{\text{Bn}} = \eta^5\text{-C}_5(\text{CH}_2\text{Ph})_5$ ) and CuI, which shows a structure beyond the fullerene topology. Going from methyl to benzyl substituents at the  $\text{Cp}^{\text{R}}$  ligand, the steric influence of the ligand to the metal center remains similar,<sup>[7]</sup> but the formation of an even larger spherical molecule is achieved for the first time. This compound does not show a fullerene topology despite having 12 five-membered rings derived from pentaphosphaferrocenes because there are no six-membered rings in the spherical scaffold.<sup>[8]</sup> In addition, the flexible organic groups of the  $\text{Cp}^{\text{Bn}}$  ligand provide a good solubility of the resulting compound.

### 6.3 Results and Discussion

Layering a solution of CuI in a mixture of  $\text{CH}_2\text{Cl}_2$  and MeCN over a solution of **1** in  $\text{CH}_2\text{Cl}_2$  leads to the formation of  $(\text{CH}_2\text{Cl}_2)_{3.4}@[\{\text{Cp}^{\text{Bn}}\text{Fe}(\eta^5\text{-P}_5)\}_{12}(\text{CuI})_{54}(\text{MeCN})_{1.46}]$  (**2**) isolated in good yields (69%) [Equation (1)].



Unusually for this class of compounds **2** is soluble in  $\text{CH}_2\text{Cl}_2$ . Thus, NMR spectroscopic and mass spectrometric investigations have been carried out. The  $^1\text{H}$  NMR

spectrum shows broad signals for both the phenyl H atoms ( $\delta = 7.0 - 6.0$  ppm) and the methylene protons ( $\delta = 5.0 - 3.2$  ppm) with an intensity ratio of 5:2. Weak signals in the range from  $\delta = 1.36$  to 1.24 ppm can be assigned to coordinated acetonitrile ligands. The  $^{31}\text{P}\{^1\text{H}\}$  NMR of **2** displays a broad signal at  $\delta = 77.3$  ppm ( $\omega_{1/2} = 630$  Hz), which is in a comparable region to those found for 90-vertex supramolecules containing **1a**<sup>[5c]</sup> and is indicative for a 1,2,3,4,5-Coordination mode of the *cyclo*-P<sub>5</sub> ligand to the Cu atoms. There is no signal found at 162 ppm for uncoordinated **1**. Thus, the scaffold of the giant molecule **2** remains intact in solution, what was demonstrated by diffusion ordered spectroscopy (DOSY) experiments. The DOSY-NMR experiment reveals a hydrodynamic radius of 2.07 nm, which is in very good agreement with the crystal-derived radius of 1.85 nm in the solid state.

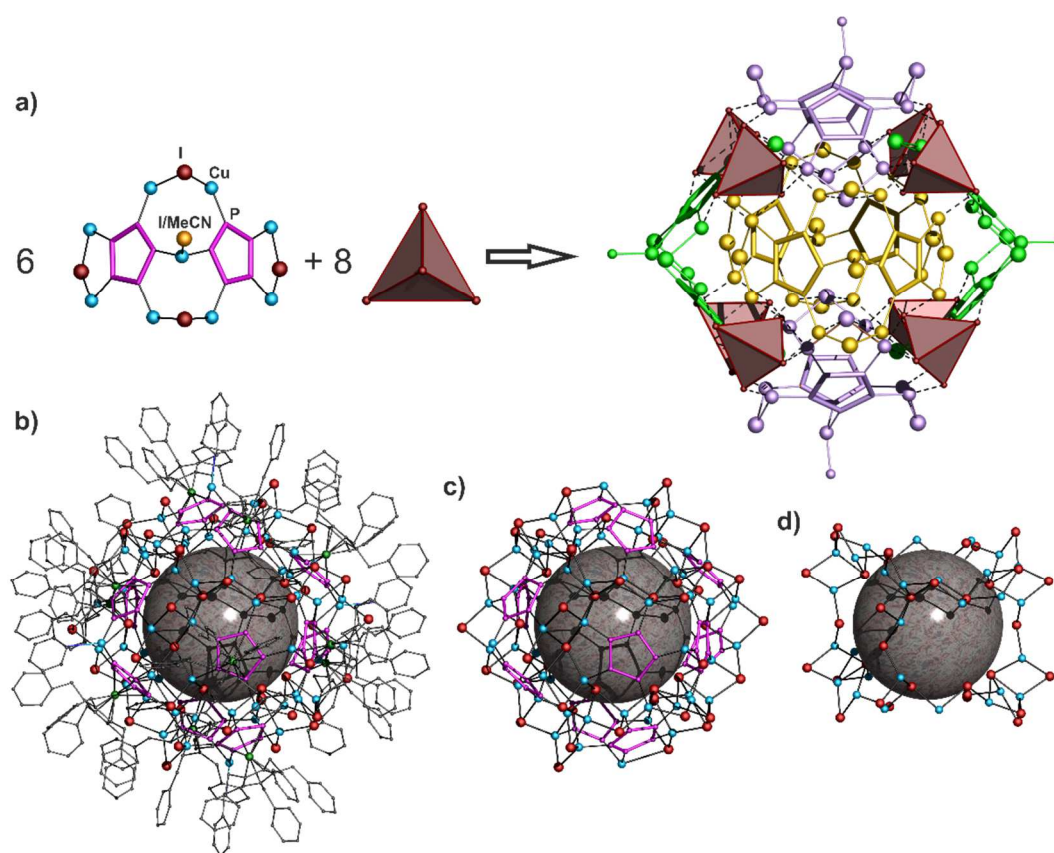


**Figure 2.** a) A combination of six  $(\text{Cp}^{\text{Bn}}\text{FeP}_5)_2(\text{CuX})(\text{Cu}_2\text{I})_4$  ( $X = \text{I}, \text{MeCN}$ ) building blocks and eight  $\text{CuI}$  tetrahedra gives the idealized scaffold  $(\text{Cp}^{\text{Bn}}\text{FeP}_5)_{12}\text{Cu}_{62}\text{I}_{58}(\text{MeCN})_4$ . b) One of the supramolecules in **2**. Hydrogen atoms are omitted for clarity. c) The idealized scaffold of **2**. d) The irreducible scaffold of **2**.

The ESI mass spectrum displays the cations  $\{[\text{Cp}^{\text{Bn}}\text{Fe}(\eta^5\text{-P}_5)]_2\text{Cu}_3\text{I}_2\}^+$  and  $[\text{Cu}_9\text{I}_8]^+$  as the largest phosphorus-containing and phosphorus-free fragments, respectively, and  $\{[\text{Cp}^{\text{Bn}}\text{Fe}(\eta^5\text{-P}_5)]_2\text{Cu}\}^+$  as the base peak. In addition, several anionic fragments, indicative for the existence of large  $\text{CuI}$  frameworks, were detected:  $[\text{Cu}_{14}\text{I}_{15}]^-$  is the largest one and under subsequent elimination of  $\text{CuI}$  units all of the subsequent fragments down to  $[\text{CuI}_2]^-$ .

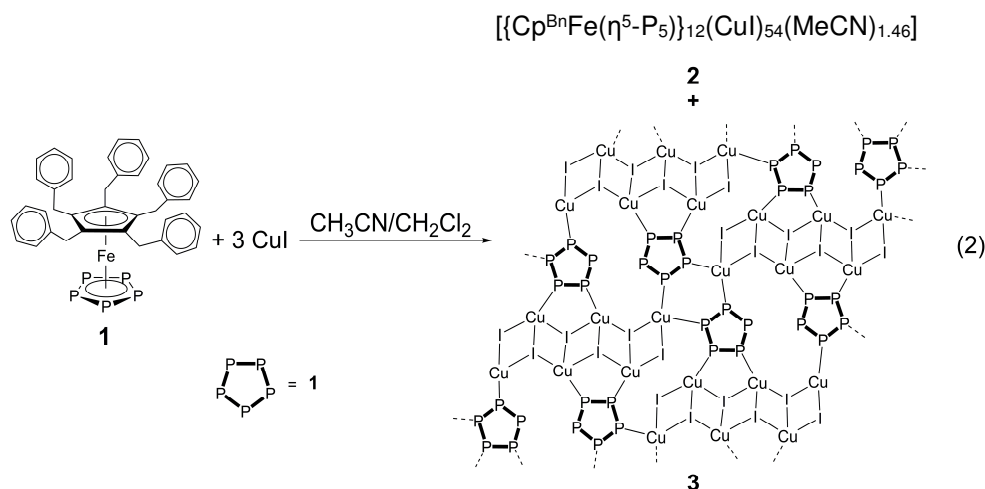
Even in the MALDI mass spectrum only fragments of **2** with the cation  $\{[\text{Cp}^{\text{Bn}}\text{Fe}(\eta^5\text{-P}_5)]_2\text{Cu}_2\}^+$  as the largest mass peak and again  $\{[\text{Cp}^{\text{Bn}}\text{Fe}(\eta^5\text{-P}_5)]_2\text{Cu}\}^+$  as the base peak are detected.

Compound **2** crystallizes as deep red-brown blocks in the triclinic space group  $P\bar{1}$ . The supramolecule occupies the center of symmetry.<sup>[9]</sup> Its idealized scaffold can be represented as a combination of eight  $\{\text{CuI}_4\}$  tetrahedral units and six similar building blocks,  $(\text{Cp}^{\text{Bn}}\text{FeP}_5)_2(\text{CuL})(\text{Cu}_2\text{I})_4$ , where  $\text{L} = \text{I}$  in two and  $\text{L} = \text{MeCN}$  in four ones (Figure 2a). The core of the  $\text{L} = \text{MeCN}$  building block comprises two molecules of **1** joint by one  $\{\text{CuL}\}$  and two  $\{\text{Cu}_2\text{I}\}$  bridging units. The  $\{\text{CuL}\}$  unit is the only similarity to earlier reported 80-vertex supramolecules based on **1a**,<sup>[5]</sup> where each  $\text{CuX}$  ( $\text{X} = \text{Cl}, \text{Br}$ ) unit coordinates three molecules of **1a**. In addition, each *cyclo*- $\text{P}_5$  ligand of **1** is coordinated by two chelate  $\{\text{Cu}_2\text{I}\}$  units. Therefore, each phosphorus atom is available for coordination to copper ions allowing an 1,2,3,4,5-coordination mode as in other pentaphosphaferrocene-based supramolecules.<sup>[5]</sup> Each of the  $(\text{Cp}^{\text{Bn}}\text{FeP}_5)_2(\text{CuL})(\text{Cu}_2\text{I})_4$  building blocks is connected to four  $\{\text{CuI}_4\}$  tetrahedra and four other similar building blocks, which are rotated by  $90^\circ$  in two perpendicular directions (Figure 2a). The building blocks are thus aggregated in an extended  $\{\text{CuI}\}_{56}$  ladder-like framework by formation of  $\text{Cu-I}$  bonds (see Supporting Information), constructed of eight  $\{\text{CuI}_4\}$  tetrahedra and 12  $\{\text{Cu}_4\text{I}_2\}$  units, that can be found in some  $\text{CuX}$  frameworks.<sup>[10]</sup> The eight  $\{\text{CuI}_4\}$  tetrahedra are arranged according to the corners of a giant “cube” with six  $(\text{Cp}^{\text{Bn}}\text{FeP}_5)_2(\text{CuL})(\text{Cu}_2\text{I})_4$  building blocks as the folded convex faces. The  $\text{CuI}$ -rich idealized scaffold constructed in this way has the formula  $[(\text{Cp}^{\text{Bn}}\text{FeP}_5)_{12}\text{Cu}_{62}\text{I}_{58}(\text{MeCN})_4]$  and must be positively charged owing to the excess of copper ions (Figure 2c). However, according to the diffraction data for the single crystals of **2**, an average composition of  $(\text{CH}_2\text{Cl}_2)_{3.4} @ [(\text{Cp}^{\text{Bn}}\text{FeP}_5)_{12}(\text{CuI})_{54}(\text{MeCN})_{1.46}] \cdot 2.54 \text{ MeCN} \cdot 0.8 \text{ C}_7\text{H}_8$  is obtained. It is charge-balanced because some copper, iodine and coordinated acetonitrile positions are statistically vacant. The vacant positions are distributed such that each copper atom retains its tetrahedral environment and each iodide is two-, three- or four-fold coordinated. The idealized ladder-like framework  $\{\text{CuI}\}_{56}$  is thus reduced to its ordered part comprising of 34 copper and 40 iodine ions (Figure 2d) with  $\text{Cu-I}$  bonds being in the range of 2.577(4)-2.800(3) Å. 20 copper and 14 iodide ions statistically decorate the ordered part (see Supporting Information). The vacancies in some positions of copper-ion positions can vary the coordination mode of the *cyclo*- $\text{P}_5$  rings from 1,2 and 1,2,3 found in the ordered  $\{\text{Cu}_{34}\text{I}_{40}\}$  part to the 1,2,3,4,5 mode that is achieved in the idealized structure. The  $\text{Cu-P}$  bonds vary in the range of 2.109(17) to 2.335(18) Å. The bonds  $\text{Fe-P}$  (2.345(8)-2.404(7) Å) and  $\text{P-P}$  (2.071(10)-2.123(11) Å) are comparable to 2.37 and 2.11 Å, respectively, in the non-coordinated pentaphosphaferrocene.<sup>[7]</sup>

Therefore, the crystal of **2** represents a solid solution of different similar supramolecules with the identical structural core comprising of an ordered  $\{\text{Cu}_{34}\text{I}_{40}\}$  framework that predetermines the mutual spatial arrangement of 12 molecules of **1** as well as the shape of the supramolecules with an external size of 3.70 nm (Figure 2b). They are the largest of the supramolecules built up by  $\text{P}_n$  ligand complexes, being by 1.2 nm, 0.3 nm, and 0.64 nm, respectively, larger than  $[\text{Cp}^*\text{Fe}(\eta^5\text{-P}_5)]$ -containing spherical clusters.<sup>[5c,d,6]</sup> For a more vivid comparison, the supramolecules in **2** are approximately 3.5 times larger in volume than the Buckminster fullerene  $\text{C}_{60}$ . Even without the organic ligands, it is larger than the largest anionic copper(I) halide aggregate  $[\text{Cu}_{36}\text{I}_{56}]^{20-}$  reported so date.<sup>[11]</sup>

The supramolecules **2** have internal cavities of 0.75 nm, which is only 0.05 nm less in comparison to the 80-vertex supramolecule with **1a** as building block.<sup>[5b]</sup> The cavities incorporate an average of 3.4 molecules of  $\text{CH}_2\text{Cl}_2$  disordered over six possible positions (see Supporting Information). The surface of the inner cavities is formed by six idealized  $(\text{Cp}^{\text{Bn}}\text{FeP}_5)_2(\text{CuL})(\text{Cu}_2\text{I})_4$  building blocks that have folded convex geometry. Every guest molecule can occupy one of these six positions in the cavity oriented so that the Cl atoms point towards every idealized  $(\text{Cp}^{\text{Bn}}\text{FeP}_5)_2(\text{CuL})(\text{Cu}_2\text{I})_4$  building block according to the ‘concave to convex’ principle (see Supporting Information). The intermolecular distances between the P atoms of the *cyclo*- $\text{P}_5$  rings and the Cl atoms of the guest molecule are about 3.8-3.9 Å, which correspond to weak van der Waals interactions.

The supramolecule **2** contains 4.5  $\text{CuI}$  units per pentaphosphaferrocene. When the reaction is carried out with three or less equivalents of  $\text{CuI}$ , the polymeric by-product  $[(\text{Cp}^{\text{Bn}}\text{Fe}(\eta^5\text{-P}_5))_2\{\text{Cu}_6(\mu\text{-I})_2(\mu_3\text{-I})_4\}]_n$  (**3**) can occasionally be observed [Equation (2)]. In contrast to **1a** as building block, the tendency for the formation of polymeric products is much lower for **1** and can completely be avoided by using a higher amount of  $\text{CuI}$ .



The 2D coordination polymer **3** crystallizes as yellow-orange plates in the triclinic space group  $P\bar{1}$ .<sup>[9]</sup> It can easily be separated from the deep-red blocks of **2** either mechanically under the microscope or by washing the mixture with  $\text{CH}_2\text{Cl}_2$ , since **3** is insoluble in all common solvents. Single crystals of **3** were obtained from  $\text{CH}_2\text{Cl}_2/\text{MeCN}$  mixtures as solvate with one molecule  $\text{CH}_2\text{Cl}_2$  per repeating unit. The structure of **3** is built up by planar layers of building block **1**, which binds to  $\text{Cu}_6\text{I}_6$  units in the rather uncommon 1,2,3,4-coordination mode.<sup>[12]</sup> The framework therefore comprises *cyclo*- $\text{P}_5$  ligands from the pentaphosphaferrocene, four-membered  $\text{Cu}_2\text{I}_2$  rings of the ladder, five-membered  $\text{Cu}_2\text{P}_2\text{I}$  rings and six-membered  $\text{Cu}_2\text{P}_4$  rings (Figure 3). The unit of **1** alternates up and down respective to the layer because of the bulky benzyl substituents. Hence, the layers are faced by the phenyl rings of  $\text{Cp}^{\text{Bn}}$ . A coordination polymer with **1a** as building block and the same elemental formula was obtained earlier.<sup>[12]</sup> However, there the  $\text{Cu}_6\text{I}_6$  units are not arranged in a ladder, but in six-membered rings instead. Hence, this demonstrates again the versatility of CuI in supramolecular and coordination chemistry.

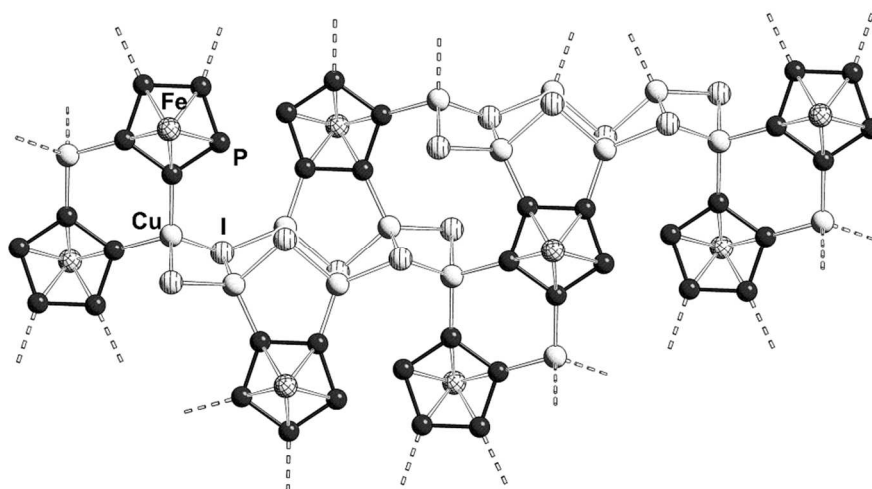


**Figure 3.** Section of the polymeric network of **3**.  $\text{Cp}^{\text{Bn}}$  ligands are omitted for clarity. Selected bond lengths [ $\text{\AA}$ ]: Cu–I 2.5764(14)–2.7920(17), Cu–P 2.262(3)–2.301(3), P–P 2.099(3)–2.117(3) and Fe–P 2.363(3)–2.426(3).

## 6.4 Conclusions

In conclusion, the  $\text{Cp}^{\text{Bn}}$ -substituted pentaphosphaferrocene **1** has proven to be a building block for unique spherical supramolecular aggregates. The replacement of  $\text{Cp}^*$  by  $\text{Cp}^{\text{Bn}}$  can reverse the tendency for the formation of polymeric instead of spherical coordination compounds. In addition, the benzyl ligands provide unique solubility of the products that allowed the use of NMR and MS investigations. While polymeric products are favored in the case of **1a**, the reaction of **1** and six equivalents of CuI selectively leads

to the formation of a gigantic supramolecule **2** featuring an unprecedented scaffold. The inorganic scaffold consists of *cyclo*-P<sub>5</sub> units and an expanded CuI framework with partial occupancies of few copper and iodine positions. It does not follow the fullerene-topology, because the CuI ladder structural motif provides no six-membered units, although twelve *cyclo*-P<sub>5</sub> rings are present. Having 180 heavy atoms in the scaffold and an outer diameter of 3.70 nm, **2** represents the largest discrete polynuclear complex built up either by five-fold symmetric building blocks or copper(I) halide aggregates.

## 6.5 Supporting Information

### 6.5.1 Experimental Part

All reactions were performed under an inert atmosphere of dry nitrogen or argon with standard vacuum, Schlenk, and glove-box techniques. Solvents were purified and degassed by standard procedures. Commercially available chemicals were used without further purification. Complex **1** was prepared as described before.<sup>[13]</sup>

#### 6.5.1.1 Synthesis of $(\text{CH}_2\text{Cl}_2)_{3.4}@[\{\text{Cp}^{\text{Bn}}\text{Fe}(\mu_6\text{-}\eta^5\text{:}\eta^1\text{:}\eta^1\text{:}\eta^1\text{:}\eta^1\text{-P}_5)\}_{12}(\text{CuI})_{54}(\text{CH}_3\text{CN})_{1.46}]$ (**2**)

Complex **1** (40 mg, 0.055 mmol) was dissolved in  $\text{CH}_2\text{Cl}_2$  (6 mL) in a long, thin Schlenk tube. On top of the resulting green solution was layered a solution of CuI (63 mg, 0.330 mmol) in a solvent mixture of  $\text{CH}_2\text{Cl}_2$  (2 mL) and MeCN (3 mL). The reaction mixture immediately turned red at the phase boundary. It was allowed to stand in an undisturbed area at room temperature in the dark for complete diffusion. Within one month dark crystals of **2** were formed. The mother liquor was decanted and the crystals were washed with pentane ( $3 \times 5$  mL) and dried under vacuum at room temperature to yield deep-red crystals of **2** (58 mg).

Crystals suitable for X-Ray diffraction analysis were obtained by the following procedure: A solution of CuI (31 mg, 0.16 mmol) in MeCN (3 mL) was carefully layered over a mixture of **1** (40 mg, 0.055 mmol) in toluene. Within one month red multiple twinned crystals were formed. The crystalline material was isolated and washed with hexane ( $3 \times 3$  mL). Afterwards,  $\text{CH}_2\text{Cl}_2$  (6 mL) was added and the mixture was treated in the ultrasonic bath for 20 minutes. The resulting orange-red solution was filtrated, transferred into a thin Schlenk tube and layered with toluene (6 mL). Within three weeks red crystals of **2** were formed.

Analytical data of  $(\text{CH}_2\text{Cl}_2)_{3.4}@[\{\text{Cp}^{\text{Bn}}\text{Fe}(\mu_6\text{-}\eta^5\text{:}\eta^1\text{:}\eta^1\text{:}\eta^1\text{:}\eta^1\text{-P}_5)\}_{12}(\text{CuI})_{54}(\text{CH}_3\text{CN})_{1.46}]$  (**2**):

**Yield:** 58 mg (3.17  $\mu\text{mol}$ , 69 %)

**$^1\text{H}$  NMR** ( $\text{CD}_2\text{Cl}_2$ , 400.13 MHz, 300 K):  $\delta$  [ppm] = 7.0–6.0 (m {br}, 300 H; Ph), 5.0–3.2 (m {br}, 120 H;  $\text{CH}_2$ ), 1.36–1.24 (m {br}, 3 H;  $\text{CH}_3$ )

**$^{31}\text{P}\{^1\text{H}\}$  NMR** ( $\text{CD}_2\text{Cl}_2$ , 161.98 MHz, 300 K):  $\delta$  [ppm] = 77.3 (s {br},  $\omega_{1/2}$  = 280 Hz)

**Positive ion ESI-MS** ( $\text{CH}_2\text{Cl}_2/\text{CH}_3\text{CN}$ ):  $m/z$  (%) = 1897.3 (18)  $[\{\text{Cp}^{\text{Bn}}\text{FeP}_5\}_2\text{Cu}_3\text{I}_2]^+$ , 1707.4 (39)  $[\{\text{Cp}^{\text{Bn}}\text{FeP}_5\}_2\text{Cu}_2\text{I}]^+$ , 1587.9 (8)  $[\text{Cu}_9\text{I}_8]^+$ , 1515.5 (100)  $[\{\text{Cp}^{\text{Bn}}\text{FeP}_5\}_2\text{Cu}]^+$ , 1395.8 (6)  $[\text{Cu}_8\text{I}_7]^+$ , 1247.2 (13)  $[\text{Cu}_7\text{I}_6(\text{MeCN})]^+$ , 1206.0 (26)  $[\text{Cu}_7\text{I}_6]^+$ , 1170.8 (65)  $[\{\text{Cp}^{\text{Bn}}\text{FeP}_5\}\text{Cu}_3\text{I}_2]^+$ , 978.9 (35)  $[\{\text{Cp}^{\text{Bn}}\text{FeP}_5\}\text{Cu}_2\text{I}]^+$

**Negative ion ESI-MS** ( $\text{CH}_2\text{Cl}_2/\text{CH}_3\text{CN}$ ):  $m/z$  (%) = 2793.6 (0.09)  $[\text{Cu}_{14}\text{I}_{15}]^-$ , 2603.6 (0.1)  $[\text{Cu}_{13}\text{I}_{14}]^-$ , 2413.4 (0.21)  $[\text{Cu}_{12}\text{I}_{13}]^-$ , 2221.6 (0.22)  $[\text{Cu}_{11}\text{I}_{12}]^-$ , 2031.8 (0.53)  $[\text{Cu}_{10}\text{I}_{11}]^-$ , 1841.9 (0.84)  $[\text{Cu}_9\text{I}_{10}]^-$ , 1649.8 (1.0)  $[\text{Cu}_8\text{I}_9]^-$ , 1460.0 (0.8)  $[\text{Cu}_7\text{I}_8]^-$ , 1270.1 (1.0)  $[\text{Cu}_6\text{I}_7]^-$ , 1078.2 (1.2)  $[\text{Cu}_5\text{I}_6]^-$ , 888.3 (2.5)  $[\text{Cu}_4\text{I}_5]^-$ , 698.5 (12)  $[\text{Cu}_3\text{I}_4]^-$ , 506.6 (35)  $[\text{Cu}_2\text{I}_3]^-$ , 316.8 (100)  $[\text{CuI}_2]^-$

**MALDI-TOF** (DCTB matrix):  $m/z$  (%) = 1706 (38)  $[(\text{Cp}^{\text{Bn}}\text{FeP}_5)_2\text{Cu}_2]^+$ , 1515.0 (100)  $[(\text{Cp}^{\text{Bn}}\text{FeP}_5)_2\text{Cu}]^+$

**IR** (KBr):  $\tilde{\nu}$  [ $\text{cm}^{-1}$ ] = 3105 (vw; CH), 3085 (w; CH), 3060 (m; CH), 3027 (m; CH), 3003 (vw; CH), 2918 (w;  $\text{CH}_2$ ), 1948 (w), 1881 (w), 1803 (w), 1624 (m), 1603 (s; CC), 1495 (vs; CC), 1454 (s;  $\delta(\text{CH}_2)$ ), 1445 (s;  $\delta(\text{CH}_2)$ ), 1076 (m), 1030 (m), 732 (vs;  $\delta(\text{Ph})$ ), 696 (vs;  $\delta(\text{Ph})$ ), 520 (w), 489 (m), 462 (w)

**Elemental analysis:** Calculated (%) for  $[(\text{C}_{40}\text{H}_{35}\text{FeP}_5)_{12}(\text{CuI})_{54}(\text{CH}_3\text{CN})_{1.46}(\text{CH}_2\text{Cl}_2)_{3.4}]$  (19347 g/mol): C 30.18, H 2.25, Cu 17.74, Fe 3.46, I 35.42, N 0.10, P 9.61; found: C 31.45, H 2.41, Cu 16.7, Fe 4.00, I 34.65, N 0.1, P 9.99.

### 6.5.1.2 Synthesis of $[\{\text{Cp}^{\text{Bn}}\text{Fe}(\mu_5\text{-}\eta^5\text{:}\eta^1\text{:}\eta^1\text{:}\eta^1\text{-P}_5)\}_2\{\text{Cu}_6(\mu\text{-I})_2(\mu_3\text{-I})_4\}]_n$ (**3**)

A Schlenk tube was charged with a solution of **1** (60 mg, 0.083 mmol) in  $\text{CH}_2\text{Cl}_2$  (10 mL). Onto this a solution of CuI (47 mg, 0.25 mmol) in  $\text{CH}_3\text{CN}$  (10 mL) was layered. The reaction mixture immediately turned red at the phase boundary and was allowed to stand in an undisturbed area at room temperature for complete diffusion. After one month deep red blocks of **2** and yellow plates of **3** were formed. The yellow plates of **3** were separated mechanically from **2**, washed with  $\text{CH}_2\text{Cl}_2$  (2  $\times$  4 mL) and pentane (2  $\times$  4 mL) and dried under vacuum at room temperature (25 mg, 35% based on CuI). Analytical data of **3**: Elemental analysis: Calculated (%) for  $(\text{C}_{40}\text{H}_{35}\text{FeP}_5)_2(\text{CuI})_6 \cdot \text{CH}_2\text{Cl}_2$  (2680 g/mol): C 36.29, H 2.71; found: C 36.10, H 2.67.

Analytical data of  $[\{\text{Cp}^{\text{Bn}}\text{Fe}(\mu_5\text{-}\eta^5\text{:}\eta^1\text{:}\eta^1\text{:}\eta^1\text{-P}_5)\}_2(\text{CuI})_6]_n$  (**3**)

**Yield:** 25 mg (9.33  $\mu\text{mol}$ , 22 %)

**Elemental analysis:** Calculated (%) for  $(\text{C}_{40}\text{H}_{35}\text{FeP}_5)_2(\text{CuI})_6 \cdot \text{CH}_2\text{Cl}_2$  (2680 g/mol): C 36.29, H 2.71; found: C 36.10, H 2.67.



## 6.5.2 X-Ray Structure Analysis

### 6.5.2.1 Data Collection and Refinement

Crystals of **2** and **3** were taken from a Schlenk flask under a stream of argon and immediately covered with mineral oil (**2**) or perfluorinated Fomblin® mineral oil (**3**) to prevent both decomposition and a loss of solvent. The quickly chosen single crystals covered by a drop of the oil were taken to the pre-centered goniometer head with CryoMount® and directly attached to the diffractometer into a stream of cold nitrogen. X-ray diffraction study of **2** faced many challenges, since the crystals have relatively small size and decompose rapidly losing solvent molecules. Several X-ray diffraction experiments of different single crystals of **2** were performed during the attempts to achieve the best diffraction data. The diffraction power of crystals was very low, and the collection of data at high theta angles required high exposure times.

The diffraction data for structures **2** and **3** were collected at 123 K on an Agilent Technologies SuperNova CCD diffractometer equipped with Atlas detector (**2**) and Gemini R-Ultra diffractometer equipped with Ruby detector (**3**) with CuK $\alpha$  radiation ( $\lambda = 1.54178\text{\AA}$ ) using  $\omega$  scans of 1° frames (Table 1S). Absorption corrections were applied analytically from crystal faces using CrysAlisPro software.<sup>[14]</sup> The structures **2** and **3** were solved by direct methods and refined by full-matrix least-squares method against  $|F|^2$  in anisotropic approximation using SHELX97<sup>[15]</sup> for **3** and SHELX2013<sup>[16]</sup> programs set for **2**. All non-hydrogen atoms were refined anisotropically. Hydrogen atoms were refined as riding on pivot atoms.

Despite the crystals of **2** contain many heavy atoms, the diffraction pattern fades quickly at  $d_{hkl} < 1\text{\AA}$ . Therefore, only data with  $d_{hkl} \geq 0.93\text{\AA}$  were used in the structure refinement. The structure refinement faced various problems due to low triclinic symmetry resulted in 96 crystallographically independent positions of heavy atoms, severe disorder of Cp<sup>Bn</sup> ligands accompanied by partial disorder of Cu and Br atoms of inorganic core, and lack of observed high-angle reflections. At the preliminary stages refinement was performed using Konnert-Hendrickson conjugate-gradient algorithm (CGLS instruction in SHELXL97 program), and only final model was refined by full-matrix least-squares method.

The occupancies for partly vacant Cu and I positions were determined after refinement with their isotropic displacement parameters fixed at  $U_{iso}$  of  $0.06\text{\AA}^{-2}$  that is approximately equal to  $U_{iso}$  of fully occupied Cu, I and Fe atoms. The resulting occupancies were then fixed, and conventional refinement procedure with refining displacement

parameters was performed in iso- and then in anisotropic approximation. Some positions of heavy atoms were split as a result of unreasonably elongated a.d.p. ellipsoids and relatively high surrounding residual density. Final occupancy factors for iodine atoms were set using information on chemical composition, crystallochemical and charge balance requirements. The carbon atoms of Cp rings belonging to a Cp(CH<sub>2</sub>Ph)<sub>5</sub> substituents were refined anisotropically using ISOR instructions of SHELX. The positions of severely disordered CH<sub>2</sub>Ph fragments and NCMe ligands were located from  $\Delta\rho$  maps and refined in the rigid body approximation with  $U_{\text{iso}}$  at 0.15 Å<sup>-1</sup> level as a single position to reduce the number of refined parameters. The hydrogen atoms were not set in calculated positions, because of uncertain positions of the pivot carbon atoms. Some of the coordinated MeCN molecules, which are to complete Cu ions environment, were not located from electron density map due to their disorder.

The guest molecules of CH<sub>2</sub>Cl<sub>2</sub> in the inner cavity of supramolecules are disordered over 6 positions, note that only three of them are crystallographically independent. The refinement of occupancies for Cl atoms gave sum occupancy of 3.4 CH<sub>2</sub>Cl<sub>2</sub> molecules per supramolecule. Due to uncertainty of the position of C atom the C-Cl distances were restrained with SADI instructions.

A few solvent molecules were located from residual electron density map; however, the solvent portion of the compound **2** cannot be even approximately estimated from the crystal structure. The crystal structure contains voids in the packing of supermolecules of ~3619 Å<sup>3</sup> per unit cell, in which single electron density peaks are only found that however do not allow localization of any solvent molecule. The estimation based on residual electron density made with SQUEEZE/PLATON allows assigning the non-localized solvent portion as 16 C<sub>7</sub>H<sub>8</sub>, 17 CH<sub>2</sub>Cl<sub>2</sub> or 37 MeCN per unit cell.

The structural formula for the crystal structure **3** derived from the structural data is therefore (CH<sub>2</sub>Cl<sub>2</sub>)<sub>3.4</sub>@[(CuI)<sub>54</sub>((C<sub>40</sub>H<sub>35</sub>)FeP<sub>5</sub>)<sub>12</sub>(CH<sub>3</sub>CN)<sub>1.46</sub>]<sub>2</sub>·2.54(CH<sub>3</sub>CN)·0.8C<sub>7</sub>H<sub>8</sub> without taking into account non-localized solvent molecules.

Packing motifs were analyzed with TOPOS 4.0 Professional program suit for crystal chemical analysis.<sup>[17]</sup> Bond lengths and bond angles are summarized in Tables 2S and 3S. CCDC-1008152 (compound **2**), -1008153 (compound **3**) contain the supplementary crystallographic data for this publication. These data can be obtained free of charge at [www.ccdc.cam.ac.uk/conts/retrieving.html](http://www.ccdc.cam.ac.uk/conts/retrieving.html) (or from the Cambridge Crystallographic Data Centre, 12 Union Road, Cambridge CB2 1EZ, UK; Fax: + 44-1223-336-033; e-mail: [deposit@ccdc.cam.ac.uk](mailto:deposit@ccdc.cam.ac.uk)).

**Table 1S.** Experimental details for compounds 2 and 3

Crystal data	<b>2</b>	<b>3</b>
Chemical formula	C <sub>491.40</sub> H <sub>438.80</sub> Cl <sub>6.80</sub> Cu <sub>54</sub> Fe <sub>12</sub> I <sub>54</sub> N <sub>4</sub> P <sub>60</sub>	C <sub>40</sub> H <sub>35</sub> Cu <sub>3</sub> FeI <sub>3</sub> P <sub>5</sub> ·0.5(CH <sub>2</sub> Cl <sub>2</sub> )
<i>M<sub>r</sub></i>	19453.26	1340.16
Crystal system, space group	Triclinic, <i>P</i> 1	Triclinic, <i>P</i> 1
Temperature (K)	123.0	123.0
<i>a</i> , <i>b</i> , <i>c</i> (Å)	27.7249(8), 27.7730(7), 27.9764(8)	10.2110(8), 10.8762(8), 19.4787(12)
$\alpha$ , $\beta$ , $\gamma$ (°)	119.783(3), 105.310(2), 96.155(2)	96.601(6), 102.067(6), 92.147(6)
<i>V</i> (Å <sup>3</sup> )	17286.3(8)	2097.2 (3)
<i>Z</i>	1	2
<i>F</i> (000)	9171	1286
Radiation type	Cu <i>K</i> $\alpha$	Cu <i>K</i> $\alpha$
<i>D<sub>x</sub></i> (g·cm <sup>-3</sup> )	1.869	2.122
$\mu$ (mm <sup>-1</sup> )	24.468	24.40
Crystal shape	prism	plate
Colour	red-brown	yellow-orange
Crystal size (mm)	0.06 × 0.06 × 0.11	0.45 × 0.35 × 0.02
Data collection		
Diffractometer	Agilent Technologies SuperNova diffractometer, Atlas detector	Agilent Technologies Gemini R-Ultra diffractometer, Ruby detector
Absorption correction	multi-scan, CrysAlisPro, Oxford Diffraction Ltd., Version 1.171.33.61 (release 04-03-2010 CrysAlis171 .NET) (compiled Mar 4 2010, 15:49:12) Empirical absorption correction using spherical harmonics, implemented in SCALE3 ABSPACK scaling algorithm.	Analytical CrysAlis PRO, Oxford Diffraction Ltd., Version 1.171.33.41 (release 06-05-2009 CrysAlis171 .NET) (compiled May 6 2009, 17:20:42) Analytical numeric absorption correction using a multifaceted crystal model based on expressions derived by R.C. Clark & J.S. Reid. (Clark, R. C. & Reid, J. S. (1995). Acta Cryst. A51, 887-897)
<i>T<sub>min</sub></i> , <i>T<sub>max</sub></i>	0.609, 1.000	0.028, 0.620
No. of measured, independent and observed [ <i>I</i> > 2 $\sigma$ ( <i>I</i> )] reflections	103712, 44589, 20080	13889, 7204, 5463
<i>R<sub>int</sub></i>	0.064	0.083
(sin $\Theta$ / $\lambda$ ) <sub>max</sub> (Å <sup>-1</sup> )	0.540	0.597
Range of <i>h</i> , <i>k</i> , <i>l</i>	<i>h</i> = -29→27, <i>k</i> = -29→28, <i>l</i> = -29→15	<i>h</i> = -11→12, <i>k</i> = -10→12, <i>l</i> = -23→22
Refinement		
<i>R</i> [ <i>F</i> <sup>2</sup> > 2 $\sigma$ ( <i>F</i> <sup>2</sup> )], <i>wR</i> ( <i>F</i> <sup>2</sup> ), <i>S</i>	0.0884, 0.2811, 0.938	0.065, 0.171, 0.97
No. of reflections	44589	7204
No. of parameters	1661	487
No. of restraints	226	0
H-atom treatment	-	H-atom parameters constrained
Weighting scheme	$w = 1/[\sigma^2(F_o^2) + (0.1639P)^2]$ where $P = (F_o^2 + 2F_c^2)/3$	$w = 1/[\sigma^2(F_o^2) + (0.1214P)^2]$ where $P = (F_o^2 + 2F_c^2)/3$
$\Delta\rho_{max}$ , $\Delta\rho_{min}$ (e Å <sup>-3</sup> )	1.842, -1.584	2.95, -2.05

Computer programs for **2**: *CrysAlis PRO*, Agilent Technologies, Version 1.171.33.61 (release 04-03-2010 CrysAlis171.NET) (compiled Mar 4 2010, 15:49:12), *SHELXS97* (Sheldrick, 1998), *SHELXL2013* (Sheldrick, 2013).

Computer programs for **3**: *CrysAlis PRO*, Agilent Technologies, Version 1.171.33.41 (release 06-05-2009 CrysAlis171.NET) (compiled May 6 2009, 17:20:42), *SHELXS97* (Sheldrick, 1990), *SHELXL97* (Sheldrick, 1997).

## 6.5.2.2 Description of crystal structure 2

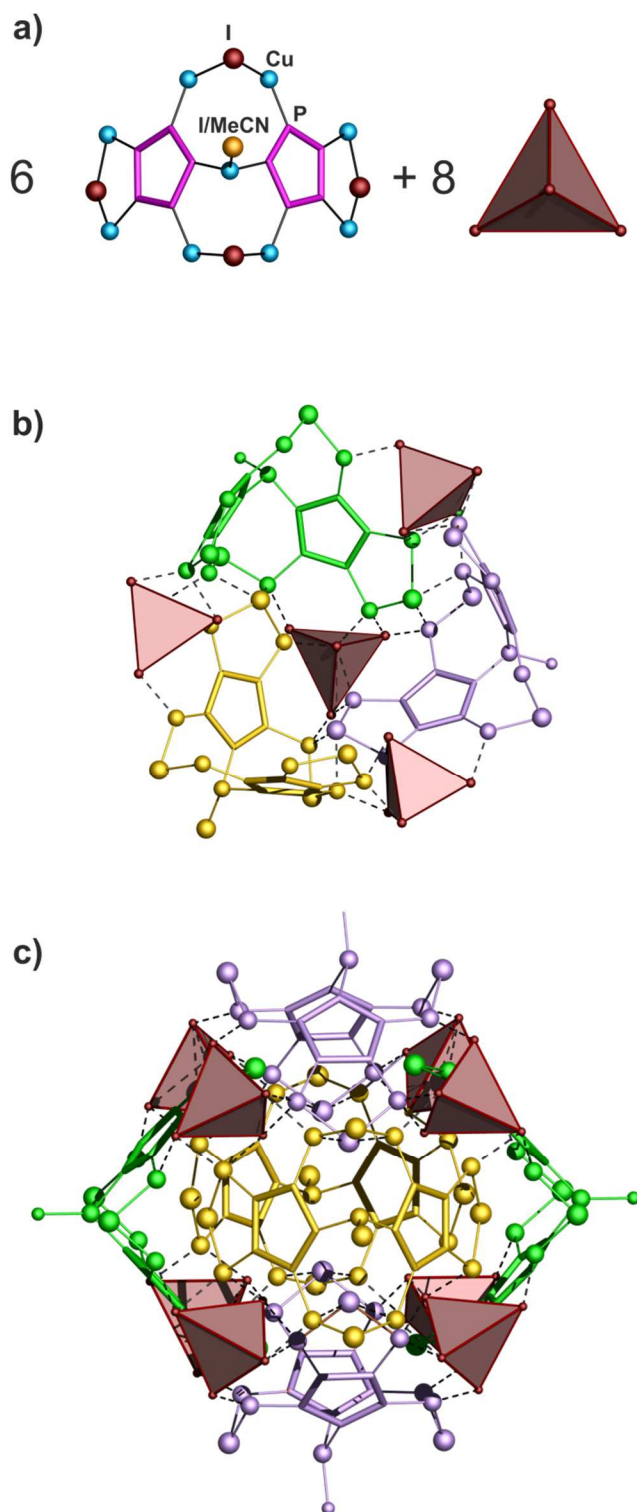


**Figure 1S.** The stepwise construction of the idealized scaffold (without taking into account partly occupied positions) of **2**. A combination of 6  $(\text{Cp}^{\text{Bn}}\text{FeP}_5)_2(\text{CuX})(\text{Cu}_2\text{I})_4$ , ( $\text{X} = \text{I}, \text{MeCN}$ ) fragments and 8  $\text{CuI}_4$  tetrahedrons (a) gives half-shell (b) and the idealized scaffold  $(\text{Cp}^{\text{Bn}}\text{FeP}_5)_{12}\text{Cu}_{62}\text{I}_{58}(\text{MeCN})_4$  (c).

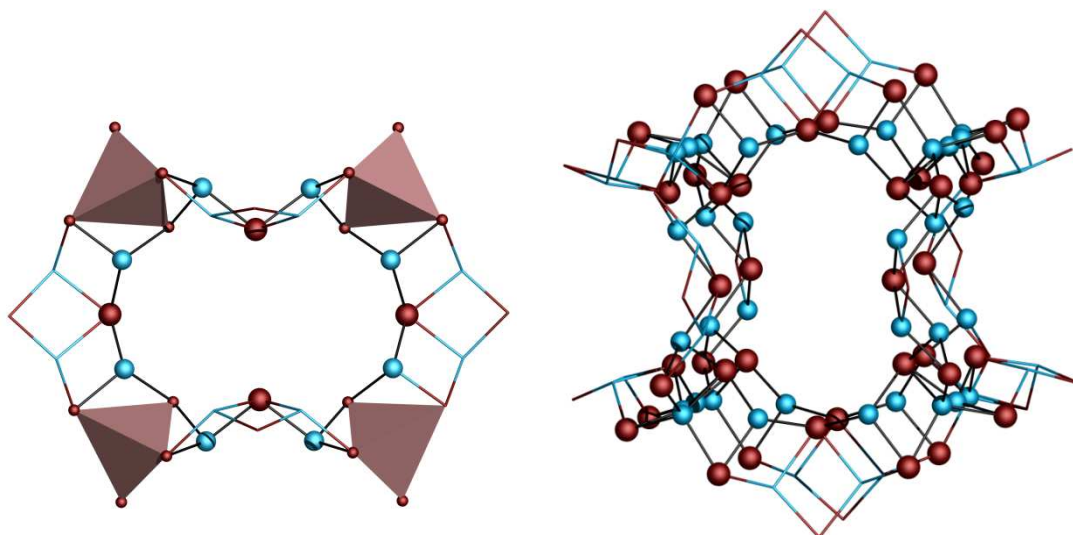


**Figure 2S.** The way of bonding of  $\{\text{Cu}_4\}$  tetrahedra and  $\{\text{Cu}_4\text{I}_2\}$  units giving the  $\{\text{CuI}\}_{56}$  framework in idealized inorganic scaffold in **2** (left) and its fully occupied part comprising 34 copper and 40 iodine ions (right). The disordered positions of Cu and I are shown as sticks.

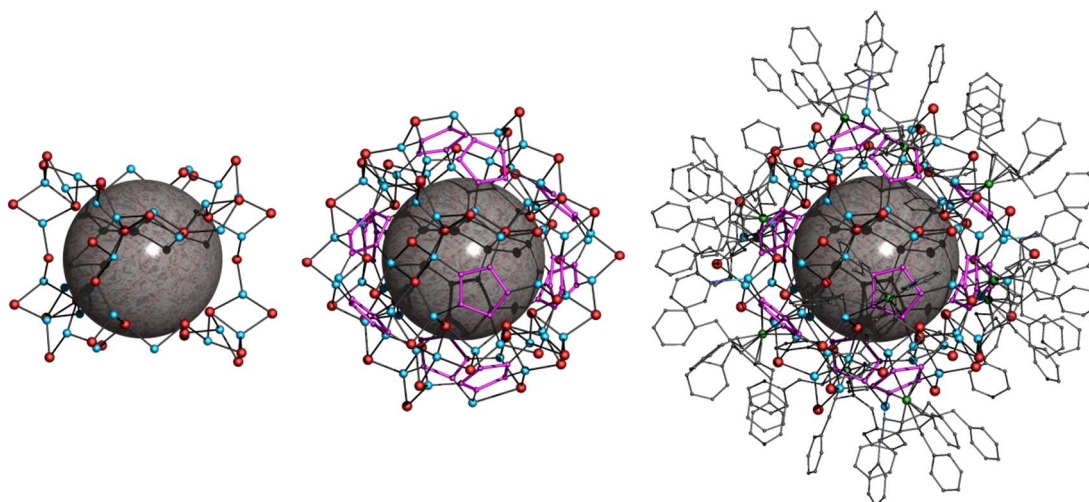


**Figure 3S.** *left:* The irreducible scaffold of **2**. *middle:* The idealized scaffold of **2**. *right:* One of the possible supramolecules in **2**. Hydrogen atoms are omitted for clarity.

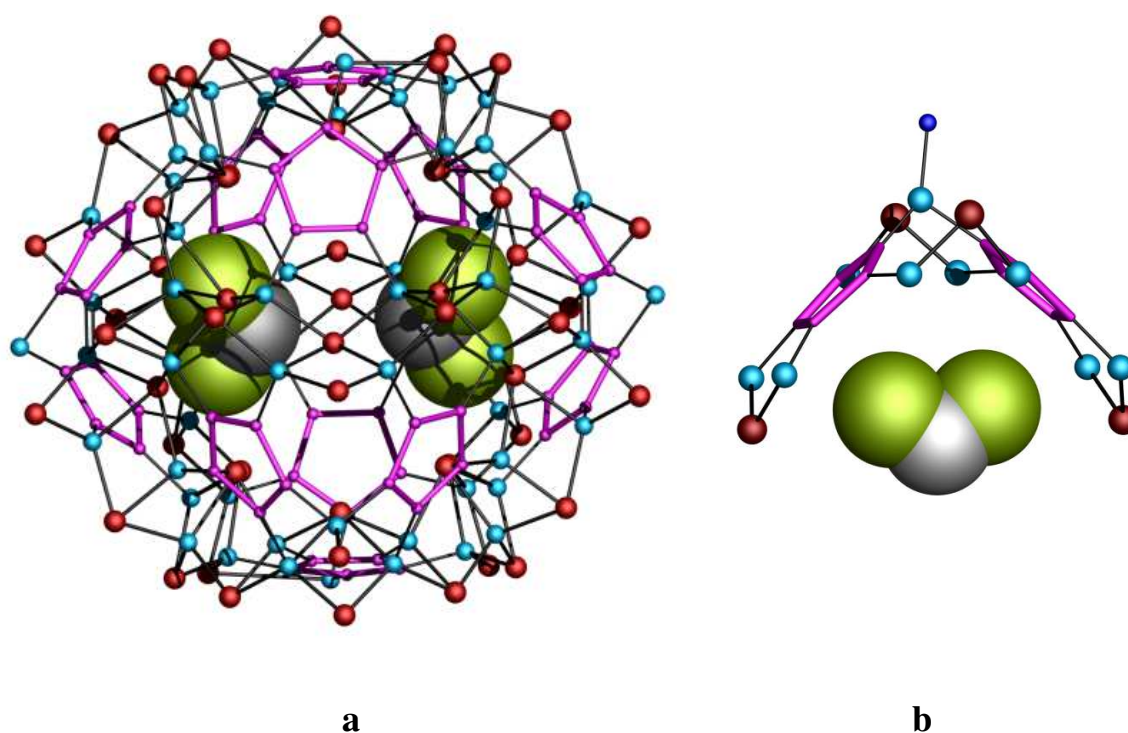


**Figure 4S.** *left:* The arrangement of two guest  $\text{CH}_2\text{Cl}_2$  molecules in the cavity of supramolecule **2**. *right:* The complementarity of a guest molecule to one of the  $(\text{Cp}^{\text{Bn}}\text{FeP}_5)_2(\text{CuMeCN})(\text{Cu}_2\text{I})_4$  building block of **2**.

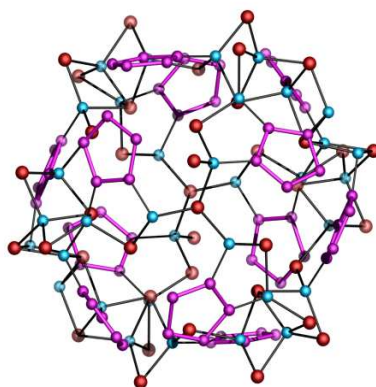


**Figure 5S.** Fully occupied part of the scaffold with coordinated *cyclo*- $\text{P}_5$  ligands of **2**.

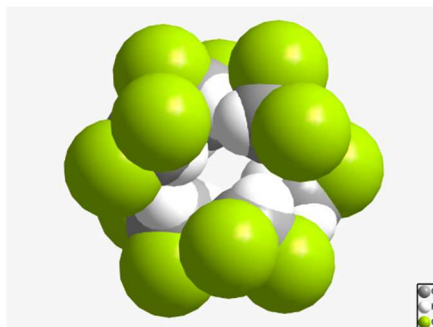


**Figure 6S.** Arrangement of 6 non-contradictory positions of guest  $\text{CH}_2\text{Cl}_2$  molecules inside the cavity.

## 6.5.2.3 Selected Bond distances

Table 2S. Selected bond lengths (Å, °) for compound 2.

Cu-P		Cu-I	
Cu1A—P34	2.168 (18)	Cu1A—I5B <sup>i</sup>	2.95 (2)
Cu1A—P54	2.281 (18)	Cu2A—I7B	2.931 (18)
Cu1B—P34	2.16 (3)	Cu3A—I3B	2.548 (11)
Cu1B—P54	2.23 (2)	Cu3A—I3A	2.615 (14)
Cu2A—P62	2.109 (17)	Cu3A—I3C	2.631 (4)
Cu2A—P43	2.335 (18)	Cu3A—I16	2.792 (4)
Cu2B—P62	2.16 (4)	Cu3B—I3B <sup>i</sup>	2.515 (11)
Cu2B—P43	2.29 (4)	Cu3B—I25	2.644 (5)
Cu3A—P35	2.251 (9)	Cu3B—I3A <sup>i</sup>	2.734 (14)
Cu3B—P53 <sup>i</sup>	2.226 (6)	Cu3B—I16 <sup>i</sup>	2.768 (4)
Cu4A—P24	2.259 (8)	Cu3C—I21	2.664 (5)
Cu5A—P55 <sup>i</sup>	2.220 (8)	Cu3C—I3C	2.676 (4)
Cu5B—P33	2.232 (8)	Cu3C—I12	2.683 (3)
Cu6A—P63 <sup>i</sup>	2.237 (8)	Cu3C—I4C	2.689 (5)
Cu6B—P44 <sup>i</sup>	2.257 (9)	I3A—Cu3B <sup>i</sup>	2.734 (14)
Cu7A—P42	2.211 (8)	I3B—Cu3B <sup>i</sup>	2.515 (11)
Cu7B—P61	2.244 (8)	I3C—Cu3	2.585 (3)
Cu8A—P15	2.19 (5)	Cu4A—I4B	2.411 (13)
Cu8A—P25	2.22 (4)	Cu4A—I28	2.641 (5)
Cu1—P21	2.242 (8)	Cu4A—I4A	2.748 (13)
Cu2—P11	2.240 (7)	Cu4A—I20	2.826 (5)
Cu3—P41	2.253 (8)	Cu4B—P14	2.259 (8)
Cu11—P12	2.255 (8)	Cu4B—I4A	2.412 (19)
Cu12—P13	2.259 (7)	Cu4B—I4C	2.646 (5)
Cu13—P52 <sup>i</sup>	2.242 (8)	Cu4B—I4B	2.690 (15)
Cu14—P23	2.241 (7)	Cu4B—I20	2.803 (4)
Cu18—P32	2.274 (8)	I4C—Cu19	2.583 (3)
Cu19—P31	2.279 (8)	Cu5A—I5A	2.532 (6)
Cu20—P65	2.245 (7)	Cu5A—I24	2.689 (5)
Cu21—P22	2.261 (7)	Cu5A—I23	2.733 (5)
Cu22—P51 <sup>i</sup>	2.253 (7)	Cu5A—I5B	2.932 (12)
Cu23—P45 <sup>i</sup>	2.239 (7)	Cu5B—I5A <sup>i</sup>	2.564 (6)
Cu24—P64 <sup>i</sup>	2.256 (7)	Cu5B—I30	2.630 (5)
P44—Cu6B <sup>i</sup>	2.257 (9)	Cu5B—I5B <sup>i</sup>	2.641 (10)
P45—Cu23 <sup>i</sup>	2.239 (7)	Cu5B—I23 <sup>i</sup>	2.799 (5)
P51—Cu22 <sup>i</sup>	2.253 (7)	I5A—Cu5B <sup>i</sup>	2.564 (6)
P52—Cu13 <sup>i</sup>	2.243 (8)	I5B—Cu5B <sup>i</sup>	2.641 (10)
P53—Cu3B <sup>i</sup>	2.226 (6)	I5B—Cu1A <sup>i</sup>	2.95 (2)
P55—Cu5A <sup>i</sup>	2.220 (8)	Cu6A—I6A	2.577 (19)

P63—Cu6A <sup>i</sup>	2.237 (8)	Cu6A—I27	2.612 (5)
P64—Cu24 <sup>i</sup>	2.256 (7)	Cu6A—I6B	2.553 (17)
<b>Fe-P</b>		Cu6A—I22	2.811 (4)
Fe1—P11	2.370 (6)	Cu6B—I6A	2.611 (18)
Fe1—P12	2.390 (7)	Cu6B—I6B	2.566 (18)
Fe1—P13	2.377 (7)	Cu6B—I29	2.650 (5)
Fe1—P14	2.363 (8)	Cu6B—I22	2.753 (4)
Fe1—P15	2.385 (7)	Cu6B—Cu21	2.891 (5)
Fe2—P25	2.373 (8)	Cu7A—I7A	2.499 (6)
Fe2—P24	2.376 (8)	Cu7A—I21	2.638 (5)
Fe2—P22	2.376 (8)	Cu7A—I19	2.761 (4)
Fe2—P21	2.378 (8)	Cu7A—I7B	2.891 (8)
Fe2—P23	2.393 (8)	Cu7B—I7A	2.555 (5)
Fe3—P31	2.345 (8)	Cu7B—I18	2.625 (4)
Fe3—P32	2.364 (7)	Cu7B—I7B	2.642 (6)
Fe3—P35	2.380 (9)	Cu7B—I19	2.781 (4)
Fe3—P34	2.398 (9)	Cu8A—I8A	2.41 (5)
Fe3—P33	2.404 (7)	I9A—Cu2	2.41 (2)
Fe4—P44	2.357 (8)	I9A—Cu1	2.59 (3)
Fe4—P43	2.357 (8)	I9B—Cu1	2.56 (2)
Fe4—P45	2.378 (6)	I9B—Cu2	2.675 (17)
Fe4—P41	2.379 (7)	Cu1—I26	2.640 (4)
Fe4—P42	2.382 (7)	Cu1—I13	2.788 (4)
Fe5—P55	2.353 (8)	Cu2—I17	2.635 (4)
Fe5—P51	2.366 (6)	Cu2—I13	2.800 (3)
Fe5—P53	2.373 (6)	Cu3—I12	2.683 (4)
Fe5—P54	2.374 (8)	Cu3—I16	2.683 (3)
Fe5—P52	2.389 (7)	Cu11—I18	2.595 (3)
Fe6—P65	2.372 (7)	Cu11—I19	2.683 (3)
Fe6—P62	2.373 (9)	Cu11—I11	2.688 (3)
Fe6—P61	2.376 (9)	Cu12—I21	2.586 (3)
Fe6—P64	2.383 (7)	Cu12—I12	2.681 (3)
Fe6—P63	2.391 (8)	Cu12—I19	2.682 (4)
<b>Fe-C</b>		Cu13—I26	2.583 (4)
Fe1—C14	2.06 (2)	Cu13—I13	2.681 (3)
Fe1—C11	2.06 (2)	Cu13—I14	2.683 (3)
Fe1—C12	2.06 (3)	Cu14—I27	2.586 (4)
Fe1—C15	2.06 (2)	Cu14—I15	2.674 (4)
Fe1—C13	2.12 (2)	Cu14—I22	2.679 (4)
Fe2—C25	2.060 (18)	Cu15—I25	2.673 (4)
Fe2—C21	2.065 (19)	Cu15—I29	2.675 (4)
Fe2—C24	2.082 (18)	Cu15—I26	2.675 (4)
Fe2—C22	2.09 (2)	Cu15—I14	2.683 (4)



## 6.5 Supporting Information

Fe2—C23	2.101 (18)	Cu16—I24	2.665 (4)
Fe3—C34	2.061 (19)	Cu16—I18	2.666 (3)
Fe3—C33	2.069 (17)	Cu16—I17	2.672 (4)
Fe3—C35	2.074 (17)	Cu16—I11	2.687 (3)
Fe3—C32	2.088 (17)	Cu17—I15	2.666 (4)
Fe3—C31	2.091 (17)	Cu17—I27	2.674 (4)
Fe4—C41	2.05 (2)	Cu17—I28	2.678 (4)
Fe4—C43	2.09 (3)	Cu17—I30	2.683 (5)
Fe4—C44	2.08 (3)	Cu18—I28	2.584 (4)
Fe4—C45	2.18 (3)	Cu18—I15	2.673 (4)
Fe4—C42	2.22 (2)	Cu18—I20	2.680 (4)
Fe5—C53	2.05 (2)	Cu19—I12	2.668 (4)
Fe5—C55	2.05 (2)	Cu19—I20	2.701 (4)
Fe5—C52	2.08 (2)	Cu20—I24	2.577 (4)
Fe5—C54	2.08 (2)	Cu20—I11	2.688 (4)
Fe5—C51	2.09 (2)	Cu20—I23	2.694 (3)
Fe6—C61	2.01 (3)	Cu21—I29	2.582 (3)
Fe6—C62	2.03 (3)	Cu21—I14	2.667 (4)
Fe6—C64	2.05 (3)	Cu21—I22	2.697 (4)
Fe6—C63	2.08 (3)	Cu22—I17	2.590 (3)
Fe6—C65	2.09 (3)	Cu22—I11	2.676 (3)
<b>P-P</b>		Cu22—I13	2.680 (4)
P11—P15	2.096 (10)	Cu23—I25	2.579 (3)
P11—P12	2.100 (9)	Cu23—I14	2.684 (3)
P12—P13	2.090 (9)	Cu23—I16 <sup>i</sup>	2.690 (4)
P13—P14	2.077 (10)	Cu24—I30	2.586 (4)
P14—P15	2.097 (10)	Cu24—I23 <sup>i</sup>	2.678 (4)
P21—P22	2.089 (9)	Cu24—I15	2.684 (4)
P21—P25	2.118 (10)	I16—Cu23 <sup>i</sup>	2.689 (4)
P22—P23	2.106 (10)	I16—Cu3B <sup>i</sup>	2.768 (4)
P23—P24	2.090 (9)	I23—Cu24 <sup>i</sup>	2.678 (4)
P24—P25	2.075 (11)	I23—Cu5B <sup>i</sup>	2.799 (5)
P31—P35	2.071 (10)		
P31—P32	2.083 (10)		
P32—P33	2.076 (10)		
P33—P34	2.123 (11)		
P34—P35	2.100 (10)		
P41—P42	2.082 (9)		
P41—P45	2.110 (9)		
P42—P43	2.106 (11)		
P43—P44	2.093 (10)		
P44—P45	2.091 (10)		
P51—P55	2.084 (10)		

P51—P52	2.103 (8)		
P52—P53	2.111 (9)		
P53—P54	2.095 (11)		
P54—P55	2.080 (9)		
P61—P65	2.082 (9)		
P61—P62	2.097 (10)		
P62—P63	2.098 (10)		
P63—P64	2.097 (9)		
P64—P65	2.097 (10)		

**Table 3S.** Selected geometric parameters (Å, °) for compound 3.

Cu1—P1	2.301 (3)	I3—Cu3 <sup>iii</sup>	2.6816 (15)
Cu1—P5 <sup>ii</sup>	2.268 (3)	Fe1—P1	2.363 (3)
Cu2—P2	2.266 (3)	Fe1—P2	2.426 (3)
Cu3—P3	2.262 (3)	Fe1—P3	2.372 (3)
Cu1—Cu2 <sup>i</sup>	3.0013 (19)	Fe1—P4	2.386 (2)
Cu2—Cu1 <sup>i</sup>	3.0013 (19)	Fe1—P5	2.391 (3)
Cu1—I1 <sup>i</sup>	2.6452 (14)	Fe1—C1	2.122 (10)
Cu1—I2	2.5966 (15)	Fe1—C2	2.090 (10)
Cu2—I1	2.7920 (17)	Fe1—C3	2.099 (9)
Cu2—I2 <sup>i</sup>	2.5765 (14)	Fe1—C4	2.105 (9)
Cu2—I3 <sup>iii</sup>	2.6537 (16)	Fe1—C5	2.135 (9)
Cu3—I3	2.6690 (16)	P1—P2	2.102 (3)
Cu3—I3 <sup>iii</sup>	2.6816 (15)	P1—P5	2.115 (3)
Cu3—I1 <sup>iii</sup>	2.5884 (15)	P2—P3	2.099 (3)
I1—Cu1 <sup>i</sup>	2.6453 (14)	P3—P4	2.117 (3)
I1—Cu3 <sup>iii</sup>	2.5885 (15)	P4—P5	2.102 (3)
I2—Cu2 <sup>i</sup>	2.5764 (14)	P5—Cu1 <sup>ii</sup>	2.268 (3)
I3—Cu2 <sup>iii</sup>	2.6536 (16)		
I1 <sup>i</sup> —Cu1—Cu2 <sup>i</sup>	58.87 (4)	P2—Cu2—I1	115.21 (9)
I2—Cu1—Cu2 <sup>i</sup>	54.22 (4)	P2—Cu2—I2 <sup>i</sup>	114.35 (8)
I2—Cu1—I1 <sup>i</sup>	109.73 (5)	P2—Cu2—I3 <sup>iii</sup>	105.86 (8)
P1—Cu1—Cu2 <sup>i</sup>	129.01 (8)	I1 <sup>iii</sup> —Cu3—I3	103.56 (5)
P1—Cu1—I1 <sup>i</sup>	109.45 (8)	I1 <sup>iii</sup> —Cu3—I3 <sup>iii</sup>	107.93 (5)
P1—Cu1—I2	96.68 (8)	I3—Cu3—I3 <sup>iii</sup>	103.97 (5)
P5 <sup>ii</sup> —Cu1—Cu2 <sup>i</sup>	121.19 (8)	P3—Cu3—I1 <sup>iii</sup>	126.85 (9)
P5 <sup>ii</sup> —Cu1—I1 <sup>i</sup>	112.19 (8)	P3—Cu3—I3	102.91 (9)
P5 <sup>ii</sup> —Cu1—I2	118.26 (9)	P3—Cu3—I3 <sup>iii</sup>	109.12 (8)
P5 <sup>ii</sup> —Cu1—P1	109.27 (10)	Cu1 <sup>i</sup> —I1—Cu2	66.94 (4)
I1—Cu2—Cu1 <sup>i</sup>	54.19 (4)	Cu3 <sup>iii</sup> —I1—Cu1 <sup>i</sup>	109.70 (5)
I2 <sup>i</sup> —Cu2—Cu1 <sup>i</sup>	54.85 (4)	Cu3 <sup>iii</sup> —I1—Cu2	75.45 (5)
I2 <sup>i</sup> —Cu2—I1	105.91 (5)	Cu2 <sup>i</sup> —I2—Cu1	70.92 (5)
I2 <sup>i</sup> —Cu2—I3 <sup>iii</sup>	116.11 (6)	Cu2 <sup>iii</sup> —I3—Cu3	76.52 (5)
I3 <sup>iii</sup> —Cu2—Cu1 <sup>i</sup>	104.03 (5)	Cu2 <sup>iii</sup> —I3—Cu3 <sup>iii</sup>	90.03 (5)
I3 <sup>iii</sup> —Cu2—I1	98.65 (5)	Cu3—I3—Cu3 <sup>iii</sup>	76.03 (5)
P2—Cu2—Cu1 <sup>i</sup>	149.63 (9)		

Symmetry code(s): (i) -x+1, -y+2, -z; (ii) -x, -y+2, -z; (iii) -x+1, -y+1, -z.

### 6.5.3 Size Estimation from DOSY

#### 6.5.3.1 Spectroscopic Details

The DOSY spectra were recorded on an Avance III HD 600 (600.13 MHz) spectrometer equipped with a z-gradient (53.5 Gauss/cm), 5 mm triple resonance CPP-BBO and BCU II unit at 300 K and on a Avance III 600 (600.25 MHz) spectrometer equipped with a z-gradient (53.5 Gauss/cm), 5 mm TCI cryo probe and BVT 3000 unit at 298 K. The NMR data was processed with the Bruker program TopSpin® 3.2 and the diffusion coefficient was calculated with the Bruker software *T1/T2* relaxation package. For the calibration of the  $^1\text{H}$  chemical shifts and for the temperature- and viscosity-correction of the diffusion coefficients, TMS (tetramethylsilane) was added. The  $^1\text{H}$ -diffusion measurement was performed with the convection suppressing DSTE (double stimulated echo) pulse sequence, developed by Mueller and Jerschow<sup>[18a]</sup> in a pseudo 2D mode. 120 dummy scans and 16 scans were used with a relaxation delay of 2 s. Sinusoidal shapes were used for the gradient and a linear gradient ramp with 20 increments between 5 and 95 % of the maximum gradient strength was applied for the diffusion relevant gradients. For the homospoil gradients, -13.7, 20 and -17.13 G cm<sup>-1</sup> were applied. The length of the gradient pulse  $\delta$  was adjusted for every species in the sample to achieve appropriate signal attenuation curves, giving values for  $\delta$  of 2.0 ms for TMS and 3.7 ms for the supramolecule. A diffusion time  $\Delta$  of 50 ms was used.

#### 6.5.3.2 Size Estimation

From crystallographic data the diameter of the **2** cluster was estimated to be  $d = 37.0 \text{ \AA}$  ( $r = 18.5 \text{ \AA}$ ) from the maximum H-H distance plus twice the Van-der-Waals radius of a proton ( $1.2 \text{ \AA}$ <sup>[19]</sup>).

From diffusion-ordered spectroscopy (DOSY) experiments<sup>[18b-c]</sup> the translational self-diffusion coefficient  $D$  of molecules in solution can be calculated according to the Stejskal-Tanner equation.<sup>[6]</sup> With the diffusion coefficients  $D$  of the analyte and of TMS (acting as viscosity reference), the hydrodynamic radius  $r_{\text{H}}$  of the analyte can be estimated following the Stokes-Einstein equation<sup>[20]</sup> to be  $r_{\text{H}} = 20.72 \text{ \AA}$ .

This is in very good agreement with the crystal-derived radius of  $18.5 \text{ \AA}$  in the solid state. Therefore, these results clearly indicate the presence of the intact supramolecule in solution.

## 6.6 References

- [1] a) S. I. Stupp, L. C. Palmer, *Chem. Mater.* **2014**, *26*, 507-518; b) N. Lanigan, X. Wang, *Chem. Commun.* **2013**, *49*, 8133-8144; c) R. W. Saalfrank, A. Scheurer, *Top. Curr. Chem.* **2012**, *319*, 125-170; d) S. J. Dalgarno, *Annu. Rep. Prog. Chem., Sect. B: Org. Chem.* **2010**, *106*, 197-215; e) M. Mastalerz, *Angew. Chem. Int. Ed.* **2010**, *49*, 5042-5053; *Angew. Chem.* **2010**, *122*, 5164-5175; f) T. H. Rehm, C. Schmuck, *Chem. Soc. Rev.* **2010**, *39*, 3597-3611; g) J.-M. Lehn, *Proceedings of the National Academy of Sciences* **2002**, *99*, 4763-4768; h) F. A. Cotton, C. Lin, C. A. Murillo, *Acc. Chem. Res.* **2001**, *34*, 759-771; i) J. Bradley, B. J. Holliday, C. A. Mirkin, *Angew. Chem. Int. Ed.* **2001**, *40*, 2022-2043; *Angew. Chem.* **2001**, *113*, 2076-2097.
- [2] J. M. Lehn, *Angew. Chem. Int. Ed. Engl.* **1988**, *27*, 89-112; *Angew. Chem.* **1988**, *100*, 91-116.
- [3] a) L. F. Lindoy, K.-M. Park, S. S. Lee, *Chem. Soc. Rev.* **2013**, *42*, 1713-1727; b) S. R. Seidel, P. J. Stang, *Acc. Chem. Res.* **2002**, *35*, 972-983.
- [4] a) N. J. Young, B. P. Hay, *Chem. Commun.* **2013**, *49*, 1354-1379; b) R. W. Saalfrank, A. Scheurer, *Top. Curr. Chem.* **2012**, *319*, 125-170; c) W. Meng, J. K. Clegg, J. R. Nitschke, *Angew. Chem. Int. Ed.* **2012**, *51*, 1881-1884; *Angew. Chem.* **2012**, *124*, 1917-1920; d) Z. Laughrey, B. C. Gibb, *Chem. Soc. Rev.* **2011**, *40*, 363-386; e) Y. Inokuma, M. Kawano, M. Fujita, *Nat. Chem.* **2011**, *3*, 349-358; f) P. Jin, S. J. Dalgarno, J. L. Atwood, *Coord. Chem. Rev.* **2010**, *254*, 1760-1768; g) S. J. Dalgarno, N. P. Power, J. L. Atwood, *Coord. Chem. Rev.* **2008**, *252*, 825-841; h) T. S. Koblenz, J. Wassenaar, J. N. H. Reek, *Chem. Soc. Rev.* **2008**, *37*, 247-262; i) C. Schmuck, *Angew. Chem. Int. Ed.* **2007**, *46*, 5830-5833; *Angew. Chem.* **2007**, *119*, 5932-5935; j) T. Heinz, D. M. Rudkevich, J. Rebek, Jr., *Nature* **1998**, *394*, 764-766.
- [5] a) A. Schindler, C. Heindl, G. Balazs, C. Groeger, A. V. Virovets, E. V. Peresyphkina, M. Scheer, *Chem. Eur. J.* **2012**, *18*, 829-835; b) M. Scheer, A. Schindler, C. Gröger, A. V. Virovets, E. V. Peresyphkina, *Angew. Chem. Int. Ed.* **2009**, *48*, 5046-5049; *Angew. Chem.* **2009**, *121*, 5148-5151; c) M. Scheer, A. Schindler, J. Bai, B. P. Johnson, R. Merkle, R. Winter, A. V. Virovets, E. V. Peresyphkina, V. A. Blatov, M. Sierka, H. Eckert, *Chem. Eur. J.* **2010**, *16*, 2092-2107; d) S. Welsch, C. Groeger, M. Sierka, M. Scheer, *Angew. Chem. Int. Ed.* **2011**, *50*, 1435-1438; *Angew. Chem.* **2011**, *123*, 1471-1474; e) J. Bai, A. V. Virovets, M. Scheer, *Science* **2003**, *300*, 781-783; f) M. Scheer, J. Bai, B. P. Johnson, R. Merkle, A. V. Virovets, C. E. Anson, *Eur. J. Inorg. Chem.* **2005**, 4023-4026.

- [6] For the only existing example of a small baseball-like aggregate<sup>[8]</sup> cf.: C. Schwarzmaier, A. Schindler, C. Heindl, S. Scheuermayer, E. V. Peresyphkina, A. V. Virovets, M. Neumeier, R. Gschwind, M. Scheer, *Angew. Chem. Int. Ed.* **2013**, *52*, 10896-10899; *Angew. Chem.* **2013**, *125*, 11097-11100.
- [7] F. Dielmann, R. Merkle, S. Heintl, M. Scheer, *Z. Naturforsch.* **2009**, *64*, 3-10.
- [8] Beside **2** there is only one example of a pentaphosphaferrocene-based supramolecule<sup>[6]</sup> known possessing non-fullerene topology. Its core consists of eight units of P<sub>5</sub> ligands. A fullerene-like scaffold would require 12 five-membered rings and n-20/2 six-membered rings.
- [9] Crystal data for **2**: C<sub>491.40</sub>H<sub>438.80</sub>N<sub>4</sub>P<sub>60</sub>Cl<sub>6.80</sub>Fe<sub>12</sub>Cu<sub>54</sub>I<sub>54</sub>, triclinic, space group *P*1̄, *a* = 27.7249(8), *b* = 27.7730(7), *c* = 27.9764(8) Å, α = 119.783(3), β = 105.310(2), γ = 96.155(2)°, *V* = 17286.3(8) Å<sup>3</sup>, *Z* = 1, *D*<sub>calc.</sub> = 1.869 g·sm<sup>-3</sup>, crystal dimensions 0.06 × 0.06 × 0.11 mm; Cu Kα radiation, 123.0(2) K, 103712 reflections, 44589 independent, μ = 24.468 mm<sup>-1</sup>, refinement (on *F*<sup>2</sup>) with SHELX2013, 1661 parameters, *R*<sub>1</sub> = 0.0884 (*I* > 2σ), *wR*<sub>2</sub> = 0.2811 (all data), *Goof* = 0.938, max/min residual electron density 1.842 and -1.584 e·Å<sup>-3</sup>. Crystal data for **3**: C<sub>40.5</sub>H<sub>36</sub>ClP<sub>5</sub>FeCu<sub>3</sub>I<sub>3</sub>, triclinic, space group *P*1̄, *a* = 10.2110(8), *b* = 10.8762(8), *c* = 19.4787(12) Å, α = 96.601(6), β = 102.067(6), γ = 92.147 (6)°, *V* = 2097.2(3) Å<sup>3</sup>, *Z* = 2, *D*<sub>calc.</sub> = 2.122 g·sm<sup>-3</sup>, crystal dimensions 0.45 × 0.35 × 0.02 mm; Cu Kα radiation, 123.0(2) K, 13889 reflections, 7204 independent, μ = 24.40 mm<sup>-1</sup>, refinement (on *F*<sup>2</sup>) with SHELX97, 487 parameters, *R*<sub>1</sub> = 0.065 (*I* > 2σ), *wR*<sub>2</sub> = 0.171 (all data), *Goof* = 0.97, max/min residual electron density 2.95 and -2.05 e·Å<sup>-3</sup>. For more details of the X-ray structure analyses see the Supporting Information. CCDC-1008152 (**2**) and -1008153 (**3**) contain the supplementary crystallographic data for this publication. These data can be obtained free of charge at [www.ccdc.cam.ac.uk/conts/retrieving.html](http://www.ccdc.cam.ac.uk/conts/retrieving.html) (or from the Cambridge Crystallographic Data Centre, 12 Union Road, Cambridge CB2 1EZ, UK; Fax: +44-1223-336-033; e-mail: [deposit@ccdc.cam.ac.uk](mailto:deposit@ccdc.cam.ac.uk)).
- [10] R. Peng, M. Li, D. Li, *Coord. Chem. Rev.* **2010**, *254*, 1-18.
- [11] H. Hartl, J. Fuchs, *Angew. Chem. Int. Ed. Engl.* **1986**, *25*, 569-570; *Angew. Chem.* **1986**, *98*, 550-551.
- [12] F. Dielmann, A. Schindler, S. Scheuermayer, J. Bai, R. Merkle, M. Zabel, A. V. Virovets, E. V. Peresyphkina, G. Bruncklaus, H. Eckert, M. Scheer, *Chem. Eur. J.* **2012**, *18*, 1168-1179.
- [13] F. Dielmann, R. Merkle, S. Heintl, M. Scheer, *Zeitschrift für Naturforschung* **2009**, *64*, 3-10.
- [14] *CrysAlis PRO*, Agilent Technologies, 2006-2014.

- [15] G. M. Sheldrick, *Acta Cryst.* **2008**, *A64*, 112-122.
- [16] G. M. Sheldrick. SHELX2013, University of Göttingen, 2013.
- [17] V.A. Blatov, *Cryst. Comp. Newsletter*, **2006**, *7*, 4-38 (<http://www.iucr.org/iucr-top/comm/ccom/newsletters/>).
- [18] a) A. Jerschow, N. Müller, *J. Magn. Reson.* **1997**, *125*, 372-375. b) C. S. Johnson, *Prog. Nucl. Magn. Reson. Spectrosc.* **1999**, *34*, 203-256; c) W. S. Price, *Concepts Magn. Reson.* **1998**, *10*, 197-237; d) E. O. Stejskal, J. E. Tanner, *The Journal of Chemical Physics* **1965**, *42*, 288-292.
- [19] M. Scheer, A. Schindler, C. Groeger, A. V. Virovets, E. V. Peresykina, *Angew. Chem., Int. Ed.* **2009**, *48*, 5046-5049.
- [20] A. Macchioni, G. Ciancaleoni, C. Zuccaccia, D. Zuccaccia, *Chem. Soc. Rev.* **2008**, *37*, 479-489.





## 7 NMR investigations on Phosphoramidite Palladium Complexes and the Supramolecular Balance

Unpublished work.



The work for this chapter was done in close cooperation with Dr. Matej Zabka. All symmetric phosphoramidites up to the first reaction path of Figure 8 as well as extensive initial synthetic and spectroscopic work was performed by Florian Hastreiter. Furthermore, Florian Hastreiter did the full assignment of the presented complexes, the figures and the writing of this chapter.

## 7.1 Abstract

We report on an experimental approach to measure dispersive interactions. For this purpose, the concept of the supramolecular balance by Gschwind and coworkers was used.<sup>[1]</sup> Because of a conformational change in one of the two heterocomplexes investigated in the model system, the principle was found not to be applicable since the value of  $\Delta\Delta G^0$  does no longer represent exclusively the dispersive interactions. Therefore, chiral phosphoramidite ligands with non- $C_2$ -symmetric amine side chains were used. Here, one interligand interaction can be formed, thus, anchoring the complex in a single conformation. The other part of the amine side chain is free for rotation. Asymmetric phosphoramidite ligands seem most promising to fulfill the basic requirements for the supramolecular balance and thus, may potentially enable a direct experimental measurement technique for dispersive interactions.

## 7.2 Introduction

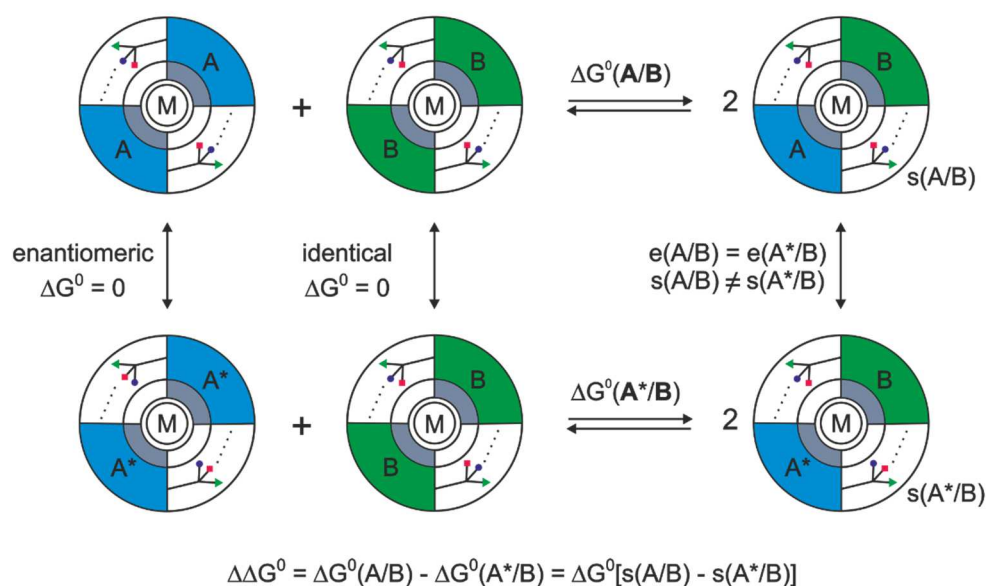


**Figure 1.** Schematic representation of the concept of the supramolecular balance proposed by Gschwind and coworkers<sup>[1]</sup> including the calculation for the dispersive interactions from the difference of free energy of both equilibria. Using two phosphoramidite ligands, one biphenyl-based phosphoramidite ligand (**A**) and one BINOL-based (**B**), their respective homocomplexes are formed, which are in equilibrium with the heterocomplex of both phosphoramidite ligands **A** and **B** (top). A second equilibrium is established using the same BINOL-based phosphoramidite ligand and the enantiomeric ligand of **A**, i.e. **A\*** (bottom). Comparing the difference of free energies for each equilibrium  $\Delta G^0$ , the contribution of the homocomplexes can be neglected, since they are either enantiomeric (for **A/A\***;  $\Delta G^0 = 0$  by definition) or identical (for **B**;  $\Delta G^0 = 0$ ). Therefore, the difference of free energy  $\Delta\Delta G^0$  corresponds only to the difference in free energies of the heterocomplexes. Furthermore, in case that the main structures of the heterocomplexes remain for both the same, the difference of stereoelectronic and electrostatic contributions amounts to zero and can also be neglected ( $e(\mathbf{A/B}) =$

$e(\mathbf{A}^*/\mathbf{B})$ ). The difference of free energy  $\Delta\Delta G^0$  of both equilibria then directly correlates to the difference of the dispersive interactions in the heterocomplexes ( $s(\mathbf{A}/\mathbf{B}) \neq s(\mathbf{A}^*/\mathbf{B})$ ).

Dispersive interactions are generally considered weak interactions. However, the addition of a single  $\text{CH}_2$  unit in alkenes increases the enthalpy for the transition from liquid to gas ( $\Delta H_{\text{vap}}$ ) by approximately  $4 \text{ kJ}\cdot\text{mol}^{-1}$ , which represents in this case a direct measurement of the dispersive interaction and is in the range of a hydrogen bond between two amides in chloroform.<sup>[2]</sup> Thus, dispersive interactions may play a greater role than anticipated so far. However, most investigations on this topic have been solely *in silico*,<sup>[3-8]</sup> since an unambiguous experimental determination of dispersive interaction is extremely challenging owing to e.g. solvent effects.<sup>[9, 10]</sup> Only a few concepts were suggested thus far, which are based on the molecular torsion balance proposed by Wilcox and coworkers.<sup>[11-13]</sup> One very promising experimental approach was suggested by Gschwind and coworkers using a supramolecular balance with phosphoramidite palladium complexes for a direct measurement of dispersive interactions (Figure 1).<sup>[1]</sup> Here, phosphoramidite ligands ( $\mathbf{L} = \mathbf{A}/\mathbf{A}^*$  and  $\mathbf{B}$ ) were chosen, which are widely used in asymmetric catalysis.<sup>[14]</sup> These ligands contain a flexible amine sidechain and a biphenyl-based backbone ( $\mathbf{A}/\mathbf{A}^*$ ), which can adapt due to rotation about the C-C  $\sigma$ -bond, or a rigid BINOL-based backbone ( $\mathbf{B}$ ), respectively (Figure 2). Upon conversion of  $\text{Pd}(\text{cod})\text{Cl}_2$  with two equivalents of phosphoramidite ligand ( $\mathbf{L}$ ) first the square planar *trans*-complex  $\text{PdL}_2\text{Cl}_2$  is formed (Figure 3). Typically, over the course of several weeks the *trans*-complex rearranges to a *cis*-complex driven by the phosphoramidite ligands getting into close proximity to each other enabling the development of dispersive interligand interactions.

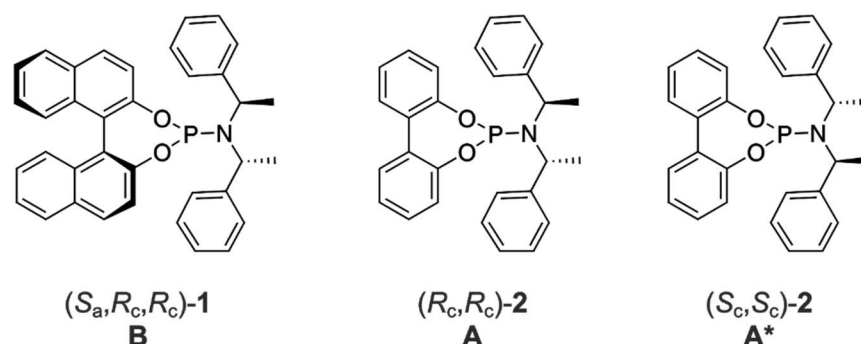


**Figure 2.** Phosphoramidite ligands used as model system for the supramolecular balance with either rigid chiral BINOL-based backbone  $(S_a, R_c, R_c)\text{-1}$  (ligand **B**; left), or flexible biphenyl-based backbone, which can adapt to the chirality in the palladium complexes (ligands **A** and **A\***, right). Ligands **A** and **A\*** are enantiomeric to each other;  $(R_c, R_c)\text{-2}$  and  $(S_c, S_c)\text{-2}$ . Each ligand has a flexible amine sidechain with a phenylethyl group.

**Figure 3.** Formation of the phosphoramidite palladium complexes. Starting from the square planar Pd(cod)Cl<sub>2</sub>, one cyclooctadienyl ligand (cod) is exchanged by two phosphoramidite ligands. Initial formation of the *trans*-PdL<sub>2</sub>Cl<sub>2</sub> with subsequent rearrangement to the *cis*-PdL<sub>2</sub>Cl<sub>2</sub> driven by the formation of dispersive interaction surfaces between the phosphoramidite ligands.

These interligand interactions arise between the phenylethyl groups of the amine sidechain of one phosphoramidite ligand and the aromatic moieties of the BINOL or biphenyl backbone of the other ligand (Figure 4). In addition, intraligand interactions between the amine sidechain and the aromatic moiety of the same ligand are formed. Using two different phosphoramidite ligands (e.g. **A** or **A\*** and **B**) the formation of a heterocomplex PdLL'Cl<sub>2</sub> (L = **B**, L' = **A** or **A\***) is achieved, which is accompanied by an equilibrium with its respective homocomplexes PdL<sub>2</sub>Cl<sub>2</sub> (L = **A** or **A\*** and **B**).

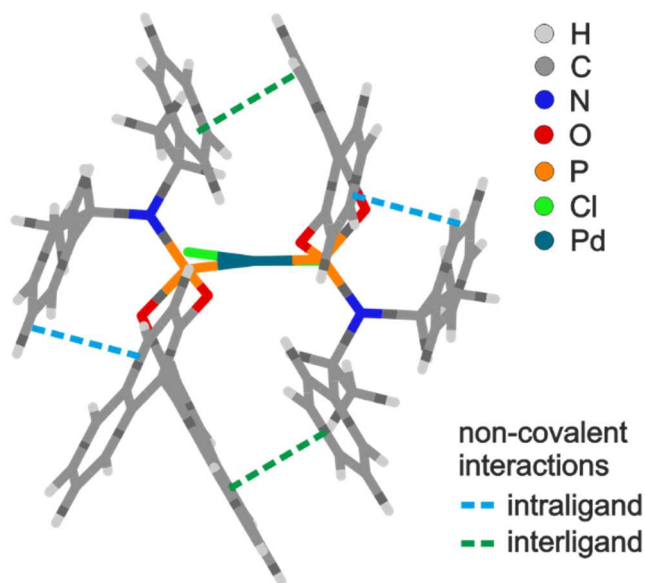


**Figure 4.** Inter- and intraligand interactions between the aromatic moieties and the phenylethyl surfaces of the amine sidechains.

The free energy  $\Delta G^0$  can be derived from equation (1) with K being the quotient of the squared concentration of the heterocomplex over the product of the homocomplexes' concentrations, which can easily be determined from integration of the corresponding <sup>31</sup>P resonances. The free energy difference  $\Delta\Delta G^0$  of both equilibria (Pd**AB**Cl<sub>2</sub> and Pd**A\*B**Cl<sub>2</sub>) can be calculated using equation (2).

$$\Delta G^0 = -RT \ln K ; K = \frac{c^2(\text{PdABCl}_2)}{c(\text{PdA}_2\text{Cl}_2) \cdot c(\text{PdB}_2\text{Cl}_2)} \quad \text{Eq. (1)}$$

$$\Delta\Delta G^0 = -RT(\ln K - \ln K^*) = -RT \ln \frac{K}{K^*} \quad \text{Eq. (2)}$$

The terms of the homocomplexes can be eliminated as these are either identical ( $\Delta G^0 = 0$ ) or enantiomeric ( $\Delta G^0 = 0$  by definition). Therefore, the free energy difference  $\Delta\Delta G^0$  only amounts to the difference of the heterocomplexes. Furthermore, in case the structure of both heterocomplexes can be considered the same, stereoelectronic and electrostatic interactions  $e(\mathbf{A}/\mathbf{B}) = e(\mathbf{A}^*/\mathbf{B})$  cancel out and thus the free energy difference directly reflects the dispersive interactions  $s(\mathbf{A}/\mathbf{B}) \neq s(\mathbf{A}^*/\mathbf{B})$ . Therefore, the dispersive interaction becomes accessible by an experimental setup.

Thus far, only a single example of this supramolecular balance was investigated. As investigations of dispersive interactions as well as the increase of scope for different substituted phosphoramidite ligands are of utmost importance, here we attempt a more detailed investigation.

## 7.3 Results and Discussion

### 7.3.1 Symmetric Phosphoramidite Ligands

First, the expansion of the scope of chiral, flexible phosphoramidite ligands was attempted. Therefore, different substituents were introduced in the BINOL- or biphenyl-backbone as well as in the amine sidechain forming CH- $\pi$  and  $\pi$ - $\pi$  interactions. In Figure 5 an overview of the modifications is shown. Sterically more demanding phosphoramidite ligands were selected to introduce extended interaction surfaces. For ligand **3** with R = Me,<sup>[15]</sup> a similar situation as in the unsubstituted model system was found previously based on the NOE pattern and the chemical shift anisotropy.<sup>[16]</sup> The synthesis of the other phosphoramidite ligands **4** (with R = F), **5** and **6** turned out to be more challenging.

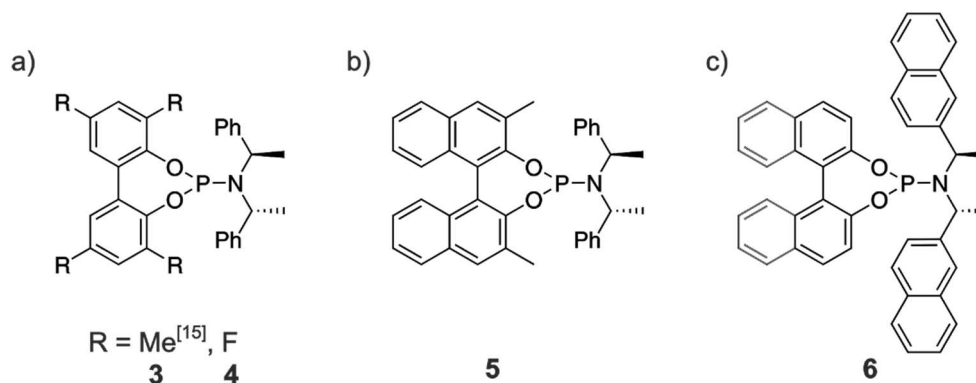


**Figure 5.** Overview of the modifications of the phosphoramidite ligands planned for different intermolecular interactions. a) Methyl- or fluoride substituted biphenyl-based phosphoramidite ligands (**3** and **4**), b) methyl substituted BINOL-based phosphoramidite ligand **5**, and c)  $\beta$ -naphthyl substituted amine sidechain of either BINOL- or biphenyl-based phosphoramidite ligands **6**.

The preparation of ligand **4** with R = F was attempted using 2,4-difluorophenol (see Figure 6). Introduction of an iodine functional group in 6-position with iodine and KI as well

as protection of the hydroxy group with MeI allows for an Ullmann coupling of two molecules of 2,4-difluoro-6-iodoanisole with activated Cu. The subsequent removal of the protecting groups with BBr<sub>3</sub> was reported to yield the fluorinated biphenyldiol.<sup>[17]</sup> However, the introduction of the iodine functional group in the first step yielded no product.

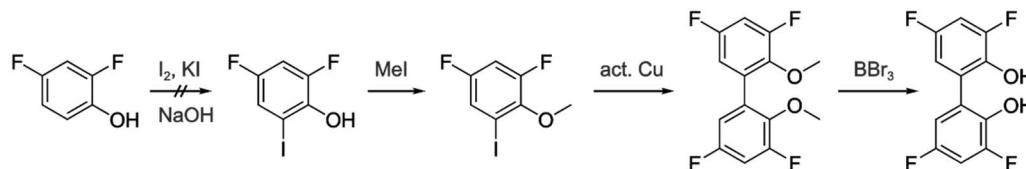


**Figure 6.** Reaction scheme for the synthesis of fluorinated biphenyl-2,2'-diol. Iodination, protection of the hydroxy group with subsequent Ullmann coupling and deprotection of the hydroxy groups.

The synthesis of ligand **5** was attempted using two equivalents 3-methylnaphthalen-2-ol and coupling reaction via a copper catalyst CuCl(OH)·TMEDA (see Figure 7, top pathway).<sup>[18]</sup> An enantiomeric mixture was obtained, but the enantiomers could not be resolved using (8*S*,9*R*)-(-)-*N*-benzylcinchonidinium chloride.<sup>[19]</sup> In addition, another approach was used, starting from (*S*)-BINOL (see Figure 7, bottom pathway). In the first step the hydroxy groups were converted to methoxy protecting groups with MeF.<sup>[20]</sup> Subsequent methylation at 3/3'-position with *n*-BuLi and MeI and conversion of the methoxy groups back to hydroxy groups via addition of BBr<sub>3</sub> yielded the desired methyl-substituted BINOL derivative.<sup>[21]</sup> However, in the last step, the conversion to the phosphoramidite ligand<sup>[22]</sup> yielded no product.

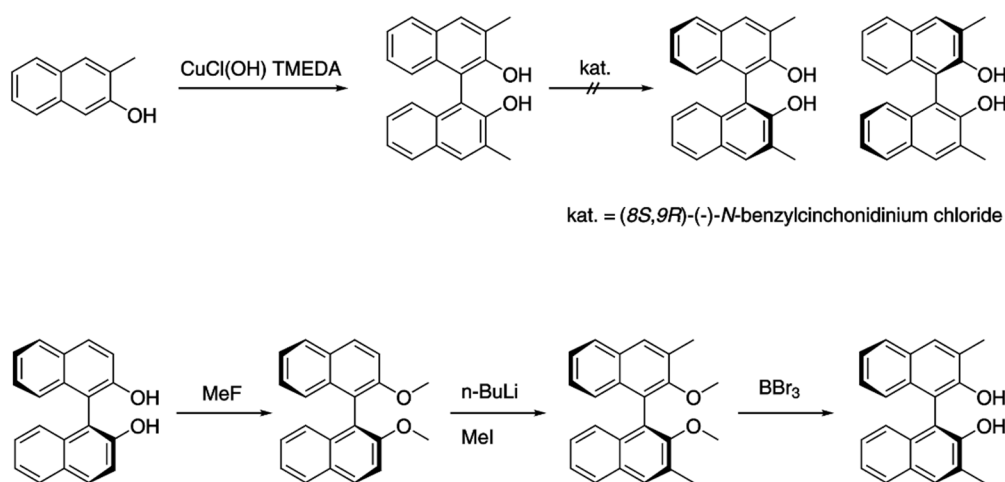


**Figure 7.** Two reaction pathways for 3,3'-methyl-substituted BINOL. Top pathway: Coupling reaction with CuCl(OH)·TMEDA yielded an enantiomeric mixture, which could not be separated. Bottom pathway: Protection of the hydroxy groups of (*S*)-BINOL and subsequent methylation in 3,3' positions. Removal of the protecting groups with BBr<sub>3</sub> yielded the substituted BINOL. However, the conversion to ligand **5** yielded no product.

For ligand **6** a one-pot synthesis pathway was used starting from (*R*)-1-(naphthalen-2-yl)ethan-1-amine and 1-(naphthalen-2-yl)ethan-1-one in ethylacetate (Figure 8, top pathway).<sup>[23]</sup> Addition of either  $\text{Ti}(\text{O}^i\text{Pr})_4$  and an appropriate  $\text{H}_2$  source (ambient pressure, autoclave or Hantzsch ester) or  $\text{HSiCl}_3$ <sup>[24]</sup> yielded no product.

Therefore, another pathway was used starting from the same amine and ketone stirring the mixture together with  $\text{NaBH}(\text{OAc})_3$  for several days at room temperature (see Figure 8, bottom pathway).<sup>[25]</sup> After separating the diastereomer (*R,S*)-amine, the hydrochloride adduct of the (*R,R*)-amine was isolated with 20% yield. The adduct was then converted with biphenyl-2,2'-diol to give ligand **6** in 50% yield.

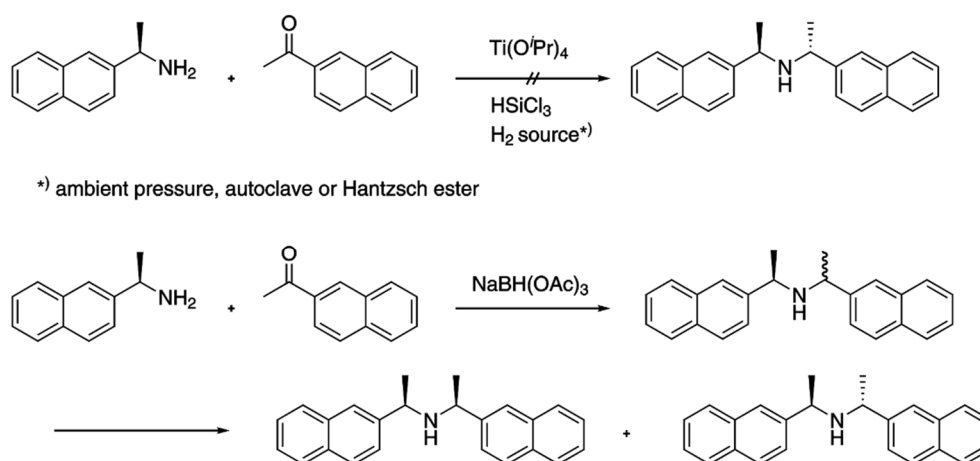


**Figure 8.** Two pathways for the synthesis of (*R*)-bis((*R*)-1-(naphthalen-2-yl)ethyl)amine. Top pathway: One-pot synthesis starting from the amine and ketone with  $\text{Ti}(\text{O}^i\text{Pr})_4$  and an adequate  $\text{H}_2$  source (ambient pressure, autoclave or Hantzsch ester) or  $\text{HSiCl}_3$ . However, this pathway yielded no product. Bottom pathway: Reaction of the amine and ketone with  $\text{NaBH}(\text{OAc})_3$  yielded an enantiomeric 2:1 mixture of diastereomers. After crystallization, the (*R,R*)-amine was isolated as a hydrochloride salt in 20% yield.

### 7.3.2 Theoretical Calculations and Asymmetric Phosphoramidite Ligands

However, theoretical calculations on the structures of the heterocomplexes for the unsubstituted model system revealed a conformational change exclusively of one of the *cis*-heterocomplexes, i.e.  $\text{PdA}^*\text{BCl}_2$  (see Figure 9). Previously the determination of its structure was done by specific NOE pattern and chemical shift dispersion analysis, which is very similar in both cases of double or triple stacking. However, the stereoelectronic and electrostatic contributions cannot be neglected in this case as  $e(\mathbf{A}/\mathbf{B}) \neq e(\mathbf{A}^*/\mathbf{B})$ . Therefore, the difference of the free energies of both equilibria  $\Delta\Delta G^0$  no longer reflects exclusively the dispersive interactions. Thus, the principle of the supramolecular balance is not applicable for the previously described model system as this was one of its basic requirements.

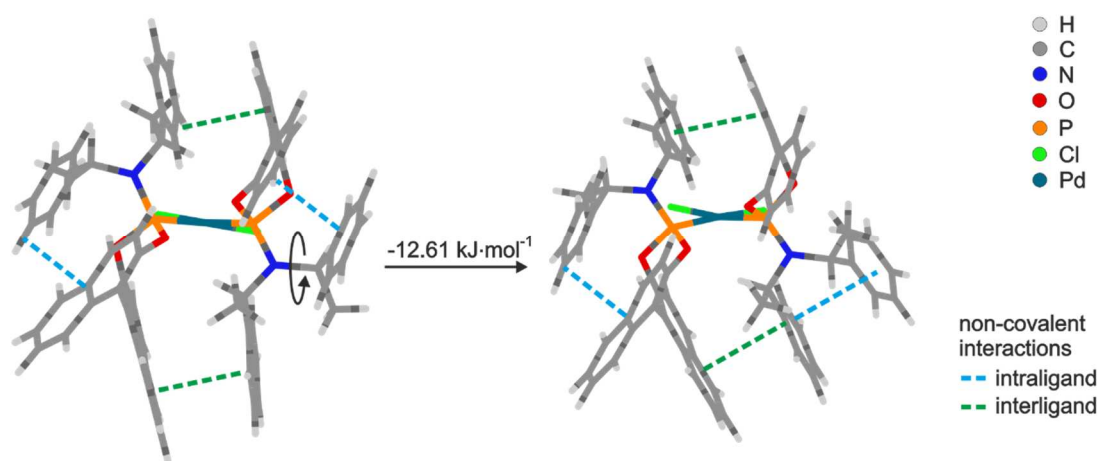


**Figure 9.** Lowest energy structures for *cis*-Pd(1)(2\*)Cl<sub>2</sub> accessible by rotation about the C-N  $\sigma$ -bond. The conformer with two single intra- and interligand interactions (left) is energetically less favorable (by 12.61 kJmol<sup>-1</sup>) than the conformer with a triple stacking between one phenylethyl surface with the other phenyl-methyl-methine surface of the same ligand (2\*) and the BINOL backbone of the other ligand (1).

Another approach had to be used to ensure the preservation of same conformations for both heterocomplexes. The phosphoramidite ligands **A** and **A\*** must be modified in a way that this rotation can be neglected. Therefore, asymmetric phosphoramidite ligands were chosen to keep the interligand interaction with the BINOL backbone fixed in the heterocomplex and remove the intraligand interaction. The asymmetric phosphoramidite ligands **7-10** were chosen for synthesis, as they potentially fulfill these requirements and vary in their dispersion interaction donors (Figure 10).

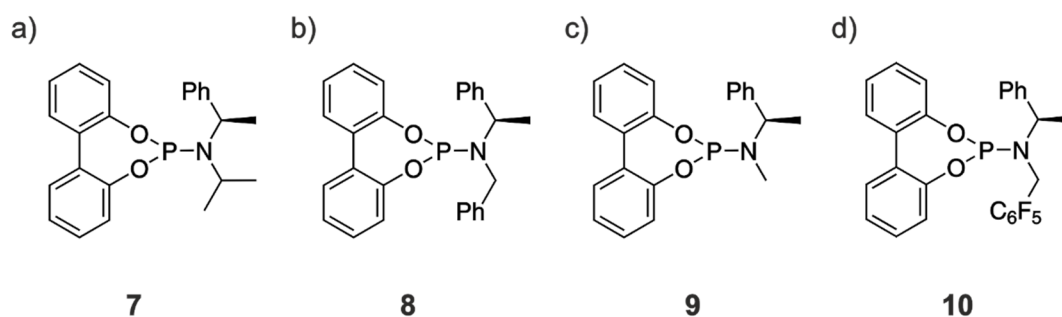


**Figure 10.** Asymmetric phosphoramidite ligands anchoring one part of the amine side chain in both heterocomplexes. a) isopropyl (**7**), b) benzyl (**8**), c) methyl (**9**), and d) perfluorobenzyl (**10**) functionalization.

The ligands **7**, **8** and **10** were prepared by the general method,<sup>[19]</sup> i.e. the synthesis of the respective secondary amine starting from (*R*)-1-(phenyl)ethan-1-amine with the respective carbonyl compound, namely acetone for **7**, benzaldehyde for **8**, and perfluorinated benzaldehyde for **10** (see Figure 11). The mixtures were stirred together



with  $\text{NaBH}(\text{OAc})_3$  at ambient temperature for several days. After workup and purification, the amines were coupled with biphenyl-2,2'-diol to give the ligands **7**, **8** and **10**.

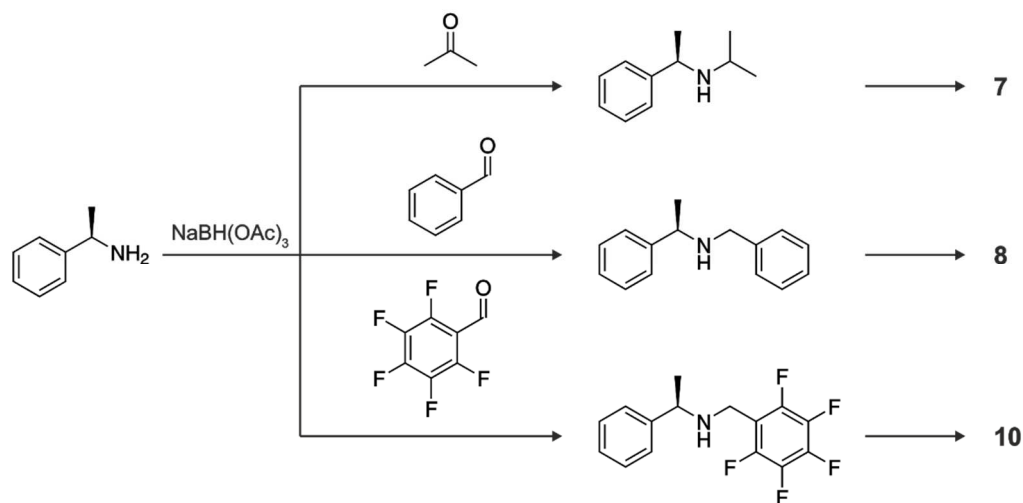


**Figure 11.** Reaction scheme for the ligands **7**, **8** and **10** starting from (*R*)-1-phenylethan-1-amine with  $\text{NaBH}(\text{OAc})_3$  and the respective ketone (acetone, benzaldehyde and pentafluorobenzaldehyde). The resulting secondary amines were reacted subsequently with biphenyl-2,2'-diol and  $\text{PCl}_3$  to yield the ligands **7**, **8** and **10**.

For ligand **9**, a similar approach was used (see Figure 12): The same amine (*R*)-1-phenylethan-1-amine was condensed with ethyl formate to the corresponding amide. Subsequently, the amide was reduced with  $\text{LiAlH}_4$  to the secondary amine (*R*)-*N*-methyl-1-phenylethan-1-amine. Further conversion with biphenyl-2,2'-diol yielded ligand **9**.

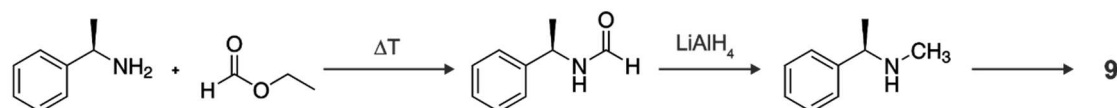


**Figure 12.** Reaction pathway for the synthesis of ligand **9**. Formation of the amide via reaction of (*R*)-1-phenylethan-1-amine with ethyl formate. Subsequent reduction with  $\text{LiAlH}_4$  yielded (*R*)-*N*-methyl-1-phenylethan-1-amine. Conversion with biphenyl-2,2'-diol yielded ligand **9**.

### 7.3.3 Assignment Strategy for Phosphoramidite Ligands

The assignment of the phosphoramidite ligands in the heterocomplexes turned out to be rather challenging, because of superposition of the aromatic resonances. In the worst situation, a total of six palladium complexes can be present in a single sample of one heterocomplex: the *cis*- and *trans*-configured homocomplexes (*cis*-PdL<sub>2</sub>Cl<sub>2</sub>, *trans*-PdL<sub>2</sub>Cl<sub>2</sub> with L = A or B) and heterocomplex (*cis*-PdLL'Cl<sub>2</sub>, *trans*-PdLL'Cl<sub>2</sub> with L = A and L' = B). Therefore, the process for a full assignment will be addressed in the following. For many complexes a full assignment was not possible unambiguously. Exemplarily for *cis*-Pd(1)(7)Cl<sub>2</sub> the general idea for the assignment will be discussed in the following (for the complete assignment see the Supporting Information). For the characterization of the phosphoramidite ligands in each of the heterocomplexes, standard 1D and 2D <sup>1</sup>H, <sup>13</sup>C and <sup>31</sup>P NMR experiments were performed. First, the distinction of *trans*- and *cis*-complexes was determined by their characteristic coupling constants in the <sup>31</sup>P spectra (<sup>2</sup>J<sub>PP</sub>(*trans*) ≈ 1000 Hz; <sup>2</sup>J<sub>PP</sub>(*cis*) ≈ 100 Hz) and by direct correlation using <sup>31</sup>P<sup>31</sup>P COSY experiments (see Figure 13).

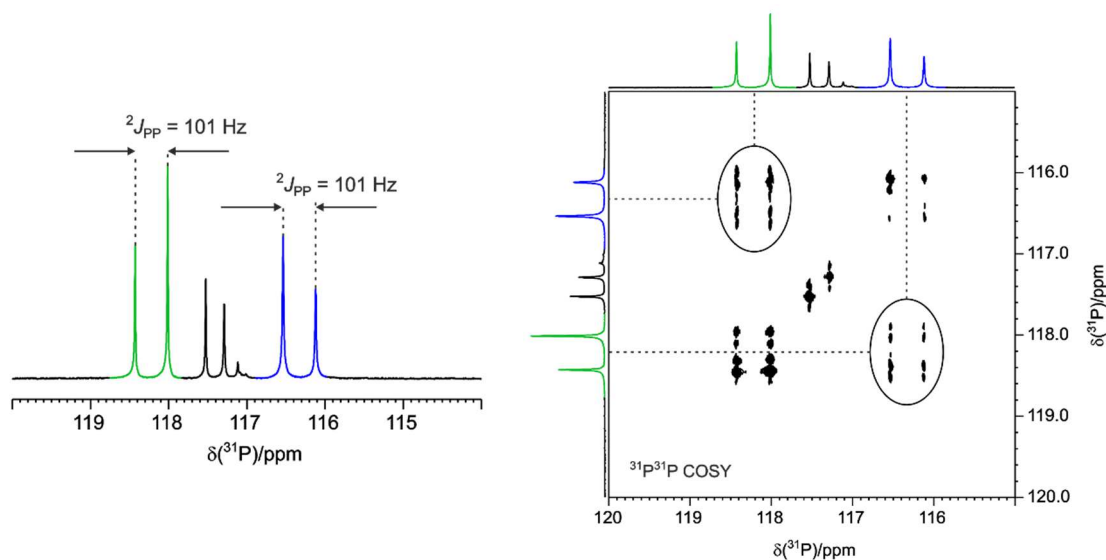


**Figure 13.** <sup>1</sup>H<sup>31</sup>P spectra of *cis*-Pd(7)(1)Cl<sub>2</sub> in dichloromethane-d<sub>2</sub> (left) with characteristic <sup>2</sup>J<sub>PP</sub> = 101 Hz coupling constant for *cis*-complexes. <sup>31</sup>P<sup>31</sup>P COSY experiment for direct correlation of phosphorus atoms in the *cis*-complex. The <sup>31</sup>P signal of ligand 1 is marked in green, that of ligand 7 is marked in blue.

In addition, interligand interactions in the *cis*-complexes become apparent by the signal dispersion and the chemical shift anisotropy in the <sup>1</sup>H spectra (see Figure 14). A denser signal dispersion of the aromatic <sup>1</sup>H signals in the *trans*-complexes implies similar aromatic protons, i.e. none or only little dispersive interactions to other ligands. On the other hand, a larger signal dispersion for the *cis*-complexes suggests many different

chemical environments for the aromatic protons, i.e. dispersive interligand interactions to the close-by ligand in *cis*-conformation.

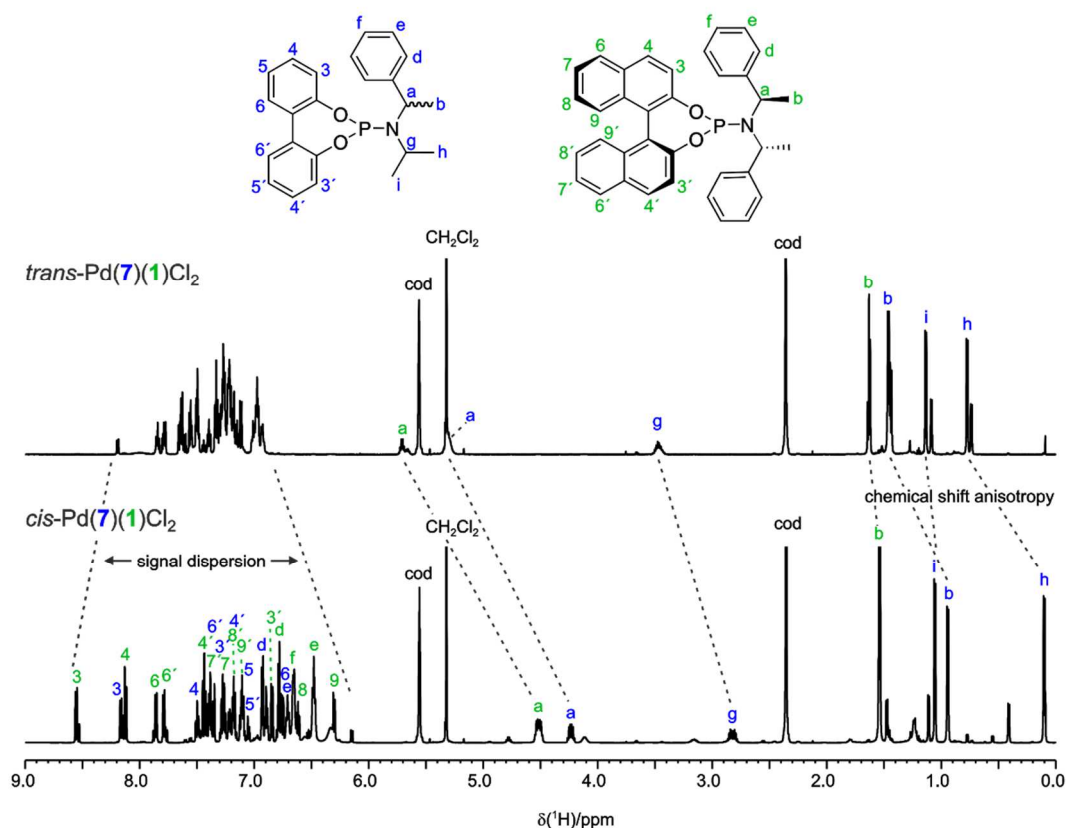


**Figure 14.**  $^1\text{H}$  spectra of *trans*-Pd(7)(1)Cl<sub>2</sub> and *cis*-Pd(7)(1)Cl<sub>2</sub> in dichloromethane-*d*<sub>2</sub> at 300 K. Upon transformation from *trans*- to *cis*-complex, the signals in the aromatic region significantly disperse owing to the formation of multiple weak, non-covalent interactions. The signals of the methyl groups of the amine sidechains are highfield shifted due to chemical shift anisotropy. The  $^1\text{H}$  resonances of ligand **1** are marked in green, the ones of ligand **7** are marked in blue.

Using  $^1\text{H}^{31}\text{P}$  HMBC experiments the phosphorus signals can be correlated to  $^1\text{H}$  signals of both the amine sidechains and the aromatic moieties (Figure 15).

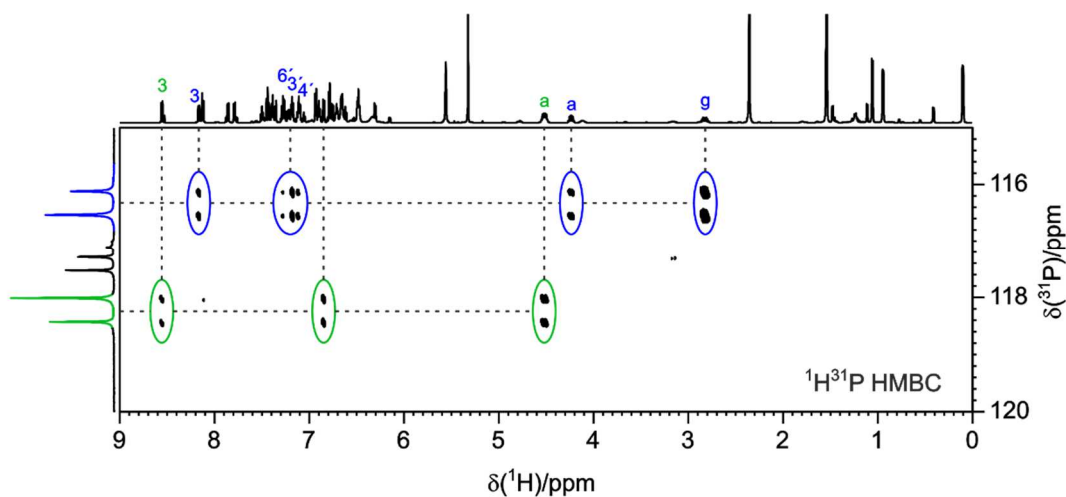


**Figure 15.**  $^1\text{H}^{31}\text{P}$  HMBC experiment of *cis*-Pd(7)(1)Cl<sub>2</sub> in dichloromethane-d<sub>2</sub> at 300 K showing the correlation of the P atoms to several  $^1\text{H}$  resonances, thus, allowing a coarse assignment to ligand 1 or 7. The P atom of ligand 1 is marked in green, that one of ligand 7 in blue.

Thereafter, the full assignment was worked out by a combination of standard  $^1\text{H}^1\text{H}$  COSY,  $^1\text{H}^{13}\text{C}$  HSQC and  $^1\text{H}^{13}\text{C}$  HMBC experiments. Especially the latter were helpful for the assignment, since the spectra are extremely crowded in the aromatic region (see Figures 16-18).

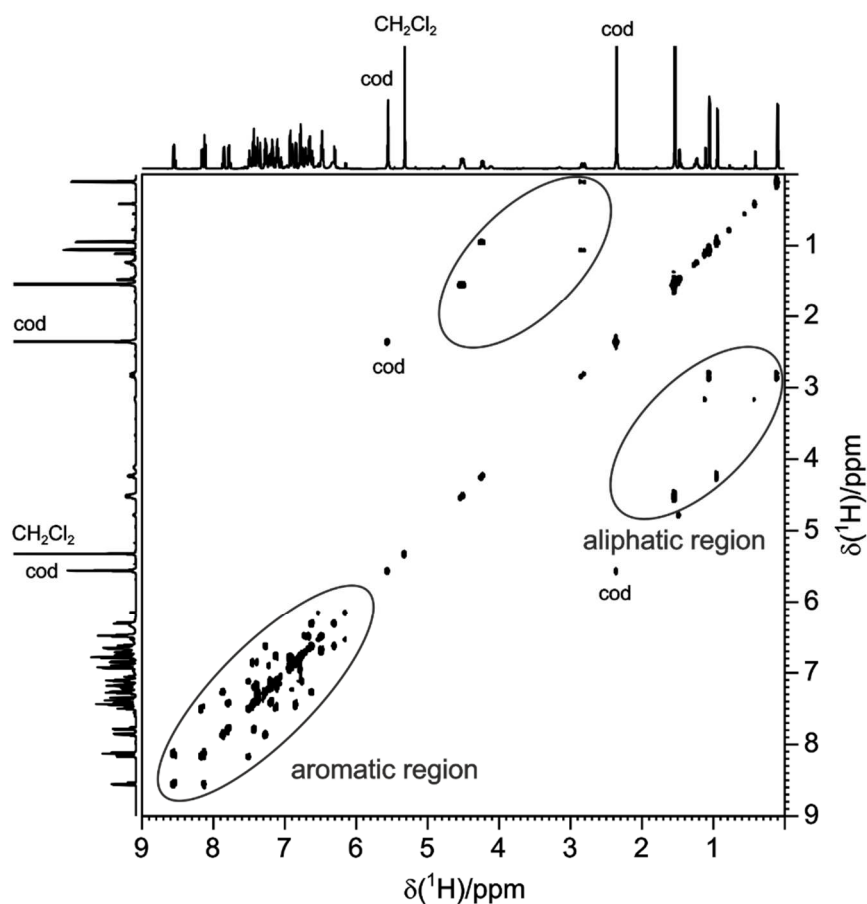


**Figure 16.**  $^1\text{H}^1\text{H}$  COSY experiment of *cis*-Pd(7)(1)Cl<sub>2</sub> in dichloromethane-d<sub>2</sub> at 300 K. The signals in the aliphatic region are well separated. However, the signals in the aromatic region are densely packed.

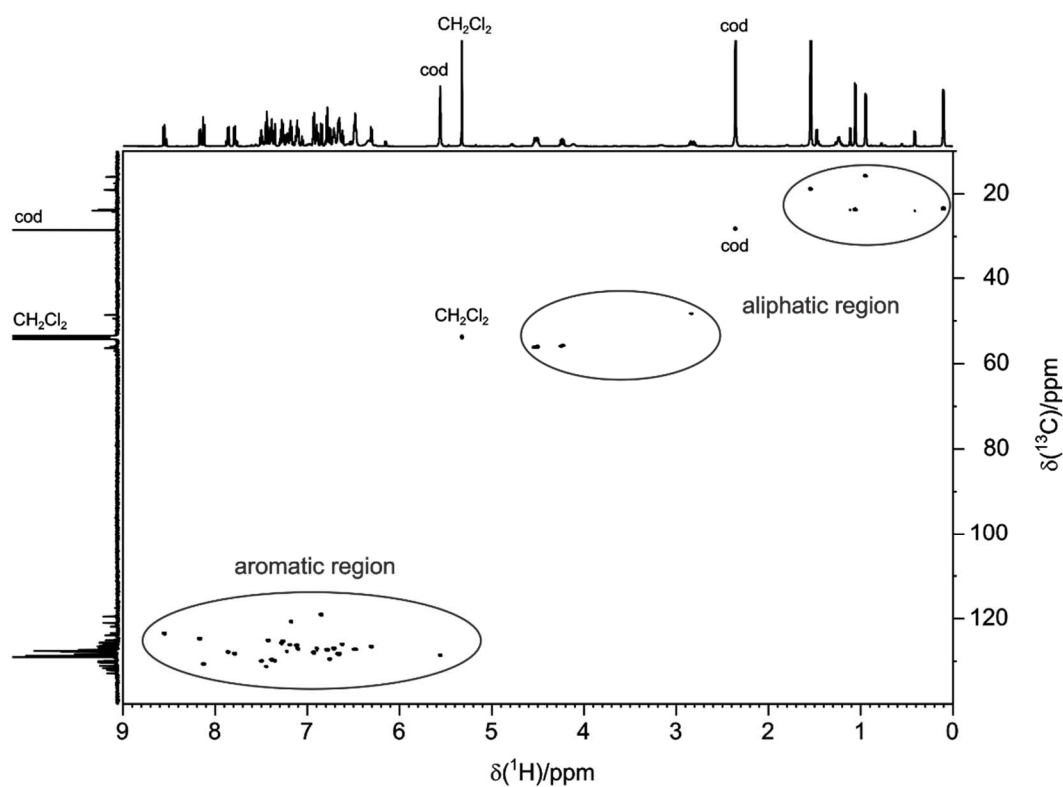


**Figure 17.**  $^1\text{H}^{13}\text{C}$  HSQC experiment of *cis*-Pd(7)(1)Cl<sub>2</sub> in dichloromethane-*d*<sub>2</sub> at 300 K. The signals in the aliphatic region are well separated. However, the signals in the aromatic region are densely packed.

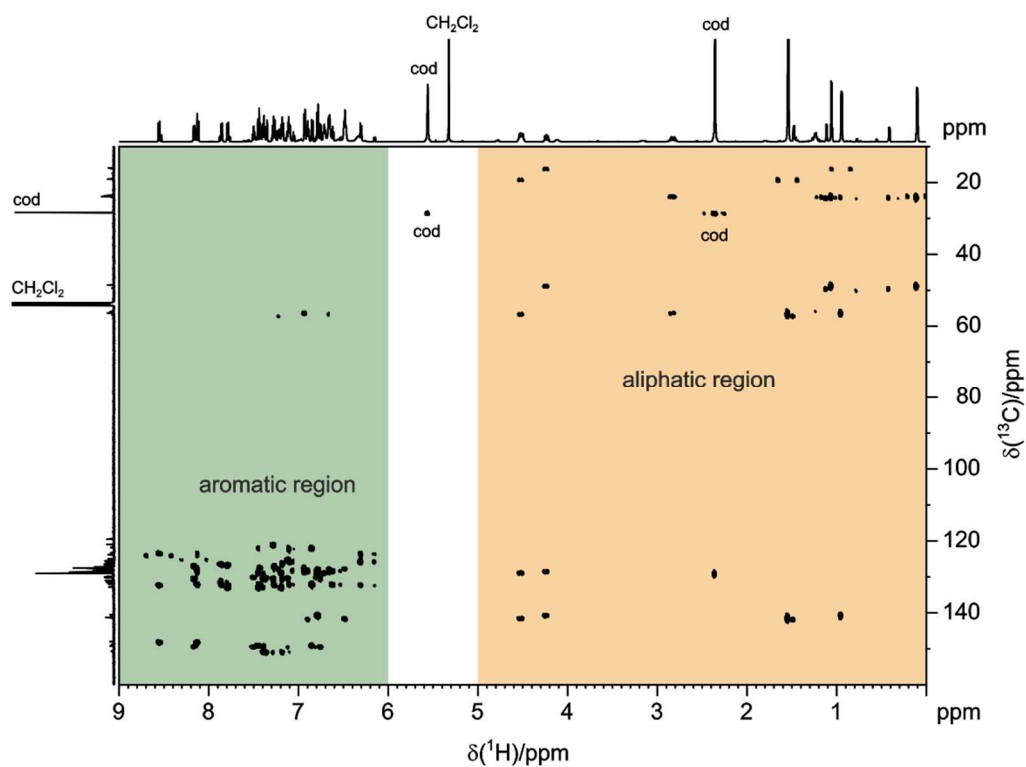
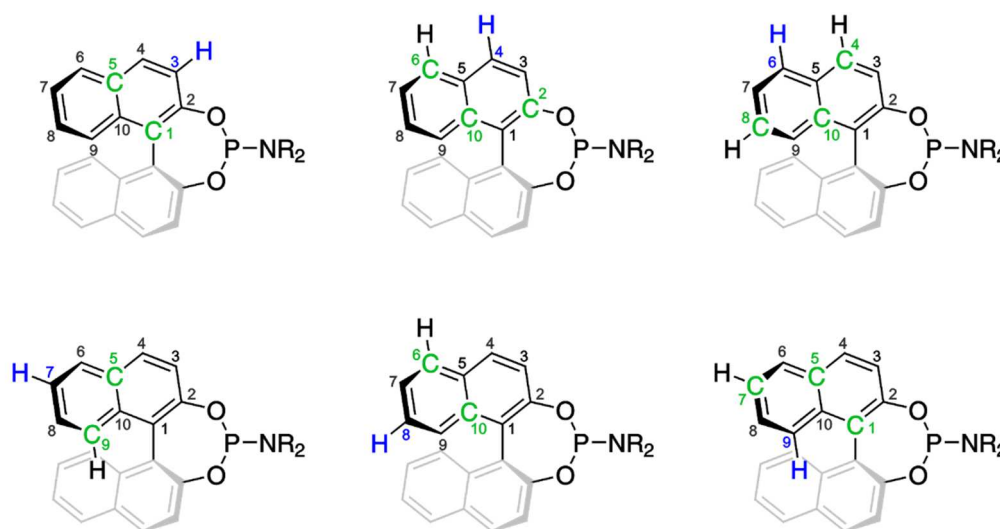


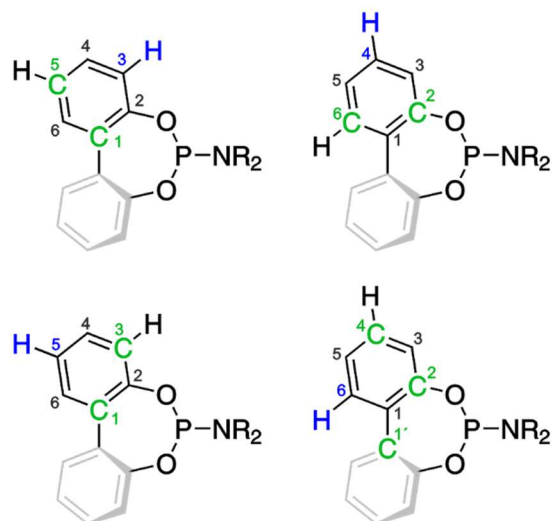
**Figure 18.**  $^1\text{H}^{13}\text{C}$  HMBC experiment of *cis*-Pd(7)(1)Cl<sub>2</sub> in dichloromethane-*d*<sub>2</sub> at 300 K. The signals in the aliphatic region are well separated. However, the signals in the aromatic region are densely packed.

Most of the aromatic signals of both the BINOL- and the biphenyl-based ligands are densely packed in a range between 6.00 to 9.00 ppm and the chemical shifts partly overlap each other. Therefore, the theoretical cross signals for each H atom of the aromatic moieties were predicted: the most intense cross signals in aromatic systems are expected to be those through magnetization transfer over the  $^3J_{\text{HC}}$  couplings, e.g. the hydrogen atom 3 marked in blue should show cross signals in the  $^1\text{H}^{13}\text{C}$  HMBC experiment to the carbon atoms 1 and 5 marked in green (see Figure 19, top-left). The theoretically predicted cross signals are summarized in Figure 19 for the BINOL-based ligand and in Figure 20 for the modified biphenyl-based ligand.



$^1\text{H}$	Expected HMBC cross signals to carbon
3	1, 5
4	2, 6, 10
6	4, 8, 10
7	5, 9
8	6, 10
9	1, 5, 7

**Figure 19.** Expected cross signals in the  $^1\text{H}^{13}\text{C}$  HMBC experiment owing to magnetization transfer over  $^3J_{\text{HC}}$  couplings in the aromatic BINOL backbone; The respective proton is marked in blue, the corresponding carbons in green.



<sup>1</sup> H	Expected HMBC cross signals to carbon
3	1, 5
4	2, 6
5	1, 3
6	2, 4, 1'

**Figure 20.** Expected cross signals in the <sup>1</sup>H<sup>13</sup>C HMBC experiment owing to magnetization transfer over <sup>3</sup>J<sub>HC</sub> couplings in the aromatic biphenyl backbone; The respective proton is marked in blue, the corresponding carbons in green.

### 7.3.4 Formation Trends for different ligand combinations

Next, the formation tendencies of the individual *cis*-heterocomplexes of ( $S_a, R_c, R_c$ )-**1** and the ligands **7-9**, respectively are addressed. Table 1 shows the ratios  $Q_L$  of the *cis*-complexes *cis*-Pd(**1**)(**L/L\***)Cl<sub>2</sub> (**L/L\*** = **7-9**) to their respective *cis*-homocomplexes, *cis*-Pd(**1**)<sub>2</sub>Cl<sub>2</sub> and *cis*-Pd(**L**)<sub>2</sub>Cl<sub>2</sub> (**L/L\*** = **7-9**):

$$Q_L = c(\textit{cis}\text{-Pd}(\mathbf{1})(\mathbf{L}/\mathbf{L}^*)\text{Cl}_2) : c(\textit{cis}\text{-Pd}(\mathbf{1})_2\text{Cl}_2) : c(\textit{cis}\text{-Pd}(\mathbf{L})_2\text{Cl}_2)$$

The amount of each complex was determined by integration of their respective <sup>31</sup>P signals and thereby the values of  $\Delta\Delta G^0$  (given in kJ·mol<sup>-1</sup>) can be derived from Eq. 1 and 2.

**Table 1.** Ratios  $Q_L$  of *cis*-homo- and *cis*-heterocomplexes for different ligand combinations.

Ligand <b>L</b>	<b>2</b>	<b>2*</b>	<b>7</b>	<b>7*</b>	<b>8</b>	<b>8*</b>	<b>9</b>	<b>9*</b>
$Q_L$ ratios	2.1:1:1.1	4.5:1:0.9	8:1:1	22:0.9:1	3.5:1:1	2:1:1	1:1:1	1.2:1:0.7
$\Delta\Delta G^0$ [kJ·mol <sup>-1</sup> ]	4.3		5.3		2.8		1.8	

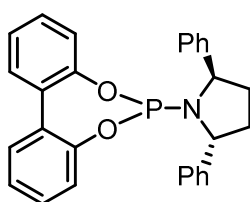
The values of  $\Delta\Delta G^0$  for ligands **7-9** and **7\*-9\*** respectively are in all cases smaller compared to the model system (**L/L\*** = **2/2\***) owing to the increased flexibility of the asymmetric ligands. Increasing isomerization rates were observed for less bulky substituents. Here, apparently the access to the CH<sub>3</sub> groups seems to play the key role, allowing for CH- $\pi$  interaction with the aromatic moiety.

The hetero dimer is in all cases the preferred species, which exhibit extensive dispersion areas owing to the formation of many weak, non-covalent interactions. This is in agreement with the application of mixed phosphoramidite ligands in asymmetric catalysis rather than two phosphoramidite ligands of the same kind.<sup>[26]</sup>



## 7.4 Outlook

The application of the supramolecular balance on the asymmetric substituted seems to be very promising in case that the conformational retention of both heterocomplexes holds true. However, by means of NMR spectroscopy it is not possible thus far to unambiguously validate their structure. Quantum chemical investigation not only complements this but rather seems to be imperative for its validation. Despite of the accuracy demonstrated by theoretical calculations, the high flexibility of the amine sidechain is a challenging aspect for both theoretical and experimental interpretation of these systems. Therefore, the introduction of a more rigid cyclic amine, e.g. ligand **11** in Figure 8, might access an even more detailed investigation.



**11**

**Figure 8.** Phosphoramidite ligand with a cyclic amine sidechain to reduce the degree of rotational freedom and thus simplifying the model system for theoretical calculations.

Additionally, an alternative model system for a supramolecular balance was proposed by our working group. Here, the intermediates of the asymmetric Brønsted acid catalysis of imines, i.e. the binary complexes type I E and type II E, form an equilibrium (see Figure 9). Again, comparing two equilibria for different substituted imine phosphoric acid complexes, yields the difference of free energy  $\Delta\Delta G^0$ . This difference is composed of the dispersive interactions between the imine and the catalyst, whereas only the dispersive interaction between the substituent and either the naphthalene-backbone or the 3/3' substituents must be accounted for.  $\Delta\Delta G^0$  then directly correlates to  $(s(A/33') - s(B/33')) + (s(B/nap) - s(A/Nap))$  with  $A = CH_3$  and  $B = CF_3$ . In case that A is a H atom and its terms can be considered zero, the  $\Delta\Delta G^0$  value can be further simplified to  $s(B/Nap) - s(B/33')$ .

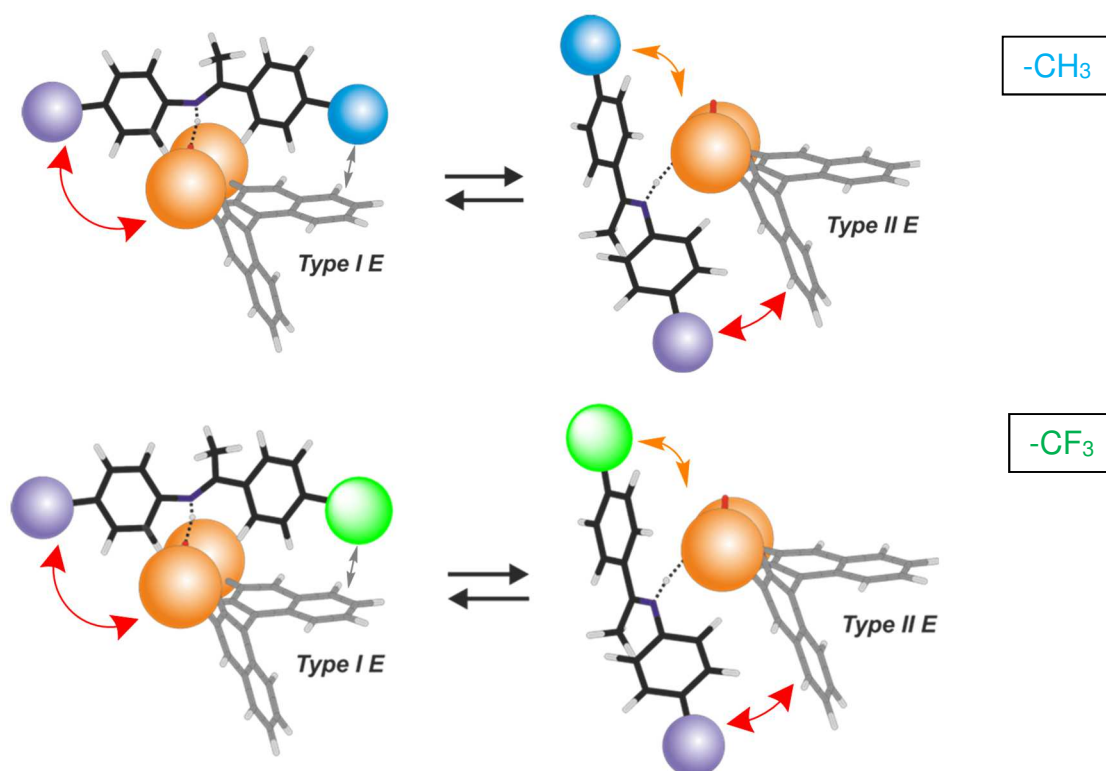


**Figure 9.** Equilibria of the binary imine phosphoric acid complexes in Type I E and Type II E for  $\text{CH}_3$  and  $\text{CF}_3$  substituted imines.  $\Delta G$  represents the population difference in each equilibrium. Their difference  $\Delta\Delta G$  reflects the dispersion interactions differences between  $\text{CH}_3$ - and  $\text{CF}_3$ -groups.

## 7.5 Conclusions

Size matters! To conclude, it was shown that despite the previous inadequate model system in which not all basic requirements were fulfilled and thus the supramolecular balance was not applicable, its general principle still holds true. For further investigations asymmetric phosphoramidite ligands seem to be the instrument of choice as they show a promising design to keep both hetero complexes in the same structural conformation, thus, making the experimental measurement of dispersive interactions possible.

Another approach was suggested introducing a rigid cyclic amine sidechain to decrease its rotational motion, thus simplifying theoretical calculations tremendously for future investigations. Furthermore, a different model system was suggested, i.e. the intermediates of the asymmetric Brønsted acid catalyzed imine reduction. Here, so far only the combined dispersive interactions are experimentally accessible, but not separable.

## 7.6 Supporting Information

### 7.6.1 Preparation of phosphoramidite ligands

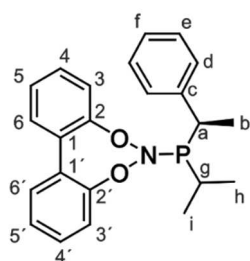
To a solution of  $\text{PCl}_3$  (2 mmol, 275 mg, 175  $\mu\text{L}$ ) in DCM (14 mL) at 0 °C,  $\text{NEt}_3$  (1.4 mL) was added and the mixture was allowed to warm up to ambient temperature. The respective amine (2 mmol) was added dropwise and the mixture was then stirred at ambient temperature for 3.5 h. Upon addition of solid biphenyl-2,2'-diol (2 mmol, 372 mg) the mixture was stirred additional 18 h at ambient temperature. The formed precipitate was filtered through Celite/silica gel and washed with DCM. The filtrate was purified by column chromatography (PE:DCM: $\text{Et}_3\text{N}$  80:20:1 to DCM:MeOH: $\text{Et}_3\text{N}$  90:10:1) to give the isolated product.

#### 7.6.1.1 Sample preparation for NMR

The samples for the NMR spectroscopic investigations were prepared by combining two equivalents of the respective phosphoramidite ligands (one equivalent each for hetero complexes) with one equivalent of  $\text{Pd}(\text{cod})\text{Cl}_2$  in  $\text{CD}_2\text{Cl}_2$  and stirring the mixture for 1 h.

#### 7.6.1.2 General remarks on NMR

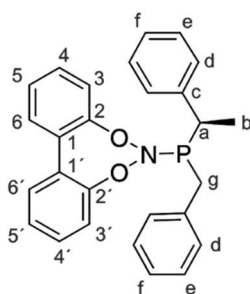
All NMR spectroscopic measurements were recorded on a Bruker Avance III 600 MHz spectrometer equipped with a 5 mm TBI-probe ( $^1\text{H}$ , X,  $^{19}\text{F}$ ) with z-gradient. The measurements were performed using a standard Bruker pulse program (zg) with 2k number of scans, TD = 65k with relaxation delay of 2 s. Data were processed with the Bruker software TOPSPIN 3.2 using the processing parameters SI = 130k, WDW = EM and LB = 0.3 Hz. The chemical shifts are reported in ppm relative to TMS.

**Pd(7)<sub>2</sub>Cl<sub>2</sub>**

**Table S1.** Assignment of *trans*-Pd(7)<sub>2</sub>Cl<sub>2</sub> and *cis*-Pd(7)<sub>2</sub>Cl<sub>2</sub><sup>1)</sup>. Values of the <sup>1</sup>H and <sup>13</sup>C chemical shifts are given in ppm.

<i>trans</i> -Pd(7) <sub>2</sub> Cl <sub>2</sub>			<i>cis</i> -Pd(7) <sub>2</sub> Cl <sub>2</sub>		
$\delta(^{31}\text{P}) = 117.7 \text{ ppm}$			$\delta(^{31}\text{P}) = \text{N/A}$		
	$\delta(^1\text{H})$	$\delta(^{13}\text{C})$		$\delta(^1\text{H})$	$\delta(^{13}\text{C})$
1	-	130.1	1	-	N/A
2	-	149.5	2	-	N/A
3	7.65	123.6	3	N/A	N/A
4	7.50/7.33	130.0/128.2	4	N/A	N/A
5	7.29	126.1	5	N/A	N/A
6	7.50/7.33	130.0/128.2	6	N/A	N/A
1'	-	129.8	1'	-	N/A
2'	-	150.0	2'	-	N/A
3'			3'	N/A	N/A
4'	7.26 – 7.30,	129.6, 125.8, 122.7, 130.0	4'	N/A	N/A
5'	7.50		5'	N/A	N/A
6'			6'	N/A	N/A
a	5.71	55.6	a	N/A	N/A
b	1.62	18.9	b	N/A	N/A
c	-	141.8	c	-	N/A
d	7.63	128.5	d	N/A	N/A
e	7.34	129.7	e	N/A	N/A
f	7.26	127.5	f	N/A	N/A
g	3.48	48.7	g	N/A	N/A
h	0.77	24.1	h	N/A	N/A
i	1.13	24.3	i	N/A	N/A

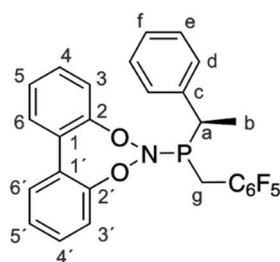
<sup>1)</sup> Exclusively the *trans*-complex was observed in the spectra.

**Pd(**8**)<sub>2</sub>Cl<sub>2</sub>**

**Table S2.** Assignment of *trans*-Pd(**8**)<sub>2</sub>Cl<sub>2</sub><sup>2)</sup> and *cis*-Pd(**8**)<sub>2</sub>Cl<sub>2</sub>. Values of the <sup>1</sup>H and <sup>13</sup>C chemical shifts are given in ppm.

<i>trans</i> -Pd( <b>8</b> ) <sub>2</sub> Cl <sub>2</sub>			<i>cis</i> -Pd( <b>8</b> ) <sub>2</sub> Cl <sub>2</sub>		
$\delta(^{31}\text{P}) = 113.7 \text{ ppm}$			$\delta(^{31}\text{P}) = 115.8 \text{ ppm}$		
	$\delta(^1\text{H})$	$\delta(^{13}\text{C})$		$\delta(^1\text{H})$	$\delta(^{13}\text{C})$
1	-	-	1	-	-
2	-	N/A	2	-	148.8
3	N/A	N/A	3	8.13	124.3
4	N/A	N/A	4	7.40	130.3
5	N/A	N/A	5	6.98	126.3
6	N/A	N/A	6	6.81	129.9
1'	-	N/A	1'	-	-
2'	-	N/A	2'	-	151.2
3'	N/A	N/A	3'	-	-
4'	N/A	N/A	4'	7.42, 7.16,	126.3, 120.7,
5'	N/A	N/A	5'	7.09, 7.35	127.4, 126.6
6'	N/A	N/A	6'	-	-
a	N/A	N/A	a	4.97	57.6
b	N/A	N/A	b	1.07	18.9
c	-	N/A	c	-	139.5
d	N/A	N/A	d	7.18	128.3
e	N/A	N/A	e	7.08	127.2
f	N/A	N/A	f	6.97	127.9
g	N/A	N/A	g	3.31/4.20	47.9

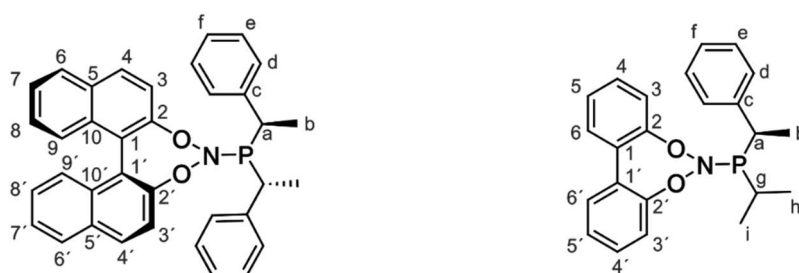
<sup>2)</sup> Exclusively the *cis*-complex was observed in the spectra.

**Pd(10)<sub>2</sub>Cl<sub>2</sub>**

**Table S4.** Assignment of *trans*-Pd(10)<sub>2</sub>Cl<sub>2</sub><sup>3)</sup> and *cis*-Pd(10)<sub>2</sub>Cl<sub>2</sub>. Values of the <sup>1</sup>H and <sup>13</sup>C chemical shifts are given in ppm.

<i>trans</i> -Pd(10) <sub>2</sub> Cl <sub>2</sub>			<i>cis</i> -Pd(10) <sub>2</sub> Cl <sub>2</sub>		
$\delta(^{31}\text{P}) = \text{N/A}$			$\delta(^{31}\text{P}) = 115.8 \text{ ppm}$		
	$\delta(^1\text{H})$	$\delta(^{13}\text{C})$		$\delta(^1\text{H})$	$\delta(^{13}\text{C})$
1	-	N/A	1	-	N/A
2	-	N/A	2	N/A	149.4
3	N/A	N/A	3	7.67	123.8
4	N/A	N/A	4	6.94	130.0
5	N/A	N/A	5	7.41	129.8
6	N/A	N/A	6	N/A	N/A
1'	-	N/A	1'	N/A	N/A
2'	-	N/A	2'	N/A	N/A
3'	N/A	N/A	3'	N/A	N/A
4'	N/A	N/A	4'	N/A	N/A
5'	N/A	N/A	5'	N/A	N/A
6'	N/A	N/A	6'	N/A	N/A
a	N/A	N/A	a	6.03	55.5
b	N/A	N/A	b	1.72	16.6
c	N/A	N/A	c	-	139.6
d	N/A	N/A	d	7.36	126.7
e	N/A	N/A	e	7.07	127.9
f	N/A	N/A	f	-	-
g	N/A	N/A	g	4.04	35.2
	N/A			4.21	
ortho	$\delta(^{19}\text{F}) = \text{N/A}$		ortho	$\delta(^{19}\text{F}) = -139.7 \text{ ppm}$	
meta	$\delta(^{19}\text{F}) = \text{N/A}$		meta	$\delta(^{19}\text{F}) = -164.1 \text{ ppm}$	
para	$\delta(^{19}\text{F}) = \text{N/A}$		para	$\delta(^{19}\text{F}) = -156.4 \text{ ppm}$	

<sup>3)</sup> Exclusively the *cis*-complex was observed in the spectra.

**cis-Pd(1)(7)Cl<sub>2</sub>****Table S1.** Assignment of *cis*-Pd(1)(7)<sub>2</sub>Cl<sub>2</sub>. Values of the <sup>1</sup>H and <sup>13</sup>C chemical shifts are given in ppm.

Ligand 1			Ligand 7		
$\delta(^{31}\text{P}) = 118.2 \text{ ppm}$			$\delta(^{31}\text{P}) = 116.3 \text{ ppm}$		
	$\delta(^1\text{H})$	$\delta(^{13}\text{C})$		$\delta(^1\text{H})$	$\delta(^{13}\text{C})$
1	-	123.4	1	-	130.8
2	-	148.0	2	-	149.7
3	8.56	123.9	3	8.17	125.2
4	8.12	131.1	4	7.50	130.5
5	-	131.9	5	7.12	126.9
6	7.85	128.2	6	6.76	130.1
7	7.26	125.7			
8	6.62	126.3			
9	6.30	126.9			
10	-	131.5			
1'	-	121.9	1'	-	122.0
2'	-	148.8	2'	-	151.2
3'	6.85	119.5	3'	7.28	126.3
4'	7.44	131.6	4'	7.18	126.7
5'	-	131.9	5'	7.09	121.1
6'	7.79	128.6	6'	7.39	130.3
7'	7.42	125.5			
8'	7.17	126.5			
9'	7.10	127.3			
10'	-	132.9			
a	4.52	56.4	a	4.24	56.3
b	1.54	19.0	b	0.95	16.2
c	-	141.3	c	-	141.0

## 7 NMR investigations on Phosphoramidite Palladium Complexes and the Supramolecular Balance

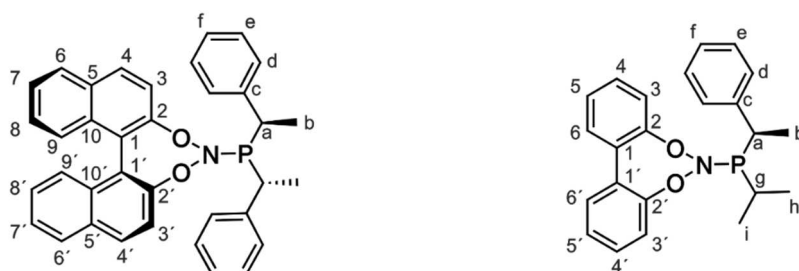
---

d	6.71	127.4	d	6.93	128.6
e	6.48	127.5	e	6.78	127.9
f	6.66	128.6	f	N/A	N/A
			g	2.83	48.8
			h	0.10	23.9
			i	1.06	24.0

---

N/A: These signals could not be assigned unambiguously.



**cis-Pd(1)(7\*)Cl<sub>2</sub>****Table S1.** Assignment of *cis*-Pd(1)(7\*)<sub>2</sub>Cl<sub>2</sub>. Values of the <sup>1</sup>H and <sup>13</sup>C chemical shifts are given in ppm.

Ligand 1			Ligand 7*		
$\delta(^{31}\text{P}) = 119.2 \text{ ppm}$			$\delta(^{31}\text{P}) = 115.7 \text{ ppm}$		
	$\delta(^1\text{H})$	$\delta(^{13}\text{C})$		$\delta(^1\text{H})$	$\delta(^{13}\text{C})$
1	-	123.1	1	-	130.2
2	-	148.1	2	-	149.1
3	8.53	123.6	3	8.19	125.0
4	7.77	128.6	4	7.49	N/A
5	N/A	132.4	5	N/A	N/A
6	N/A	129.2	6	N/A	N/A
7	N/A	N/A			
8	N/A	N/A			
9	N/A	N/A			
10	-	N/A			
1'	-	N/A	1'	-	N/A
2'	-	N/A	2'	-	N/A
3'	N/A	N/A	3'	N/A	N/A
4'	N/A	N/A	4'	N/A	N/A
5'	N/A	N/A	5'	N/A	N/A
6'	N/A	N/A	6'	N/A	N/A
7'	N/A	N/A			
8'	N/A	N/A			
9'	N/A	N/A			
10'	-	N/A			
a	4.59	56.3	a	4.40	55.2
b	1.53	19.2	b	0.85	18.4
c	-	141.3	c	-	138.9
d	6.67	128.7	d	7.04	129.0

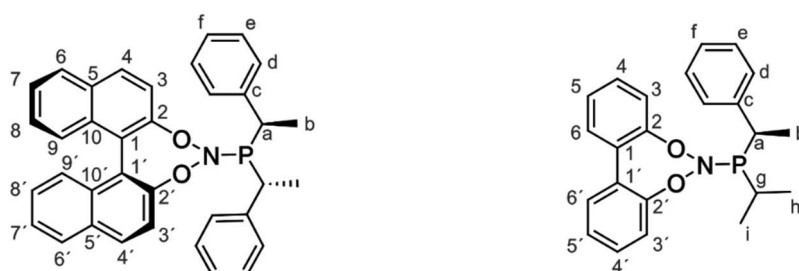
## 7 NMR investigations on Phosphoramidite Palladium Complexes and the Supramolecular Balance

---

e	6.50	128.5	e	N/A	N/A
f	6.71	127.3	f	N/A	N/A
			g	2.80	49.3
			h	0.42	24.2
			i	0.62	23.0

---

N/A: These signals could not be assigned unambiguously.

**cis-Pd(1)(9)Cl<sub>2</sub>****Table S1.** Assignment of *cis*-Pd(1)(9)<sub>2</sub>Cl<sub>2</sub>. Values of the <sup>1</sup>H and <sup>13</sup>C chemical shifts are given in ppm.

Ligand 1			Ligand 9		
$\delta(^{31}\text{P}) = 118.3 \text{ ppm}$			$\delta(^{31}\text{P}) = 116.4 \text{ ppm}$		
	$\delta(^1\text{H})$	$\delta(^{13}\text{C})$		$\delta(^1\text{H})$	$\delta(^{13}\text{C})$
1	-	N/A	1	-	N/A
2	-	148.1	2	-	149.3
3	8.56	123.7	3	8.17	124.8
4	8.12	130.9	4	7.50	130.1
5	N/A	N/A	5	7.12	126.5
6	N/A	N/A	6	6.75	129.7
7	N/A	N/A			
8	N/A	N/A			
9	N/A	N/A			
10	-	N/A			
1'	-	N/A	1'	-	N/A
2'	-	N/A	2'	-	150.8
3'	N/A	N/A	3'	7.28	125.9
4'	N/A	N/A	4'	7.18	126.3
5'	N/A	N/A	5'	7.09	120.7
6'	N/A	N/A	6'	7.39	129.9
7'	N/A	N/A			
8'	N/A	N/A			
9'	N/A	N/A			
10'	-	N/A			
a	4.52	56.2	a	4.23	55.9
b	1.54	18.9	b	0.94	15.8
c	-	141.5	c	-	140.6

## 7 NMR investigations on Phosphoramidite Palladium Complexes and the Supramolecular Balance

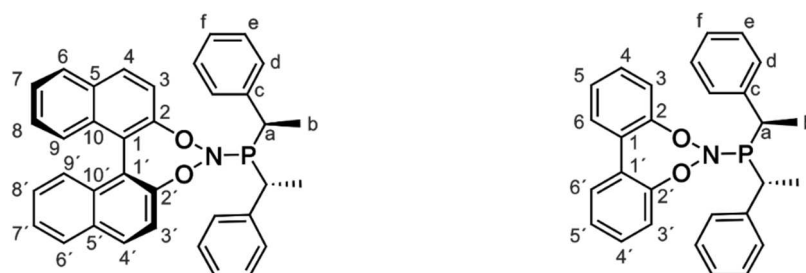
---

d	7.80	128.3	d	6.93	128.2
e	N/A	N/A	e	6.78	127.5
f	N/A	N/A	f	N/A	N/A
			g	2.83	48.4
			h	0.10	23.5
			i	1.06	23.6

---

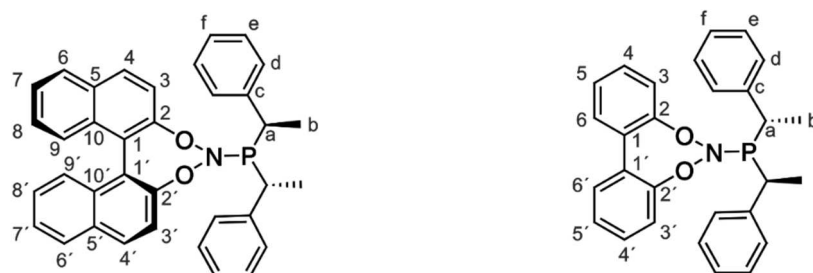
N/A: These signals could not be assigned unambiguously.

## 7.6.2 Theoretical Calculations

*cis*-Pd(1)(2)Cl<sub>2</sub>

**Table S1.** Comparison of experimental <sup>1</sup>H chemical shifts of each ligand **A** and **B** with calculated <sup>1</sup>H chemical shifts derived from double (2) stacked conformations. Values of the <sup>1</sup>H chemical shifts are given in ppm.

Ligand <b>B</b> ( <i>S<sub>a</sub>, R<sub>c</sub>, R<sub>c</sub></i> )- <b>1</b>				Ligand <b>A</b> ( <i>R<sub>c</sub>, R<sub>c</sub></i> )- <b>2</b>			
	$\delta_{\text{exp}}$	$\delta_{\text{calcd}}$ (2)		$\delta_{\text{exp}}$	$\delta_{\text{calcd}}$ (2)		
3	8.55	8.93	-	3	8.23	8.51	-
4	8.12	8.36	-	4	7.51	7.67	-
5	7.85	8.12	-	5	7.02	7.21	-
6	7.24	7.57	-	6	7.06	6.06	-
7	6.52	6.68	-				
8	6.18	6.11	-				
3'	6.71	6.56	-	3'	6.47	6.10	-
4'	7.39	7.47	-	4'	6.92	6.96	-
5'	7.77	8.07	-	5'	7.11	7.12	-
6'	7.41	7.72	-	6'	6.63	7.19	-
7'	7.17	7.48	-				
8'	7.07	7.43	-				
a	4.42	5.61	-	a	4.11	5.20	-
b	1.54	1.54	-	b	1.26	1.20	-
d	6.56	6.66	-	d	6.39	6.27	-
e	6.40	6.28	-	e	6.57	6.60	-
f	6.66	6.92	-	f	6.77	6.95	-

**cis-Pd(1)(2\*)Cl<sub>2</sub>**

**Table S1.** Comparison of experimental <sup>1</sup>H chemical shifts of each ligand **A\*** and **B** with calculated <sup>1</sup>H chemical shifts derived from triple (3) and double stacked (2) conformations. Values of the <sup>1</sup>H chemical shifts are given in ppm.

Ligand <b>B</b> ( <i>S<sub>a</sub>, R<sub>c</sub>, R<sub>c</sub></i> )- <b>1</b>				Ligand <b>A*</b> ( <i>S<sub>c</sub>, S<sub>c</sub></i> )- <b>2*</b>			
	$\bar{\delta}_{\text{exp}}$	$\bar{\delta}_{\text{calcd}}$ (3)	$\bar{\delta}_{\text{calcd}}$ (2)		$\bar{\delta}_{\text{exp}}$	$\bar{\delta}_{\text{calcd}}$ (3)	$\bar{\delta}_{\text{calcd}}$ (2)
3	6.88	6.85	6.70	3	8.01	8.78	8.76
4	7.42	7.50	7.41	4	7.45	7.81	7.77
5	7.78	8.06	7.96	5	7.12	7.42	7.40
7	7.45	7.78	7.74	6	6.82	6.58	6.47
8	7.24	7.54	7.50				
9	7.24	7.48	7.35				
3'	8.52	8.94	8.72	3'	7.16	7.50	6.43
4'	7.77	7.74	7.81	4'	7.52	7.73	7.07
6'	7.32	7.19	7.64	5'	7.39	7.52	7.17
7'	7.11	7.39	7.62	6'	6.82	7.50	7.28
8'	7.05	7.38	7.49				
9'	7.05	7.31	7.38				
a	4.58	5.77	5.62	a	4.43	5.14	6.11
b	1.52	1.55	1.45	b	0.78	0.72	0.76
d	6.66	6.77	6.56	d	6.76	6.79	7.26
e	6.49	6.45	6.30	e	6.89	6.90	6.95
f	6.70	7.03	6.89	f	7.01	7.14	7.27

## 7.7 References

- [1] E. Hartmann, R. M. Gschwind, *Angew. Chem. Int. Ed.* **2013**, 52, 2350-2354.
- [2] I. Yang, C. Adams, G. S. Nichol, S. L. Cockroft, *Nature* **2013**, 5, 1006-1010; C. A. Hunter, *Angew. Chem. Int. Ed.* **2004**, 43, 5310–5324.
- [3] S. Grimme, R. Huehnerbein, S. Ehrlich, *ChemPhysChem.* **2011**, 12, 1258-1261.
- [4] a) P. Schreiner, L. Chernish, P. Gunchenko, E. Tikhonchuk, H. Hausmann, M. Serafin, S. Schlecht, J. Dahl, R. Carlson, A. Fokin, *Nature* **2011**, 477, 308-312. b) A. A. Fokin, D. Gerbig, P. R. Schreiner, *J. Am. Chem. Soc.* **2011**, 133, 20036-20039.
- [5] S. E. Wheeler, *J. Am. Chem. Soc.* **2011**, 133, 10262-10274.
- [6] C. A. Hunter, *Angew. Chem. Int. Ed.* **2004**, 43,5310-5324.
- [7] L. Goerigk, S. Grimme, *Phys. Chem. Chem. Phys.* **2011**, 13, 6670-6688.
- [8] M. Lewis, C. Bagwill, L. K. E. Hardebeck, S. Wireduaah, *Comput. Struct. Biotechnol. J.* **2012** Mar 6, 1:e201204004. doi: 10.5936/csbj.201204004.
- [9] D. Chandler, *Nature* **2005**, 437, 640–647.
- [10] R. Cabot, C. A. Hunter, *Chem. Soc. Rev.* **2012**, 41, 3485–3492; C. A. Hunter, *Chem. Sci.* **2013**, 4, 834-848.
- [11] B. Bhayana, C. S. Wilcox, *Angew. Chem. Int. Ed.* **2007**, 46, 6833-6836; S. Paliwal, S. Geib, C. S. Wilcox, *J. Am. Chem. Soc.* **1994**, 116, 4497; E.-I. Kim, S. Paliwal, C. S. Wilcox, *J. Am. Chem. Soc.* **1998**, 120, 11192.
- [12] F. R. Fischer, W. B. Schweizer, F. Diederich, *Angew. Chem. Int. Ed.* **2007**, 46, 8270; F. R. Fischer, P. A. Wood, F. H. Allen, F. Diederich, *Proc. Natl. Acad. Sci. U.S.A.* **2008**, 105, 17290; F. R. Fischer, W. B. Schweizer, F. Diederich, *Chem. Commun.* **2008**, 34, 4031.
- [13] E. Hartmann, R. M. Gschwind, *Angew. Chem. Int. Ed.* **2013**, 52, 2350-2354.
- [14] a) J. F. Teichert, B. L. Feringa, *Angew. Chem. Int. Ed.* **2010**, 49, 2486-2528. b) S. Streiff, C. Welter, M. Schelwies, G. Lipowsky, N. Miller, G. Helmchen, *Chem. Commun.* **2005**, 2957-2959. c) B. Bartels, C. García-Yebra, G. Helmchen, *Eur. L. Org. Chem.* **2003**, 1097-1103.
- [15] A. Alexakis, D. Polet, S. Rosset, S. March, *J. Org. Chem.* **2004**, 69, 5660-5667.
- [16] F. Hastreiter, *master thesis* **2014**.
- [17] R. Francke, G. Schnakenburg, S. R. Waldvogel, *Org. Lett.* **2010**, 12, 19, 4288-4291.
- [18] M. Nakajima, S. Hashimoto, M. Noji and K. Koga, *Chem. Pharm. Bull.* **1998**, 46, 11, 1814-1815.
- [19] Q.-S. Hu, D. Vitharana and L. Pu, *Tetrahedron: Asymmetry* **1995**, 6, 9, 2123-2126.

- [20] X.-W. Zou, L.-F. Zheng, L.-L. Wu, L.-L. Zong, Y.-X. Cheng, *Chin. J. Chem.* **2008**, 26, 2, 373-378.
- [21] N. H. Nguyen, C. Cougnon, F. Gohier, *J. Org. Chem.* **2009**, 74, 3955-3957.
- [22] C. R. Smith, T. V. RajanBabu, *Org. Lett.* **2008**, 10, 8, 1657-1659.
- [23] A. Alexakis, S. Gille, F. Prian, S. Rosset, K. Ditrach, *Tetrahedron Lett.* **2004**, 45, 1449-1451.
- [24] M. Bengalia, C. Biaggi, G. Celentano, *Synlett.* **2010**, 1, 0134-0136.
- [25] A. F. Abdel-Magid, K. G. Carson, B. D. Harris, C. A. Maryanoff, R. D. Shah, *J. Org. Chem.* **1996**, 61, 11, 3849-3862.
- [26] R. S. Paton, S. P. Fletcher, *ACS Catal.* **2017**, 7, 6729-6737.



## 8 Summary

In this thesis the focus lied on the NMR spectroscopic investigation of silicon Zintl anions in solution. Surprisingly, despite other Zintl anions of different homologues being well studied in solid-state, the silicon Zintl phases have been elusive for detailed studies in solution thus far. By enrichment of  $^{29}\text{Si}$  (the only NMR active isotope for silicon), NMR spectroscopy as a tool for the investigation of their behavior became accessible. Three novel silicon cluster species are presented in this thesis. Furthermore, three endohedral 12-vertex tin-antimony clusters were characterized. Diffusion-ordered spectroscopy (DOSY) was used as a tool for the detection of supramolecular aggregates. Lastly, the first experimental approach for measurement of dispersive interactions in phosphoramidite palladium complexes was discussed.

In chapter two the unprecedented protonated  $[\text{HSi}_9]^{3-}$  cluster was characterized. Using elegant 1D and 2D NMR spectroscopic methods, such as  $^1\text{H}^{29}\text{Si}$  DEPT,  $^1\text{H}^{29}\text{Si}$  HMQC and chemical exchange saturation transfer (CEST) experiments, the complete spin system of this unexpected species was found. Here, two resonances in the  $^{29}\text{Si}$  spectra were observed, i.e. one for the protonated Si-H moiety and one averaged for eight silicon atoms of a single  $\text{Si}_8$  entity. This was also verified by the observed coupling pattern (doublet of nonets at  $\delta = -158.5$  ppm for Si-H with  $^1J_{\text{SiH}} = 156$  Hz,  $\langle J_{\text{SiSi}} \rangle = 22$  Hz; and a doublet of doublets at  $\delta = -358.5$  ppm for the  $\text{Si}_8$  entity with  $\langle J_{\text{SiSi}} \rangle = 22$  Hz,  $\langle J_{\text{SiH}} \rangle = 3$  Hz). Comparison of theoretical calculations for the chemical shifts and the scalar coupling constants with the experimental values showed good agreement. Only the calculated coupling constants involving the Si-H moiety significantly deviated from the experimental ones. Indeed, CEST experiments revealed a H hopping process that leads to the observed reduced coupling constants, which was also corroborated by theoretical calculations. Additionally, theoretical calculations predicted two possible scrambling processes for the averaging of the  $\text{Si}_8$  entity, which in combination leads to a complete scrambling of all silicon atoms. In conclusion, the highly dynamic behavior of the protonated  $[\text{HSi}_9]^{3-}$  cluster was demonstrated, that was previously thought of being rigid owing to the relative strong Si-Si bonds.

Chapter three focuses on two additional silicon clusters found in solution, i.e.  $[\mu\text{-HSi}_4]^{3-}$  and  $[\text{Si}_5]^{2-}$ . For  $[\mu\text{-HSi}_4]^{3-}$  two  $^{29}\text{Si}$  resonances at  $\delta = -327.8$  ppm and  $\delta = -404.5$  ppm were observed. The former shows a triplet pattern ( $^1J_{\text{Si-Si}} = 45$  Hz), the latter a doublet of triplets ( $^1J_{\text{Si-Si}} = 45$  Hz,  $^1J_{\text{Si-H}} = 12$  Hz). Together with the extremely upfield shifted  $^1\text{H}$  resonance (triplet at  $\delta = -10.61$  ppm with  $^1J_{\text{Si-H}} = 12$  Hz) the structure of this protonated cluster was

revealed to be a tetrahedral  $[\text{Si}_4]^{4-}$  with an H atom being bridged over two vertices of the silicon tetrahedron. Thus, this bridging protonation mode depicts the missing link to borane chemistry. ELI-D and NBO analysis predicted the formation of a 3c-2e bond between Si-H-Si being the driving force in the protonation of  $[\text{Si}_4]^{4-}$  enabling the delocalization of the highly negative charges in the cluster. For the trigonal bipyramidal  $[\text{Si}_5]^{2-}$  cluster two  $^{29}\text{Si}$  resonances were observed, i.e. a quartet at  $\delta = +348.7$  ppm and a triplet at  $\delta = -347.8$  ppm ( $^1J_{\text{SiSi}} = 41.8$  Hz). Again, ELI-D and NBO analysis were performed, that revealed a non-classical Lewis structure with six electron-deficient 3c-2e bonds over each face of the cluster being highly delocalized. Thus, theoretical protonation in any position (terminally or bridging) leads to massive destabilization. In conclusion, delocalization of electrons proves to be the deciding factor for the easily achievable protonation of  $[\text{Si}_4]^{4-}$  and the unlikely protonation of  $[\text{Si}_5]^{2-}$ .

Chapter four focuses on the synthesis and characterization of three new ternary intermetalloid clusters, i.e. the asymmetrically occupied endohedral 12-vertex cluster  $[\text{Co}@\text{Sn}_6\text{Rb}_6]^{3-}$ , fully occupied  $[\text{Co}_2@\text{Sn}_5\text{Sb}_7]^{3-}$ , and  $[\text{Ni}_2@\text{Sn}_7\text{Sb}_5]^{3-}$ . Theoretical calculations and preliminary  $^{119}\text{Sn}$  NMR measurements were performed to investigate their behaviour in solution revealing their presence in solution.

Chapter five and six focus on the synthesis and characterization of supramolecules beyond the fullerene topology. In chapter five  $\text{P}_5$  building blocks, i.e.  $\text{Cp}^{\text{Bn}}$ -substituted pentaphosphaferrocene  $[\text{Cp}^{\text{Bn}}\text{Fe}(\eta^5\text{-P}_5)]$ , were used. By self-assembly with copper(I) iodide spherical supramolecular aggregates are achieved. The inorganic scaffold consists of *cyclo*- $\text{P}_5$  units and an expanded CuI framework with partial occupancies of few copper and iodine positions. It does not follow the fullerene-topology, because the CuI ladder structural motif provides no six-membered units, although twelve *cyclo*- $\text{P}_5$  rings are present. The  $\text{Cp}^{\text{Bn}}$  substituents enhance the solubility of these supramolecules thus, enabling NMR spectroscopic and MS investigations. Diffusion-ordered spectroscopy (DOSY) yielded a hydrodynamic radius  $r_{\text{H}}$  of 20.72 Å, which is in line with the crystal-derived radius of 18.5 Å. Thus, clearly indicating the supramolecule being present and stable in solution.

Chapter six addresses the reaction of *cyclo*- $\text{P}_4$  building blocks, i.e.  $[\text{Cp}^{\text{R}}\text{Ta}(\text{CO})_2(\eta^4\text{-P}_4)]$  (with  $\text{Cp}^{\text{R}} = \text{Cp}''$  or  $\text{Cp}'''$ ), with copper(I) halides yielding unprecedented supramolecules; truncated octahedrons, a peanut-shaped and a pear-shaped supramolecule. The reaction of the sterically more demanding  $\text{Cp}'''$ -substituted *cyclo*- $\text{P}_4$  building blocks with either copper(I) chloride or bromide yielded two truncated octahedron supramolecules with appropriate solubility, thus, enabling NMR investigations. Again, diffusion-ordered spectroscopy (DOSY) was used to investigate their behaviour in solution. The hydrodynamic radii of both supramolecules was estimated to be 10.73 (with CuCl)

and 9.45 Å (with CuBr). Despite the hydrodynamic radii being significantly smaller than the crystal-derived radii (12.5 and 12.7 Å, respectively), the DOSY experiments indicate the presence of intact spherical supramolecules in solution.

In chapter seven dispersive interactions in phosphoramidite palladium complexes were investigated using the supramolecular balance. A structural change of one of the hetero complexes for the model system was found by theoretical calculations, thus rendering the supramolecular balance not applicable. Therefore, the synthesis of asymmetric phosphoramidite ligands was attempted to ensure the same structure of both hetero complexes.



## 9 Appendix

### 9.1 Curriculum Vitae

**Florian Hastreiter**

born on 19<sup>th</sup> November 1988, Straubing



#### Education

- 02/2014 - 09/2018      PhD thesis, AK Gschwind, Universität Regensburg, Germany  
Focus: NMR spectroscopic elucidation of Zintl anions, dispersive interactions in palladium complexes, and fulleren topologica
- 04/2012 - 01/2014      MSc. Chemistry, Universität Regensburg, Germany  
Title of master thesis: "NMR Spectroscopic Investigation on Palladium Complexes"
- 10/2008 bis 04/2012      BSc. Chemistry, Universität Regensburg, Germany  
Title of bachelor thesis: „Synthesis of Dithienylmaleimides as Photo-Switchable Kinase Inhibitors“
- 09/1999 - 2008      Veit-Höser-Gymnasium, Bogen (Niederbayern), Germany  
Advanced courses: Mathematics, Biology

#### Experience

- 03/2010      Student trainee at VTA in Deggendorf (Niederbayern), Germany
- 04/2011      Trainee at VTA in Deggendorf (Niederbayern), Germany
- 02/2014 – 09/2018      Teaching assistant in laboratory courses and tutorials for chemists, biologists and teachers

#### Cooperations

- Prof. Dr. N. Korber, University of Regensburg  
Prof. Dr. M. Scheer, University of Regensburg  
Prof. Dr. S. Dehnen, Philipps-University of Marburg

## 9.2 Publications and Conferences

### Publications\*)

- “*A Nano-sized Supramolecule Beyond the Fullerene Topology*”:  
F. Dielmann, C. Heindl, F. Hastreiter, E. V. Peresykina, A. V. Virovets, R. M. Gschwind, and M. Scheer, *Angew. Chem. Int. Ed.* **2014**, 13605-13608.  
**DOI:** 10.1002/anie.201407120
- “*cyclo-P4 Building Blocks: Achieving Non-Classical Fullerene Topology and Beyond*”:  
F. Dielmann, E. V. Peresykina, B. Krämer, F. Hastreiter, B. P. Johnson, M. Zabel, C. Heindl, and M. Scheer, *Angew. Chem. Int. Ed.* **2016**, 14833-14837.  
**DOI:** DOI:10.1002/anie.201606074
- “*PPh<sub>4</sub>Cl in aqueous solution – the aggregation behavior of an antagonistic salt*”:  
R. Winkler, T. Buchecker, F. Hastreiter, D. Touraud, and W. Kunz, *Phys. Chem. Chem. Phys.* **2017**, 25463-25470.  
**DOI:** 10.1039/c7cp02677c
- “*The Structure of [HSi<sub>9</sub>]<sup>3-</sup> in the Solid State and Its Unexpected Highly Dynamic Behaviour in Solution*”:  
C. Lorenz, F. Hastreiter, J. Hioe, N. Lokesh, S. Gärtner, N. Korber, and R. M. Gschwind, *Angew. Chem. Int. Ed.* **2018**, 57, 39, 12956-12960.  
**DOI:** 10.1002/anie.201807080
- “*[Co@Sn<sub>6</sub>Sb<sub>6</sub>]<sup>3-</sup>: An Off-Center Endohedral 12-Vertex Cluster*”:  
R. Wilson, S. Dehnen, F. Hastreiter, P. Büschelberger, R. Wolf, R. M. Gschwind, K. Reiter, and F. Weigend, *Angew. Chem. Int. Ed.* **2018**, 57, 47, 15359-15363.  
**DOI:** 10.1002/anie.201807180
- “*Elusive Zintl Ions [ $\mu$ -HSi<sub>4</sub>]<sup>3-</sup> and [Si<sub>5</sub>]<sup>2-</sup> in Liquid Ammonia: Protonation States, Sites, and Bonding Situation Evaluated by NMR and Theory*”:  
F. Hastreiter, C. Lorenz, J. Hioe, S. Gärtner, N. Lokesh, N. Korber, and R. M. Gschwind, *Angew. Chem. Int. Ed.* **2019**, 58, 10, 3133-3137.  
**DOI:** 10.1002/anie.201812955

\*) Permission for partial or full reuse in this PhD thesis granted by Rightslink.

**International and National Conferences**

SMASH NMR Conference, Sep 2015, Baveno, Italy (Poster presentation).

SMASH NMR Conference, Sep 2016, San Diego, CA, USA (Poster presentation).

Bruker NMR User Conference, Nov 2014, Ettlingen, Germany (Poster presentation).